Thesis

Measurement of Cosmic-Ray Silicon Flux with the Alpha Magnetic Spectrometer on the International Space Station

CHEN, Yao

Abstract

The origin of the cosmic rays, high energy particles and ionized nuclei from outer space, is a long-standing question in astrophysics. In this thesis, the measurement of the cosmic-ray Silicon (Si) nuclei flux as a function of rigidity (momentum per unit charge) from 2.15 GV to 3 TV, based on 1.6 million Silicon nuclei events collected by the Alpha Magnetic Spectrometer (AMS-02) during its first 7 years (May 19, 2011 to May 26, 2018) of operations is presented. To study its spectral behavior, the measurement of the Oxygen and Neon (Ne) nuclei fluxes, based on the same 7-years data set with 12.5 million Oxygen and 1.8 million Neon nuclei events, as well as their flux ratios, Si/Ne, Ne/O and Si/O, are also discussed. Detail systematic uncertainty estimations for all three fluxes are discussed as well.

Reference

CHEN, Yao. *Measurement of Cosmic-Ray Silicon Flux with the Alpha Magnetic Spectrometer on the International Space Station*. Thèse de doctorat : Univ. Genève, 2020, no. Sc. 5481

DOI : 10.13097/archive-ouverte/unige:142602
URN : urn:nbn:ch:unige-1426023

UNIVERSITÉ DE GENÈVE
FACULTÉ DES SCIENCES
Département de Physique Nucléaire et Corpusculaire
Professeur Xin Wu

Measurement of Cosmic-Ray Silicon Flux with the Alpha Magnetic Spectrometer on the International Space Station

THÈSE

Présentée à la Faculté des sciences de l'Université de Genève
Pour obtenir le grade de Docteur ès sciences, mention physique

Par

Yao Chen
de Chine

Thèse N° 5481

GENÈVE
Atelier d'impression ReproMail
2020

UNIVERSITÉ DE GENÈVE

FACULTÉ DES SCIENCES

DOCTORAT ÈS SCIENCES, MENTION PHYSIQUE

Thèse de Monsieur Yao CHEN

intitulée :

«Measurement of Cosmic-Ray Silicon Flux with the Alpha Magnetic Spectrometer on the International Space Station»

La Faculté des sciences, sur le préavis de Monsieur X. WU, professeur associé et directeur de thèse (Département de physique nucléaire et corpusculaire), Monsieur A. TYKHONOV, professeur assistant (Département de physique nucléaire et corpusculaire) et Monsieur A. OLIVA, professeur (Istituto Nazionale di Fisica Nucleare, Bologna, Italia), autorise l'impression de la présente thèse, sans exprimer d'opinion sur les propositions qui y sont énoncées.

Genève, le 28 août 2020

Thèse - 5481 -

Le Doyen

N.B. - La thèse doit porter la déclaration précédente et remplir les conditions énumérées dans les "Informations relatives aux thèses de doctorat à l'Université de Genève".

Measurement of Cosmic-Ray Silicon Flux with the Alpha Magnetic Spectrometer on the International Space Station

Yao Chen

Abstract

The origin of the cosmic rays, high energy particles and ionized nuclei from outer space, is a long-standing question in astrophysics. The measurements of the primary cosmic ray nuclei spectra, such as Helium (He), Carbon (C) and Oxygen (O), provide essential information about the sources, acceleration mechanisms and propagation effects of the cosmic rays. As one of the most abundant primary cosmic ray species heavier than Carbon and Oxygen, the Silicon nuclei effectively samples different propagation volumes in the Galaxy and the precision measurement of its flux will deepen the understanding on the cosmic rays.

In this thesis, the measurement of the cosmic-ray Silicon (Si) nuclei flux as a function of rigidity (momentum per unit charge) from 2.15 GV to 3 TV, based on 1.6 million Silicon nuclei events collected by the Alpha Magnetic Spectrometer (AMS-02) during its first 7 years (May 19, 2011 to May 26, 2018) of operations is presented. To study its spectral behavior, the measurement of the Oxygen and Neon (Ne) nuclei fluxes, based on the same 7-years data set with 12.5 million Oxygen and 1.8 million Neon nuclei events, as well as their flux ratios, Si/Ne, Ne/O and Si/O, are also discussed. Detail systematic uncertainty estimations for all three fluxes are discussed as well.

Thesis Supervisor: Xin Wu

Title: Professeur associé

Résumé

L'origine des rayons cosmiques, des particules de haute énergie et des noyaux ionisés dans l'espace, reste de longue date une question ouverte en astrophysique. Les mesures des spectres des ions cosmiques primaires, comme l'hélium (He), le carbone (C) et l'oxygène (O), fournissent des informations essentielles sur leurs sources et leurs mécanismes d'accélération et de propagation. Étant l'une des espèces les plus abondantes parmi les rayons cosmiques plus lourds que le carbone et l'oxygène, les noyaux de silicium échantillonnent efficacement différents volumes de propagation dans la galaxie. La mesure précise de leur flux approfondira ainsi la compréhension des rayons cosmiques.

Dans cette thèse est présentée la mesure du flux de noyaux de siliciums (Si) en rayons cosmiques en fonction de la rigidité (impulsion par unité de charge) de 2,15 GV à 3 TV, basée sur 1,6 million d'événements récoltés et identifiés comme noyaux de silicium par le Spectromètre Magnétique Alpha (Alpha Magnetic Spectrometer, AMS-02) au cours de ses 7 premières années d'exploitation (du 19 mai 2011 au 26 mai 2018). Pour étudier le comportement spectral du silicium, la mesure des flux d'oxygène et néon noyaux, basée sur le même ensemble de données sur 7 ans avec 12,5 millions de noyaux d'oxygène et 1,8 million de noyaux de néon, sont aussi ainsi que leurs ratios de flux, Si/Ne, Ne/O et Si/O, sont également discutés. Finalement, les estimations détaillées des erreurs systématique pour les trois flux sont également discutées.

Acknowledgements

First or all, I would like to thank Prof. Xin Wu for offering me the chance to pursue my Ph.D with the AMS group in University of Geneva. I've been benefit a lot from valuable suggestions about my analysis and future career from Prof. Xin. I would like to thank Dr. Mercedes Paniccia for her supervision through my Ph.D. We've been discussing details on my analysis, doing enormous rehearsals and preparations for all kinds of meetings, and revising my thesis almost word by word. I would also like to thank Dr. Qi Yan for inspiring discussions on my work. My understanding on the AMS detector and data analysis was really deepened through his sharing of his expertise and experiences. I'm also very grateful to Dr. Alberto Oliva for his suggestions on my analysis, preparation of the application for fellowship together with me and Mercedes, and assistance on searching for my future position.

I've also benefited greatly from the opening environment of the AMS collaboration and the University of Geneva. Prof. Samuel Ting and other senior researchers in AMS and University of Geneva shows me that the rigorous attitude towards research is one of the most important thing in research. Participation and presentation in regular meetings gave me precious opportunities to actively involve in the research frontier. I would also like to thank my colleagues in AMS collaboration and University of Geneva for helpful discussions on both physics and daily life.

I would also like to thank my thesis committee members for their inspiring feedback and insightful questions about my thesis.

During my Ph.D life, I gained great supports from my family, especially my parents, XiaoWen Chen and Wenli Bin. At weekends, I would discussed my confusions on work and shared my daily life with them, obtaining helpful suggestions from them. Their experience, wisdom and unconditional love had guided me through all frustrated periods. And I really

hope that my grandmother, Jingqing Chi, would have known that her grandson is doing well.

At the end, I would like to say special thanks to the Korean group, Dreamcatcher. Their musics and performances have been great supports and inspirations to my life.

The experience as a Ph.D student in the University of Geneva working in AMS has deeply reshaped my way of thinking and expanded my understanding about astrophysics. During these years, I got a clearer vision of my career and gained even more interests to continue decoding the message from the cosmos. All the precise memories will be treasures to my life and I'm very grateful to everyone who have been supporting me during these years.

Contents

List of Figures

Introduction

Cosmic rays (CRs), energetic particles and completely ionized nuclei, was confirmed to come from "over the sky" and have an extraterrestrial origin after Hess's balloon experiment in 1912. Cosmic ray energy spectral had been measured over a large energy span from a few GeV up to EeV and it can be approximated by a single power law. The chemical composition of cosmic rays is found to be similar as the one of the solar system, with the exception of the overabundance of Lithium, Beryllium, Boron and sub-Iron group. These elements are thought to be mainly produced by fragmentation of heavier comic ray nuclei during their propagation. Based on these observations, cosmic rays are considered to be mainly produced at supernova remnants, accelerated by supernova shock wave and propagate in the Galaxy diffusively.

Over the last decades, the energy spectrum of individual cosmic ray species had been measured by space-borne detectors with unprecedented precision, revealing new and astonishing properties and challenging the standard picture of cosmic ray origin, acceleration and propagation. One of these experiments is the *Alpha Magnetic Spectrometer* (AMS-02), a large acceptance energetic particle detector mounted on the International Space Station (ISS) in May 19th, 2011. AMS has measure the individual cosmic ray nuclei fluxes from Helium up to Oxygen [1–4] and an unexpected spectral break are found in all fluxes at high rigidity. The precision measurement of heavier nuclei, such as Neon, Magnesium and Silicon, will determine whether the spectral break is a general feature of cosmic ray.

This thesis is organized as following:
Chapter 1 briefly reviews the observational facts of cosmic rays, the standard diagram of source, acceleration and propagation of galactic cosmic rays, and the anomaly in the galactic cosmic ray revealed by precision measurements.

Chapter 2 introduces the setup and performance of the AMS detector, the operation of AMS in the space, the trigger logic, the data acquisition system and the Monte Carlo simulation.

Chapter 3 discusses in detail the calculation of Silicon nuclei flux as a function of rigidity from 2.15 GV to 3.0 TV based on the AMS first seven year data set (May 19, 2011 to May 26, 2018). The systematic uncertainty studies are presented in detail as well.

Chapter 4 presents the Oxygen and Neon nuclei fluxes calculated based on the same data set as for Silicon. Si-to-Ne, Ne-to-O and Si-to-O flux ratios are calculated as well, and their rigidity dependences are discussed.

Chapter 1

Introduction of cosmic rays

1.1 Cosmic rays in a nutshell

By the end of 19th century, the self discharge of electroscope was explained by the ionization of nearby air while the origin of the ionization remained unknown. It was only until Hess discovered the increased of ionization with respect to altitude on manned balloon on 1912, that the mysterious radiation, known as *Cosmic Rays*, was confirmed to be coming from "over the sky", i.e. having an extraterrestrial origin.

Before the modern era of particle accelerators and accelerator based experiments starting from late 1950s, cosmic ray experiments was the leading field on new particle discoveries as the outcome of "cosmic accelerator and collider" - the positron e^+ in 1932 [5]; the muon μ^- in 1936 [6]; the pions $\pi^\pm$ in 1947 [7].

Nowadays, cosmic ray experiments are focusing on the energy spectrum precision measurement for all-particle and individual species, and the determination of composition in different energy range with balloon, space-borne and ground-based high precision detectors, which provide information about the sources, acceleration mechanisms and propagation effects of cosmic rays. In the next decades before the establishment of next generation particle accelerator, cosmic ray or astrophysics might again be the major contributor to the discoveries of new physics, including indirect dark matter detection and Lorentz invariant violation observation.

In this section, major experimental understanding on cosmic rays, including energy spectra, chemical composition and anisotropy on the arriving directions, will be presented.

Depends on the context, different energy variables might be used to describe cosmic rays, including:

1. Magnetic rigidity R, defined as the product of the gyroradius rho and the magnetic field strength B:
$$R = \frac{pc}{Ze} = \rho B, \tag{1.1}$$
with p the momentum of the particle, c the speed of light, and Ze the charge of the particle. When discussing the acceleration and propagation of cosmic ray where magnetic field plays the important role, the rigidity is preferred. Regardless of species (charge and mass), particles with same rigidity will have the same trajectory in a magnetic field.

   In magnetic spectrometer experiments, the rigidity of the incoming cosmic ray is measured directly hence the spectrum is often presented as a function of rigidity.
2. Energy-per-nucleon, which is approximately conserved during nuclear fragmentation. Therefore, this variable is used when nuclei fragmentation due to interaction with interstellar gas during propagation, or with the atmosphere when entering Earth is the key consideration.
3. Total energy of the nuclei. For space experiments using calorimeters or ground-based air shower detectors, the total energy of incoming particle is measured directly with the energy deposited in the calorimeter or in the air-shower.

1.1.1 Cosmic ray energy spectra

The measured all-particle cosmic ray spectrum as function of kinematic energy spanning from a few GeV up to EeV is shown as Fig. 1-1.

At energy below a few GeV, most charged particles observed near Earth are produced by the nearest particle accelerator - the sun, or trapped particle in the Earth's magnetic field. For low energy charged particles coming from outside the solar system, the presence of the solar wind, an interplanetary plasma carrying turbulent magnetic field, largely modulate their property. Time variations and anti-correlation with solar activities are observed for the intensity of cosmic rays with rigidity below 10 GV [9]. The presence of the Earth's magnetic field also shields the penetration of low energy cosmic rays. In

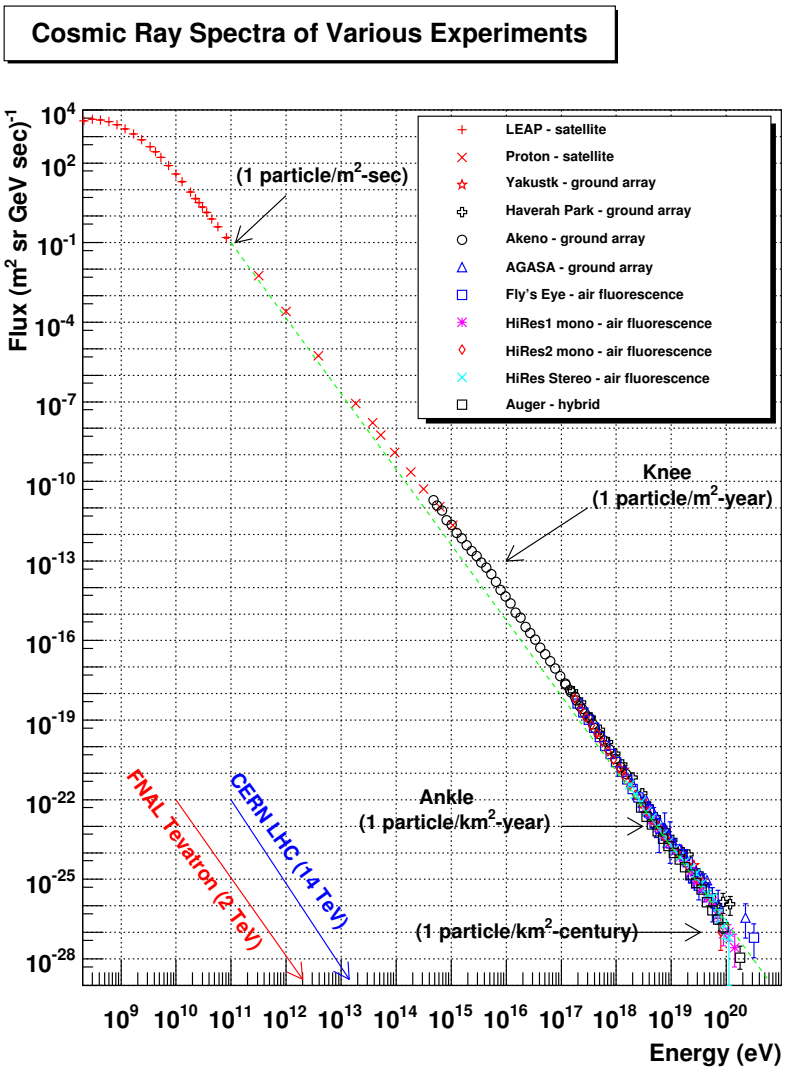

Figure 1-1: Differential all-particle cosmic ray energy spectrum [8].

conclusion, the observed spectra of cosmic rays, especially at low energy, could be largely modulated by the solar system before being measured by experiments near Earth.

Starting from a few tens of GV, where the influence of the solar wind and the Earth's magnetic field are negligible, the cosmic rays can be measured directly by balloon and space-borne detectors or indirectly by ground-based detectors through their air-shower production after penetrating the atmosphere. Through the continuous measurements after Hess's experiment, the all-particle energy spectrum is observed to be an approximate single power law, spanning from a few GeV up to beyond 100 TeV with rapidly decrease

of intensity with respect to the cosmic ray energy, and it can be described as

$$\frac{dN}{dE} \propto E^{-\alpha}, \tag{1.2}$$

with differential spectral index $\alpha \approx 2.7$.

Another way to present the spectrum is to multiply it by an exponential factor E^{β}. By choosing $\beta = 2.6$, the spectrum reveals deviations from a single power law, as shown in Fig. 1-2.

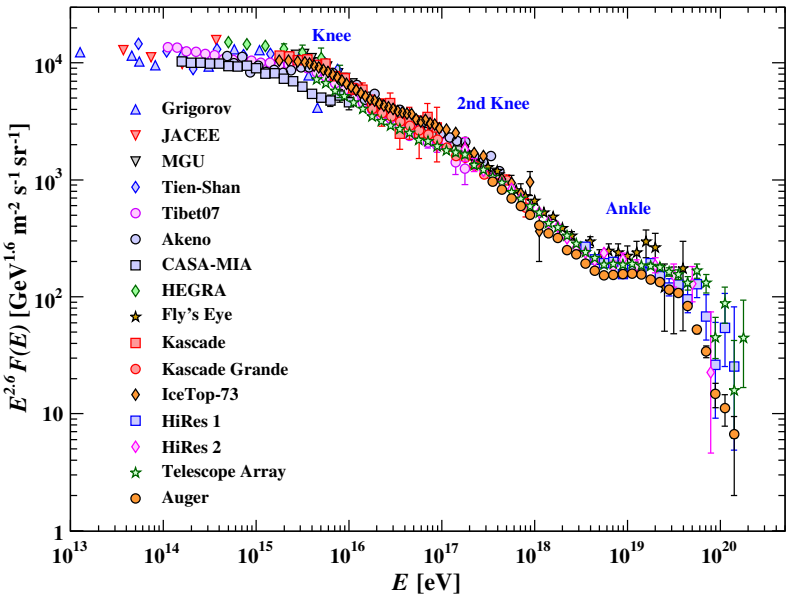

Figure 1-2: The all-particle spectrum as a function of E (energy-per-nucleus) from air shower measurements. The spectrum has been multiplied by $E^{2.6}$ [9].

Deviations of energy spectrum from single power law are often called softening (hardening) with smaller (larger) spectral index, indicating the reduced (increased) population of higher energy. From Fig. 1-2, transition points of the all-particle energy spectrum where the spectrum clearly deviates from a single power law can be spotted:

1. at energy $\sim 3 \times 10^{15}$ eV, the spectrum becomes steeper, i.e. softer, and this spectral feature is known as the *knee* of energy spectrum [10];

2. at energy $\sim 4 \times 10^{17}$ eV, the spectrum has a further softening and the transition is called the *second knee*;
3. at energy $\sim 4 \times 10^{18}$ eV, the spectrum has a hardening, which is called the *ankle* of cosmic ray spectrum [11];
4. finally, a cutoff is found at the energy $\sim 10^{20}$ eV [12, 13], representing the maximum cosmic ray energy ever measured on Earth.

The understanding of these structures will be discussed at Section 1.2.4.

1.1.2 Chemical composition

Cosmic rays are mostly protons ($\sim$ 90%), Helium nuclei ($\sim$ 10%), heavier nuclei with charge Z larger than 2 ($\sim$ 1%) together with electrons ($\sim$ 1%) and trace of anti-matter. By comparing the chemical composition of cosmic rays with those of different astrophysical objects, the sites at which cosmic rays are injected into acceleration might be determined [14]. Figure 1-3 shows the comparison between the chemical abundance of cosmic rays and of the solar system for Z up to 29 (Copper). These two similar compositions indicate a common origin of stellar nucleosynthesis for cosmic rays.

Abundances of cosmic rays and the solar system both show the odd-even effect, with the even Z nuclei being more abundant than the odd Z nuclei. However, there are two distinct differences between these chemical abundances.

Firstly, the relative abundances for proton (H) and Helium (He) in cosmic rays are smaller compared to those in the solar system, the origin of which is not fully understood. The smaller abundances might be related to 1) the less injection of protons into the acceleration processes due to that hydrogen is relatively more difficult to ionize, or 2) less abundances of H and He in the source of cosmic ray compared to those of the solar system [14].

Another difference, broadly understood as cosmic ray propagation effect in the galaxy, is the enrichment of two groups of elements which are not the end-product of the stellar nucleosynthesis: Li, Be, B and the sub-Fe group Sc, Ti, V, Cr, Mn. The overabundance of these elements is the result of spallation of heavier nuclei interacting with the interstellar medium (ISM): Li, Be and B (sub-Fe group) are mainly produced from C and O (Fe)

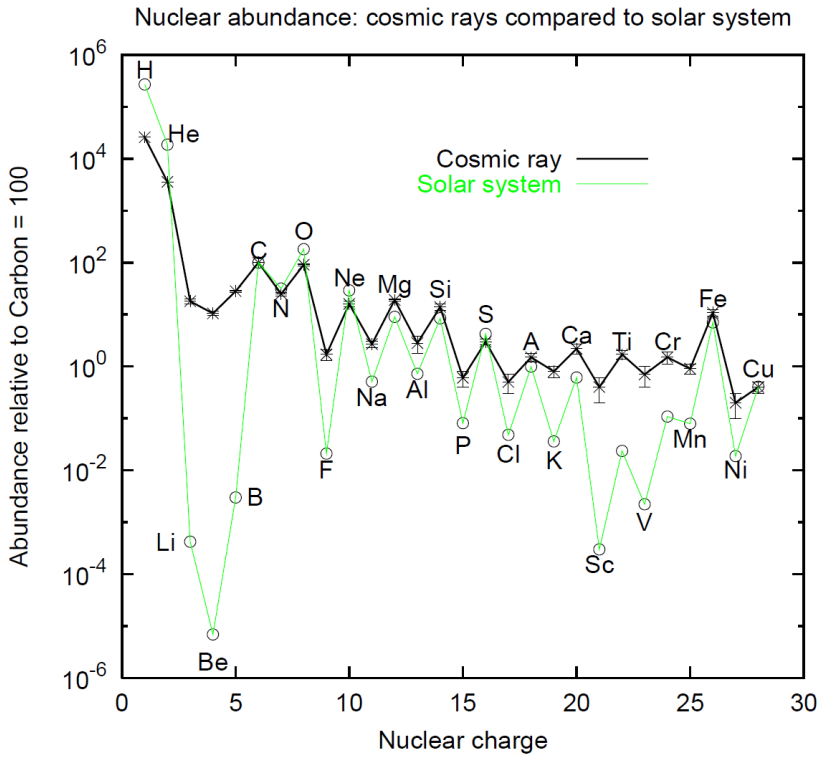

Figure 1-3: Relative abundance in cosmic rays comparing with the one in the solar system. The abundances of carbon are normalized to 100. Taken from [15].

as they're the most abundant nearby heavier nuclei. The orders of magnitude higher abundances for all the other odd Z nuclei in the cosmic ray also indicate the dominant origins due to the fragmentation of heavier nuclei during propagation.

Because of different origins, cosmic ray species that are produced and accelerated at sources and injected into ISM are called *primary cosmic rays*, while those majorly produced by nuclei spallation of heavier nuclei during propagation are called *secondary cosmic rays*. Together with the precise knowledge of nuclei inelastic cross sections, the secondary-to-primary ratios of cosmic ray can be used as a powerful tool to study the cosmic ray propagation and its confinement in the galaxy, for example the residence time τ_{res} of cosmic rays in the galaxy disk, which is condensed and considered as the place where most of the fragmentation happens.

1.1.3 Anisotropy

Highly isotropic arriving directions of galactic cosmic rays at large energy ranges is an evidence of the diffusion propagation of cosmic rays in the galaxy, which efficiently randomizes their directions. Such a diffusion also introduces a small dipole moment in the arriving direction of cosmic rays [16], with dipole vector points roughly to the center of the Galaxy center and its amplitude has a similar energy dependence as the diffusion coefficient which is a single power law as will be seen in Section 1.2.1.

A more complicate pattern of anisotropies, however, is observed in the arriving direction distribution of TeV-PeV cosmic rays (Tibet ASγ [17, 18], Super-Kamiokande [19], Milagro [20], EAS-TOP [21], MINOS [22], ARGO-YBJ [23, 24] and HAWC [25]; IceCube [26] and IceTop [27]). These residual anisotropies, on top of the dipole moment due to spatial diffusion, could be explained as inhomogeneities in the cosmic ray source locations, especially the existence of nearby sources. Hence the anisotropy can be used for the study of nearby cosmic ray sources. The relative motion of the observer, the solar system, to the frame where cosmic ray is isotropic [28, 29] could be another source to the cosmic ray anisotropies.

1.1.4 Detection of cosmic ray

Detection of cosmic rays can be categorized into:

- Direct measurement: detection before cosmic rays fragmentation when traversing the atmosphere or even before entering the atmosphere, which is very precise as cosmic rays are detected intact;
- Indirect measurement: detecting cosmic rays through secondary showers produced when traversing the atmosphere.

1.1.4.1 Direct measurements

Limited by the space technology of sending large detector into the space, in most cases direct measurements have limited acceptance or/and exposure time. Hence direct measurement might not be able to accumulate enough statistic for the detection of high energy cosmic rays due to the exponential drop of the cosmic ray spectrum. After Hess identified

the extraterrestrial origin of cosmic rays, with ever improving space direct measurements are done by balloons and satellites or detectors mounted in space stations.

1.1.4.2 Indirect measurements

Built on the ground with the ability of achieving extremely large acceptance and/or exposure time, the indirect cosmic ray measurements can detect cosmic ray with ultra-high energy. However, indirect measurements have two major drawbacks due to the nature of the dependence on the electromagnetic and/or hadronic cascades in the atmosphere above the ground:

- they're not efficient on distinguishing the chemical composition since indirect measurements only detect the secondary particles from the shower of cosmic rays. Composition measurement from indirect ground measurement depends strongly on the specific simulation models thus have large uncertainty;
- the accuracy of energy measurements is limited due to the large fluctuation on the shower generation for individual events.

1.2 Theoretical understanding of cosmic rays

As discussed before, the composition of cosmic ray and the steep spectra implies that the energy density of cosmic ray are carried mostly by GeV proton and Helium nuclei. Given that the typical few μG magnetic field of ISM, the gyroradius of the bulk of cosmic ray nuclei, $\sim 10^{12}$ cm, is orders of magnitude smaller than any galactic length scale, such as the size of the Milky way 30 kpc $\approx 10^{22}$ cm. Hence the bulk of cosmic rays should have a Galactic origin, i.e. accelerated and confined within the galaxy, thus called *galactic cosmic ray*. For cosmic ray with ultra-high energy (above a few PeV), the magnetic field is not strong enough to confine them inside the galaxy and they're considered as *extragalactic* origin instead.

In this section, the source, acceleration and propagation of the galactic cosmic rays will be discussed in a "reverse" manner: Cosmic ray propagation will be discussed first and, together with the observed cosmic ray fluxes, properties of the injection spectrum will be presented; acceleration mechanisms will then be discussed; finally, possible sources

of cosmic rays providing matching chemical composition and the capability of acceleration will be introduced. At the end, some open problems related to both the galactic and the extragalactic cosmic rays will be covered.

1.2.1 Propagation within the Interstellar Medium

As charged particles, cosmic rays are coupled to the magnetic field of ISM, and will be disturbed, lose energy or even be re-accelerated during the propagation. Cosmic rays propagation in ISM is then in most cases considered as a magneto-hydrodynamic (MHD) problem.

1.2.1.1 propagation equation

Cosmic rays propagation can be modeled by a propagation equation starting from the conservation of particle without generation (source) or annihilation (sink) [14], i.e. the continuity equation:

$$\frac{\partial N_i}{\partial t} + \boldsymbol{\nabla} \cdot \boldsymbol{J} = 0, \tag{1.3}$$

where $N_i = N_i(\boldsymbol{x}, t, E)$ is the number of particles at given space-time with energy E for species i, and $\boldsymbol{J}$ is the particle flow.

Considering that the particle flow is generated by diffusion, i.e. the Fisk's Law of diffusion,

$$\boldsymbol{J} = -D\boldsymbol{\nabla} N_i(\boldsymbol{x}, t, E), \tag{1.4}$$

with D the diffusion coefficient. The movement of the ISM with velocity field $\boldsymbol{V}$, by galactic wind for example, adds a convection term $\boldsymbol{\nabla} \cdot (\boldsymbol{V} N)$ to the particle flow. Eq. (1.3) then becomes the propagation equation with only diffusion and convection:

$$\frac{\partial N_i}{\partial t} - \boldsymbol{\nabla} \cdot (D\boldsymbol{\nabla} - \boldsymbol{V}) N_i = 0. \tag{1.5}$$

Now the gain and loss of cosmic rays along their propagation needs to be considered. Sources distributed on the disk of galaxy, which produce, accelerate and inject cosmic rays into the ISM, bringing a source term $Q_i(\boldsymbol{x}, t, E)$ for nuclei species i into the propagation equation. During the propagation, cosmic rays will be lost due to the collision with ISM

or decay for unstable nuclei. They can also be produced by spallation or decay from heavier nuclei. Including all these gain and loss processes, Eq. (1.5) becomes

$$\begin{aligned}&\frac{\partial N_i}{\partial t} - \boldsymbol{\nabla}\cdot(D\boldsymbol{\nabla} - \boldsymbol{V})N_i = \\ &Q_i(\boldsymbol{x}, t, E) - (\beta c n_{gas}\sigma^i_{inel} + \Gamma^i)N_i + \Sigma_j\left[\int_E^\infty dE' \frac{d\sigma^{j\to i}(E', E)}{dE} + \Gamma^{j\to i}\right] N_j.\end{aligned} \tag{1.6}$$

$n_{gas} = \rho/m_H$ is the number density of ISM gas assuming ISM only composed of Hydrogen, σ^i_{inel} and Γ^i the total inelastic cross section and the decay rate of particle i, $\sigma^{j\to i}$ the cross section for particle j producing particle i, $\Gamma^{j\to i}$ the decay rate for particle j producing particle i.

The differential propagation equation is highly non-linear and depends on a detail description of particles decay and their inelastic cross section. Hence the equation can either be solved numerically or solved analytically for simplified forms based on different assumptions and boundary conditions. One of the most broadly adopted simplified model of cosmic ray propagation, the Leaky box model, will be introduced. Propagation properties interpreted from the measured cosmic rays data will be discussed as well.

1.2.1.2 solving the propagation equation - the Leaky box model

The leaky box model [30] is a steady-state simplification of the cosmic ray propagation, basing on the assumption that cosmic rays freely propagate in a finite volume of galaxy with a constant probability per unit of time of escaping the confinement volume, $1/\tau_{esc}$.

The leaky box assumption simplifies the diffusion and convection term into:

$$-\boldsymbol{\nabla}\cdot(D\boldsymbol{\nabla} - \boldsymbol{V})N_i \to N_i/\tau_{esc} \tag{1.7}$$

Considering cosmic ray N_i to be in an equilibrium state, i.e. the diffusion and convection is compensated by all the other gain and loss processes, the time variation of N_i vanished. With the approximation that the energy per nucleon is conserved during spallation, the integration on energy for cross sections can be simplified to: $\int_E^\infty dE' \frac{d\sigma^{j\to i}(E',E)}{dE} \to \sigma^{j\to i}(E)$.

Finally, the propagation equation Eq. (1.6) will be simplified for an equilibrium state into:

$$\frac{N_i}{\tau_{esc}} = Q_i(\boldsymbol{x}, t, E) - (\frac{\beta c \rho}{m_H}\sigma^i_{inel} + \Gamma^i)N_i + \Sigma_j \left[\sigma^{j\to i}(E) + \Gamma^{j\to i}\right] N_j. \tag{1.8}$$

From Eq. (1.8), expressions of primary and secondary cosmic ray energy spectrum can be derived with further assumption.

Considering a stable primary cosmic ray nuclei for which the secondary production from heavier nuclei fragmentation and decay during propagation is negligible, i.e. $\Gamma^P = 0$, $\sigma^{j\to P} = 0$ and $\Gamma^{j\to P} = 0$, the solution for Eq. (1.8) is

$$\frac{N_P}{\tau_{esc}} = Q_P - \frac{\beta c \rho}{m_H}\sigma^P_{inel} N_P \to N_P = \frac{Q_P \tau_{esc}}{1 + \lambda_{esc}/\lambda_P} \tag{1.9}$$

with $\lambda_P = m_H/\sigma^P_{inel}$ the interaction length for nuclei and λ_{esc} the escape length (or the so-called *grammage* [31])

$$\lambda_{esc} = \beta c \rho \tau_{esc}. \tag{1.10}$$

λ_P (λ_{exc}) can be understood as the average amount of ISM material traversed by cosmic rays before interaction (escape).

For pure secondary cosmic ray nuclei which has no primary sources, the source term vanishes ($Q_S(E) = 0$). Hence Eq. (1.8) becomes

$$\frac{N_S(E)}{\tau_{esc}} = -(\frac{\beta c \rho}{\lambda_S} + \Gamma^S)N_S(E) + \frac{\beta c \rho}{m_p}\sum_j \sigma_{j\to S} N_j(E), \tag{1.11}$$

with j sums over all heavier nuclei. If the secondary is stable, i.e. $\Gamma^S = 0$, Eq. (1.11) further simplifies to

$$\frac{N_S(E)}{\tau_{esc}} = -\frac{\beta c \rho}{\lambda_S} N_S(E) + \frac{\beta c \rho}{m_p}\sum_j \sigma_{j\to S} N_j(E). \tag{1.12}$$

1.2.1.3 ratio of the stable secondary to primary cosmic ray

First, the secondary-to-primary ratio where both are stable will be discussed. The Boron-to-Carbon ratio is one of them, which has been measured by many experiments with large energy coverage.

Boron is stable and can be viewed as purely secondary cosmic rays with no primary contribution. Furthermore, the secondary production of Boron is dominated by productions from Carbon and Oxygen, hence the solution of propagation equation for boron will be

$$\frac{N_B}{\tau_{esc}} = -\frac{\beta c\rho}{\lambda_B} N_B + \frac{\beta c\rho}{m_p} \left[\sigma_{C\to B} N_C + \sigma_{O\to B} N_O\right]. \tag{1.13}$$

Since the Carbon flux is nearly identical to the Oxygen flux ($N_C \approx N_O$), the Boron-to-Carbon ratio can be approximated as

$$\frac{N_B(E)}{N_C(E)} \approx \frac{\lambda_{esc}(E)}{1+\lambda_{esc}(E)/\lambda_B} \frac{\sigma_{C\to B} + \sigma_{O\to B}}{m_p}. \tag{1.14}$$

At high rigidity, the relation $\lambda_{esc} \ll \lambda_B$ holds, i.e. Boron is much more likely to escape the confinement volume before interaction with ISM, hence the spectrum of Boron-to-Carbon ratio becomes

$$\frac{N_B}{N_C} \approx \frac{\sigma_{C\to B} + \sigma_{O\to B}}{m_p} \lambda_{esc} \propto \lambda_{esc}, \tag{1.15}$$

i.e. the B/C ratio reflects the rigidity dependence of the λ_{esc} at high energy. The precision measurement of the B/C ratio by AMS-02 [32] shows that the escape length λ_{esc} has a power law behavior at high rigidity:

$$\lambda_{esc} \propto R^{-\delta}, \tag{1.16}$$

with $\delta \simeq 1/3$. A few implications on cosmic ray sources can be drawn from the power law behavior of λ_{esc}.

First of all, from Eq. (1.9) together with Eq. (1.16), the behavior of source term for primary cosmic rays can be interpreted. For protons, the relation $\lambda_{esc} \ll \lambda_p$ holds for all energies, i.e. protons are very likely to escape before interaction with ISM. Hence Eq. (1.9) for proton can be simplified to

$$N_p(E) \approx Q_p(E)\tau_{esc}(R) \tag{1.17}$$

Considering the single power law behavior of observed proton spectrum $N(E) \propto E^{-\gamma \approx -2.7}$ and Eq. (1.16), the energy dependence of source term for protons will also be single power

law:

$$Q_p(E) \propto E^{-(\gamma-\delta)} = E^{-\alpha}, \tag{1.18}$$

with $\alpha = \gamma - \delta \approx 2.1$. In other words, for a proton flux that its density is decreased in the confinement volume purely due to propagation effects, the observed spectrum is softer compared to the source term due to the escape of particles through diffusion.

Another extreme case will be $\lambda_{esc} \gg \lambda_p$, indicating that nuclei are most likely to fragment before escaping from the confinement volume, which is valid for low energy Iron nuclei as its inelastic cross section is much higher than proton. The spectrum for low energy Iron can be obtained from Eq. (1.9) as

$$\begin{aligned} N_{Fe}(E) &= \frac{(Q_{Fe}(E)\tau_{esc}) \cdot \lambda_{Fe}/\lambda_{esc}}{(1 + \lambda_{esc}/\lambda_{Fe}) \cdot \lambda_{Fe}/\lambda_{esc}} \\ &= \frac{1}{\beta c \rho} \frac{Q_{Fe}(E)\lambda_{Fe}}{\lambda_{Fe}/\lambda_{esc} + 1} \\ &\approx \frac{1}{\beta c \rho} Q_{Fe}(E)\lambda_{Fe} \propto Q_{Fe}(E), \end{aligned} \tag{1.19}$$

by neglecting the energy dependence of ρ and λ_{Fe} at the last step. It means that the observed low energy Iron spectrum represents the injection spectrum from sources after acceleration, hence the Iron injection spectrum can be directly obtained from the local Iron flux measurement without consideration of propagation effects. A softer Iron spectrum at high energy is also predicted since the relation $\lambda_{esc} \ll \lambda_p$ will finally achieved as λ_{esc} decreases faster than λ_{Fe} for increasing energy [33]. In other words, the Iron spectrum will start as Eq. (1.19) at low energy and soften to Eq. (1.18) at high energy by a single power law $E^{-\delta}$.

Finally, the total required power from cosmic ray sources can also be calculated. The power of cosmic rays leaking out of the Galaxy, or the luminosity L_{CR} is:

$$L_{CR} = \int dE \int_V dx \frac{E N_{CR}(E, x)}{\tau_{esc}(E)} \tag{1.20}$$

with $N_{CR}(E, x)$ the energy differential number density of cosmic rays. By assuming an identical density for cosmic rays over the Galaxy and using the local measured result as

reference, the spatial integration simplifies to

$$\int_V dx E N_{CR}(E,x) \rightarrow E N_{CR,local}(E) V = \rho_{CR,local} V,$$

with $\rho_{CR,local}$ the local total cosmic ray energy density and V the volume of the Galaxy. Furthermore, due to the steep power law, the bulk energy of cosmic rays is carried by GeV particles. Hence the energy integration can be replaced by the value of density at $\sim$ GeV. Also replacing the τ_{esc} with $\lambda_{esc} = \beta c \rho \tau_{esc}$, the luminosity of cosmic ray finally becomes

$$L_{CR} \approx \frac{\rho_{CR,local}(\sim GeV)\rho_{ISM} V}{\lambda_{esc}(\sim GeV)} \approx \frac{\rho_{CR,local}(\sim GeV)\rho_{disk} V_{disk}}{\lambda_{esc}(\sim GeV)}, \tag{1.21}$$

by considering that the density of the Galaxy disk dominates while the halo is almost empty. With the typical disk density of 1 proton/cm^3, the disk thickness of 200 pc and the disk radius of 15 kpc, together with the $\rho_{CR,local} \sim 1$eV/cm^3 and the expression for λ_{esc} (Eq. (1.16)), the total luminosity of cosmic ray is found to be $\sim 10^{41}$ erg/s [34].

1.2.1.4 ratio of unstable secondary - "cosmic ray radioactive clock"

From the ratio of the stable secondary (such as boron) to primary ratio, only the energy dependence of λ_{esc} is obtained, which is the product of ρ and τ_{esc}. It can be understood in the following way: the probability for primary cosmic ray to fragment and produce secondaries depends not only on the time it travels (τ_{esc}) but also on the density of the target, i.e. the ISM density ρ.

The decay of nuclei depends only on the traveling time τ_{esc} and is independent of the density ρ of the confinement material. In order to separate the degeneracy between ρ and τ_{esc}, the unstable to stable secondary cosmic ray flux ratio can be used.

Dividing the expression for unstable and stable secondary flux obtained from the Leaky box model, Eq. (1.11) and Eq. (1.12), the unstable to stable secondary ratio is

$$\frac{N_{US}}{N_{SS}} = \frac{\sigma_{P\rightarrow US}}{\sigma_{P\rightarrow SS}} \frac{1/\tau_{esc} + \beta c\rho/\lambda_{SS}}{1/\tau_{esc} + \beta c\rho/\lambda_{US} + \Gamma^{US}} = \frac{\sigma_{P\rightarrow US}}{\sigma_{P\rightarrow SS}} \frac{1 + \lambda_{esc}/\lambda_{SS}}{1 + \lambda_{esc}/\lambda_{US} + \tau_{esc}\Gamma^{US}}, \tag{1.22}$$

by assuming that one primary nuclei species P dominates the production of these two secondary cosmic rays, with $\sigma_{P\rightarrow US}$ and $\sigma_{P\rightarrow SS}$ cross sections for nuclei P producing

unstable and stable secondary respectively. The assumption is also equivalence to that all the primary nuclei contributions to both secondaries have same spectrum shape, in this case the cross sections will be the total cross section of all these primary cosmic rays. The obtained unstable to stable secondary ratio is a function of the escape length λ_{esc} and explicitly of the escape time τ_{esc} as well. With the escape length estimated from stable secondary-to-primary ratio, the escape time can be obtained from the unstable to stable secondary ratio with a careful consideration of all possible partial inelastic cross sections, which is found to be 14.5 ± 1.3 Myr from the ^{10}Be/^{9}Be ratio measured by the Cosmic-Ray Isotope Spectrometer (CRIS) [35].

With the obtained λ_{esc} and τ_{esc}, the average matter density encountered by primary cosmic rays before escaping is found, with Eq. (1.10), to be 0.358 ± 0.032 cm^{-3}, which is smaller than the typical value of ~ 1cm^{-3} for the galactic disk. This can be understood as that cosmic rays see an average lower density than that in the galaxy disk, indicating a large fraction of propagation outside the dense galactic disk before escaping.

1.2.2 Acceleration mechanism

In the Universe, there are several phenomena which are capable of accelerating particles to high energy. Up to now, many acceleration mechanisms have been proposed based on these phenomena while none of them have been firmly confirmed or excluded as the actual acceleration mechanism for cosmic rays. It indicates not only the lack of knowledge of cosmic ray acceleration, but also a possible combination of different acceleration mechanisms dominating in different energy regions.

1.2.2.1 Interpretation for single power law spectrum

The power law behavior of the cosmic ray spectrum is a result of an energy-independent *relative* energy gain process, which doesn't depend on the details of acceleration mechanisms. This energy-independent relative gain property can be expressed as:

$$E_n = E_0(1+\varepsilon)^n, \tag{1.23}$$

with E_n the energy of particle after n energy-gaining loops, E_0 the energy at the initial stage right after the particle was injected to the acceleration region, and ε the constant relative gain for each acceleration loop. In other words, the number of required loop n for accelerating particle to energy E is

$$n = \frac{ln(E/E_0)}{ln(1+\varepsilon)}. \tag{1.24}$$

Assuming a constant escape probability P from acceleration for each loop, which is again energy independent, the proportion of particles with energy greater than E after acceleration is the sum for all the probability of accelerating particles with $m \geq n$ loops (noticing that the probability for particle to encounter only m loops before escaping is $P(1-P)^m$):

$$N(\geq E) = \sum_{m\geq n}^{\infty} P(1-P)^m = P(1-P)^n \sum_{m\geq 0}^{\infty}(1-P)^m = P\frac{(1-P)^n}{P} = (1-P)^n, \tag{1.25}$$

where the identity $\sum_0^\infty x^m = 1/(1-x)$ is used at the second step. Inserting the expression of n from Eq. (1.24), the particle fraction is found to be a single power law of E

$$N(\geq E) = (1-P)^{\frac{ln(E/E_0)}{ln(1+\varepsilon)}} = \left(\frac{E}{E_0}\right)^{\frac{ln(1-P)}{ln(1+\varepsilon)}} = \left(\frac{E}{E_0}\right)^{-\gamma}, \tag{1.26}$$

with the spectrum index

$$\gamma = \frac{ln(\frac{1}{1-P})}{ln(1+\varepsilon)}. \tag{1.27}$$

Typically, particles gain small energy in each acceleration loop ($\varepsilon \ll 1$). Furthermore, if the escape probability P is small as well ($P \ll 1$), the spectrum index γ Eq. (1.27) is simplified to

$$\gamma \approx \frac{ln(1+P)}{ln(1+\varepsilon)} \approx \frac{P}{\varepsilon}, \tag{1.28}$$

Noticing that $N(\geq E)$ is the integral spectrum of particle after acceleration with energy larger than E, the energy differential spectrum can also be obtained as

$$N(E)dE \propto E^{-\alpha}dE \tag{1.29}$$

where $\alpha = \gamma + 1$.

Eq. (1.25) is valid in general and independent from the exact relation between energy E and the required number of loops n, i.e. the value of ε. The single power law nature of $N(\geq E)$ Eq. (1.26) is the consequence of the logarithms relation between E and n Eq. (1.24), which is a reflection of the energy-independent *relative* energy gain Eq. (1.23).

1.2.2.2 Fermi acceleration

As discussed above in Section 1.2.1, cosmic ray propagation in general adds an additional single power law to the injected spectrum after acceleration. Since the local cosmic ray spectrum after propagation shows a power law energy dependence as well, a power law injection spectrum after the acceleration must be achieved for proper cosmic ray acceleration mechanisms. Hence, acceleration mechanisms with energy-independent *relative* energy gains are required. The Fermi acceleration is one of the acceleration mechanisms that satisfied this requirement.

General form of the energy change in the Fermi acceleration

The Fermi acceleration, originally derived considering charge particle gain and loss energy encountering moving clouds of plasma [36] and was later found to be also applicable to the case of plane shock wave, describes the acceleration of charge particle in the turbulent magnetic fields and has the form of energy-independent *relative* energy gain.

The case of moving clouds of plasma as the original thoughts of Fermi will be discussed first. Let the incoming and outgoing angle of charge particles to be θ_1 and θ_2, with energy E_1 and E_2 (for simplicity, only the case of relativistic particles: $E \approx pc$ is considered) together with the speed of moving plasma as $\beta = V/c$ and it's Lorentz factor $\gamma_{plasma} = \sqrt{1/(1-\beta^2)}$, the energy of particles in the rest frame of the moving plasma is expressed as:

$$E_1' = \gamma_{plasma} E_1 (1 - \beta \cos\theta_1). \tag{1.30}$$

In the case of elastic scattering inside the plasma, the energy of particle remains unchanged after the scattering with the plasma, i.e. $E_2' = E_1'$. Transforming back to the laboratory

frame, the energy of particle after "acceleration" by the moving plasma is

$$E_2 = \gamma_{plasma} E_2'(1 + \beta \cos\theta_2). \tag{1.31}$$

Inserting the expression of E_1', the relative energy charge $\Delta E = E_2 - E_1$ over E_1 for particle elastically scattered by the moving plasma is expressed as a function of θ_1 and θ_2

$$\begin{aligned} \frac{\Delta E}{E_1} = \frac{E_2}{E_1} - 1 &= \gamma_{plasma} \frac{E_1'}{E_1}(1 + \beta \cos\theta_2) - 1 \\ &= \frac{1 - \beta\cos\theta_1 + \beta\cos\theta_2 - \beta^2 \cos\theta_1 \cos\theta_2}{1 - \beta^2} - 1 \end{aligned} \tag{1.32}$$

Eq. (1.32) is valid also for another situation, namely the particle energy gain and loss with a plane shock front and the shocked gas. If the shock front is moving with velocity u_1 and the gas is moving away from the shock with velocity u_2, then the velocity of gas in the lab frame becomes $V = -u_1 + u_2$. By simply replacing the velocity of moving plasma V to the velocity of shocked gas $V = -u_1 + u_2$, Eq. (1.32) can also be used to describe the energy change of gas particle elastically scattered by plane shock front.

Noticed that Eq. (1.32) represents an energy-independent relative energy change. Hence, as derived in Section 1.2.2.1, the Fermi acceleration naturally leads to a single power law energy spectrum for accelerating in both a moving plasma and a plane shock front.

Exact form of energy change for moving plasma and plane shock front

The average energy change of the Fermi acceleration is obtained by averaging the incoming and outgoing angles, θ_1 and θ_2 respectively. Sharing the same form of energy change, Eq. (1.32), the difference between moving plasma and plane shock wave is that they have different angle relation between particle and the object, as well as different results after averaging over angles with $\langle\cos\theta\rangle = \int P(\cos\theta)\cos\theta d\cos\theta$. As there is no correlation between θ_1 and θ_2, i.e. the outgoing angle of particle is independent of the incoming angle, the average can be performed separately for each of them.

Firstly, the average of the incoming angle $\cos\theta_1$ and the outgoing angle $\cos\theta_2$ for each case will be calculated:

- **Moving plasma**: Particles left the moving plasma isotropically. Integral out the uniformly distributed ϕ, the probability of $\cos\theta_2$ is again uniform, i.e.

$$P(\cos\theta_2) = constant, -1 \leq \cos\theta_2 \leq 1, \tag{1.33}$$

hence

$$\langle\cos\theta_2\rangle_{plasma} \propto \int_{-1}^{1} \cos\theta_2 d\cos\theta_2 = \frac{1}{2}x^2\Big|_{-1}^{1} = 0. \tag{1.34}$$

As for the incoming angle $\cos\theta_1$, the probability for particle to collide with the moving plasma is proportional to the relative velocity between them, i.e.

$$P(\cos\theta_1) = \frac{1}{2c}(c - V\cos\theta_1) = \frac{1}{2}(1 - \beta\cos\theta_1), -1 \leq \cos\theta_1 \leq 1, \tag{1.35}$$

with $1/(2c)$ serves for normalization and considering the incoming particle as relativistic $\beta \approx 1$. This leads to the average of $\cos\theta_1$

$$\langle\cos\theta_1\rangle_{plasma} = \int_{-1}^{1} \frac{1}{2}(1 - \beta\cos\theta_1)\cos\theta_1 d\cos\theta_1 = (\frac{1}{4}x^2 - \frac{\beta}{c}x^3)\Big|_{-1}^{1} = -\frac{\beta}{3}. \tag{1.36}$$

- **Plane shock front**: The probability for isotropic particle entering a plane is proportional to the projection of the plane on the velocity direction, i.e.

$$P(\cos\theta_2) = 2\cos\theta_2, 0 \leq \cos\theta_2 \leq 1, \tag{1.37}$$

with 2 the normalization factor in $[0, 1]$. This leads to

$$\langle\cos\theta_2\rangle_{shock} = \int_{0}^{1} 2\cos\theta_2 \times \cos\theta_2 d\cos\theta_2 = \frac{2}{3}x^3\Big|_{0}^{1} = \frac{2}{3}. \tag{1.38}$$

Similarly, the probability for particles escaping the plane isotropically is the same as for entering the plane but with different direction, i.e. the range for $\cos\theta_1$ is $[-1, 0]$ instead of $[0, 1]$ and the normalization has opposite sign:

$$P(\cos\theta_1) = -2\cos\theta_1, -1 \leq \cos\theta_2 \leq 0. \tag{1.39}$$

So now the average over $\cos\theta_1$ is

$$\langle \cos\theta_1 \rangle_{shock} = -\frac{2}{3}x^3\Big|_{-1}^{0} = -\frac{2}{3}. \tag{1.40}$$

Inserting the expression for $\langle \cos\theta_1 \rangle$ and $\langle \cos\theta_2 \rangle$ into Eq. (1.32), the final average energy change, i.e. ε in Eq. (1.23), becomes:

- **Moving plasma**:

$$\varepsilon_{plasma} = \left\langle \frac{\Delta E}{E} \right\rangle_{plasma} = \frac{1-\beta\frac{-\beta}{3}}{1-\beta^2} - 1 = \frac{\frac{4}{3}\beta^2}{1-\beta^2}; \tag{1.41}$$

- **Plane shock front**:

$$\varepsilon_{shock} = \left\langle \frac{\Delta E}{E} \right\rangle_{shock} = \frac{1+\frac{2}{3}\beta+\frac{2}{3}\beta+\frac{2}{3}\frac{2}{3}\beta^2}{1-\beta^2} - 1 = \frac{\frac{4}{3}\beta+\frac{7}{3}\beta^2}{1-\beta^2}. \tag{1.42}$$

At the limit that the plasma or shock moving has non-relativistic speed ($\beta \sim 0$), the expression of energy change can be further simplified to:

- **Moving plasma**:

$$\varepsilon_{plasma} \sim \frac{\frac{4}{3}\beta^2}{1-\beta^2}\Big|_{\beta^2=0} + \left(\frac{\frac{4}{3}}{(1-\beta^2)^2}\right)\Big|_{\beta^2=0}\beta^2 = \frac{4}{3}\beta^2, \tag{1.43}$$

  with Taylor expansion to first order of β^2;

- **Plane shock front**:

$$\varepsilon_{shock} \sim \frac{\frac{4}{3}\beta+\frac{7}{3}\beta^2}{1-\beta^2}\Big|_{\beta^2=0} = \frac{4}{3}\beta = \frac{4}{3}\frac{u_1-u_2}{c}, \tag{1.44}$$

  with u_1 the velocity of the shock wave front and u_2 the velocity of the shocked gas moving away from the front.

It's clear that the energy change for moving plasma is proportional to the second order of its velocity while for the plane shock wave is to the first order. Hence, the Fermi acceleration on moving plasma (plane shock wave) is referred as the second-order (first-order) Fermi acceleration.

Spectral index for second-order and first-order Fermi acceleration

The spectral index from the second-order and first-order Fermi acceleration can be calculated using Eq. (1.28) and the expression of the energy change ε, Eq. (1.43) and Eq. (1.44). The only missing part is the expression of the escape probability P. The probability can be expressed as the ratio of two characteristic time $P = T_{acc}/T_{esc}$, with T_{acc} the time particles spent between each encounter of acceleration and T_{esc} the time for particles to escape from the acceleration region.

In the case of the second-order Fermi acceleration, the acceleration region is suggested as the galactic disk, hence the T_{esc} is the resident time for cosmic rays inside the disk, which is at the order of 1 Myr. The rate for relativistic particles ($\beta \sim 1$) colliding with the moving clouds of plasma is proportional to the density of the plasma ρ and the cross section σ. Hence $T_{acc} \sim 1/(c\rho\sigma)$ depends on the property of the clouds. It finally leads to the expression of the spectral index from the second-order Fermi acceleration (accelerated in moving clouds of plasma)

$$\gamma \approx \frac{P}{\varepsilon_{plasma}} \approx \frac{1}{\frac{4}{3}\beta^2}\frac{1/c\rho\sigma}{T_{esc}}. \tag{1.45}$$

The most noticeable conclusion is that the particle spectrum after the second-order Fermi acceleration is non-universal, i.e. depends on the properties of the actual process.

For the first-order Fermi acceleration, the acceleration rate is the projection of isotropic cosmic ray fluxes with velocity $\beta \sim 1$ onto the plane shock wave front, which is proportional to

$$\frac{1}{4\pi}\int_0^{2\pi} d\phi \int_0^1 d\cos\theta \cos\theta = \frac{1}{4} \tag{1.46}$$

and proportional to their density n_{CR}, i.e. $1/T_{acc} = \frac{1}{4}cn_{CR}$. The escape of cosmic rays from the acceleration processes is due to the convection away from the plane shock front by downstream gas, as it has a relatively smaller speed than the upstream shock wave, so the rate is $1/T_{esc} = n_{CR}u_2$. Hence the escape probability is

$$P = \frac{1/(cn_{CR}/4)}{1/n_{CR}u_2} = \frac{4u_2}{c}, \tag{1.47}$$

which no longer depends on the density of cosmic rays. Consequently, the spectral index

for the first-order Fermi acceleration is

$$\gamma = \frac{4u_2/c}{\frac{4}{3}\frac{u_1-u_2}{c}} = \frac{3}{u_1/u_2 - 1}, \tag{1.48}$$

which depends only on the ratio between the upstream and downstream velocity of the plane shock wave (not on the velocity separately). The spectral index is then universal in the sense that it's independent on the detail properties of the shock wave.

1.2.2.3 other acceleration mechanisms

The observation of deviation from a universal single power law for the cosmic ray spectra, which is discussed in Section 1.3, hints the involvement of other accelerating mechanisms. Possible acceleration mechanisms include:

1. **Acceleration by Sunspot**: particle can be accelerated by the electric field induced by time-dependent magnetic field from normal stars, the so-called star spots or sunspots, with the existence of guiding force in order to circular around the sunspots, i.e. *Cyclotron Mechanism*. Due to the limited magnetic field strength and the short lifetime, sunspots can accelerate particles only up to a few GeV.

   A more plausible mechanism will be the *acceleration by Sunspot Pairs*. A pair of sunspots with opposite magnetic polarity will approach to each other and finally merge at the end. Like the cyclotron, the moving magnetic field will induce electric field with the capability of accelerating particle to GeV level without the presence of a guiding force.
2. **Pulsars**: At the end of supernova explosion, the remnants might form a fast spinning neutron star, the Pulsar. The neutrons are produced by protons and electrons through the weak interaction:

   $$p + e^- \rightarrow n + \nu_e, \tag{1.49}$$

   at the present of a strong gravitational collapse, which shrinks the star from a typical radii of 10^6 km to the size of ~ 20 km. The collapse conserves the angular momentum of the star; hence the pulsar has ultra-high rotational speed. The magnetic flux is

also roughly conserved, which leads to a very high magnetic field of the pulsar due to the orders of magnitude smaller radii. Usually the spinning axis is not parallel to the magnetic field, producing a strong electric field where particles can be accelerated. Pulsars have been considered as one of the new astrophysical sources for high energy positrons, as discussed in Section 1.3.1.

3. **Binaries**; Binaries are formed by a pair of a pulsar or neutron star and a normal star. Matter from the normal star is permanently dragged towards the compact neutron star, forming an accretion disk around it. These motions of plasma create large electromagnetic fields. The dragged matters are accelerated through the gravitational potential of the neutron star as well as the strong electromagnetic fields, with the potential to be accelerated up to $\sim 10^{19}$ eV.
4. **Other energetic objects in universe**: Accretion disks are formed around black holes and active galaxy nuclei (AGN) as well. They have the potential of accelerating particles to the highest observed energy for cosmic ray, injecting into the galaxy in the form of highly relativistic jets, which is a common feature of compact objects.

1.2.3 Supernova remnants as source of cosmic rays

In Section 1.2.1, the required energy budget for maintaining the steady state of cosmic rays and the injection spectrum of cosmic rays from sources were calculated. Comparing the results from supernova remnants calculated below, the assumption that supernova remnants produce and accelerate cosmic rays become broadly accepted, although the first suggestion of the supernovae-origin of cosmic rays back in 1934 by Baade and Zwicky [37] was given with outdated reasoning.

As calculated in Section 1.2.1.3, the required power for keeping cosmic rays in equilibrium is at the order of $\sim 10^{41}$erg/s. The power of supernova explosion can be calculated by first assuming an explosion rate of about 3 per century, (i.e. $\sim 10^{-9}s^{-1}$) and then noticing the typical 10^{51} erg energy released for each explosion. This comes up to a power at the order of $\sim 10^{42}$erg/s. Hence the connection between the cosmic ray injection from the galactic disk and the galactic supernovae can be made by assuming an approximate 10% conversion efficiency of the supernovae kinetic energy into the cosmic ray energy.

The explosion of supernovae produces strong shock wave, where the plane approxima-

tion is valid, and the first-order Fermi acceleration mechanism takes place. As the shock wave formed by the supernovae is very strong, the ratio of the upstream and downstream speed satisfied that $u_1/u_2 \approx 4$ for fully ionized gas [38], leading to $\gamma = 3/(4-1) = 1$. According to 1.48, the (integral) spectral index for particles accelerated by the supernovae shock wave is

$$\alpha = \gamma + 1 = 2. \tag{1.50}$$

The injection spectral index estimated from the local cosmic ray fluxes is $\alpha = 2.7 - \delta$, with δ the softening of the spectrum due to cosmic ray propagation. The value of δ interpreted from the cosmic ray data is $0.3 - 0.6$, leading to an injection spectrum with $\alpha = 2.1 - 2.4$. Such α value is very closed to the spectrum after first-order Fermi acceleration in the supernovae shock wave, with slight softening.

The chemical composition from supernovae remnants is similar to the one from the solar system, as both are the products of the stellar nucleosynthesis. As compared in Fig. 1-3, the composition from supernovae remnants is also compatible with the one for cosmic rays, with a few exception discussed in Section 1.1.2.

1.2.4 Long standing open problems

The origin of spectral structures in the cosmic ray all-particle flux, where the spectrum hardened or softened away from a single power law, have been studied for decades, nevertheless no solid conclusions have been drawn. These longstanding mysteries challenge the standard cosmic ray paradigm and potentially hint the existence of new physics.

1.2.4.1 Knee

At $\sim$ 4 PeV, the cosmic ray all-particle spectrum is softened from $E^{-2.7}$ to E^{-3}, and it's called the *knee* of the spectrum. The origin of the *knee* is broadly agreed to be the transition of the cosmic ray composition from proton domination to heavier nuclei domination. As heavier nuclei are much less abundant than proton, the cosmic ray all-particle spectrum is expected to be softer at the region dominated by heavier nuclei. The different domination of proton and heavier nuclei could be based on the fact that the most reasonable cosmic ray accelerator, the shock wave from supernova remnants, accelerates

particle according to their rigidity, in other words the maximum achievable rigidity of different nuclei is the same. Hence a common limit on the rigidity for proton and heavier nuclei translates to different limits on energy due to different mass, i.e. different energy domination of light and heavier nuclei.

Such a rigidity-dependent limitations could have two origins. First, as explained above the limitations of highest possible rigidity might due to that cosmic ray sources in the galaxy are inefficient to accelerate particle to energy above these limitations [39, 40]. Such limitations could also be explained through propagation effects that the galaxy is not able to confine particles with such high rigidity due to limitations of the size of the galaxy and the strength of the galactic magnetic field [41]. These two assumptions, from source and from propagation, both predict a rigidity dependent knee position hence they cannot be distinguished by the determination of cosmic ray composition at the knee energy.

Knee positions of individual cosmic ray species shed lights on the origin of the *knee*. At energy range around the *knee*, the cosmic ray direct detection is not feasible with the current generation of space missions due to the limited statistic from limited acceptance or/and exposure time. So far, indirect detections on the ground are performed, which has large particle identification uncertainty, introducing difficulties to determine the exact knee energies of individual cosmic ray species. The knee energy for proton has been measured indirectly and found to be 500 TeV by Tibet Asγ [42], and to be up to 4 PeV by KASCADE and KASCADE-Grande [43] which is the same energy as the knee of the all-particle spectrum. The variation on the measured knee energy introduces different issues:

1. At the situation of low knee energy (few hundred TeV), which is easily achieved by current acceleration models, the cutoff of the galactic cosmic ray spectrum would fall well below 0.1 EeV [33]. To match with the observed cosmic ray spectrum cutoff at $\sim 10^{20}$ eV = 100 EeV, an additional high energy galactic cosmic ray component or the present of extragalactic CRs at relatively low energy is required;
2. Instead, a knee energy at $\sim$4 PeV naturally fill up the gap between the knee up to the cutoff without the requirement of the additional galactic high-energy component. However, another problem arises: whether the galactic cosmic ray sources have the

ability of accelerating particles up to PeV, i.e. the existence of galactic PeVatron (see Section 1.3.3).

1.2.4.2 the second knee and the ankle - transition from galactic to extra-galactic?

At $\sim$ 500 PeV, there is the *second knee* of the cosmic ray all-particle spectrum, where the spectrum is softened again by $\sim$0.2. This is a relatively new discovery by Akeno experiment in 1992 [44]. Another transition exists at $\sim 3 \times 10^{18}$ eV, known as the *ankle*, where the spectrum is hardened. These structures are very likely related to the transition of the galactic component to the extragalactic component of cosmic rays.

It's quite reasonable to consider the ankle as the transition [45] since it offers a natural explanation of the sharp raise of the spectrum. Considering the knee of cosmic rays is rigidity dependent and it has the highest possible knee energy for proton at 4 PeV, the corresponding knee rigidity will be 4 PV for all particle species. Hence the knee of Iron, the most abundant heavy nuclei in cosmic ray, will be at $4 \times 26 \sim 100$ PeV $= 10^{17}$ eV. The second knee can then be recognized as the knee of the Iron spectrum, the bulk of cosmic rays at such energy. The second knee is still an order of magnitude lower than the ankle energy, so another cosmic ray component, galactic or even extragalactic, is required to fill up the gap between the second knee and the ankle. If the third component is unrelated to the low energy galactic one from standard supernovae remnants below the second knee, the "fine-tuning problem" arises since the observed smooth transition indicates a close normalization between these two cosmic ray components.

If instead the transition energy is assigned to the second knee, the ankle will be a structure on the extragalactic cosmic ray spectrum through either propagation effects or from the sources of extragalactic cosmic rays.

The determination of the transition energy between the second knee and the ankle bases on the difference between the galactic and extragalactic cosmic rays in such energy range, namely the composition and the anisotropy:

- Due to the rigidity dependent knee position, the galactic cosmic ray spectrum should be Iron dominated close to the its end. Similar behavior is expected for extragalactic

component however with a shift to higher energies. Hence at the transition energy, the extragalactic components should be lighter than the galactic one.

- The galactic components should be "well mixed" through diffusion in the ISM while a larger anisotropy is expected for extragalactic components since they travel inside the galaxy almost on straight line with ultra-high energy.

The composition measurement [46] observed that the Iron dies out before 7×10^{17} eV. Combining with the anisotropy measurement [47], cosmic rays above 3×10^{17} eV must be of extragalactic origin. Hence the second knee should be considered as the sign of the transition from galactic component to extragalactic component for cosmic rays. On the other hand, the origin of the ankle as a structure of the extragalactic cosmic rays remains unclear. The ankle might be explained as the pipe-up protons [48] that have lost energy at the GZK cutoff, which will be explained in Section 1.2.4.3. However, the indication of a mixture composition between the light and heaver nuclei [49] disfavored such a propagation origin of the ankle, which requires a proton domination for cosmic rays at ultra-high energy.

1.2.4.3 Cutoff of the spectrum

Fig. 1-2 clearly shows a cutoff at $\sim 10^{20}$ eV for the all-particle cosmic ray spectrum.

The famous Greisen–Zatsepin–Kuzmin (GZK) cutoff introduces a steepening on the proton spectrum at $\sim 5 \times 10^{19}$ eV [50, 51]. Ultra-high energy protons are assumed to lose energy rapidly by the interaction with the cosmic microwave background (CMB) photon through photo-pion production:

$$p + \gamma \rightarrow p + \pi^0, p + \gamma \rightarrow n + \pi^+. \tag{1.51}$$

If the high energy cosmic rays are still dominated by protons, the GZK cutoff naturally produced the spectrum cutoff on all-particle spectrum.

However, ground base measurements indicated that the ultra-high energy cosmic ray (UHECR) has mixed mass composition rather than purely light or purely heavy component [49]. Such a mix composition disfavors the explanation of the cutoff by propagation effects such as GZK cutoff, which requires proton dominated composition. Note that

the mass composition measurement has large uncertainty due to the description of cross sections at such energy and further studies are still needed.

1.3 Anomaly in the galactic cosmic rays in the precise era

Thanks to the development in detector and space technologies, cosmic ray experiments were launched into the space over the last decade, measuring the energy spectrum of individual cosmic ray species with unprecedented precision and with much larger energy coverage. These precise measurements unveiled new and astonishing anomalies beside those discussed in 1.2.4 at ultra high energy, challenging the standard cosmic ray models.

1.3.1 positron excess

The positron excess above a few hundreds of GeV was first suggested by HEAT [52, 53], PAMELA [54] and confirmed by AMS-02 [55]. The latest result from AMS-02 shows that the positron spectrum from 0.5 GeV to $\sim$ 1 TeV has two components [56]: a diffuse term at low energy as a single power law, describing the positron of secondary origin produced from cosmic ray interactions during their propagation in the ISM; a source term at higher energy as a power law together with an exponential cutoff, the origin of which cannot be explained by standard propagation model. The existence of such exponential cutoff at $\sim$800 GeV is found to have 4σ significance. Interestingly, the DAMPE satellite experiment has also observed a cut-off around 1 TeV in the total electron plus positron spectrum [57].

The explanation of the positron excess can be included into 3 categories: dark matter annihilation, new astrophysical sources and new propagation models. Some dark matter models can produce the positron spectrum together with a collision term at low energy. Astrophysical sources such as pulsars are another frequently cited possibility for the positron excess. These models might be confirmed or ruled out by the combination of other measurements including gamma rays and anti-protons. The measurement of diffused gamma rays seems to support the idea that at least pulsars are injecting particles into the galaxy, indicating the major role of pulsar origin for the positron excess [58].

However, the AMS-02 measurement of anti-proton shows a similar trend as positron at high energy [59], although the confirmation of the spectrum cutoff still needs more statistic to extend the energy range. If a cutoff on the anti-proton flux similar as the one for the positron is found, indicating a common source for both positron and anti-proton, the pulsar origin of the positron will be disfavored since pulsars cannot produce anti-proton. Finally, modifications of cosmic ray propagation model can also describe the positron excess. Again, the successful description of the measured positron flux might cause conflict with other measurements. One example is shown in Fig. 1-4, which is the comparison of the positron fraction ($\phi_{e^+}/(\phi_{e^-}+\phi_{e^+})$) measured by the AMS-02 together with the consistent prediction of the measured positron flux with a modified propagation model [60]. However, this model requires a different B/C ratio from the measurement by the AMS-02 at high energy above ~100 GV [32], hence it's ruled out by the B/C measurement, shown in Fig. 1-5.

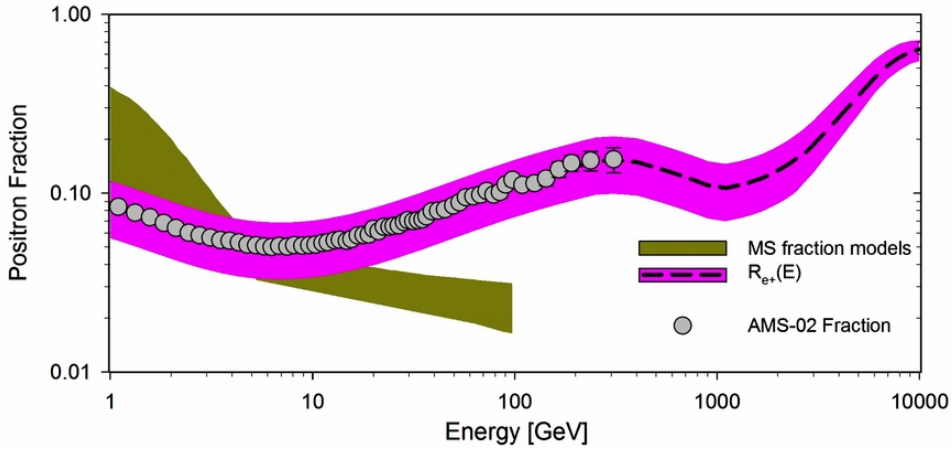

Figure 1-4: AMS-02 positron fraction (grey circle) together with prediction from Cowsik's model [60].

1.3.2 Primary cosmic ray spectrum anomaly

1.3.2.1 Global spectrum hardening

As shown in Section 1.1.1, the all-particle energy spectrum of cosmic ray seems to follow a featureless single power law up to the *knee*. However, the proton and Helium flux measurements by the PAMELA [61] and later by the AMS-02 with improved accuracy [1, 62] are found to deviate from a single power law and harden above 100 GV. Similar

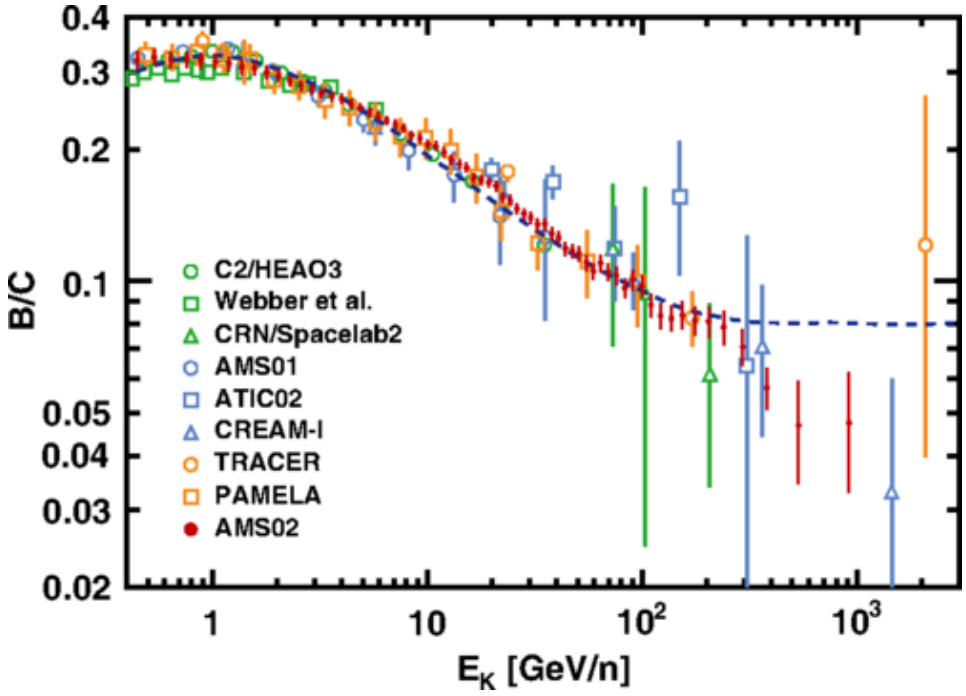

Figure 1-5: AMS-02 boron-to-carbon ratio (red circle) together with the one used in Cowsik's model [60]. Plot taken from [32].

spectrum behaviors, break and hardening at high rigidity, are also found for nuclei up to Oxygen for both the primary and secondary cosmic rays by the AMS-02 [2, 3].

Global hardening of cosmic ray spectra at high rigidity might be either a feature of the injection spectrum for primary cosmic rays or be produced during their propagation in the galaxy (such as a break in diffusion coefficient). Accurate flux measurements for both primary and secondary cosmic rays, or the secondary-to-primary ratio can distinguish between these two hypotheses. For primary cosmic rays, both hypotheses will harden the spectrum only once. While for secondary cosmic rays, the break at the injection spectrum of primary cosmic ray will also only harden the spectrum once. On the contrary, a break from propagation will harden again the secondary fluxes, therefore the secondary cosmic rays will harden twice as much as primary cosmic rays.

The AMS-02 B/C measurement [32] indicates the existence of a break on diffusion coefficient [63]. The measurements of secondary cosmic ray nuclei Lithium, Beryllium, Boron spectra and their ratio to Carbon and Oxygen show that secondary cosmic rays harden about twice more than primary ones, which is consistent with the broken diffusion coefficient hypothesis [3].

The break in the diffusion coefficient reflects the change of cosmic ray diffusion property among different galaxy volume. Such a change can be understood as the transition of the origin of magnetic field turbulence, which are the domination term of cosmic ray diffusion. In the galaxy volume close to the disk, turbulence is mainly injected by SNRs. On the contrary, in the outer space of galaxy where there are no SNRs, cosmic rays mainly encounter the self-generated turbulence. The spatial-dependent cosmic ray diffusion can be described by a *two-halo model* with different diffusion coefficients in the inner halo (close to the galaxy disk) and the outer one (far away from the galaxy disk), and this model produces a spectrum hardening as observed in the cosmic ray spectra near Earth [64, 65]. A more detailed modeling of cosmic ray diffusion in the region dominated by the self-generated turbulence through the consideration of the coupling between cosmic rays and the ISM also introduces similar spectrum hardening [66–68].

1.3.2.2 Spectral difference between proton and Helium

Besides the same hardening behavior of proton and Helium, the proton spectrum is softer than the Helium one at least up to ~ 2 TV.

Only key difference between proton and Helium is that Helium fragments in the ISM during propagation. However, ^{4}He fragments into ^{3}He in most cases, which will not change the total Helium spectrum considering the approximate conservation of energy-per-nucleon during spallation. In summary, without radical deviation from the standard scenario, the difference between the proton and the Helium spectrum up to ~ 2 TV cannot be explained by purely propagation effects.

On the other hand, the spectral difference can happen already at the acceleration or/and when escaping from the sources. If proton and Helium are injected during different stage of the sources, the spectral difference can be naturally explained. As the shock speed might decrease with time, if the injection of Helium happens at the early stage with large Mach number of the shock while the injection of proton happens at a later stage with lower Mach number, a harder Helium spectrum can be produced [69]. The injection scenario could be caused by a non-uniform helium distribution around the source [70]. In other models, considering the larger He gyroradius, He ions are assumed to be injected preferably when the shock is strong compared to proton [71]. However, all these models

predict a different spectrum between proton and Helium up to the highest possible energy from galactic accelerators, which conflicts with the observation that protons and Helium seems to share an identical spectrum shape above $\sim$ 2 TV.

1.3.3 Hint of the existence of PeVatrons

As mentioned in 1.2, ultra high energy cosmic rays are thought to have an extragalactic origin, since the galactic magnetic field of the ISM is not able to confine them and no known cosmic ray sources are capable of accelerating particle up to $\sim$ PeV $= 10^{15}$ eV.

However, diffusive gamma rays from the center of the galaxy, which are produced from the interaction of high energy protons with the ISM, are observed to have a smooth power law spectrum extending up to $\sim$ 10 TeV $= 10^{13}$ eV [72]. This implies a spectrum of parent protons extending up to PeV, requiring the existence of the galactic PetaelectronVolt accelerators, the so called *PeVatrons*. As these diffusive gamma rays tracing back to the region near the supermassive black hole Sgr A* at the center of the galaxy, Sgr A* is suggested as a candidate of the galactic PeVtron.

1.4 Silicon as primary cosmic ray

As discussed in Section 1.1.2, primary cosmic rays are produced and accelerated at the sources before their propagation in the ISM. Silicon is one of the most abundant primary cosmic ray species with charge larger than Carbon and Oxygen, and the precision measurement of Silicon flux can deepen the understanding of sources, acceleration mechanisms and propagation for cosmic rays [73].

The cosmic ray Silicon flux have been measured by previous experiments [74–80], which are characterized with large errors (more than 20% at 50 GeV/n) and not able to reveal possible spectrum structures. An accurate Silicon flux measurement will determine whether a similar spectral break, as those observed in lighter cosmic ray fluxes from proton up to Oxygen, also present in the Silicon flux. It will enrich the cosmic ray data for the examination of different models explaining the spectrum hardening.

Silicon have larger inelastic cross section compared to lighter nuclei, which corresponds to a smaller interaction length. Hence Silicon will die out faster before escaping

the confinement volume in the galaxy. In other words, the local Silicon nuclei can only come from closer regions than the lighter nuclei, such as C and O, effectively probing different parts of the galaxy. The Silicon flux measurement, together with the lighter nuclei flux, allows the study of cosmic ray non-homogeneous propagation effects [81].

Fluxes of nuclei heavier than Helium up to Oxygen can be fitted by a common injection spectrum from AMS-02 and PAMELA data [82]. With the measured Silicon nuclei flux and the propagation models tuned using lighter nuclei flux, the injection spectrum of Silicon can be obtained. Comparison between the injection spectrum of Silicon and lighter nuclei provides insights into the cosmic ray acceleration mechanism.

The measurement of the cosmic ray Silicon flux with unprecedented precision using the AMS-02 data collected during the first 7 years operation is the central topic of this thesis and will be explained in detail in following chapters.

Chapter 2

The Alpha Magnetic Spectrometer

The Alpha Magnetic Spectrometer, or AMS-02, is a large acceptance cosmic ray detector mounted on the International Space Station (ISS) in May 19th, 2011 (Fig. 2-1). AMS-02 is the only magnetic spectrometer currently operating in space since the termination of PAMELA [83]. In the near future, there are no other missions planning to operate a magnetic spectrometer in space. AMS-02 will continue taking data for the entire lifetime of the ISS, which is currently confirmed up to 2028, a possible further extension of operations beyond this date is being discussed. The AMS-02 detector has been designed to identify incoming cosmic ray nuclei by combining several charge measurements with the charge sign determined from the particle track bending direction.

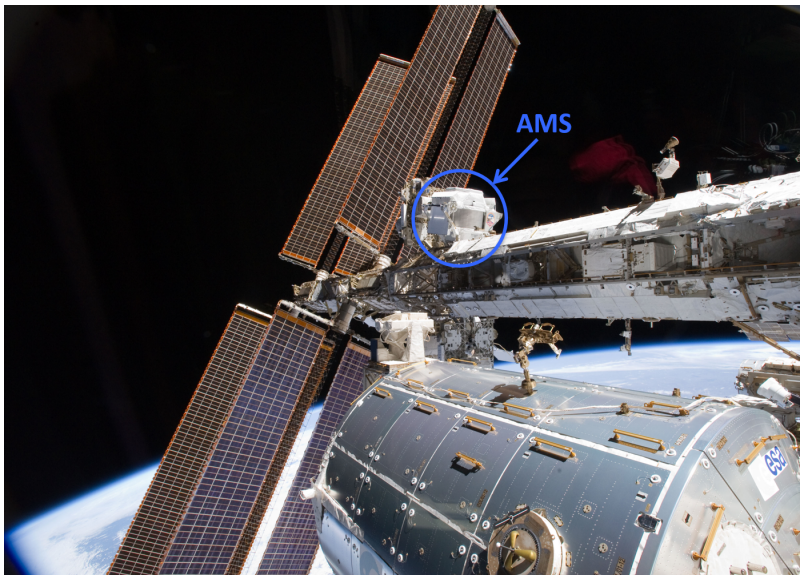

Figure 2-1: Picture of the AMS-02 mounted on the ISS. Credits to NASA.

The AMS-02, shown in Fig. 2-2, consists of nine layers of silicon sensors, the silicon tracker, with 6 of them placed in the bore of permanent magnet; a transition radiation detector (TRD); four time of flight (TOF) scintillation counter planes, two above and two below the permanent magnet; an array of 16 anti-coincidence counters (ACC) settle inside the permanent magnet; a ring imaging Cerenkov detector (RICH); and an electromagnetic calorimeter (ECAL).

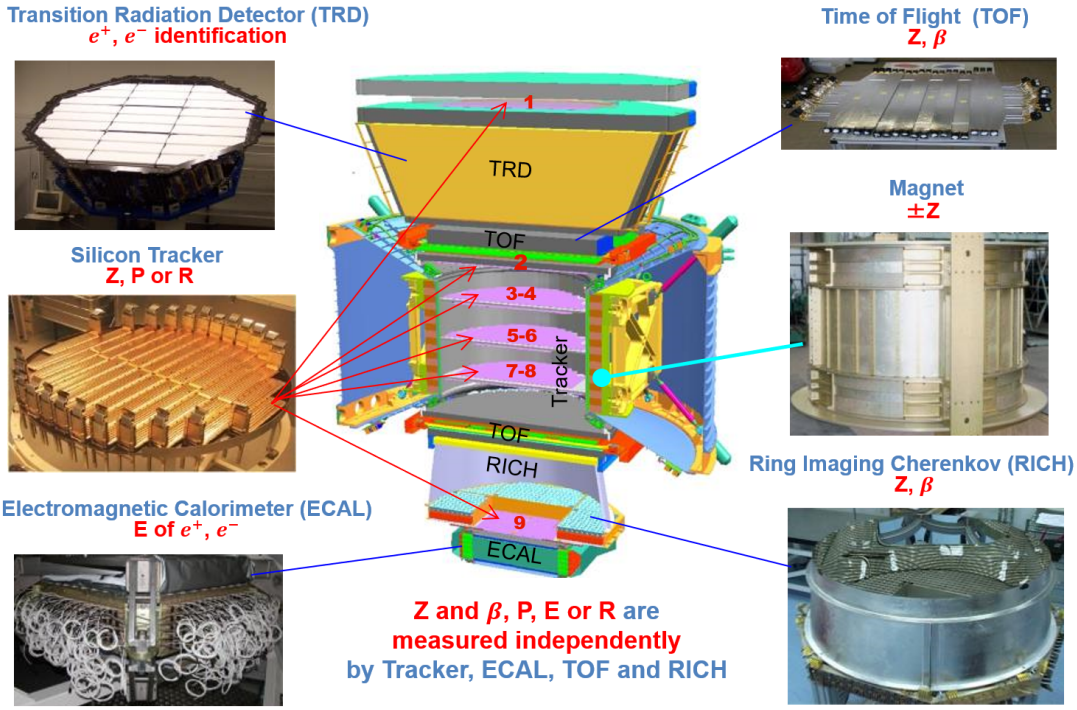

Figure 2-2: The AMS-02 and its sub-detectors.

2.1 The AMS-02 operation on orbit

There are three interfaces between the AMS-02 and the ISS, including one for power supplement of the payload and two for data transfer: The Low Rate Data Link (LRDL) and the High Rate Data Link (HRDL). The *science data* (SCI), sub-detectors signals generated by physical events, is transferred through the HRDL between the AMS-02 and the ISS. *Housekeeping data* (HK), information about the status of the detector including temperature readings, as well as commands from the Payload Operations and Control Center (POCC) for the AMS-02 operation are transferred through both the LRDL and

the HRDL. Data then proceeds through the Ku-band system, which connects the ISS to the ground through the Tracking and Data Relay Satellite (TDRS) via radio beam. To enable real time monitoring and operation of the payload, a parallel data paths, the S-band, has been implemented as well.

Orbiting around the Earth in a period of $\sim$ 96 min, the temperature outside the AMS-02 changes periodically from $\sim -25°$C to $\sim +55°$C. The constant changing thermal environment includes the short-term variation due to the temperature cycle per orbit and the long-term variation caused by the periodic change of solar *beta angle*, the angle between the orbital plane and the direction to the Sun. To have optimal performance against the periodically changing thermal environment, it's essential to maintain the temperature of the AMS-02 within the suitable operational range for all electronics. Thermostatically controlled heaters are implemented for thermal control of the AMS-02. A Tracker Thermal Control System (TTCS) has been designed and mounted to the AMS-02 specifically for the thermal control of the Silicon Tracker (Section 2.2.2.1).

2.2 The AMS-02 Detector

2.2.1 The Permanent Magnet

The magnetic field for AMS-02 is provided by a permanent magnet [84], which has been used for the AMS-01, a precursor experiment of the AMS-02 [85]. The 1.2 tons permanent magnet is constituted by 64 sectors and each of them is composed by 100 blocks of Neodymium-Iron-Boron. These sectors were arranged into a 0.8 m long cylinder with an inner diameter of 1.1 m, shown in Fig. 2-3. This arrangement, forming a Hallbach array, provides a uniform dipolar magnetic field of 0.14 T together with a negligible dipole moment ($< 2 \times 10^{-2}$ T), avoiding torque force and interference with the AMS-02 electronics.

In 2010, before integrating the magnet with the AMS-02 sub-detectors, a mapping of the magnetic field with 120,000 measurement locations with accuracy more than 2×10^{-4} T has been performed. The magnetic field has been found to be stable within 1% compared to the mapping of 1997, before the AMS-01 flight, as shown in Fig. 2-4. Due

to the temperature variation from −3°C to +15°C on orbit, the magnetic field strength is corrected accordingly.

The impact of uncertainties on the mapping of the magnetic field and the temperature corrections on the nuclei fluxes measurements will be studied in Section 3.6.4.

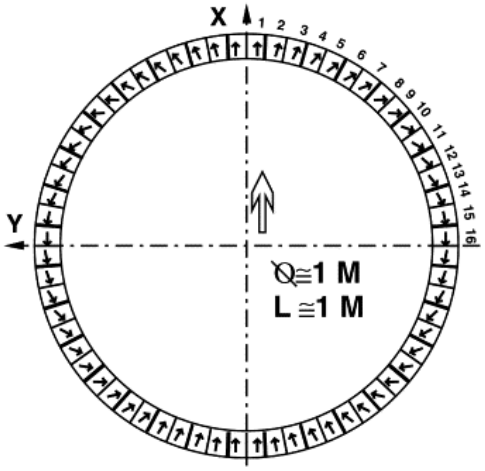

Figure 2-3: Configuration of the permanent magnet sectors viewed from the top. Taken from [85].

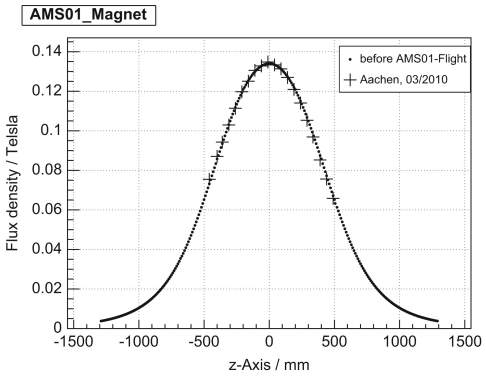

Figure 2-4: Permanent magnet field intensity along Z-axis mapped in 1997 (black curve) and 2010 (black cross) with Z=0 the magnet center. Taken from [84].

The dipolar magnetic field naturally defines the coordinate system of AMS-02. The coordinate origin is defined as the center of the permanent magnet. The Z-axis points upward, the X-axis is defined as the direction of the magnetic field lines, and the Y-axis is the bending-direction. In other words, charged particles travel in straight line in the X-Z plane and bend in the Y-Z plane due to the magnetic field.

2.2.2 The Silicon Tracker

The AMS-02 Silicon Tracker [86] has been designed to perform:

- precise coordinate measurement hence the trajectory determination;
- rigidity measurement;
- charge sign determination;
- charge measurement.

The AMS-02 Silicon Tracker is composed of 2284 double-sided silicon micro-strip sensors arranged into 192 ladders. These silicon sensors are made of 300 μm thick lightly n-doped silicon substrate, sketched in Fig. 2-5. p^+-doped and n^+-doped strips implemented on orthogonal directions. This allows a two-dimensional position measurement of incoming particles impact points [87]. The p^+-doped side (p-side), forming a pn junction and collecting the holes, has a implantation pitch of 27.5 μm while the n^+-doped side (n-side), forming an ohmic contact and collecting the electrons, has a coarser implantation pitch of 104 μm. In order to reduce power consumption and size for readout electronics, both sides adopt floating strip readout, i.e. one out of four (two) strips is read out for p(n)-side achieving a readout pitch of 27.5×4=110 μm (104×2=208 μm). These configurations bring 640 (192) readout strips out of 2568 (384) implanted strips on p(n)-side for each sensor.

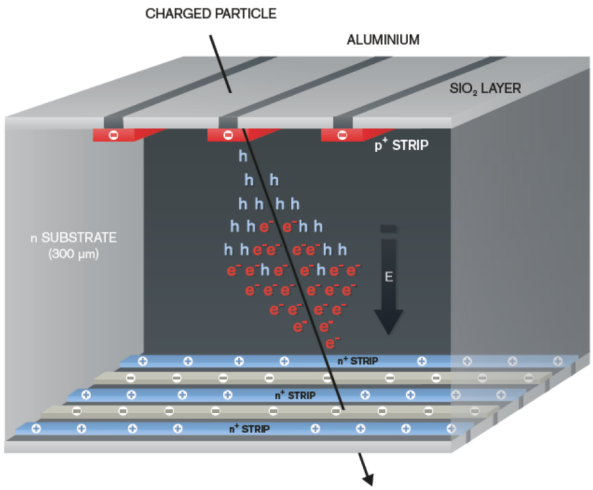

Figure 2-5: Illustration of AMS double-sided micro-strip silicon sensor. Taken from [87].

Silicon sensors are assembled into 192 ladders with readout electronics and mechanical

support, which are then arranged in 9 layers. Six Layers (L3 to L8), are installed in three doubled-sided planes inside the bore of the permanent magnet. Layer 2 is placed just above the magnet, together with the 6 layers inside the magnet constitute the so-called Inner Tracker, as Fig. 2-6. The Tracker Alignment System (TAS) monitors the stability of the Inner Tracker using 20 laser beams of 1082 nm wavelength which measures the relative position of Inner Tracker with sub-micron precision [88]. The other two Tracker layers, Layer 1 and Layer 9, called external layers, are placed at the top of the AMS-02 and at the bottom, just above the electromagnetic calorimeter, respectively. These external layers enlarge the lever arm of AMS-02 up to $\sim$ 3m.

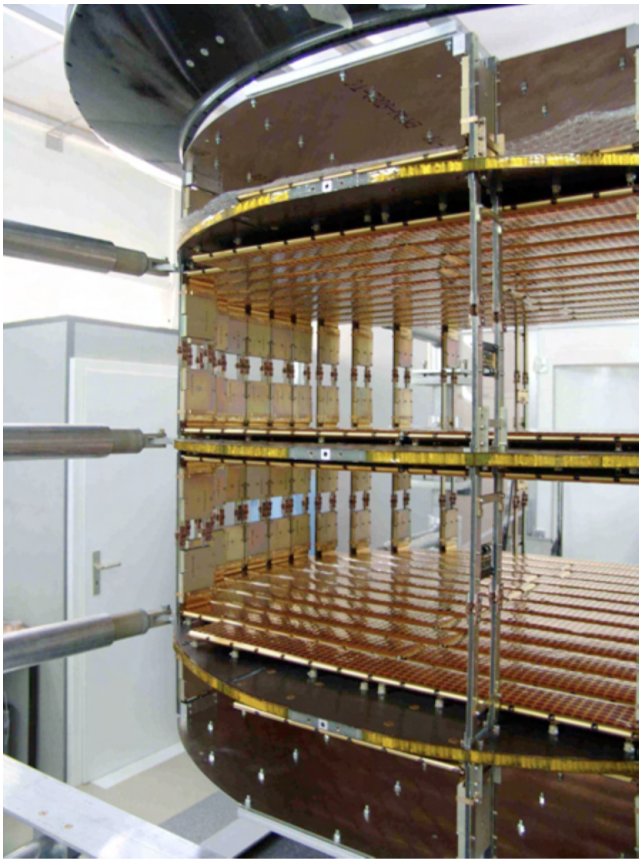

Figure 2-6: Picture of AMS-02 Inner Tracker.

When traversing the silicon layer, charged particles deposit energy through ionization and create electron-hole pairs in the sensors. The electrons (holes) are then collected by the nearest strips on X-side (Y-side). The position of the hit strip allows to reconstruct the impact position of the incoming particle. With precision measurement of the particle coordinate in multiple layers, the trajectory of the particle inside AMS-02 is determined

and the particle rigidity, $R = p/Z$, is reconstructed from the curvature of the trajectory inside the magnetic field. Finally, the charge Z of the incoming particle is determined from the energy deposited in the silicon sensors, which is proportional to Z^2 according to the Bethe-Bloch formula.

The accurate knowledge of coordinates of each sensor and the relative position of nine tracker layers is essential for the coordinate measurement, trajectory determination and rigidity measurement. Detail study about tracker alignment calibration can be found in [89].

Hit reconstruction and coordinate estimation

After subtracting the pedestal and common noise, strips with signal-to-noise ratio (S/N) above given threshold for both sides of all tracker layers are stored, forming the so-called raw clusters. The strip of the local signal maximum, the closest strip to the impact point of the incoming particles which is called the seed strip, together with nearby strips are grouped into higher level clusters (TrCluster). Based on the position and the signal amplitude, TrClusters from X-side and Y-side are correlated into 3-dimensional reconstructed hits (TrRecHit). All the Y-side TrClusters also make Y-only TrRecHits. Both XY-combined and Y-only TrRecHits will be the basic elements for track finding and charge estimation.

The impact position of the incoming particle is calculated as the Center-of-Gravity (CoG) of the TrClusters, achieving an optimal spatial resolution of 10 (30) μm in the Y(X)-coordinate [86]. An updated track position reconstruction algorithm, considering the non-linearity of the detector response, has been developed [90]. The new algorithm improves the Y-side (bending) coordinate resolution to 5-9 μm for charge from 2 (Helium) to 26 (Iron) with a negligible inaccuracy from the linearization algorithm of <0.5 μm.

Track finding algorithm and rigidity measurement

Due to the large amount of readout channels of the AMS-02 Silicon tracker, the number of reconstructed TrRecHits is large even for the simplest case when only one particle traversing the detector with only one track.

Optimized track finding procedure [91] instead of effective but time-consuming brute

force approach is studied to reduce the computational budget. The procedure starts from searching for a curved track requiring hits on the three tracker planes inside the magnet. Hits on remaining Inner tracker are connected to the curved track if possible. Only tracks containing at least four XY-combined TrRecHits and at least one hit for each track plane are accepted as candidate tracks and are called Inner Track. Matching between TRD track or TOF cluster is then performed for each Inner Tracks in order to connect signals from other subdetectors. Finally, hits on external track layers are searched around the extrapolation of the Inner Track and the closest hits are then attached to the track. Different tracks besides Inner Track can be reconstructed:

- L1Inner Track: with only Layer 1 hit attached to Inner Track;
- InnerL9: with only Layer 9 hit attached to Inner Track;
- L1InnerL9: with both Layer 1 and Layer 9 hits attached to Inner Track.

Rigidity of incoming particles is obtained by the curvature of track trajectory in the magnetic field. A path integral fit algorithm taking into account the multiple scattering [92] is used to retrieve the curvature hence the particle rigidity. The maximum detectable rigidity (MDR) for given nuclei species depends on the rigidity resolution, which is decided by the coordinate resolution. The new track position reconstruction algorithm [90] with a spatial resolution of 5-9 μm leads to the MDR as $\sim$3 TV.

Charge calibration

Each tracker layers can perform two charge measurements by the deposited energy in double sides of the layer, the so-called X-side and Y-side charges. The detector response as a function of the charge of the incoming particles for single tracker layer is shown as Fig. 2-7.

For incoming particles with low charge ($Z \leq 8$), the deposited energy in the Silicon Tracker is small and able to be collected by the seed strip along. The X-side electronic is designed to have a good linear correspondence between the signal response of the seed strip $\sqrt{A_1}$ to the charge of the incoming particles, as can be seem from Fig. 2-7. A charge measurement based on the X-side detector response has been design and are used for particle identification in the range of $Z \leq 8$ [87].

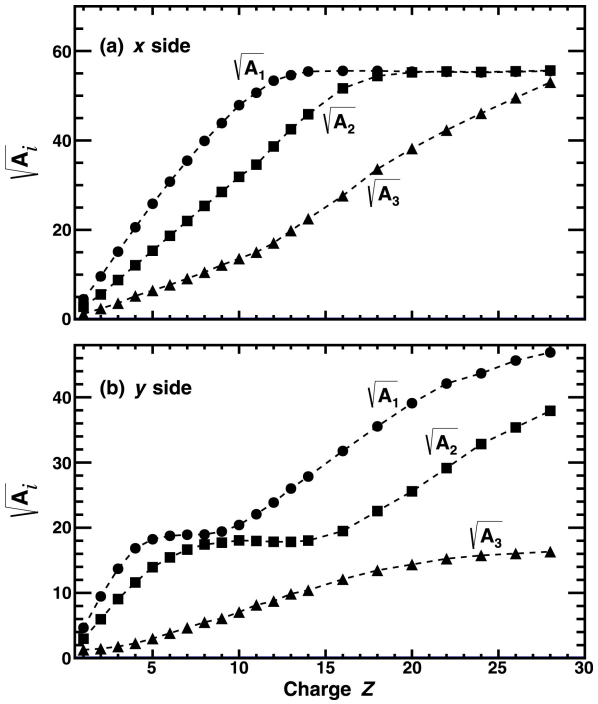

Figure 2-7: Typical value of square root of ADC as a function of charge measured by upper ToF for seed strip A_1 (red), first nearby strip with maximum signal A_2 (blue) and second nearby strip A_3 (green) with (a) X-side and (b) Y-side. Taken from [93].

However, as shown by Fig. 2-7, for heavier nuclei, the X-side seed strip saturates gradually due ADC limitation and the signals will be shared by nearby strips, A_2 and A_3. The usage of nearby strips will recover the linearity between the detector response and the charge of incoming particles. Furthermore, the Y-side has been designed to have different electronic compared to the X-side, in order to have better linear response at higher charge. A charge measurement based on signals collected by seed and its nearby strips as well as combining both X-side and Y-side charge has been developed to enlarge the dynamic range of Silicon Tracker charge measurement [93].

The Inner tracker has very light material so particles are unlikely to fragment and change their charge within the Inner tracker. Hence the estimated charge from seven Inner tracker layers are combined to the so-called Inner Tracker charge estimation, which has better charge resolution than single layer. In total, 3 kinds of charge measurements are used in following flux analysis, namely the charge measured by Tracker Layer 1 (L1Q), by Tracker Layer 9 (L9Q) and combined charge measurement from seven Inner Tracker layers (InnerQ). The charge resolution $\Delta Z/Z$ is $\sim 2\%$ for Oxygen and $\sim 1\%$ for Silicon.

2.2.2.1 The Tracker thermal control system

A mechanically pumped two-phase CO_2 cooling loop system, the Tracker Thermal Control System (TTCS), has been integrated in AMS-02 to control the temperature of Silicon Tracker [94].

Recently, the AMS TTCS has been replaced by the so-called Upgraded Tracker Thermal Pump System (UTTPS), which has required four space walks (ExtraVehicular Activities, EVA) between November 2019 and January 2020. The success of UTTPS installation has enabled AMS-02 to continue the data taking for the entire lifetime of the ISS.

2.2.3 The Time of Flight Counter (TOF)

The Time of Flight Counter [95] provides the main trigger to the AMS-02 detector, which will be discussed in details in Section 2.3, and measures:

- the velocity ($\beta = v/c$) and incoming direction of cosmic-ray particles based on time of flight. The direction of incoming particles is important for the matter/anti-matter separation;
- the charge of cosmic-ray particles through the energy deposited by ionization.

The TOF is composed by two double layers of plastic scintillator paddles placed above Tracker Layer 2 and below the magnet, namely the Upper TOF (uTOF) and Lower TOF (lTOF) respectively. The scintillator paddles in each double layer run along orthogonal directions. Within each layer, the paddles overlap to maximize the geometrical coverage and are read out by two or three photo-multiplier tubes (PMTs) through plexiglass light guides on each end, allowing a rough coordinate measurement based on the time difference in the signals collected by two sides. Independent readout from PMT anode and dynode are collected, with anode signals are used for time and charge measurements while the dynode signals are only used for charge measurements. Drawing of the Upper TOF, the Lower TOF and one TOF paddle are shown in Fig. 2-8.

Three thresholds are designed for TOF as:

- Low Threshold (LT): set at ~20% of the minimum ionizing Proton (MIP) signal for time measurement;

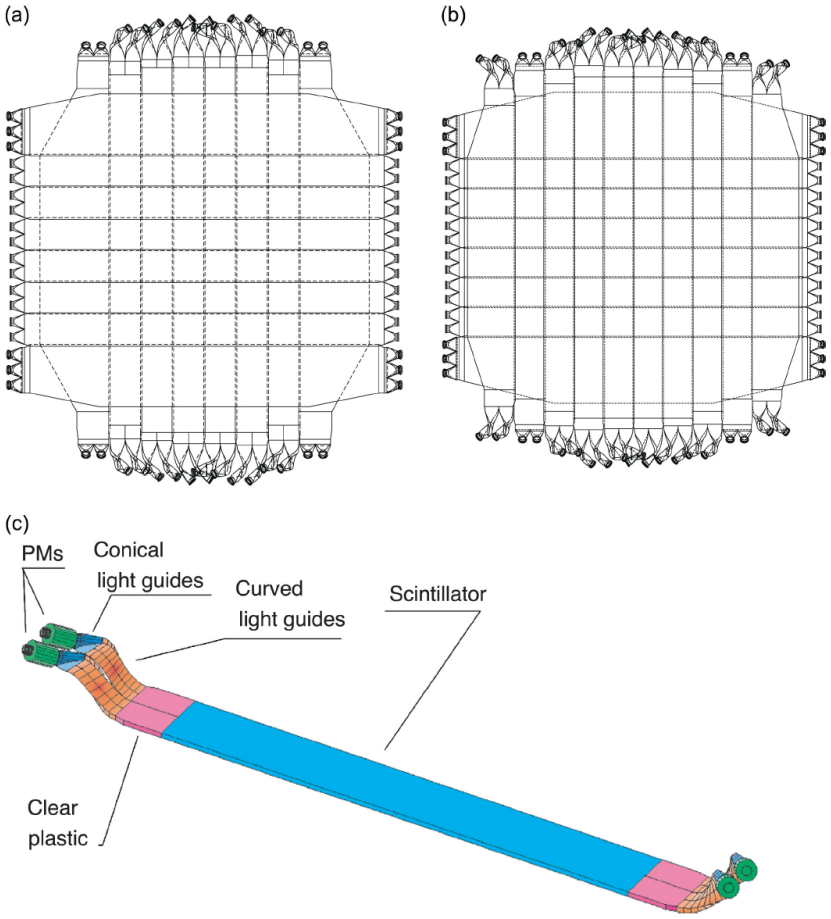

Figure 2-8: Top view of (a) Upper TOF, (b) Lower TOF and (c) TOF paddle. Taken from [95].

- High Threshold (HT): set at ∼60% of the MIP signal, used for triggering particles with charge ≥1;
- Super High Threshold (SHT): set at ∼400% of the MIP signal, used for triggering particle with charges ≥2;

The anode signals are then split into two parts. 95% of it is used for time measurement and trigger generation by comparing with these thresholds. The TOF time calibration of has been performed in orbit using high rigidity particles (R≥20 GV) which has known velocity $\beta \sim 1$. The calibration procedure is repeated every 15 days considering the anode gain changes, scintillator and PMT aging and threshold fluctuations. The velocity of particle is then measured as $v = \Delta s/\Delta T$, with ΔT the time of flight between Upper and Lower TOF, and Δs the trajectory length given by the Silicon Tracker or TOF itself. The velocity resolution ($\Delta(1/\beta)$) is measured to be 1.2% for Carbon and 1% for charge

up to 14. The incoming direction of particles is determined by the sign of the ΔT.

The remaining 5% anode signals and all dynode signals are used for charge measurement. Based on the different charge resolutions, they are used in different charge range: light charges ($1 \leq Z \leq 3$) are measured only by anodes; middle charges ($4 \leq Z \leq 8$) are measured by both anodes and dynodes; high charges ($Z > 8$) are only measured by dynodes. After calibration, the corrected signal of each counter, obtained by summing up signals from all PMTs, gives an estimation of particle charge. Combining the estimated charge from two upper (lower) planes gives a charge estimation of higher resolution, the so-called Upper (Lower) TOF charge. The Upper and Lower TOF charge distributions for different ions are shown in Fig. 2-9. The corresponding charge resolution ($\Delta Z/Z$) for Upper TOF charge is 5% for proton, 3% for Oxygen, 2% for Neon up to Silicon, which is similar for the Lower TOF charge one.

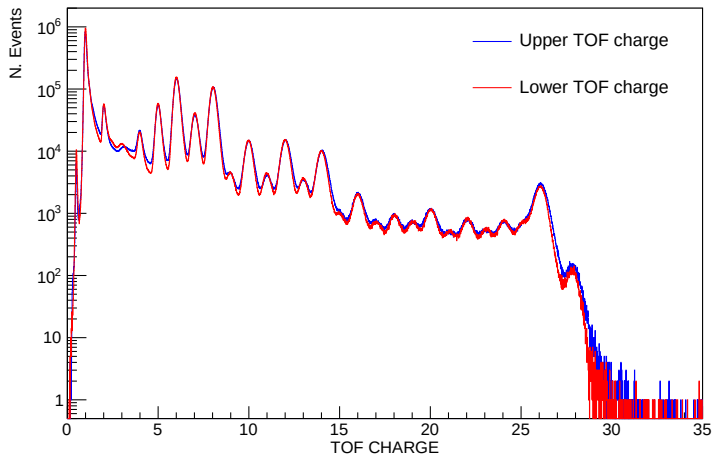

Figure 2-9: The Upper TOF charge (blue) and Lower TOF charge (red) distribution.

2.2.4 Anticoincidence Counters (ACC)

The ACC counters [96] are mainly designed to veto events with particles passing through the Inner Tracker horizontally since these events pass only small fraction of AMS-02 leaving not enough redundant measurement for precise determination of the particle properties. It also vetoes events with large fragmentation due to interaction with the AMS material. The ACC is also able to reduce the trigger rate by rejecting spurious triggers

generated by particles trapped in the Earth's magnetosphere encountered when the ISS is in the South Atlantic Anomaly (SAA) where dramatic particle flux hits the detector.

Sixteen scintillation panels (Bicron BC-414) surround the Inner Tracker inside the magnet, shown in Fig. 2-10. Adjacent counters are combined into 8 readout in total. Ultraviolet scintillation light is generated by intersecting charged particles through ionization and collected by PMTs. The usage of ACC signals for trigger generation will be discussed in Section 2.3.

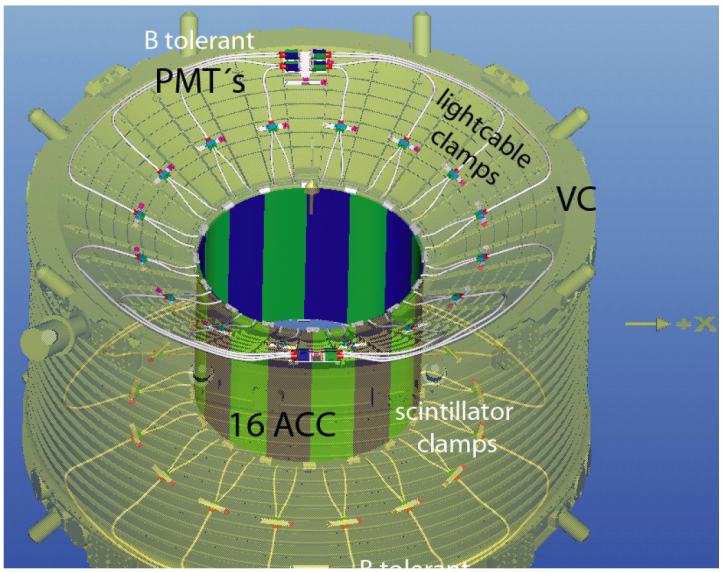

Figure 2-10: Configuration of ACC counters. Taken from [96].

2.2.5 The Transition Radiation Detector (TRD)

The TRD makes use of the emission of transition radiation, soft X-ray photons generated by ultra-relativistic charged particles traversing the boundary of two materials with different dielectric constants. The main aim of the TRD is to distinguish $e^{\pm}$ events from proton and heavier nuclei background since the TRD is tuned so that only $e^{\pm}$ emit transition radiation up to with energy up ~300 GeV.

The TRD is mounted between the Tracker Layer 1 and the upper TOF. It consists of layers of irregular polyethylene/polypropylene fleece radiators to produce transition radiation, and Xe/CO_2 filled straw tubes operated in proportional mode for the collection of emitted radiation. The probability of transition radiation emission is low hence the

TRD contains in total 20 radiator-detector layers to maximize the transition radiation emission. One layer of TRD is shown as Fig. 2-11.

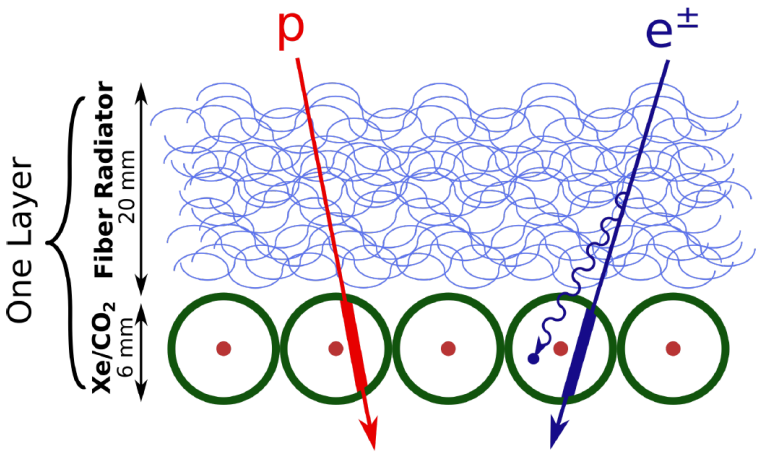

Figure 2-11: One TRD layer of fleece radiator and Xe/CO_2 filled straw tube. Taken from [97].

High energy $e^{\pm}$ lose energy through both the ionization and the emission of transition radiation when traversing proportional tubes of the TRD. Instead, protons and heavier nuclei will only deposit energy through ionization. A TRD estimator for discrimination between $e^{\pm}$ from proton and nuclei background is obtained using neural network with flight data [98]. It's able to reject protons from $e^{\pm}$ with the power $>10^3$ up to 100 GeV.

2.2.6 The Ring Imaging Cerenkov Detector (RICH)

The RICH, placed between the lower TOF and the Tracker Layer 9, provides

- high resolution velocity (β) measurement based on the Cerenkov angle, which combined with the rigidity gives a high-resolution measurement of the particle mass for isotopic composition studies;
- particle charge measurement using the number of emitted Cerenkov photons which is proportional to Z^2.

A particle traveling in a medium with speed larger than the speed of light in that medium, a cone of Cerenkov light along the particle trajectory is emitted. The opening

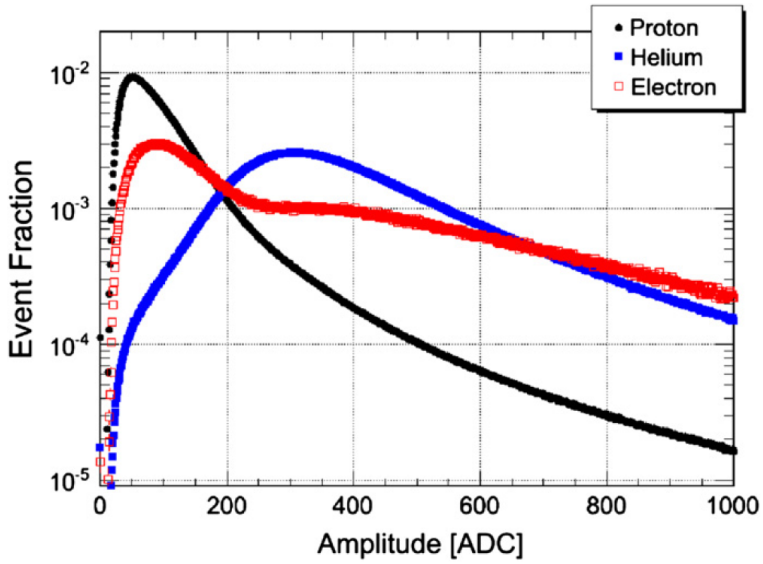

Figure 2-12: Normalized energy deposition spectra from proportional tubes for proton (black), electron (red) and helium (blue). The electron spectrum has similar peak position as proton, which is result from ionization energy loss, since both have charge 1 while the peak of helium shifts to higher ADC due to higher charge. The longer tail for electron spectrum compared to the proton one is the signal from TRs. Taken from [98].

angle of the Cerenkov cone depends on the particle velocity β as

$$\cos\theta = \frac{1}{n\beta}, \tag{2.1}$$

with n the refractive index of the medium. Hence measurement of the opening angle of the Cerenkov cone provides velocity measurement of incoming particle. Besides, the number of emitted Cerenkov photons is proportional to Z^2 which can be used to measure particle charge.

The RICH is composed by 1) two non-overlapping planar radiators, sodium fluoride (NaF) and silica aerogel, 2) an expansion volume surrounded by a reflecting mirror, in which the Cerenkov cone propagates, and 3) a photo-detection plane collecting the Cerenkov photons (Fig. 2-13). The NaF is placed in the center of the radiator plane and has a refractive index $n = 1.33$. Surrounding the NaF there are 92 silica aerogel tiles with $n = 1.05$. The NaF and aerogel radiator have different Cerenkov threshold, $\beta_{thres} = 1/n$ hence $1/1.33 = 0.75$ and $1/1.05 = 0.953$ respectively, so they measure the particle velocity in different ranges enlarging the detection region. The expansion volume is surrounded by

a high reflectivity mirror which reflects the Cerenkov light hitting on the side of the volume in order to increase the detection efficiency for large opening-angle Cerenkov cones and/or particles with large inclination angles. The photo-detection plane contains 680 multi-anode PMTs array, collecting the Cerenkov photons whose signal appears as a ring. To minimize the material in the ECAL acceptance, no PMT has been installed in the central part of the RICH detection plane.

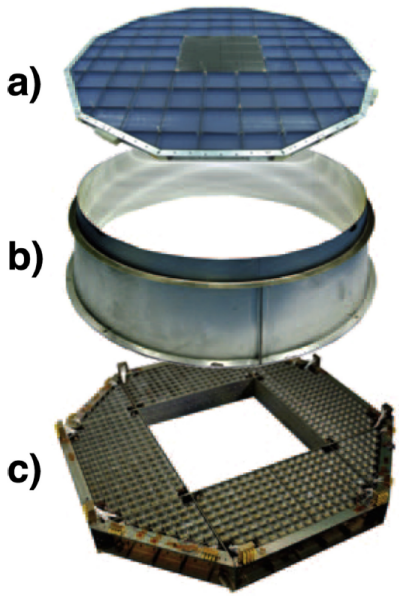

Figure 2-13: RICH components: a) dielectric radiators, b) truncated cone shaped expansion volume and reflector, c) photo-detection plane. Taken from [99].

2.2.7 The Electromagnetic Calorimeter (ECAL)

The ECAL [100] is designed for providing:

- the measurement of electron and positron energy from the electromagnetic shower deposited energy;
- proton and heavier nuclei separation from $e^{\pm}$ based on the 3D shower shape and the comparison between particle energy from calorimeter and momentum from Tracker.

The ECAL signal is also used to generate the trigger to AMS-02 in addition to the TOF and the ACC signals Section 2.3.

The ECAL is a sampling calorimeter made of 98 lead foils for shower generation and 50000 scintillating fibers for signals collection, for a total of 17 radiation length X_0 (Fig. 2-14). It has 9 *superlayers*, each of which is a sandwich of 11 lead foils and 10 layers of scintillating fibers glued to the foils, corresponding to 1.9 X_0. The scintillating fibers within each superlayers run in the same direction and the direction alternates for nearby superlayers (five parallel to the AMS-02 X-axis and four parallel to the Y-axis), providing 3D shower imaging.

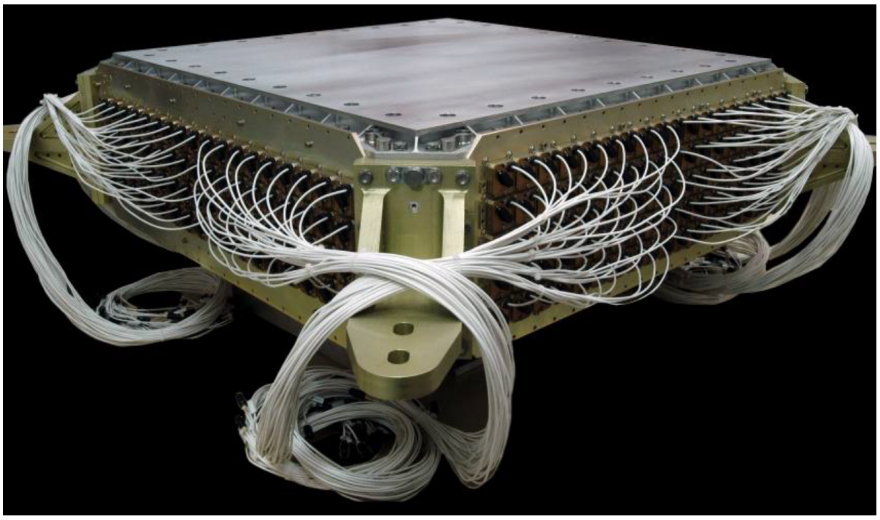

Figure 2-14: A picture of the AMS-02 assembled ECAL before launching.

The AMS material above ECAL correspond to 0.1 X_0 hence the signals of ECAL with 17 X_0 is scaled to the top of AMS-02 as the incoming energy of $e^{\pm}$ accounting the energy loss before entering ECAL. A boosted decision tree classifier is constructed for $e^{\pm}$ discrimination from proton and heavier nuclei background by using the 3D shower shape from ECAL. ECAL standalone provides a proton rejection from $e^{\pm}$ of the order of 10^4 at 90% efficiency [101].

The ECAL can directly detect photon events which only start generating electromagnetic shower in the ECAL, the so-called "single photon" method, while a photon converted to e^+e^- pair in the upper part of AMS-02 can be detected by the Tracker ("conversion" method). An ECAL standalone trigger is designed for detection of "single photon" events, which will be discussed in Section 2.3.

2.3 The Trigger logic

Particles generate signals when passing through the detector. However, only if certain condition based on combinations of signals from the TOF, ACC and ECAL are met, the so-called trigger logic, will the signals be buffered and stored. A set of signals from all the sub-detectors within a predefined time window after one trigger activation is called one event. Due to the low intensity of cosmic rays, most of events contain only one cosmic ray passing through the AMS-02 in the normal conditions. Only when incoming particles fragmented inside the detector, while ISS traverses the SAA or it is at the geomagnetic poles during the geomagnetic storms or solar energetic particles (SEP), more than one particle traversing the AMS-02 will be collected within one event. The main reason for adopting a dedicated trigger logic is to store only potentially interesting events which might be well measured by AMS-02, in order to avoid bad events whereby reducing dead time data size, as the bandwidth for data transmission and the AMS buffer storage are not infinite.

AMS-02 developed a trigger decision architecture with three progressive trigger levels: The Fast Trigger (FT), the Level1 Trigger (LVL1) and the Level3 Trigger (LVL3), based on the signals from TOF, ACC and ECAL as previously mentioned. Only if the previous trigger condition is fulfilled will the next trigger verification be activated. The data acquisition is started only if the Level1 trigger condition is met. A detailed discussion of FT and Level1 trigger will be presented below.

2.3.1 Fast Trigger (FT)

The Fast Trigger (FT) is designed to have a very rough but extremely fast decision of whether it's necessary to active the time-consuming Level 1 Trigger logic. The FT signals based only on the TOF and ECAL signals.

The TOF FT signals contains 3 categories [102]:

- **Charged Particle (CP)**: requiring at least one TOF paddle in each plane has signals above High Threshold (HT);
- **Charged particle in the Tracker acceptance (CT)**: same requirement as CP but using only those counters inside the Tracker acceptance;

- **Big Z Particle (BZ-TOF)**: similar as **CP**, requiring at least one TOF counter in each plane having signals above the Super High Threshold (SHT) without geometrical requirement.

Each TOF plane produces two signals from each side for all 3 categories, i.e. in total 6 TOF FT signals for each TOF plane.

The ECAL trigger is designed for photon events only generating electromagnetic showers in the ECAL [103]. Only signals from six out of nine ECAL superlayers, the second to seventh, are used for the ECAL trigger, since 1) most of the photons do not converted in the first superlayer, and 2) low energy photons (few GeV) only deposit a small amount of energy in the last two superlayers. Three of these superlayers used for the trigger are parallel to the AMS-02 X-axis and provide a trigger signal, **ECAL-F-x**, if at least two out of three superlayers have at least one PMT with signal above threshold. A similar **ECAL-F-y** signal is generated from the other three superlayers running along the Y-axis. These two signals are then combined in logic OR and logic AND to provide another set of fast triggers, the **ECAL-F-OR** and the **ECAL-F-AND** respectively.

The TOF FT and ECAL FT signals are then combined into three categories:

- **FTC**: requires that at least 3 out of 4 TOF layers have either **CP** or **CT** signals, which is a fast trigger for charged particle;
- **FTZ**: requires **BZ-TOF** signals from at least one layers from both upper TOF and lower TOF inside an extended time windows of 640 ns. This is a trigger dedicated to *strangelets*, which should have lower velocity with respect to normal ions of the same charge and rigidity due to exotic Z/A ratio of <0.1;
- **FTE**: requires **ECAL-F-OR** or **ECAL-F-AND**. A standalone **FTE** without **FTC** or **FTZ** usually corresponds to the detection of a photon.

All three signals are then combined in logic OR to provide the final FT trigger.

2.3.2 Level 1 Trigger

Signals used for Level 1 Trigger (LVL1) have different arrival time and need certain preprocessing hence the activation of LVL1 is time consuming which corresponds to 1 μs. That's the reason why FT is designed before triggering LVL1.

Besides signals from the TOF and the ECAL, the LVL1 also requires the ACC veto signals, which are generated when the number of fired ACC scintillators is larger than configurable thresholds. The ACC veto signals are used to veto events passing through the detector from the side or creating too many secondary particles inside the AMS-02.

Signals from TOF, ACC and ECAL are first combined into 16 signals together with three FT triggers, **FTC**, **FTZ** and **FTE**:

- Charged particle signals: a 240 ns window is opened to collect the **CP** and the **CT** signals from all TOF layers. These signals are then fed into two look-up tables (LUT), LUT-FT0 and LUT-FT1, creating 4 signals. For the flight these LUTs are set as:

  1. LUT-FT0: requiring 3 out of 4 TOF layers has **CT** or **CP** signals, producing **FTCT0** and **FTCP0**;
  2. LUT-FT1: requiring 4 out of 4 TOF layers has **CT** or **CP** signals, producing **FTCT1** and **FTCP1**.

  These signals build triggers for different charged particles together with the signals from ACC;
- Big Z signals (**BZ**): a 240 ns windows is opened for collection **BZ-TOF** signals from all TOF layers and then fed up into LUT-BZ. On the flight LUT-BZ is set to ask 4/4 signals, i.e. BZ require 4 out of 4 TOF layers has **BZ-TOF** signals. This signal is designed for triggering ion events;
- ACC signals: There are two ACC signals requiring different thresholds:

  1. **ACC-0**: no. fired ACC scintillators equal to 0, i.e. NACC=0;
  2. **ACC-1**: no. fired ACC scintillators less than certain threshold Ntr_1, i.e. NACC<Ntr_1.

  Ntr_1 was set to 5 up to February 26, 2016 and changed to 8 in order to increase the trigger efficiency for heavy nuclei. A detailed discussion can be found at Section 2.3.3;
- ECAL-F signals: including two signals **ECAL-F-or** and **ECAL-F-and** but within an extended 240 ns gate, which is used to build the unbiased electromagnetic trigger.

- ECAL-A signals: if the shape of fired cells from different x or y superlayers within 640 ns gate is found to be compatible with a shower, **ECAL-A-x** or **ECAL-A-y** signal is generated. They're combined in logic OR and logic AND into **ECAL-A-or** and **ECAL-A-and** signals, which build ECAL standalone triggers for "single photon" events.
- EXT-GATE signals: external signals within 240 ns gate, **EXT-GATE0** and **EXT-GATE1**, which are used for calibration purpose and disabled during flight.

These signals are then combined into 7 sub-triggers (five physical and two unbiased triggers) and these sub-triggers are stored with possible pre-scaling from 1 to 1024 (only storing 1 out of n events with n is the pre-scaling factor):

1. Unbiased charged: 3 out of 4 TOF layers have signals above HT, i.e. **FTC**. **FTC** is stored with pre-scaling factor of 100;
2. Single charged: 4 out of 4 TOF layers have signals from paddles within tracker acceptance above HT and NACC=0, i.e. **FTCT1** and **ACC0**;
3. Normal ions: 4 out of 4 TOF layers have signals above SHT and NACC<Ntr_1, i.e. **BZ** and **ACC1**;
4. Slow ions: 4 out of 4 TOF layers have signals above SHT within extended 640 ns time windows, i.e. **FTZ**;
5. Electrons: 4 out of 4 TOF layers have signals from paddles within tracker acceptance above HT and ECAL has signals above threshold for both x and y superlayers, i.e. **FTCT1** and **ECAL-F-and**;
6. Photons: have ECAL shower, i.e. **ECAL-A-and**;
7. Unbiased EM: ECAL has signals above threshold for x or y superlayers with 1000 pre-scaling factor, i.e. **ECAL-F-or**;

Events are required to be triggered by at least one of the five physical triggers in order to be counted as valid events. Those only passing unbiased charged trigger are stored with pre-scaling and are only used for the estimation of trigger efficiency.

2.3.3 Trigger setting change

As stated above, the threshold for ACC-1 were set to 5 after the launch of the AMS-02. However, after study of the trigger efficiency for heavy nuclei, especially for Iron, this threshold suppresses the trigger efficiency for heavy nuclei with high energy which creates too many secondaries inside AMS. After testing, the threshold was finally set to 8 in February 26, 2016. A comparison of efficiencies with old and new trigger setting for Silicon will be presented in Section 3.3.3.1.

2.3.4 Data Acquisition process

The Data Acquisition system (DAQ) for the AMS-02 has a tree structure (Fig. 2-15). After receiving the trigger signals, readouts from sub-detector Front-End electronics are packaged by Data Reduction computers (xDR, with x stands for different sub-detectors) and then collected and buffered by the DAQ computers. Through DAQ Intermediate Node (JINJ), data is transferred to the Main Data Computer (JMDC), where it's buffered and transmitted to the ISS.

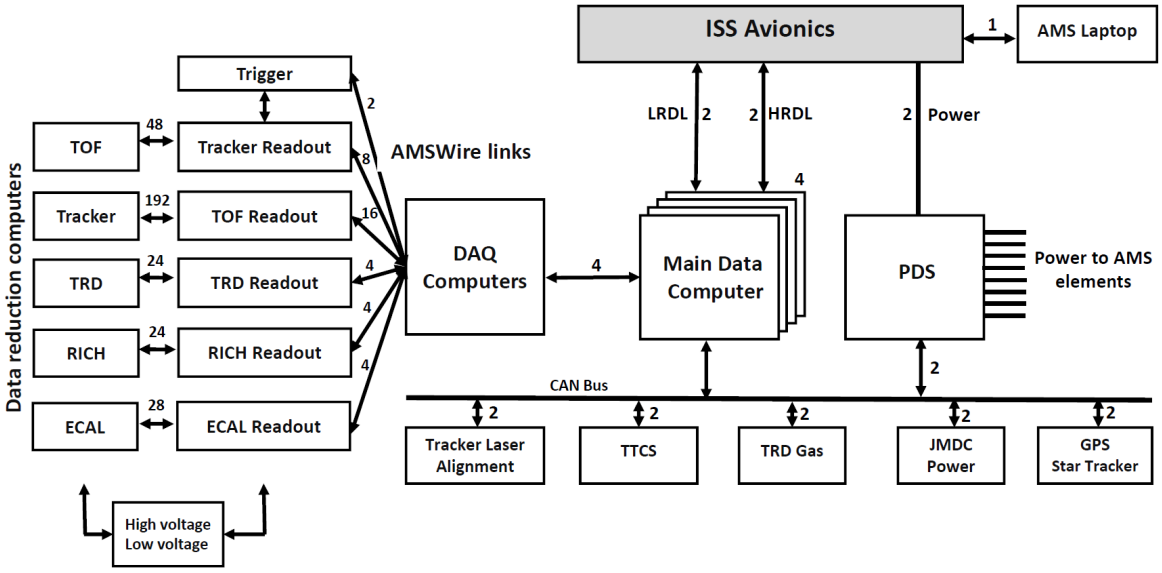

Figure 2-15: Diagram of the AMS-02 electronic together with Data acquisition, monitoring and command interface to the ISS. Taken from [104]

After the launch of the AMS-02, only one JINJ node was used for science data collection. Due to the limited buffer size of JINJ (24500 bytes), events with large data

size were truncated, which typically correspond to heavy nuclei or/and high energy events. To reduce data truncation, two JINJ nodes are used instead after November 12, 2015. The inefficiency due to limited buffer size of the JINJ is corrected by the DAQ efficiency, which will be studied in Section 3.2.3.

2.4 Detector Calibration

After integration, the AMS-02 was placed in CERN SPS, exposed to various test beams to calibrate the track coordinate resolution, the energy resolution as well as proton rejection power for electron [104]. Remaining calibration procedures were performed using sea level cosmic rays during the preparation for the Shuttle flight and operations on the ISS at Kennedy Space Center (KSC), from September 2010 to March 2011.

To achieve stable electronic responses during nominal operation, all electronic channels are calibrated twice for each orbit, i.e. for every 42 min [104]. Pedestals and noise levels for every electronic channel are measured during the on-orbit calibration.

2.5 Monte Carlo Simulation

The AMS collaboration has developed a Monte Carlo (MC) simulation software based on GEANT4 [105–107], which includes an accurate description of the AMS-02 detector geometry, material composition and response. The tracker charge and spatial resolution are fine-tuned, as shown in Fig. 2-16 and Fig. 2-17.

Monte Carlo simulated particles are generated uniformly and isotropically on a 3.9m×3.9m square on top of the AMS-02 detector. Two sets of MCs, are generated for a large set of nuclei:

- L1 focus: the extrapolation of generated particles from the generation plane is required to be within the Tracker L1 fiducial volume, the generated rigidity range is $[1, 2000]$ GV;
- L19 focus: the extrapolation of generated particles from the generation plane is required to be within both the Tracker L1 and L9 fiducial volume, the generated rigidity range is $[2, 8000]$ GV.

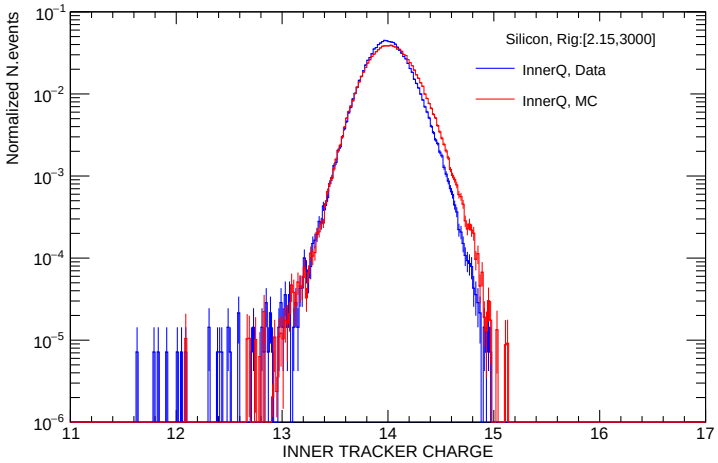

Figure 2-16: The normalized Inner Tracker charge distribution for ISS data (blue) and Monte Carlo simulation (red) in rigidity interval [2.15, 3000] GV. The samples are selected by Tracker L1 charge, Upper TOF charge, Lower TOF charge and Tracker L9 charge to be compatible with Silicon.

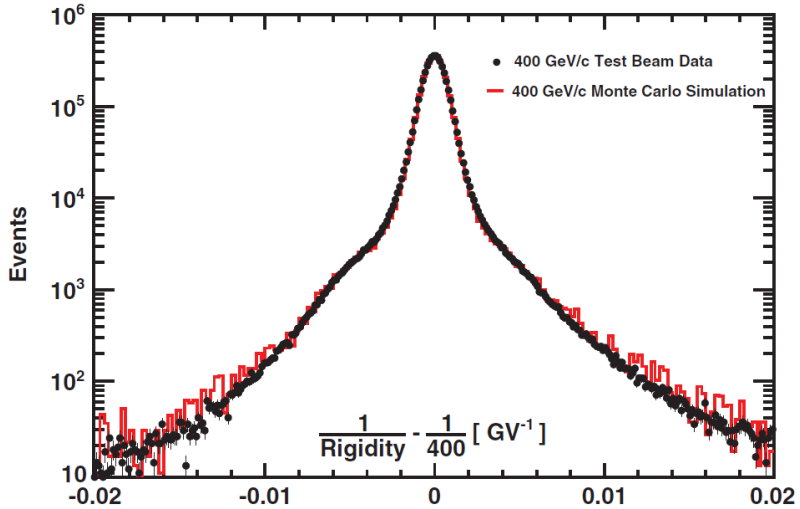

Figure 2-17: The rigidity resolution as function of inverse rigidity for 400 GeV/c protons measured in the test beam (black point) compared with the MC simulation (red line). Taken from [62].

The generated momentum spectrum is R^{-1}, and the accurate simulation of cosmic rays spectra can be achieved using an event-by-event reweighting.

2.5.1 Tuning the MC cross section

The normalization of the flux considering the loss of event count due to fragmentation inside AMS-02 largely depends on the accurate description of inelastic cross section on the AMS material (mostly C and Al). Nuclear interaction cross-section measurements are only available at low energy and/or for a few nuclei species. However, they can be measured with the AMS-02 detector itself using as target either the upper part (the TRD and the upper TOF) or the lower part (the lower TOF and the RICH) [108].

The AMS-02 MC simulation uses the Glauber-Gribov model to describe nuclear inelastic cross section and uses the MC/Data ratio of the Tracker L1→L2 and L8→L9 survival probabilities to tune the cross section model including a detailed tuning of the fragmentation channel. The estimation of the Tracker L1→L2 and L8→L9 survival probabilities will be discussed in detail in Section 3.5.

Chapter 3

Silicon nuclei flux measurement

Silicon nuclei flux Φ_i in the rigidity bin $(R_i, R_i + \Delta R)$ is obtained as:

$$\Phi_i = \frac{N_i}{A_{eff} T_i \Delta R} \quad [\mathrm{m}^{-2}\mathrm{s}^{-1}\mathrm{sr}^{-1}\mathrm{GV}^{-1}], \tag{3.1}$$

with N_i the number of events collected by AMS-02 after event selection, background subtraction, DAQ efficiency and bin-to-bin migration correction; A_{eff} the effective acceptance (detector geometrical factor multiplied by particle survival probability when traversing the AMS-02 detector and the Trigger, detection, reconstruction and selection cuts efficiencies) estimated from Monte Carlo simulation, measured in $\mathrm{m}^2\mathrm{sr}$, which is corrected by the data-to-MC efficiency ratios $\prod_i \varepsilon^i_{Data}/\varepsilon^i_{MC}$ for the small difference between the data and simulation; T_i the exposure time in seconds and ΔR the rigidity bin width in GV.

3.1 Exposure time

The average data acquisition live time of the AMS-02 is 90%. When the ISS traverses the South Atlantic Anomaly (SAA) [109], a region overwhelmed by charged particles trapped in the Earth's inner Van Allen radiation belt, the data acquisition of the AMS-02 detector saturates due to such high particle rates. Data taken during periods when AMS was not operating in nominal conditions, are excluded from the analysis. Furthermore, the Earth's magnetic field as a function of the geographic coordinates will prevent low rigidity cosmic

rays from reaching AMS-02, introducing a rigidity dependent detector exposure time. All these factors are considered when computing the AMS-02 exposure time to galactic cosmic rays.

Only those seconds passing all following selections will be accounted into exposure time:

- Good Real Time Information (RTI): a set of standard selection studied by AMS collaboration to ensure that the detector is working in nominal conditions, including:
  1. the ratio between the triggered events (N_{trig}) and the reconstructed events (N_{evt}) should be larger than 98%, i.e. $N_{trig}/N_{evt} > 0.98$;
  2. the data acquisition live time (t_l) should be larger than 0.5;
  3. the AMS z-axis pointing within 40° of the local zenith;
  4. absent events (N_{err}) should be no more than 10% over N_{evt}, i.e. $N_{err}/N_{evt} < 0.1$;
  5. at least one reconstructed particle, i.e $N_{par} > 0$, and $N_{evt} < 1800$;
  6. $\frac{N_{par}}{N_{trig}} > \frac{0.07}{1600} \times N_{trig}$ and $\frac{N_{par}}{N_{trig}} < 0.25$;
  7. alignment agreement: differences between the bending coordinate of alignment results from PG and MD should be less than 35 μm (45 μm) for L1 (L9).
- outside SAA: Only seconds when ISS was outside the SAA are included.
- Bad Run removal: The list of bad runs is
  - 1306219312; 1306219522; 1306233745; 1307125541 - 1307218054;
  - 1321198167; 1411991495 - 1417187199 (ttcs-off period);
  - 1454830398 - 1454932730 (trigger setting test period).

The weighted live time ($t_l \cdot N_{evt}/(N_{evt} + N_{err})$) are then accumulated for rigidity bins whose lower edges are larger than the 1.2 times the maximum geomagnetic cutoff R_c^{max} to account for the suppression of exposure time to galactic cosmic ray due to the Earth's magnetic field. The safety factor of 1.2 eliminated the possible contamination of trapped particles due to the uncertainty of the geomagnetic model. The geomagnetic cutoff was calculated for each second by backtracing [110] particles from the top of AMS-02 out to 50

Earth's radii using the recent International Geomagnetic Reference Field (IGRF) model [111, 112]. R_c^{max} is the maximum cutoff within AMS-02 field of view, which corresponds to 30° with respect to the detector axis for the Tracker L1+Inner acceptance (which also covers the FullSpan geometry including the Tracker L9).

The AMS-02 7 years exposure time as a function of rigidity is shown in Fig. 3-1. The exposure time is rigidity dependent below 30 GV and then reaches a plateau, reflecting the effect of the geomagnetic cutoff which only acts at low rigidities. For the first 7-years of data taking from May 2011 to May 2018, the plateau value is $\sim 1.75 \times 10^8$ s.

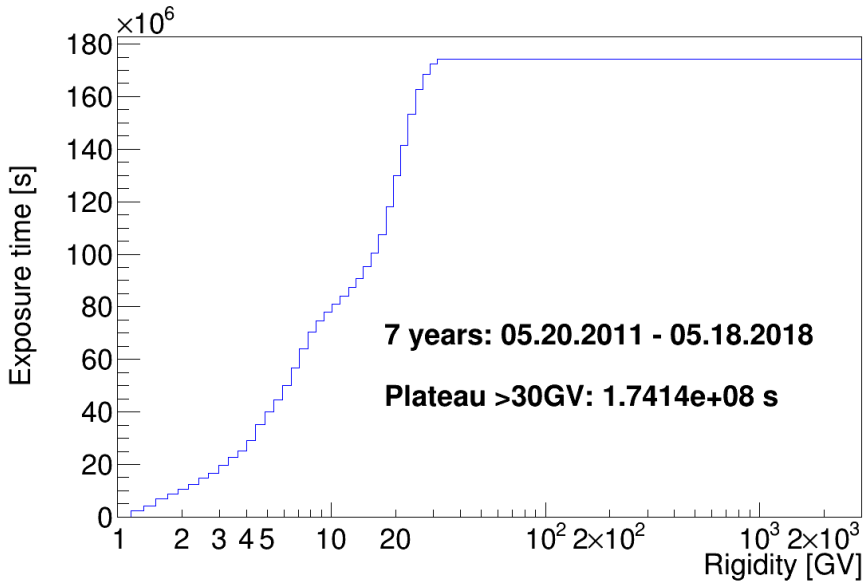

Figure 3-1: The AMS-02 7 years exposure time as a function of rigidity for the 7-years data set from the beginning of operation in May 2011 until May 2018. The effect of the geomagnetic cutoff introduces a rigidity dependence below 30 GV.

3.2 Event Counts

3.2.1 Event selection

Cosmic ray events collected by AMS-02 are required to pass certain selection cuts to be recognized as well reconstructed Silicon nuclei events, which will be used for the flux measurement. Event selection cuts include:

- pre-selections to make sure that events are collected when AMS-02 is working on

nominal operating conditions;

- reconstruction selections, which make sure that events are well reconstructed in the sub-detectors used for this analysis, namely the Silicon Tracker and the Time Of Flight (TOF);
- redundant charge selection from different sub-detectors to identify the species of incoming particles as well as to ensure no charge changing has occurred due to fragmentation when particles traverse the AMS material.

3.2.1.1 Pre-selections

All selections for the exposure time described in Section 3.1, including Good RTI, outside SAA, bad run removal and geomagnetic cutoff, are applied to make sure that 1) events are particles coming from the outer space, outside the Earth's magnetosphere, 2) events are collected in AMS-02 nominal state. Furthermore, only events triggered by physical triggers, as discussed in Section 2.3.2, are counted as valid events.

3.2.1.2 Reconstruction selections

Incoming particles are required to be downward going, have well reconstructed inner tracker track connected to the TOF track and have external tracker layer hit attached. Two detector geometries are used in the analysis:

1. FullSpan geometry, which requires the particle trajectory to pass through both external Tracker layers allowing to reach higher Maximum Detectable Rigidity (MDR);
2. L1Inner geometry, which only requires the particle trajectory to pass through Tracker L1 and Inner Tracker to increase the acceptance so as the statistic.

For FullSpan geometry, selections on Tracker L1 and L9 hit are required together with the lower TOF, while for L1Inner pattern only Tracker L1 hit selection are required. As the FullSpan selections includes almost all the L1Inner selections, the L1S samples contains almost all the events in the FullSpan one and the two samples are not independent.

The reconstruction selections for different sub-detectors include:

Inner Tracker (L2 to L8)

Selections on Inner Tracker require well reconstructed Inner Tracker Track with good fitting, ensuring a well measured rigidity:

1. inner tracker hit pattern: At least five hits in the bending coordinate (Y), and among these hits it is required that there is at least one hit in Tracker L2 and all 3 planes (L3 or L4, L5 or L6, L7 or L8);
2. inner tracker track fitting quality: normalized χ^2 of the inner track fit in the bending coordinate to be less than 10, i.e. $\chi^2_{y,Inn}/d.f. < 10$.
3. inner tracker fiducial volume: the interpolation of the inner tracker track should be within the fiducial volume of at least five inner tracker layers, and within the Tracker L2 and all 3 inner planes.

TOF selection

1. the TOF Track is built with TOF hits within the Inner Tracker Track extrapolation;
2. $\beta_{TOF} > 0.4$ (positive so as the particle is downward going, meaning that it traverses the AMS-02 detector from top to bottom).

External layer selection

Selections on the Tracker external layer hits extend the analysis to Tracker Layer 1 or/and Tracker Layer 9 to have larger level arm for rigidity measurement as well as additional charge measurements. The list of selection cuts is:

1. Tracker L1 has XY-combined hit (reconstructed hit with both X-side and Y-side clusters) associated to the Inner Tracker Track extrapolation, which is required to be within the Tracker Layer 1 fiducial volume. The Y-side cluster is needed for a good rigidity measurement, while the requirement of both X-side and Y-side clusters enables a more accurate charge measurement obtained combining the signals from the two sides of the silicon sensor;
2. (only in FullSpan geometry) Tracker L9 has XY-combined hit (reconstructed hit with both X-side and Y-side clusters) associated to the Inner Tracker Track extrapolation, which is required to be within the Tracker Layer 9 fiducial volume;

3. Selections on the Tracker Track fitting quality, which ensure a good Track fit as well as a good measured rigidity:

   - L1Inner Pattern: 1) the normalized χ^2 of the L1Inner track fit in the bending coordinate ($\chi^2_{y,L1Inn}/d.f.$) is required to be less than 10, $\chi^2_{y,L1Inn}/d.f. < 10$, and 2) difference between the χ^2 of the L1Inner track fit ($\chi^2_{y,L1Inn}$) and the χ^2 of the Inner track fit ($\chi^2_{y,Inn}$) in bending coordinate is required to be less than 10, i.e. $\chi^2_{y,L1Inner} - \chi^2_{y,Inn} < 10$;
   - FullSpan Pattern: the normalized χ^2 of the FullSpan track fit in the bending coordinate ($\chi^2_{y,L1InnL9}/d.f.$) is required to be less than 10, i.e. $\chi^2_{y,L1InnL9}/d.f. < 10$.

3.2.1.3 Charge selections

For nuclei flux measurements, the reconstructed charge values from Inner Tracker, TOF (upper and/or lower TOF) and External layers (L1 and/or L9) are used to identify incoming nuclei and to suppress fragmented particles inside the AMS-02. Charge selections for Silicon nuclei in each sub-detector are:

1) L1Q
   (a) Q_{L1} to be within $[12.4332, 14.8947]$;
   (b) good Tracker L1 charge status is required, i.e. (L1Q_status&0x10013D)==0.
2) upper TOFQ: Q_{UTOF} to be within $[13.2625, 15.5]$;
3) Inner Tracker Charge: Q_{Inn} is required to be within $[13.5, 14.5]$;

For FullSpan study, additional selections are also applied:

4) lower TOFQ: Q_{LTOF} to be > 13.2625;
5) Q_{L9} to be within $[Z-0.0284\times Z^{1.15}-0.17, Z+0.0585\times Z^{1.15}+0.35]$, i.e. $[13.2393, 15.5668]$.

3.2.1.4 Event count and Event Rate

The Silicon nuclei event counts, passing all event selections, collected during the first 7 years operation of the AMS-02 amounts to more than 1.6 million. Fig. 3-2 shows the

distribution of Silicon nuclei event counts as function of reconstructed rigidity in L1Inner and FullSpan geometries.

The Silicon nuclei event rate, i.e. the number of Silicon nuclei detected by AMS-02 per second per GV is calculated as:

$$R_{ev} = \frac{N_i}{T_i \Delta R} \tag{3.2}$$

and shown in Fig. 3-3 for L1Inner and FullSpan geometries respectively.

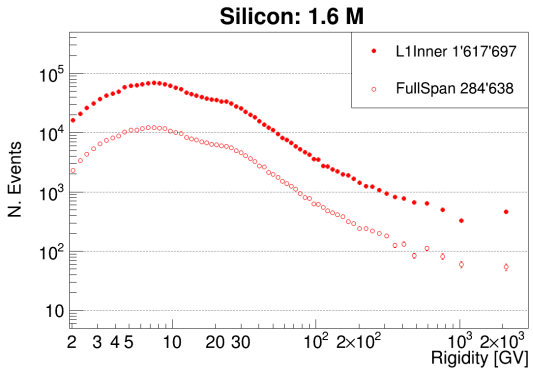

Figure 3-2: AMS-02 7 years Silicon event counts as function of reconstructed rigidity for L1Inner (red full circle) and FullSpan (red open circle) respectively.

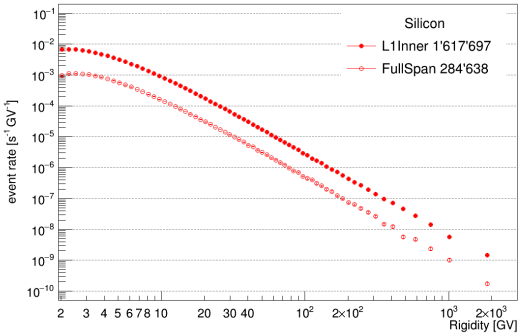

Figure 3-3: AMS-02 7 years Silicon event rates as function of reconstructed rigidity for L1Inner (red full circle) and FullSpan (red open circle) respectively.

3.2.2 Background Estimation

Heavier nuclei, such as Phosphorus and Sulfur, can fragment into Silicon nuclei by interaction with the AMS material. Two classes of background from fragmented particles can be distinguished depending on the zone of interaction:

- Below Tracker L1: materials between Tracker L1 and L2 (mainly the TRD and upper TOF). Note that even with upper TOF charge cut, events with fragmentation might not be fully removed and still introduce background into the selected event samples;
- Above Tracker L1: supporting structures above Tracker L1 (thin carbon fiber and aluminum honeycomb).

These events will pass all event selections and will be identified as Silicon nuclei, introducing contamination to the sample of Silicon nuclei entering the AMS-02 from space. The

estimation and subtraction of the background arising from these two sources are explained in the next sections, Section 3.2.2.1 and Section 3.2.2.2.

3.2.2.1 Below Tracker L1 background - fragmentation in materials between the Tracker L1 and L2

A cut on the L1 charge, L1Q< 14.8947 for Silicon, is applied to suppress the below Tracker L1 contamination by ensuring that the incoming nuclei is identified as Silicon at Tracker L1. The remaining background, due to the finite Tracker charge resolution, is then evaluated by charge template fits of the Tracker L1 charge distribution for events selected as Silicon applying the same charge selection cuts as for event counts on the upper TOF and the Inner Tracker.

Charge templates are built from the Tracker L2 charge distribution of non-interacting Silicon (Z=14), Phosphorus (Z=15) and Sulfur (Z=16) nuclei event samples. Such samples are obtained from data events in the L1Inner geometry that have compatible charge measurements in the Tracker L1, the two upper TOF layers and the Tracker L3-L8, i.e. Z to be within $[Z-0.5, Z+0.5]$ for nuclei with charge Z=14,15,16. For each samples, a one-dimensional Gaussian kernel estimation Probability Distribution Function (PDF) is obtained and used as the charge template for the corresponding nucleus. Charge templates are built in different rigidity intervals to account for possible energy dependence on the background and/or the charge resolution. Fig. 3-4 shows the examples of Tracker L2 charge distributions together with the kernel estimation PDFs for Silicon, Phosphorus and Sulfur in the rigidity bin $[3.29, 3.64]$.

Due to the small difference of the peak position between the Tracker L1 and L2 charge distribution resulting from subtle difference in the performance of the front-end electronics, charge templates then fit to the tightly-selected L1 charge sample to determine the shift of the peak, as shown in Fig. 3-5 together with the fit result. The tightly-selected L1 charge sample is obtained requiring compatible charge measurements in the two upper TOF layers and the Inner Tracker, with a tighter charge cut, [Z-0.5, Z+0.5], with respect to those applied for the event counts. The shift of the Silicon charge template PDF will be a free parameter during the Tracker L1 charge template fit using the fitted shift as initial value. For heavier nuclei (P and S), the charge template shifts are fixed to the

fitted results, because their abundance in the raw Silicon event count samples is too small to allow a good determination of the peak position.

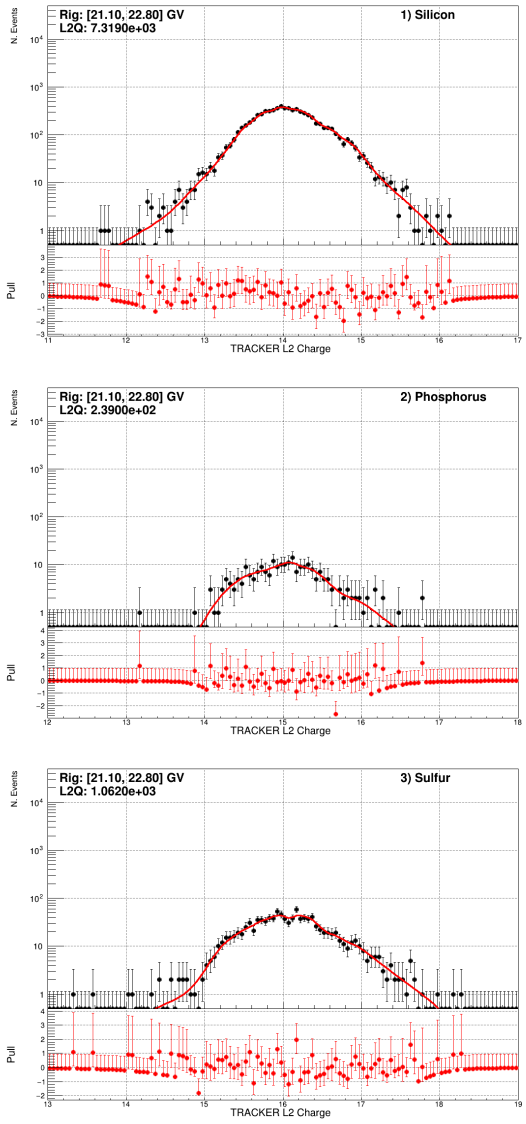

Figure 3-4: Selected Tracker L2 charge sample (black full circle) and kernel estimation PDF used as charge template (red curve) for 1) Silicon, 2) Phosphorus and 3) Sulfur. The bottom panels show the pull between the Tracker L2 charge distributions and the PDFs.

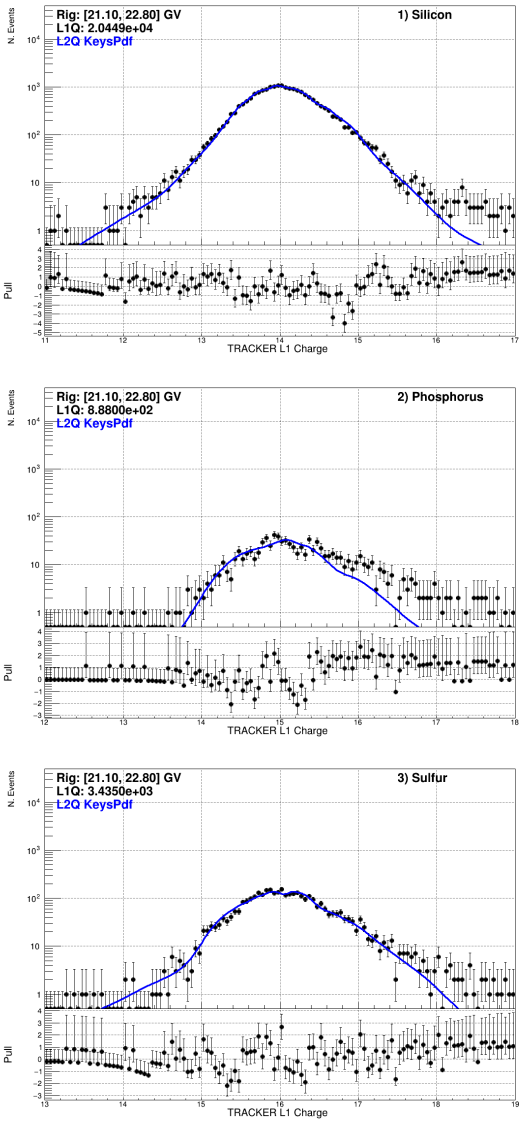

Figure 3-5: Tracker L1 charge distribution selected by two upper TOF layers and Inner Tracker (black full circle) together with shifted charge templates (blue curve) for 1) Silicon, 2) Phosphorus and 3) Sulfur. Discrepancies between the Tracker L1 charge distribution and the charge templates on the right-hand side are due to that the selected samples include Higher Z events. The bottom panels show the pull between Tracker L1 charge distributions and the shifted PDFs.

The Tracker L1 charge sample of the raw Silicon nuclei samples, selected applying the same charge selection on the upper TOF and the Inner Tracker as for event selection, is then fit with the charge templates of Silicon, Phosphorus and Sulfur with 1) the relative abundance between these elements and 2) the shift of Silicon charge template PDF as free parameters. Figure 3-6 shows the charge template fit results together with the relative abundance and the shift of the Silicon charge template in the rigidity bin $[3.29, 3.64]$ GV.

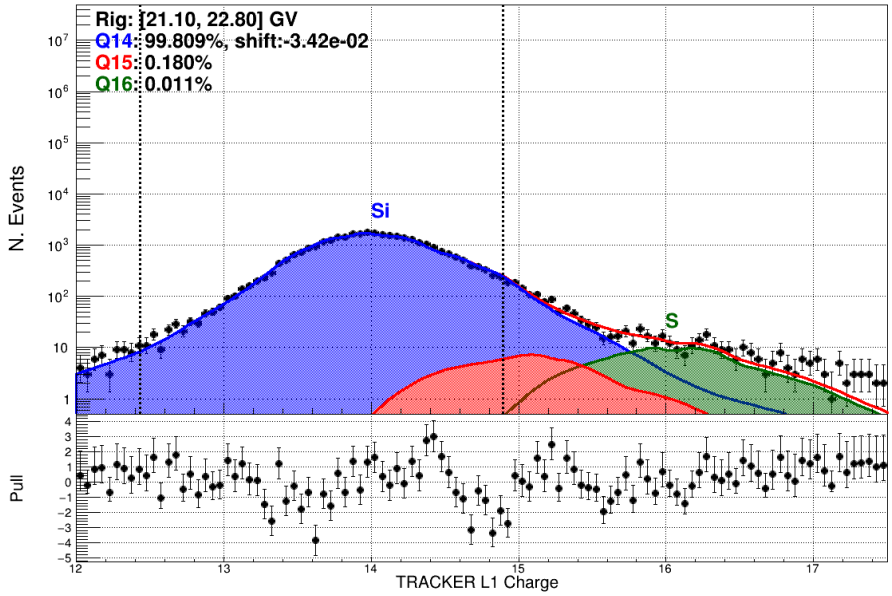

Figure 3-6: Tracker L1 charge distribution of the raw Silicon event counts (black full circle) fitted with the sum of charge templates for Silicon, Phosphorus and Sulfur (red curve). The shaded areas show the charge PDFs for Si (blue), P (red) and S (green). The L1 charge selection interval for Silicon is indicated by the black dashed lines. The bottom panel is the pull between the Tracker L1 charge distribution and the sum of charge PDFs.

The impurity of the selected L1 charge sample for Silicon is then calculated by integrating the charge template of heavier nuclei in the L1 charge selection interval for Silicon indicated by the black dashed line in Fig. 3-6, and found to be $< 0.3\%$ for the entire rigidity range, as shown in Fig. 3-7.

The Silicon charge PDF obtained by the fit is also used to estimate the efficiency of the Tracker L1 charge cut L1Q$<$ 14.8947 by the ratio of the PDF integral within and outside the L1 charge selection range, as shown in Fig. 3-8.

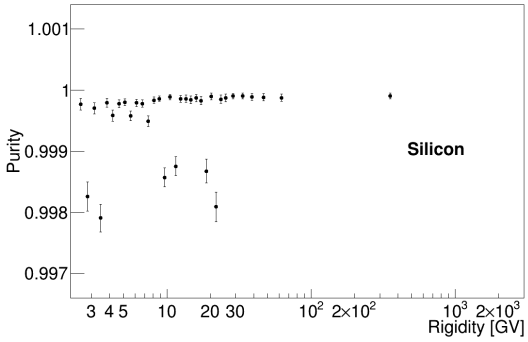

Figure 3-7: Purity of the Silicon event sample within the L1 charge selection region as function of reconstructed rigidity.

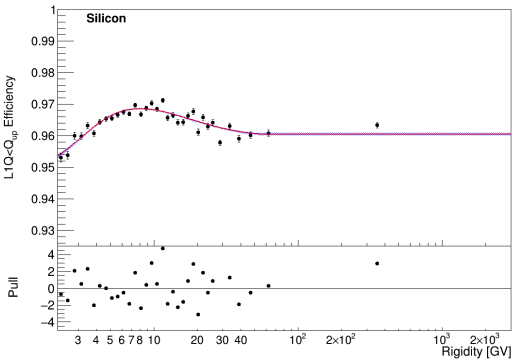

Figure 3-8: The Silicon Tracker L1 charge cut efficiency as function of rigidity.

3.2.2.2 Fragmentation in materials above Tracker L1: Top-Of-Instrument correction

Interactions above Tracker L1 cannot be identified by any of the AMS-02 sub-detectors since they happen before the very first detector, Tracker Layer 1, so this background can only be estimated using Monte Carlo simulation.

The number of events identified as Silicon nuclei in L1Inner or FullSpan geometry which are fragments from heavier nuclei interacting in the support plane of the Tracker L1 can be expressed as:

$$N_{X\to Si} = A_{X\to Si}\Phi_X T\Delta R \tag{3.3}$$

with $A_{X\to Si}$ the effective acceptance for nuclei X (with charge higher than Silicon) fragmenting into Silicon before Tracker L1 and passing event selections for Silicon Φ_X the true flux of nuclei X. $A_{X\to Si}$ can only be estimated from Monte Carlo simulation by applying Silicon selection on nuclei X simulations and depends on the simulation of partial inelastic cross section in AMS-02 Monte Carlo. The verification of the simulated partial inelastic cross sections with Data will be presented in Section 3.5.1.2.

Considering that the total collected Silicon event counts, N'_{Si} are the sum of event counts from incoming Silicon nuclei, N_{Si} and the above Tracker L1 background, i.e. $N'_{Si} =$

$N_{Si} + \sum N_{X \to Si}$, the Silicon nuclei flux without contamination can be expressed as:

$$\begin{aligned} N_{Si} = N'_{Si} - \sum N_{X \to Si} = N'_{Si}(1 - \sum \frac{N_{X \to Si}}{N'_{Si}}) = N'_{Si}(1 - \sum \frac{A_{X \to Si} T \Delta R \Phi_X}{A_{Si} T \Delta R \Phi'_{Si}}) \\ = N'_{Si}(1 - \sum \frac{A_{X \to Si}}{A_{Si}} \frac{\Phi_X}{\Phi'_{Si}}), \end{aligned} \tag{3.4}$$

with Φ'_{Si} the final Silicon nuclei flux before subtraction of the above Tracker L1 background, A_{Si} the Silicon effective acceptance (Section 3.3.2).

$A_{X \to Si}$ is obtained from samples of fragmented events and the true rigidity of fragments have changed compared to the generated rigidity of their parent particles, hence only the reconstructed rigidity measured by Silicon Tracker can be used. So, the correction will be calculated in the reconstructed rigidity space and applied to the raw event counts before unfolding. In order to correctly account for the event migration, these acceptances are estimated from Monte Carlo events, reweighing their rigidity distribution to the measured unfolded fluxes of Silicon and nuclei X respectively. The Silicon nuclei flux used for MC reweighing is the unfolded flux before the subtraction of the above Tracker L1 background. Differences on the event migration between the flux with or without this background is small since the background itself is small, as will be seen later.

The estimation of $A_{X \to Si}$ proceeds in the same way as for A_{Si} (Section 3.3.2) but from the Monte Carlo simulation of nuclei X. In order to remove the below Tracker L1 background from heavier nuclei MC sample, i.e. particle fragmenting into Silicon nuclei below Tracker L1, the selection of the sample for the estimation of the $A_{X \to Si}$ requires the L1Q upper cut, i.e. L1Q$<$ 14.8947 for Silicon. Similarly, the event selection to estimate the acceptance A_{Si} also includes this cut, which is not applied from the acceptance used for flux calculation.

The above Tracker L1 background also depends on the relative abundance between Silicon and the heavier nuclei X hence it will be dominated by nuclei with even charge since their abundance is $\sim$5 times larger than the nearby nuclei with odd charge. Furthermore, the cross section will lower with larger charge difference between parent and daughter nuclei, hence only the contribution from few nearby nuclei is important. In the case of Silicon nuclei, whose nearby heavier nuclei have at least $\sim$5 times lower abundance, only the contribution of Sulfur nuclei is considered.

The ratio between the effective acceptance for Sulfur nuclei fragmenting into Silicon nuclei and the acceptance of Silicon nuclei as function of reconstructed rigidity is shown in Fig. 3-9 together with the parametrization with a spline fit, which is used to correct the above Tracker L1 background instead of the data points to smooth out the statistical fluctuation. Considering that the flux ratio Φ_S/Φ_{Si} ~1/5, the above Tracker L1 background from Sulfur is negligible ($< 0.5\%$) for the entire rigidity range, as seen in Fig. 3-10.

The contribution from nuclei heavier than Sulfur will be even smaller due to smaller cross section and smaller flux compare to Silicon, so their contribution to the above Tracker L1 background is negligible in the entire rigidity range.

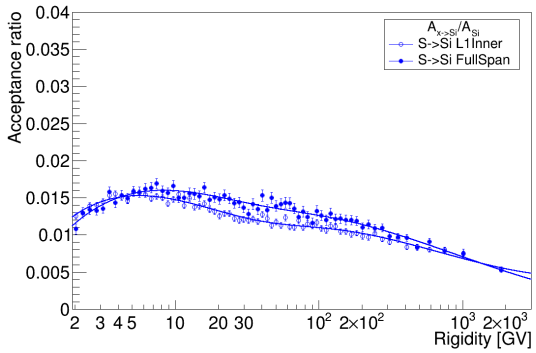

Figure 3-9: The acceptance ratio $A_{S\to Si}/A_{Si}$ for L1Inner (blue) and FullSpan (red) geometries. Both acceptances are shown as functions of reconstructed rigidity.

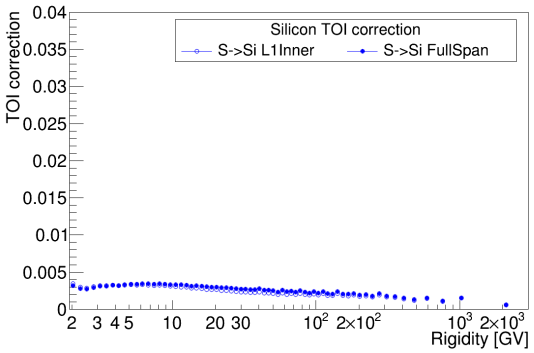

Figure 3-10: The top-of-instrument correction for Silicon produced by interaction of Sulfur nuclei above the Tracker L1 for L1Inner (blue open circle) and FullSpan (blue full circle) respectively.

3.2.3 DAQ Efficiency

As mentioned in Section 2.3.4, data is not 100% efficiently collected by the AMS-02 during 1 JINJ period, especially for high charge and/or high rigidity events. The truncated Silicon nuclei events ($N^{>24500}$) can be categorized into:

- Irrelevant truncation $N_{irr}^{>24500}$: events which have truncation on the data of irrelevant detectors (the TRD, the RICH and the ECAL) or secondary particles. All the required information from the Silicon Tracker and the TOF for nuclei flux analysis is stored, hence this kind of truncation is irrelevant. Collected events with data size

larger than the buffer limit ($N_{collected}^{>24500}$) will be irrelevant truncated events, $N_{collected}^{>24500} = N_{irr}^{>24500}$;

- Real event truncation $N_{RealTrun}^{>24500}$: events whose information of primary particles from key detectors (the Silicon Tracker and the TOF) are truncated. These events will not pass event selection and cause inefficiency.

In a summary, $N^{>24500} = N_{irr}^{>24500} + N_{RealTrun}^{>24500} = N_{collected}^{>24500} + N_{RealTrun}^{>24500}$.

For the 2 JINJs period, event distribution of JINJ-1 size vs JINJ-2 size for Silicon nuclei events (Fig. 3-11) shows that with 2 JINJs the AMS-02 has enough buffer size to prevent any truncation of Silicon nuclei events. Hence the DAQ efficiency for the 2 JINJs period ($\varepsilon_{DAQ}^{2JINJ}$) is ~100%.

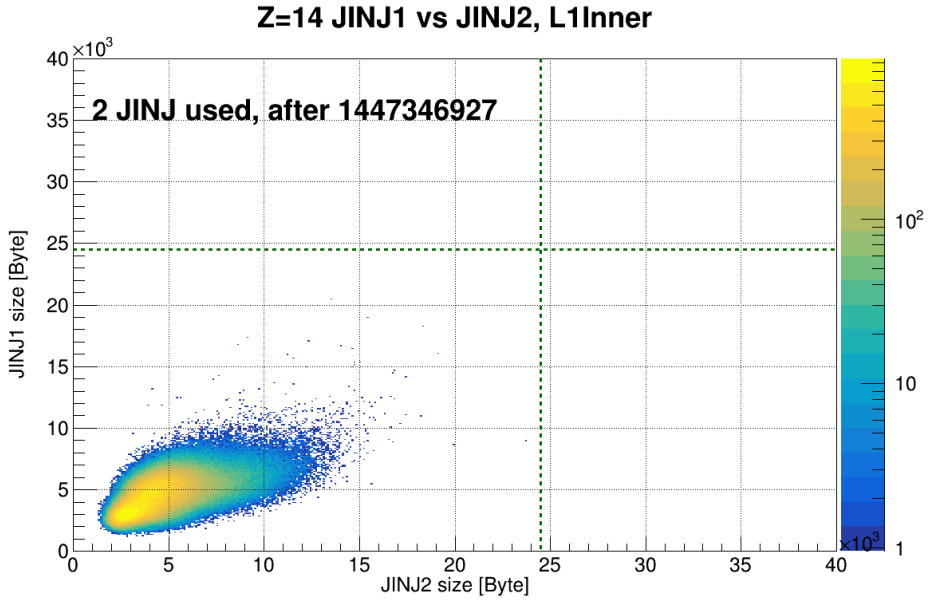

Figure 3-11: JINJ-1 size vs JINJ-2 size for Silicon nuclei events for rigidities from 2.15 GV to 3 TV. The green dashed lines indicate the 24500 bytes maximum size of a single JINJ.

The DAQ efficiency for the 1 JINJ period ($\varepsilon_{DAQ}^{1JINJ}$) can then be evaluated using the data from 2 JINJs period by assuming that the ratio between events with data size less and above 24500 bytes are the same for two periods:

$$\frac{N_{<=24500}^{1JINJ}}{N_{>24500}^{1JINJ}} \approx \frac{N_{<=24500}^{2JINJ}}{N_{>24500}^{2JINJ}} \tag{3.5}$$

where $N_{<=24500}$ ($N_{>24500}$) is the number of events with data size less (above) 24500 bytes.

$N^{1JINJ}_{>24500}$ can be estimated by:

$$N^{1JINJ}_{>24500} \approx \frac{N^{2JINJ}_{>24500}}{N^{2JINJ}_{<=24500}} N^{1JINJ}_{<=24500} \tag{3.6}$$

The DAQ efficiency can then be expressed as:

$$\varepsilon^{1JINJ}_{DAQ} = \frac{N^{1JINJ}_{<=24500} + N^{1JINJ}_{>24500,irr}}{N^{1JINJ}_{<=24500} + N^{1JINJ}_{>24500}} = \frac{N^{1JINJ}_{<=24500} + N^{1JINJ}_{>24500,irr}}{N^{1JINJ}_{<=24500} + N^{1JINJ}_{<=24500} \frac{N^{2JINJ}_{>24500}}{N^{2JINJ}_{<=24500}}} \tag{3.7}$$

with $N^{1JINJ}_{>24500,irr}$ is the number of truncated events irrelevant to the Silicon nuclei analysis. The total DAQ efficiency average over the first 7 years operation, which includes both the 1 JINJ and 2 JINJs periods, can be expressed as:

$$\varepsilon_{DAQ} = \frac{N^{1JINJ}_{<=24500} + N^{1JINJ}_{>24500,irr} + N^{2JINJ}_{<=24500} + N^{2JINJ}_{>24500}}{N^{1JINJ}_{<=24500} + N^{1JINJ}_{<=24500} \frac{N^{2JINJ}_{>24500}}{N^{2JINJ}_{<=24500}} + N^{2JINJ}_{<=24500} + N^{2JINJ}_{>24500}} \tag{3.8}$$

Fig. 3-12 shows the DAQ efficiency for the 1 JINJ period and the 7 years average, and Fig. 3-13 shows the 7 years average DAQ efficiency together with its parameterization.

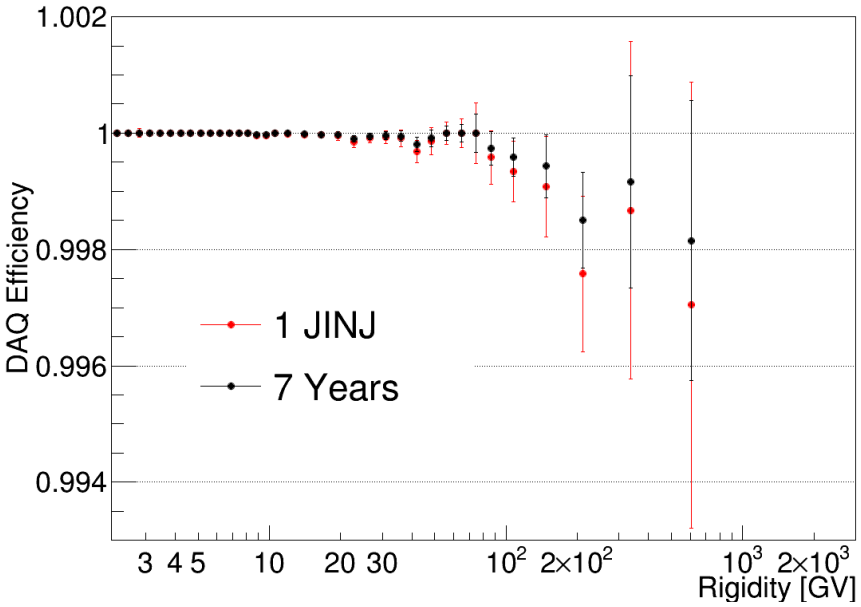

Figure 3-12: The Silicon nuclei DAQ efficiency for the 1 JINJ period (red full circle) and the 7 years average (black full circle) as function of reconstructed rigidity.

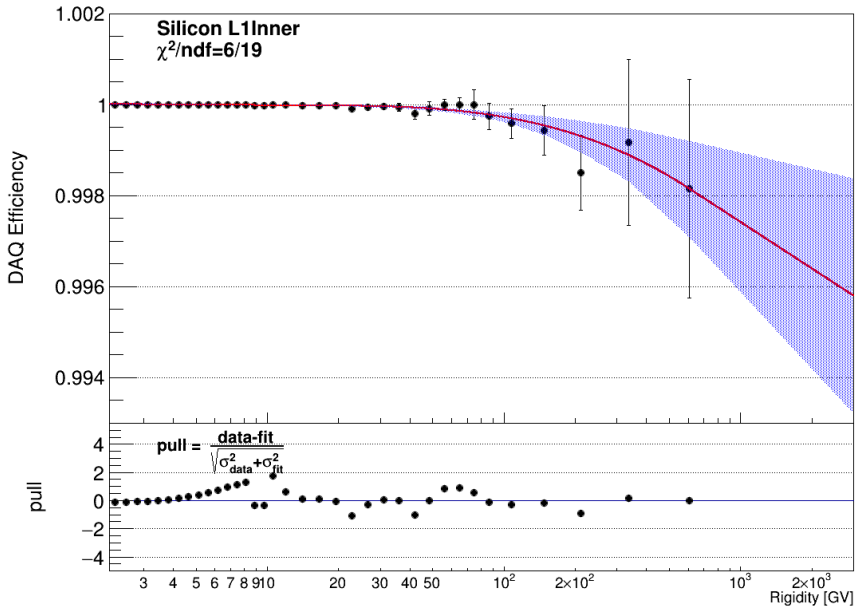

Figure 3-13: The Silicon nuclei average DAQ efficiency for the first 7 years of data taking as function of reconstructed rigidity (black full circle). The red curve and the blue band are the spline fit to the DAQ efficiency and 68% CL interval, respectively. The bottom panel shows the pull between the DAQ efficiency and its parameterization.

3.3 Acceptance and Efficiencies

3.3.1 Geometrical Acceptance

The geometrical acceptance of AMS can be obtained by toy Monte Carlo (whose total number of generated events N_{gen} is known) and AMS MC (whose N_{gen} is obtain by evaluation). The comparison of the geometrical acceptance from two MC verifies the evaluated N_{gen} of AMS MC.

Considering isotropic flux, the geometrical factor A_{geom} can be expressed as [113]:

$$A_{geom} = \int_{\Omega} d\Omega \int_{S} d\boldsymbol{S} \cdot \hat{\boldsymbol{r}} = \int_{\Omega} \sin\theta d\theta d\phi \int_{S} \cos\theta dS \sim \int_{\Omega} \int_{S} d\cos^2\theta d\phi dS. \tag{3.9}$$

Hence in order to simulate particles having an isotropic flux, the particles in toy MC are generated with uniformly distributed $\cos^2\theta$, ϕ, the x and y coordinates at the generation plane. Each generated particle is then linearly extrapolated to every Silicon Tracker layers and the extrapolated point is required to be within the fiducial volume of each Tracker layer by applying the same fiducial volume cut as for the event selection (see

Section 3.2.1). The geometrical factor is estimated from the ratio between the number of generated events within the fiducial volume over the total number of generated events.

In AMS MC, particles are generated with rigidity dependence of $1/R$. Normalization of the generation distribution will be fixed by the evaluated total number of generated events and then the number of generated particles in each rigidity bins (N_{gen}^{AMS}) can be calculated. All generated events whose extrapolation from the generation plane is within the fiducial volume are stored. Hence the geometrical acceptance from AMS MC is calculated as the ratio of the number of events passing the fiducial volume cut (N_{geom}^{AMS}) over the evaluated total number of generated events for each rigidity bin, i.e. $\varepsilon_{geom}^{AMS} = N_{geom}^{AMS}/N_{gen}^{AMS}$.

The geometrical factors obtained from AMS-02 MC for L1Inner and FullSpan together with results from the toy MC are shown in Fig. 3-14. The agreement between results from the toy MC and the AMS-02 MC confirms the evaluation of total generated events of the AMS-02 MC.

3.3.2 Effective Acceptance

The effective acceptance, A_{eff}, which is the product of the geometrical factor A_{geom} with the particle survival probability when traversing the AMS-02 detector, and the trigger, reconstruction and selection cut efficiencies, which depend on detector responses. The small difference of efficiencies between simulation and data due to the imperfect description of the detector will be corrected using the ratio of efficiencies, $\varepsilon_{Data}^{i}/\varepsilon_{MC}^{i}$, evaluated from data and simulation samples respectively, as will be seen in Section 3.3.3. The small difference of the survival probability between simulation and data introduces a rigidity-independent bias on the total flux normalization, which will be evaluated in Section 3.5.

The total number of generated events, N_{gen}, in each rigidity bin are the same as those for the geometrical factor. The event counts from MC, N_{event}^{MC}, are then selected by applying event selection cuts discussed in Section 3.2.1. As the Monte Carlo sample contains only the Silicon nuclei events, the upper cut for L1 charge, removing the below Tracker L1 contamination as discussed in Section 3.2.2.1, are not applied for MC event

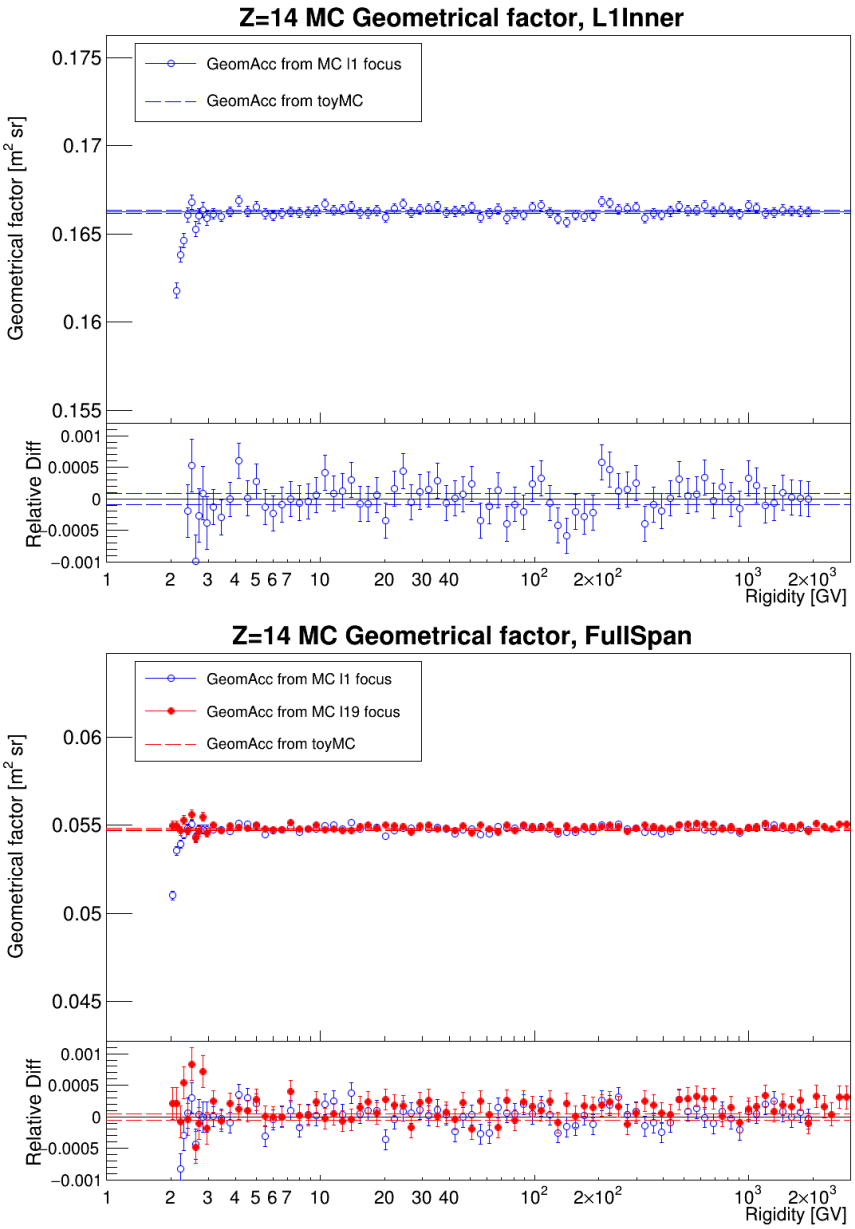

Figure 3-14: The geometrical factor for the L1Inner geometry from l1 focus MC (top), the FullSpan geometry (bottom) from l1 focus MC (blue open circles) and from l19 focus MC (red points) as well as results from toy MC (solid line). Bottom panels show the relative difference between the geometrical factors from AMS MC and from toy MC.

selection. Finally, A_{eff} in the generated rigidity bin $(R_i, R_i + \Delta R)$ is given by:

$$A_{eff} = 3.9^2\pi \frac{N_{event}^{MC}}{N_{gen}} \prod_i \varepsilon_{Data/MC}^i \quad [\mathrm{m}^2\mathrm{sr}] \tag{3.10}$$

where $(3.9m \times 3.9m)$ is the surface of the generation plane. The effective acceptances will be parameterized to smooth the statistical fluctuations and only the parameterization will be used for flux calculation.

Figure 3-15 shows the Effective Acceptance with applying the efficiency ratio corrections for Silicon nuclei in two geometries together with their parameterizations.

3.3.3 Data/MC Efficiency ratio

Data/MC corrections are evaluated for the trigger efficiency as well as the detection, reconstruction and selection cuts efficiencies for sub-detectors. The latter are factorized into

- Tracker L1 big charge Efficiency (hereafter referred as L1 BZ efficiency);
- Tracker L1 pick up Efficiency;
- Inner tracking efficiency;
- Tof charge Efficiency;
- Tracker L9 Efficiency (FullSpan only).

To evaluate these efficiencies, for each of them an unbiased sample selected applying all but the cuts that are going to be studied (N_{sample}) is used: fraction of events selected by the cuts under study ($N_{selected}$) gives the efficiency, ε, as

$$\varepsilon = \frac{N_{selected}}{N_{sample}}, \tag{3.11}$$

and the correction to the effective acceptance A_{eff} will be the product of ratios between the efficiencies evaluated from the data samples, ε_{Data}^i, and those from the Monte Carlo samples, ε_{MC}^i.

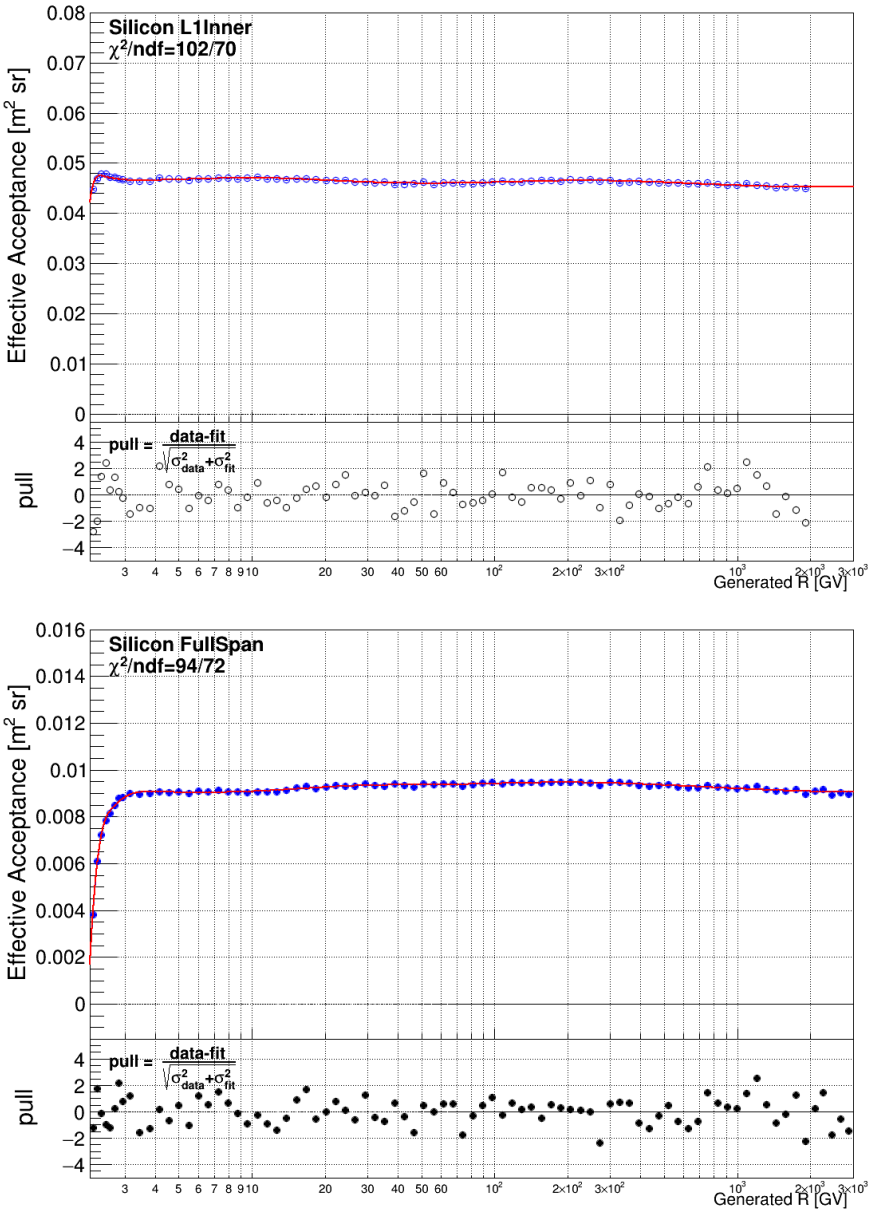

Figure 3-15: The Effective Acceptance of Silicon nuclei without applying the efficiency ratio corrections for L1Inner (top, blue open circle) and FullSpan (bottom, blue full circle) as function of generated rigidity. The red curve and blue band represent the spline fit to the acceptance and the 68% CL interval, respectively. The bottom panels show the pull between acceptances and spline fits.

3.3.3.1 Trigger efficiency

The trigger efficiency tells how many events are kept with the requirement of physical trigger.

The sample for trigger efficiency contains good events passing the physical trigger pattern $N_{physical}$, and good events not passing physical trigger pattern $N_{non-trigger}$, where "good events" are those passing all the other event selections besides trigger selection. The latter are estimated using events who passed the unbiased charged trigger pattern described in Section 2.3, N_{UBTrig}, as $N_{non-trigger} \approx prescale \times N_{UBTrig}$, where prescale is the prescaling factor applied to the unbiased charged trigger. The sample for trigger efficiency is:

$$N_{physcial} + N_{non-trigger} = N_{physcial} + prescal \times N_{UBTrig}, \tag{3.12}$$

and the trigger efficiency can then be expressed as:

$$\varepsilon_{trig} = \frac{N_{physical}}{N_{physical} + prescale \times N_{UBTrig}} \tag{3.13}$$

where $N_{physical}$ is the number of events passing the physical trigger selection.

As discussed in Section 2.3, the number of collected unbiased charged trigger events for Silicon nuclei is very low especially for the new trigger setting. Fig. 3-16 shows the unbiased charged trigger events for Silicon nuclei in the L1Inner geometry: as seen there is no event from the unbiased charged trigger collected above ∼500 GV (∼8 GV) before (after) February 2016, when the setting for BZ trigger (Section 2.3.2) is changed from NACC< 5 to NACC< 8. The corresponding trigger efficiency after 2016 with new trigger setting is higher than the one with old trigger setting as well (Fig. 3-17).

The total trigger efficiency can be expressed as:

$$\epsilon_{trig} = \frac{N^{(1)}_{phys} + N^{(2)}_{phys}}{D_1 + D_2} \tag{3.14}$$

with $N^{(1)}_{phys}$ ($N^{(2)}_{phys}$) events triggered by physical trigger and D_1 (D_2) the total events before (after) the trigger setting change in February 2016. It can then be separated into two

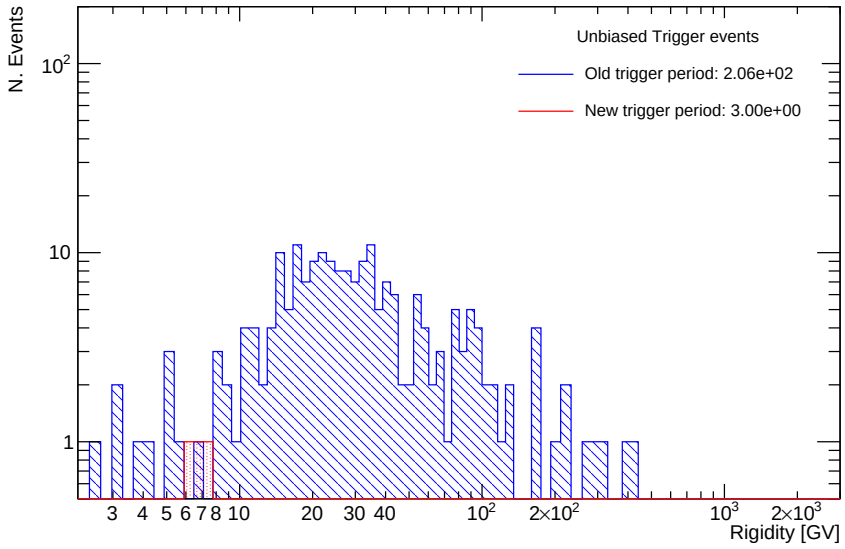

Figure 3-16: Pre-scaled unbiased triggered Silicon events as function of reconstructed rigidity before (blue) and after (red) trigger setting change in February 2016.

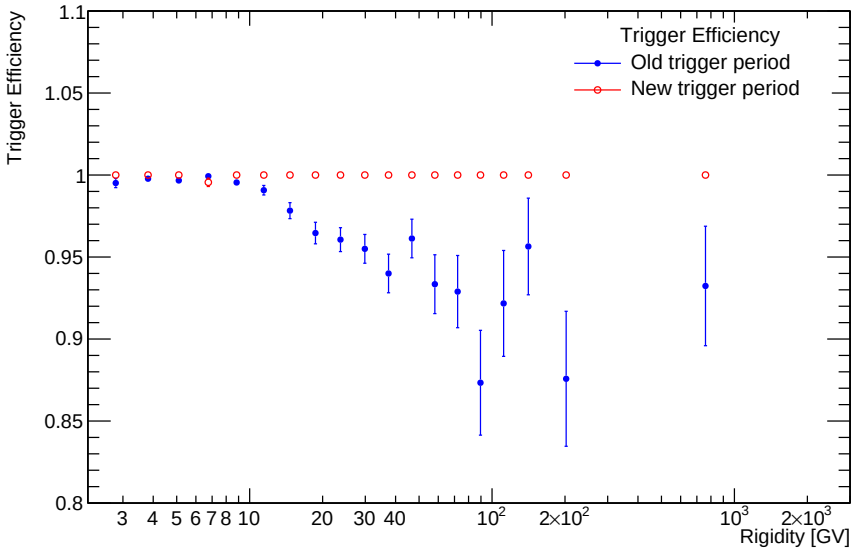

Figure 3-17: Trigger efficiency Silicon as function of reconstructed rigidity before (blue full circle) and after (red open circle) trigger setting change in February 2016.

parts:

$$\epsilon_{Trig} = \frac{N^{(1)}_{NACC<8} + N^{(2)}_{NACC<8}}{D_1 + D_2} \frac{N^{(1)}_{phys} + N^{(2)}_{phys}}{N^{(1)}_{NACC<8} + N^{(2)}_{NACC<8}} \tag{3.15}$$
$$= \epsilon_{trig,NACC<8} \cdot \epsilon_{NACC<8toPhysTrig}$$

with

- $N^{(1)}_{NACC<8}$ ($N^{(2)}_{NACC<8}$) events passing the physical trigger requiring NACC<8 for BZ trigger in old (new) trigger period;
- $\epsilon_{trig,NACC<8}$ the trigger efficiency for Physical Trigger with NACC<8;
- $\epsilon_{NACC<8toPhysTrig}$ the efficiency from events passing Physical Trigger with NACC<8 to events passing Physical Trigger (NACC<5 for old trigger period and NACC<8 for new trigger period.

For new trigger period $N^{(2)}_{NACC<8}$ is just $N^{(2)}_{phys}$ while for old trigger period $N^{(1)}_{NACC<8}$ is not collected.

Due to the stability of AMS detector, it's reasonable to assume that $\varepsilon_{trig,NACC<8}$ remain the same for two trigger periods, i.e.

$$\varepsilon_{trig,NACC<8} = \frac{N^{(1)}_{NACC<8} + N^{(2)}_{NACC<8}}{D_1 + D_2} \approx \frac{N^{(2)}_{NACC<8}}{D_2} = \varepsilon^{(2)}_{trig,NACC<8} \tag{3.16}$$

Fig. 3-18 shows that $\varepsilon_{trig,NACC<8} \approx 100\%$ for both Data and MC, hence $\varepsilon_{trig} = \varepsilon_{trig,NACC<8} \cdot \varepsilon_{NACC<8toPhysTrig} \approx \varepsilon_{NACC<8toPhysTrig}$.

To calculate the $\epsilon_{NACC<8toPhysTrig}$, $N^{(1)}_{NACC<8}$ need to be estimated using events from new trigger period by assuming the ratio between $N_{NACC<5}$ to $N_{NACC<8}$ remain the same for two periods:

$$\frac{N^{(1)}_{NACC<5}}{N^{(1)}_{NACC<8}} \approx \frac{N^{(2)}_{NACC<5}}{N^{(2)}_{NACC<8}}$$

hence $N^{(1)}_{NACC<8}$ can be estimated as $N^{(1)}_{NACC<8} \approx N^{(1)}_{NACC<5}(N^{(2)}_{NACC<8}/N^{(2)}_{NACC<5})$, and the trigger efficiency ϵ_{trig} will then be estimated as:

$$\epsilon_{Trig} \approx \frac{N^{(1)}_{phys} + N^{(2)}_{phys}}{N^{(1)}_{NACC<5} \frac{N^{(2)}_{NACC<8}}{N^{(2)}_{NACC<5}} + N^{(2)}_{NACC<8}} \tag{3.17}$$

Figure 3-19 shows the Trigger efficiency estimated using Eq. (3.17) for L1Inner and

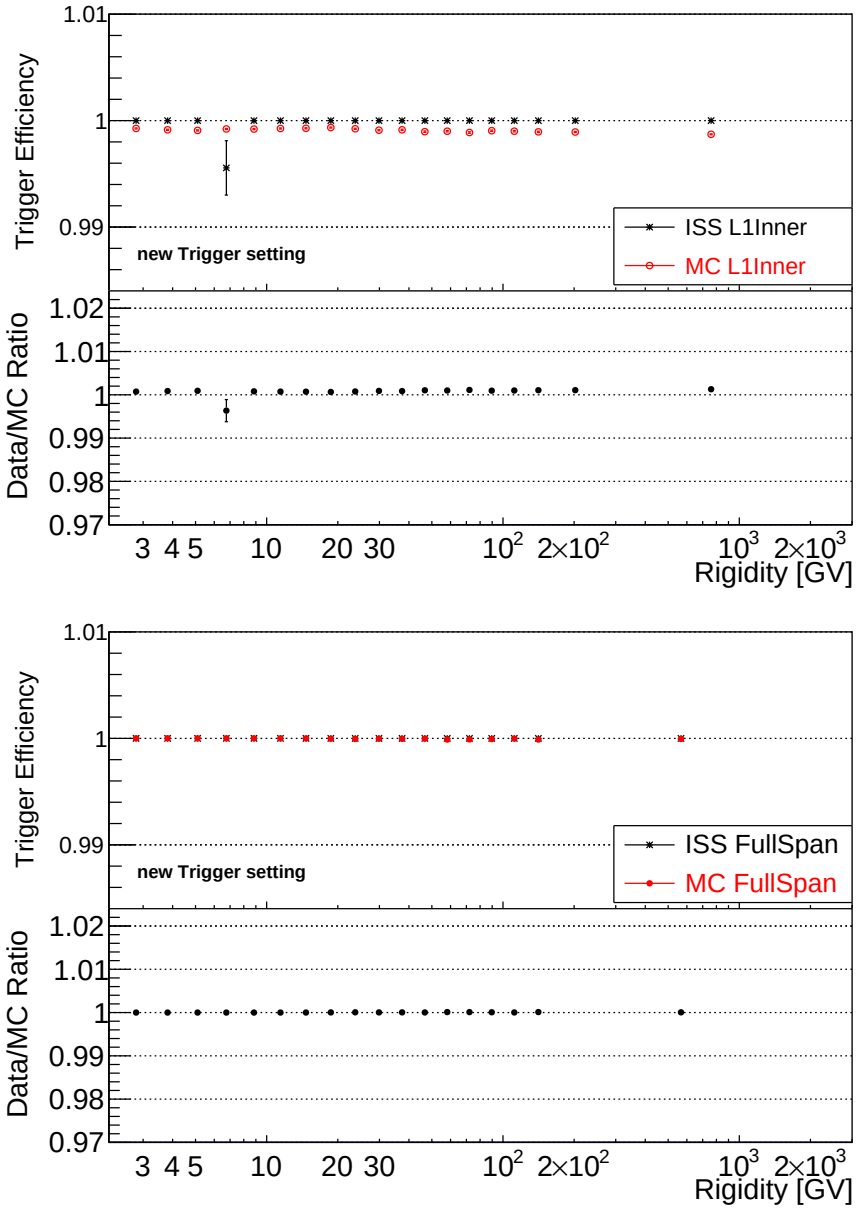

Figure 3-18: The trigger Efficiency with NACC<8 as function of reconstructed rigidity for Silicon data after February 2016 (black star) and MC (red star) in L1Inner (top) and FullSpan (bottom) geometries. The bottom panel shows the ratio between the efficiencies obtained from data and MC samples.

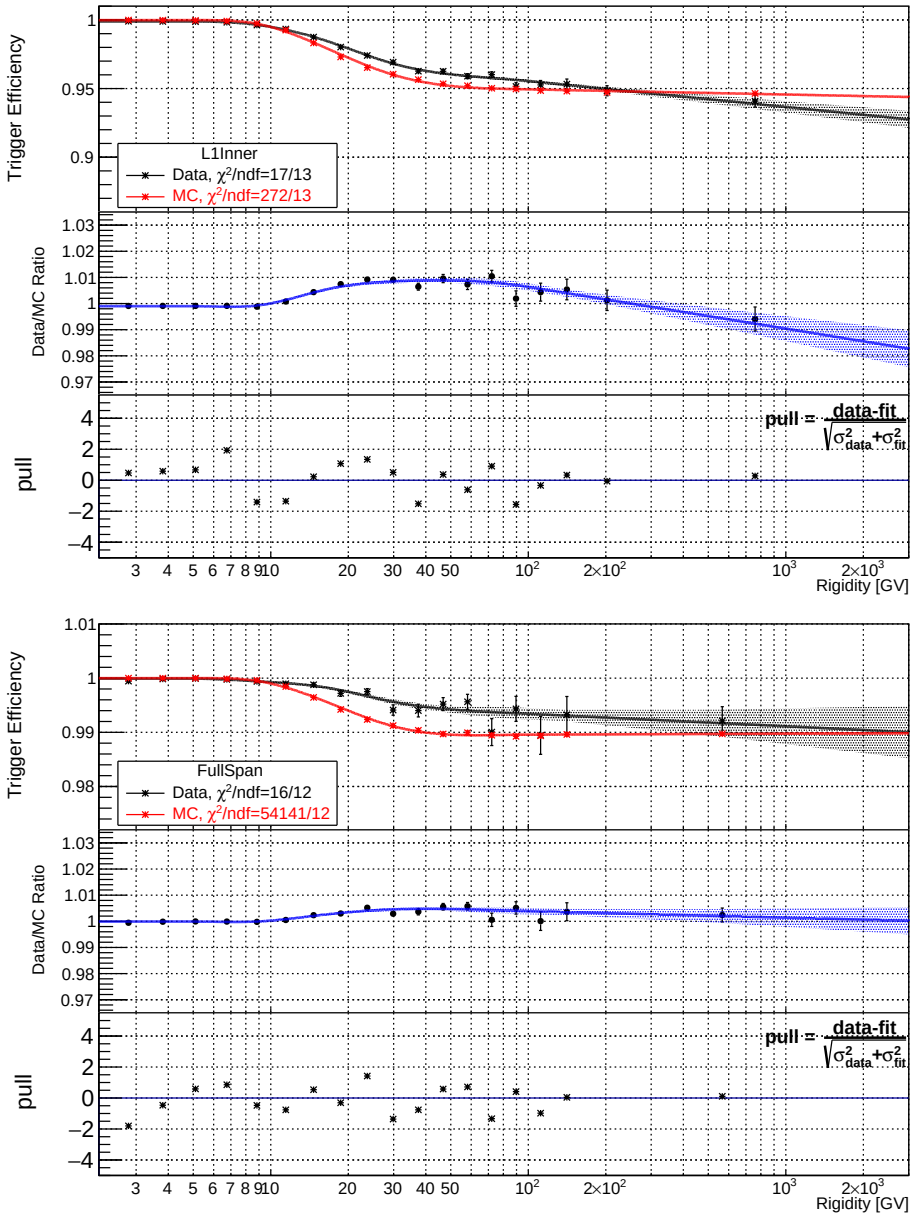

Figure 3-19: The trigger efficiency (estimated using Eq. (3.17)) as function of reconstructed rigidity for Silicon data (black star) and MC (red star) in L1Inner (top) and FullSpan (bottom) geometries in the top panel. The black (red) curve and band is the spline fit to the efficiency and 68% CL intervals for data (MC). The middle panel shows the ratio of efficiencies for data over MC (black full circle). The blue line and band are the ratio of the spline fit to data over MC and the ratio of 68% CL intervals, respectively. The bottom panel shows the pull between the ratio of efficiencies and the ratio between spline fits.

FullSpan geometries as function of reconstructed rigidity.

3.3.3.2 Tracker L1 big charge efficiency

L1 BZ efficiency is the efficiency that a well reconstructed unbiased XY-combined hits with good charge would be found on Tracker L1 when all the other sub-detectors give well reconstructed event (passing all reconstruction cuts) with compatible charge. The L1 XY-combined hit with the largest charge among all the Tracker L1 hits is chosen. The hit is "unbiased" in the sense that it's not attached to Inner Tracker track.

Sample

The sample is selected by pre-selection, reconstruction and charge selections on the upper TOF, the Inner Tracker (as well as the lower TOF and the Tracker L9 for FullSpan only), together with requiring the inner tracker track extrapolation to be within the Tracker L1 fiducial volume.

Selection

The numerator is selected from the sample defined above with the following additional requirements:

1. a well reconstructed unbiased L1 XY hit;
2. the charge of the unbiased L1 hits is compatible with that of a Silicon nucleus or a heavier one: $Q_{L1,unbiased} > 12.4332$. Because the charge cuts is applied as a lower limits hence the selected events from data samples might contain below Tracker L1 contamination from interaction below Tracker L1 (Section 3.2.2.1). These background events should have similar Tracker L1 BZ efficiency as those non-fragmented events, hence no cuts on the upper limit are required.

Tracker L1 Big Z efficiencies in L1Inner and FullSpan geometries for Silicon nuclei are shown in Fig. 3-20. The inefficiency is mostly due to incoming cosmic ray nuclei passing through the inactive regions of Tracker L1, and the efficiencies in both geometries for data and MC are similarly around 80% with no strong rigidity-dependence as the studied cuts are mainly detector geometrical requirements.

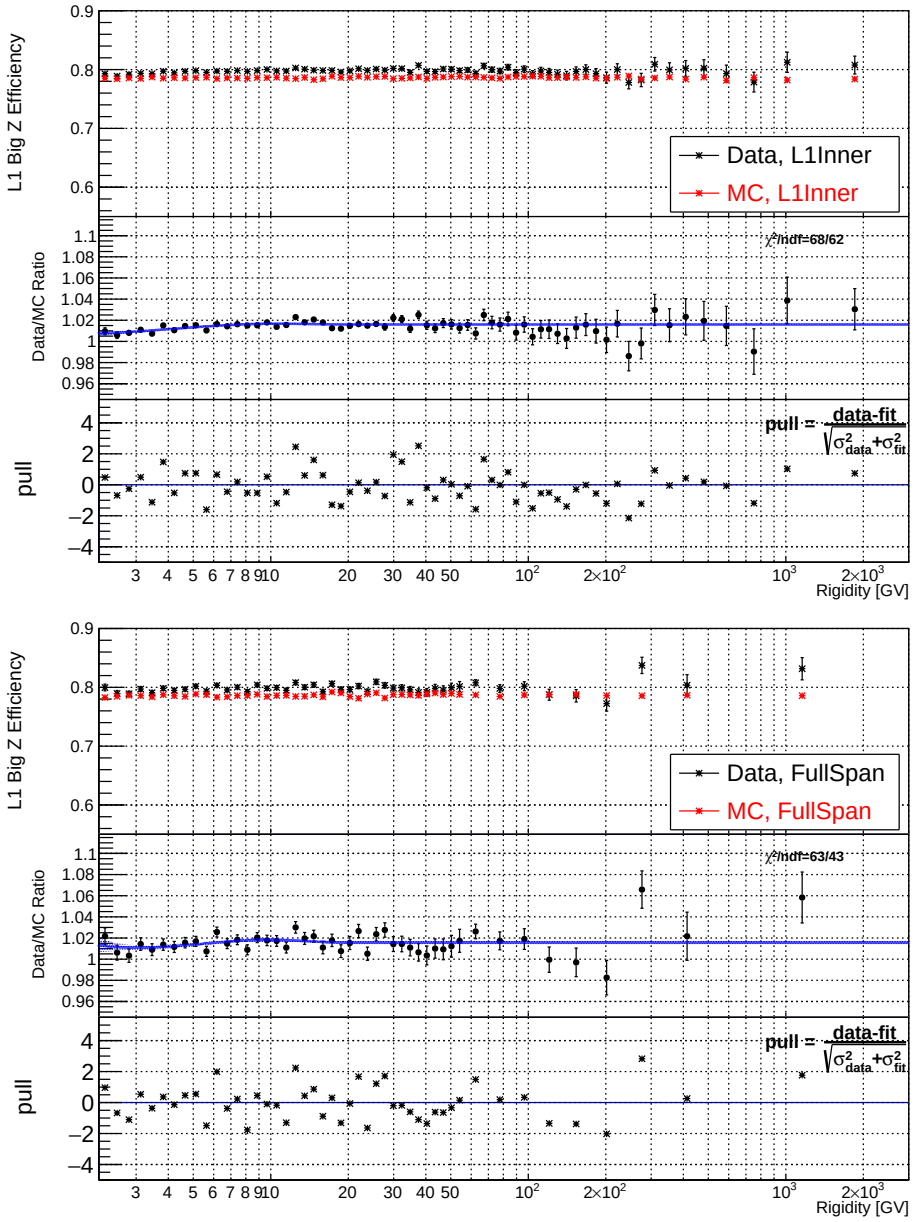

Figure 3-20: Tracker L1 Big Z efficiency as function of reconstructed rigidity for Silicon data (black star) and MC (red star) in L1Inner (top) and FullSpan (bottom) geometries. The middle panel shows the data over MC efficiency ratio (black full circle). The blue line and band are the spline fit to the ratio and the corresponding 68% CL intervals, respectively. The bottom panel shows the pull between the efficiency ratio and the spline fit to the ratio.

3.3.3.3 Tracker L1 pick up efficiency

The efficiency that a L1 hit is attached to the Inner tracker track and is well reconstructed with compatible charge, is called the Tracker L1 pick up efficiency.

Sample

The sample is the same as the selected numerator of L1 BZ efficiency in addition with a tighter cut on the unbiased L1 charge, $Q_{L1,unbiased} < 14.5$. By adding the upper limit on the L1 charge, the contamination from interactions occurring below the Tracker L1 is removed.

Selected

The numerator is selected by:

1. a well reconstructed L1 XY-combined hit attached to the Inner tracker track;
2. a good L1Inner Y-side track fit by cutting on the normalized χ^2 to be less than 10, i.e. $\chi^2_{Y,L1Inner}/d.f. < 10$;
3. L1 hits with good charge measurement: $Q_{L1} > 12.4332$ and good charge status.

Fig. 3-21 shows the Tracker L1 pick up efficiency for Silicon nuclei. For particle with low rigidity, multi-scattering might change the particle direction rapidly when particle traversing the TRD and the upper TOF. Hence the Tracker L1 hit is not found around the Inner Tracker Track linear extrapolation to Tracker L1, causing inefficiency on picking up the Tracker L1 hit, as seen in Fig. 3-21 as efficiencies which increase with increasing rigidity. Larger data MC difference at low rigidities is mainly due to the difference description of the particle multi-scattering in the AMS-02 detector between data and simulation. The drop of efficiencies above 200 GV for both data and MC in L1Inner geometry is due to bin-to-bin migration as only Inner rigidity can be used, whose MDR is around 600 GV.

3.3.3.4 Inner tracking efficiency

Inner tracking efficiency is the probability that an Inner Tracker track is reconstructed when an incoming nucleus traverses the Inner Tracker without fragmenting.

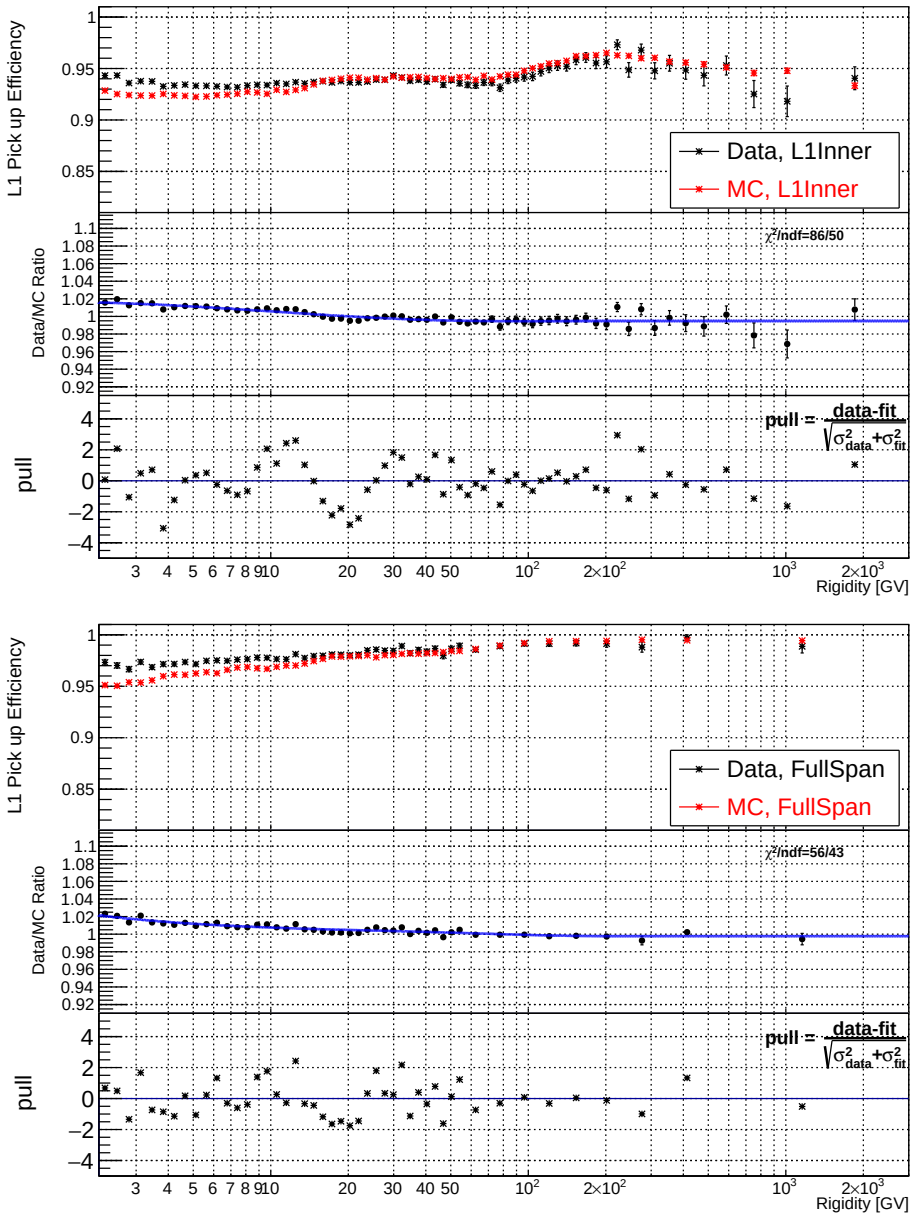

Figure 3-21: Tracker L1 pick up efficiency as function of reconstructed rigidity for Silicon data (black star) and MC (red star) in L1Inner (top) and FullSpan (bottom) geometries. The middle panel shows the data over MC efficiency ratio (black full circle). The blue line and band are the spline fit to the ratio and the corresponding 68% CL intervals, respectively. The bottom panel shows the pull between the efficiency ratio and the spline fit to the ratio.

To study Inner Tracking efficiency, a sample for which no Tracker Track and TOF Track built using the Inner Tracker track information are used, needs to be defined. Hence unbiased TOF track, TOF clusters connected using the TRD track if it exists or the TOF hits standalone, is reconstructed and all external Tracker Layer hits are connected using the unbiased TOF track. An unbiased sample with no requirement on the Inner Tracker reconstructed object is defined using such unbiased TOF Tracks.

In addition, the rigidity of incoming particles needs to be estimated independently from the Silicon tracker. There will be two estimators covering different rigidity regions: 1) the velocity of incoming particle i.e. the β measured by TOF, and 2) the maximum geomagnetic cutoff at the given geomagnetic location.

Rigidity Estimation

The estimation of the particle's rigidity, R, by the β measured by the TOF is given by

$$R_\beta = \frac{Am_p\beta}{Z\sqrt{1-\beta^2}} \tag{3.18}$$

where A and Z are the mass number and the charge of the particle respectively, and m_P the mass of proton. For the Silicon nuclei, the mass number of the most abundant isotope ^{28}Si is taken (see discussion in Section 3.8). The Beta estimator is used for rigidity up to 5.9 GV, above which the corresponding β will be close to 1 given no separation.

The Rigidity estimation from the maximum geomagnetic cutoff is obtained in a data-driven way. The distribution of the Tracker rigidity vs the maximum geomagnetic cutoff for the Silicon nuclei events (Fig. 3-22) is used to build a rigidity estimator from the maximum geomagnetic cutoff. The Silicon nuclei flux is roughly a decreasing power law in rigidity, hence events falling in each cutoff bin are most likely to have rigidity close to the lower edge of the spectrum. In each bin of the maximum geomagnetic cutoff, the Most Probable value (MPV) of the rigidity is then used as the estimated rigidity value. Then a linear fit of the estimated rigidity in each cutoff bin is performed to smooth out the statistical fluctuation and the fit result is used to retrieve the estimated rigidity for a given maximum geomagnetic cutoff value. The cutoff estimator is used up from 5.9 GV up to 19.5 GV.

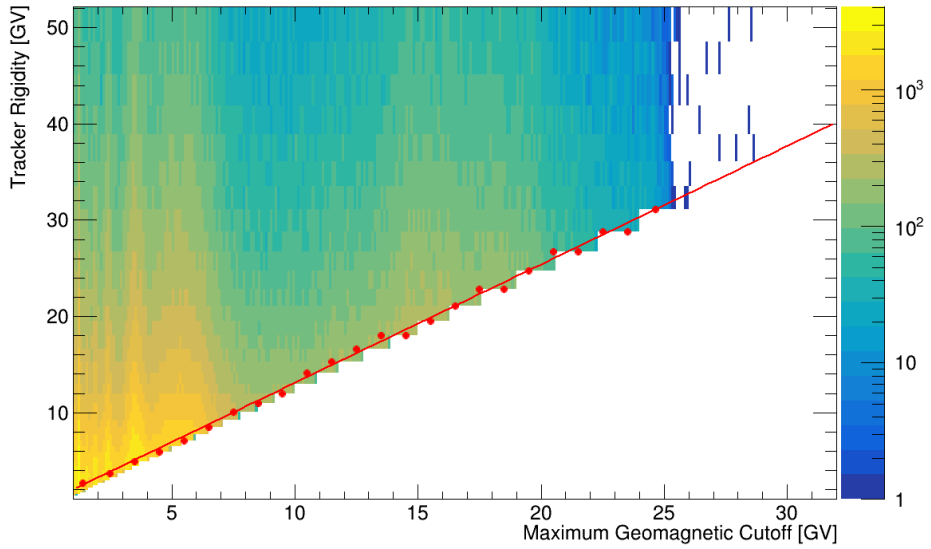

Figure 3-22: Tracker rigidity vs maximum geomagnetic cutoff for Silicon nuclei events selected in L1Inner geometry. Red points are the Most Probable value (MPV) in each cutoff bin and the red solid line is the linear fit to the MPVs used to retrieve the estimated rigidity for a given cutoff value.

As the Inner Tracking efficiency is expected to be flat at high rigidity, as verified on Monte Carlo simulated events (see Fig. 3-23), the Data to MC efficiency ratio is then treated as a constant and the potential deviation from a constant will be accounted as a source of systematic uncertainty as discussed in Section 3.6.1.1.

Sample

The sample to study the Inner Tracking efficiency is selected by:

1. Physical Trigger, Bad run removal and Good Data Acquisition;
2. has reconstructed unbiased TOF Track with β >0.4;
3. Interpolation of the unbiased TOF Track is required to be within the Silicon Tracker fiducial volume, ensuring that the incoming particle has passed through the Inner Tracker;
4. Unbiased XY-combined hits on the external Tracker Layers (Tracker L1 for L1Inner and for FullSpan geometry Tracker L9 is also required);
5. Unbiased charge measurement from external Tracker layers and the 4 TOF layers are required to be compatible with Silicon nuclei events. Charge selection on both upper

and lower TOF ensure that the incoming nuclei didn't fragment after traversing the Inner Tracker.

Selection

The studied selection cuts include all the cuts related to the Inner Tracker track (Inner Tracker hit pattern, track fit quality and charge cut) and the TOF track built using the Inner Tracker track (TOF track quality and the selection on β measured by TOF).

Inner Tracking efficiency for Silicon nuclei in L1Inner and FullSpan geometries are shown in Fig. 3-23. Multi-scattering in the Inner Tracker layers for low rigidity particles introduces the drop of the Inner Tracking efficiency at low rigidity, which increases and becomes flat at high rigidity. Larger difference between data and MC at low rigidity is due to the different description of the multi-scattering.

3.3.3.5 TOF charge efficiency

The TOF charge efficiency measures how many events are kept after requiring that TOFs (UTof only for L1Inner, UTof and LTof for Full Span) provide compatible charge measurement with measurements from other sub-detectors (External Tracker Layers and Inner Tracker). The sample to evaluate the TOF charge efficiency is selected by all selection cuts except the TOF Charge selection cuts. The numerator is then selected from the sample by upper TOF Charge selection and addition lower TOF Charge selection for Full Span pattern only.

The TOF charge efficiency for Silicon nuclei in L1Inner and FullSpan geometries is shown in Fig. 3-24. A slightly decreasing efficiency at higher rigidity can be seen in Fig. 3-24, which is due to the worse TOF charge resolution with increasing rigidity.

3.3.3.6 Tracker L9 Efficiency

The Tracker L9 efficiency is the probability that an well reconstructed Silicon nuclei, which has not fragmented from the Tracker L1 up to L8, does not fragment when traversing the material between Tracker L8 to L9, and that its hit is well reconstructed by the Tracker L9 and attached to the Inner Tracker track. Hence, this efficiency contains the L8→L9 survival probability together with the L9 reconstruction and selection cuts efficiency.

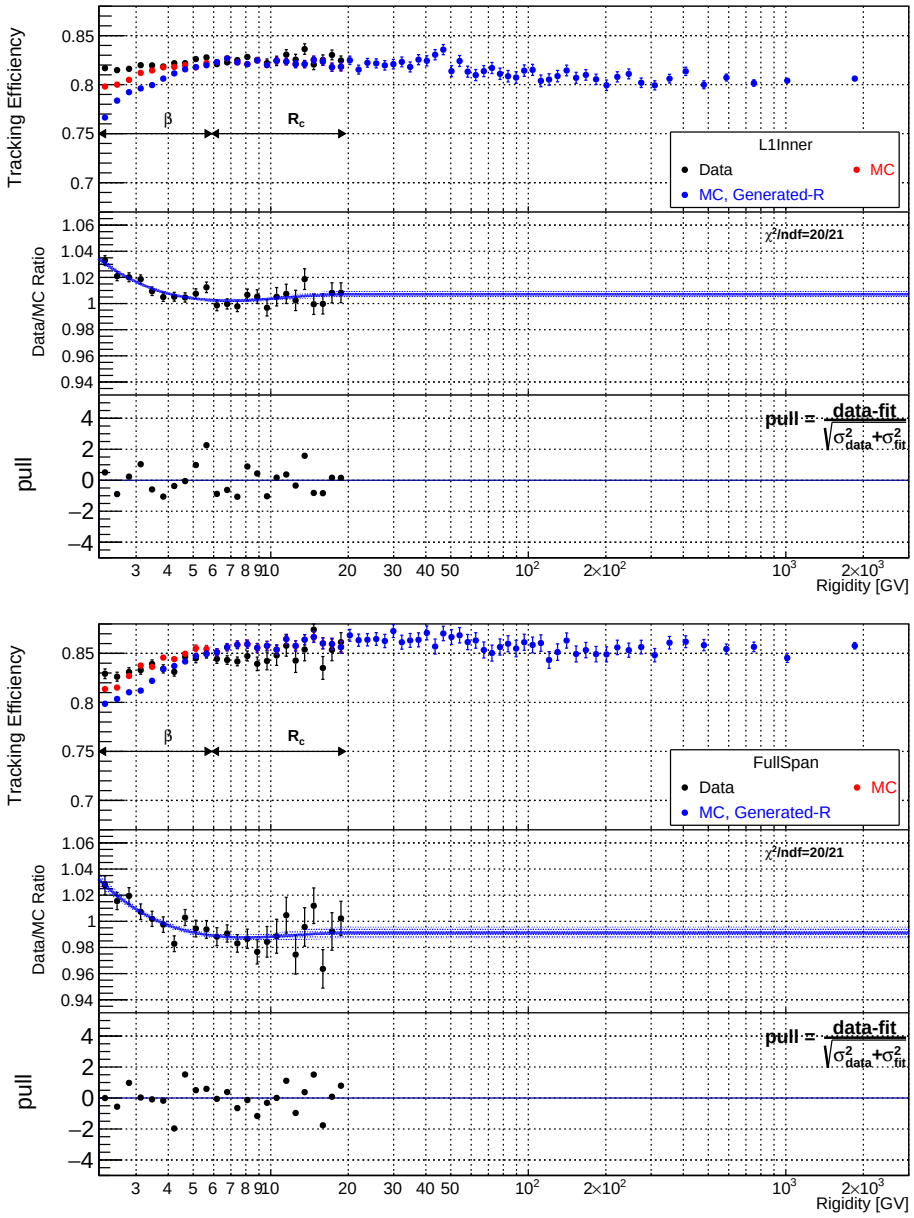

Figure 3-23: The Inner tracking efficiency for Silicon nuclei events as function of estimated rigidity (the ranges using estimation from TOF β and geomagnetic cutoff R_c are indicated by arrows) from data (black star) and MC (red star) in L1Inner (left) and FullSpan (right) geometries. The efficiency from MC as function of generated rigidity (blue star) is also shown. The middle panel shows the data over MC efficiency ratio (black full circle) together with the spline fit to the ratio (blue curve) and the corresponding 68% CL intervals (blue band). The bottom panel shows the pull between the efficiency ratio and the spline fit to the ratio.

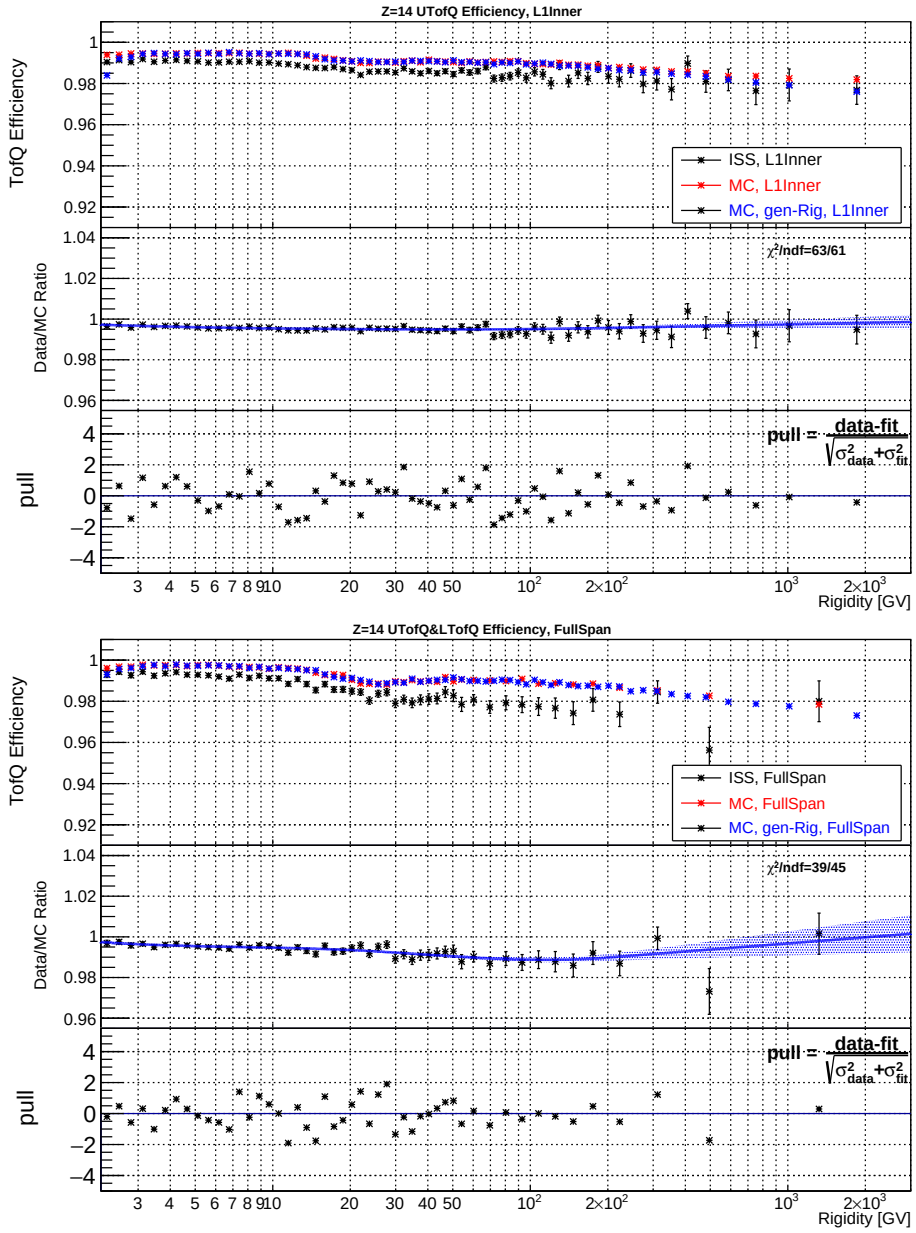

Figure 3-24: The TOF charge efficiency as function of reconstructed rigidity for Silicon data (black star) and MC (red star) in L1Inner (left) and FullSpan (right) geometries. The middle panel shows the data over MC efficiency ratio (black full circle). The blue line and band are the spline fit to the ratio and the corresponding 68% CL intervals, respectively. The bottom panel shows the pull between the efficiency ratio and the spline fit to the ratio.

Sample

The sample is selected by L1Inner event selection together with the requirement that the extrapolation of the L1Inner Track is within the Tracker L9 fiducial volume. Charge selections on Lower TOF are not applied in order to includes the full L8→L9 survival probability inside this efficiency. The data to MC efficiency ratio will then correct the small data MC difference on the survival probability between Tracker L8 and L9 due to different interaction between data and MC simulation.

Selection

The numerator is selected from the sample by applying all the Tracker L9 related cuts:

1. a Tracker L9 XY-combined hit is attached to the L1Inner Tracker track;
2. the InnerL9 Tracker track has good fitting quality, i.e. $\chi^2_{InnerL9}/d.f. < 10$;
3. Charge measured by Tracker L9 is compatible with other sub-detector, i.e. within [13.24,15.57] for Silicon nuclei.

Fig. 3-25 shows the Tracker L9 efficiency for Silicon in FullSpan geometry. The large bias between data and MC is dominated by the difference on the Tracker L8→L9 survival probability, which is discussed in Section 3.5.2.

3.3.3.7 Total data/MC correction

With all the efficiencies and the data/MC efficiency ratios, the total correction to the efficiency acceptance is obtained as the product of all individual efficiency ratios, which is shown in Fig. 3-26 for L1Inner and FullSpan geometries respectively. The total correction corrects for small differences on the detector responses and the Tracker L8→L9 survival probability between Data and MC simulation. Data MC difference on the remaining survival probability, namely above Tracker L1 up to L8, will is discussed at Section 3.5.

3.3.4 Raw Flux

The Silicon nuclei raw flux using Eq. (3.1) multiplied by $R^{2.7}$ before the bin-to-bin migration correction, which is discussed in Section 3.4, is shown in Fig. 3-27.

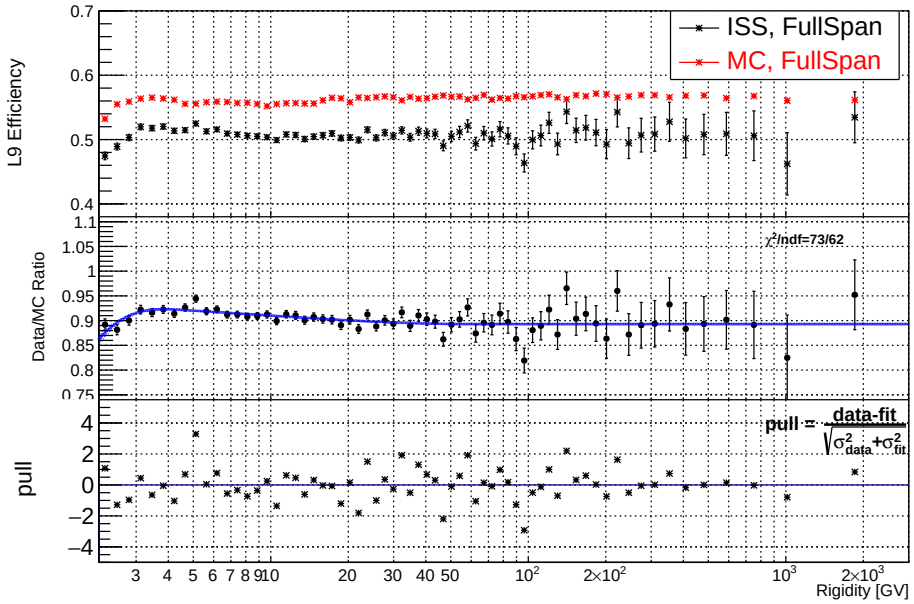

Figure 3-25: Tracker L9 efficiency as function of reconstructed rigidity for Silicon data (black star) and MC (red star) in FullSpan geometries. The middle panel shows the data over MC efficiency ratio (black full circle) while the blue line and band is the spline fit to the ratio and corresponding 68% CL intervals, respectively. The bottom panel shows the pull between the efficiency ratio and the spline fit.

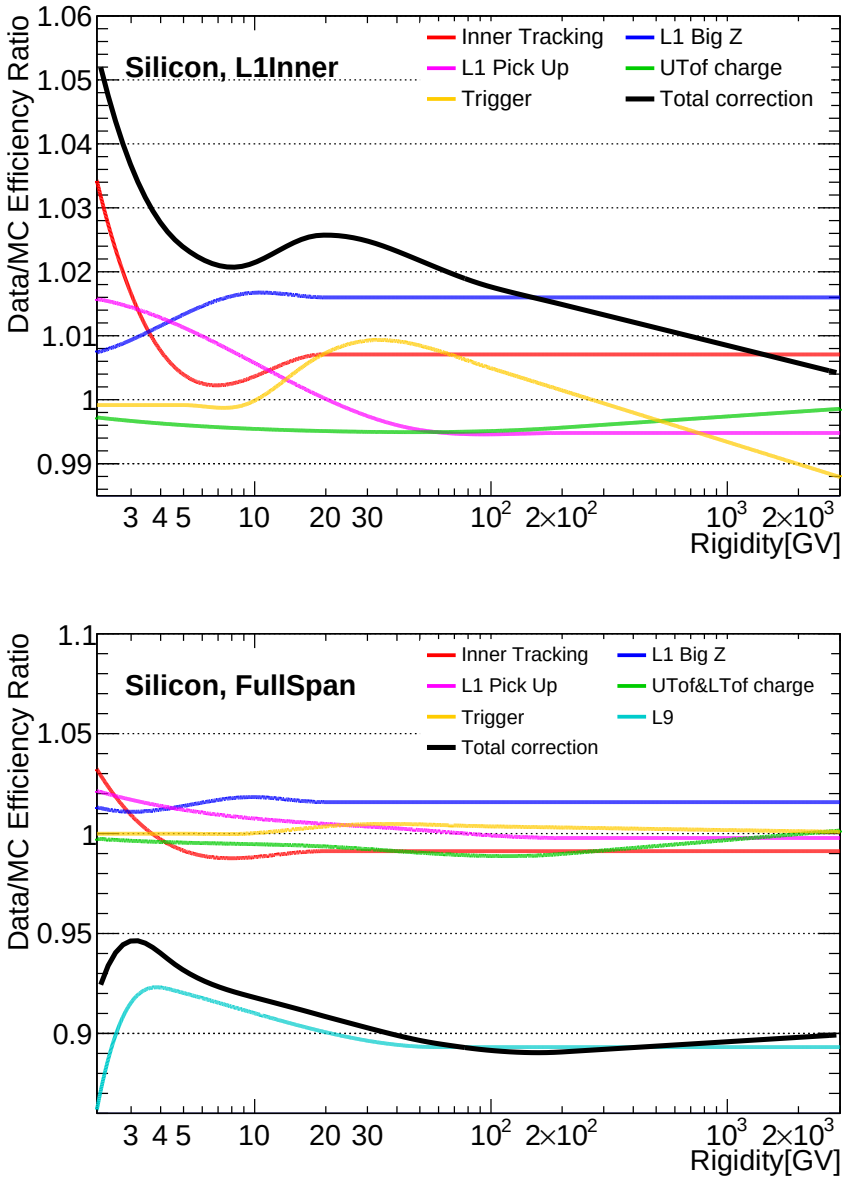

Figure 3-26: The Silicon nuclei data/MC efficiency ratio parameterizations together with the total correction (black curve) obtained from the product of the spline fits for all efficiency ratios as function of reconstructed rigidity in L1Inner (top) and FullSpan (left) geometries.

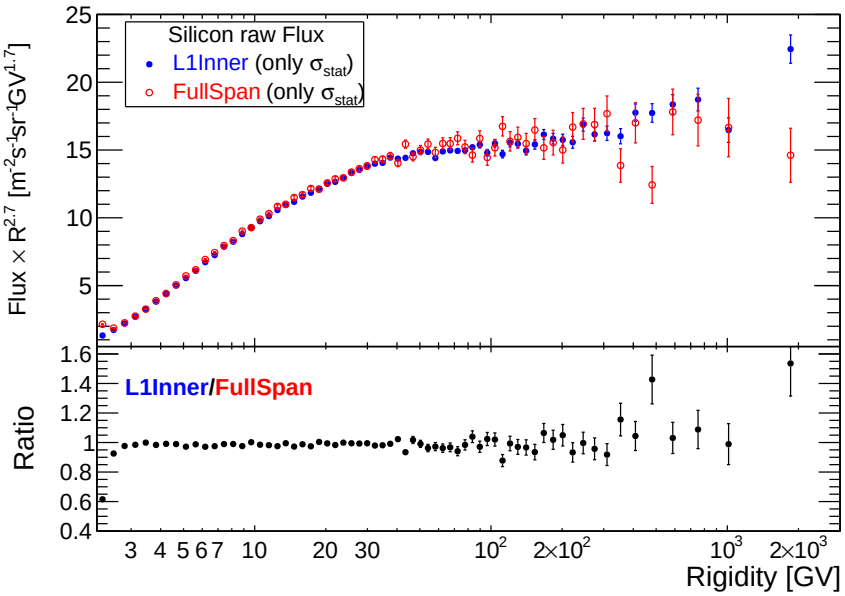

Figure 3-27: The 7 years Silicon nuclei raw flux multiplied by $R^{2.7}$ (without bin-to-bin migration correction for event counts) as a function of the reconstructed rigidity in the L1Inner (blue full circle) and the FullSpan (red empty circle) geometries.

3.4 Unfolding

The event counts as function of reconstructed rigidity might be filled into wrong bins due to finite rigidity resolution.

The AMS-02 Monte Carlo has been tuned to well reproduce the rigidity resolution from test beam results (Section 2.5). The Silicon nuclei rigidity resolution is then estimated from MC simulation and parameterized to build up a 2-dimensional resolution function. The forward unfolding method is then applied to obtain the bin-to-bin migration correction, the so-called unfolding factor, for Silicon nuclei.

3.4.1 Tracker Rigidity Resolution

The Silicon nuclei rigidity resolution is estimated from the distribution of $\Delta(1/R) = 1/R_{rec} - 1/R_{gen}$, the difference between the inverse reconstructed rigidity, $1/R_{rec}$, and the inverse generated rigidity, $1/R_{gen}$, in several generated rigidity bins for MC simulated events passing the events selection cuts.

The $\Delta(1/R)$ distributions in each rigidity bin are parameterized by two Gaussian and one Exponential Modified Gaussian (EMG) distributions with common mean, having a total of eight parameters:

- Normalization factor;
- μ: mean of the three distributions;
- σ: sigma of the 1^{st} Gaussian;
- f_1: fraction of the 1^{st} Gaussian to the overall normalization;
- σ_2/σ, with σ_2 the sigma of the 2^{nd} Gaussian;
- f_2: fraction of the 2^{nd} Gaussian to the overall normalization;
- σ_3/σ, with σ_3 the sigma of the EMG;
- τ/σ_3, with τ the exponential factor of the EMG;

The Rigidity Resolution distributions and corresponding parameterizations for Silicon nuclei in L1Inner geometry for some of the generated rigidity bins are shown in Fig. 3-28.

All parameters except the normalization factor are then parameterized as function of the generated rigidity to build up a 2-dimensional rigidity resolution function

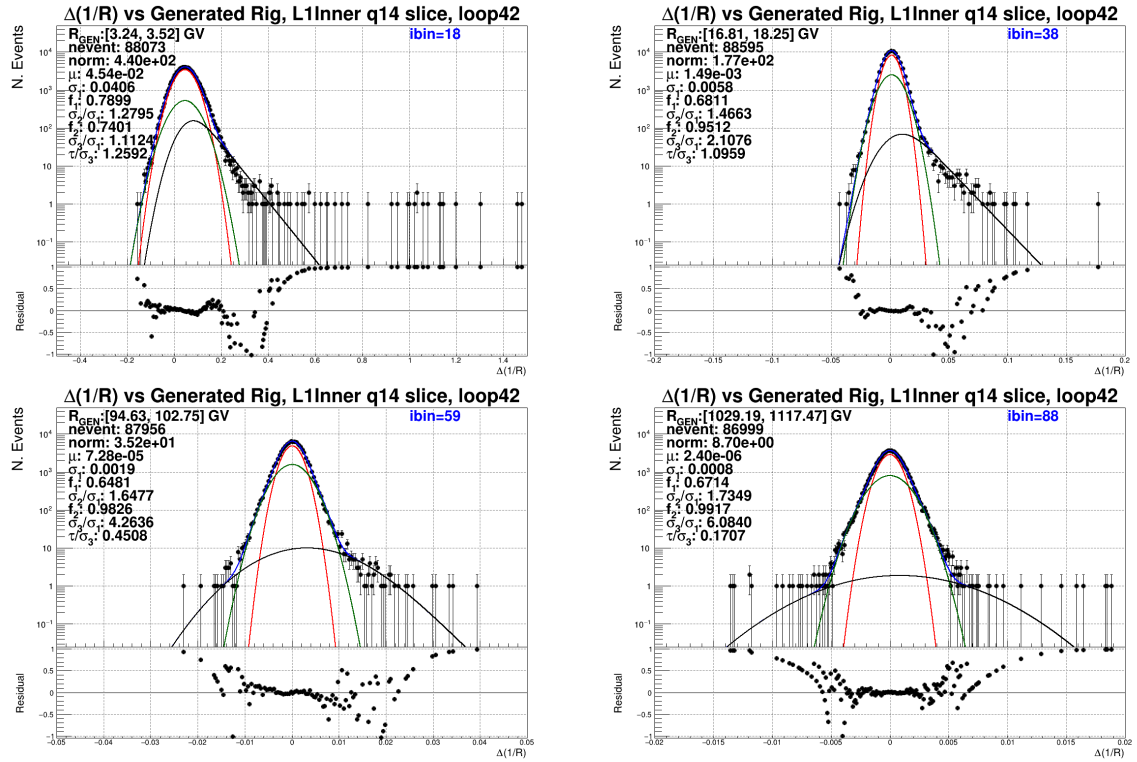

Figure 3-28: The rigidity resolution for Silicon nuclei in L1Inner geometry (black full circle) together with the parameterization (blue curve) in four different generated rigidity bins: $[3.29, 3.58]$ GV, $[16.81, 18.25]$GV, $[94.63, 102.75]$ GV, $[1029.19, 1117.47]$ GV. The components of the parameterization are shown as the red (the 1^{st} Gaussian), green (the 2^{nd} Gaussian) and the black (the EMG) curves. The bottom panels in each plot show the residual between rigidity resolutions and parameterization.

$Res(R_{gen}, \frac{1}{R_{rec}} - \frac{1}{R_{rec}})$, which will be used to describe the rigidity migration effects in Forward Unfolding, as explained in the next section.

Fig. 3-29 shows one example of these parameters: the σ of the Gaussian core as function of the generated rigidity and the parameterization for both L1Inner and FullSpan geometries. The Maximum Detectable Rigidity (MDR), defined as the rigidity value for which the relative error of the reconstructed rigidity is 100%, is obtained as $\sigma(1/R) = 1/R$. For Silicon nuclei, the MDR is found to be 1.3 TV for L1Inner geometry and 2.8 TV for FullSpan geometry respectively.

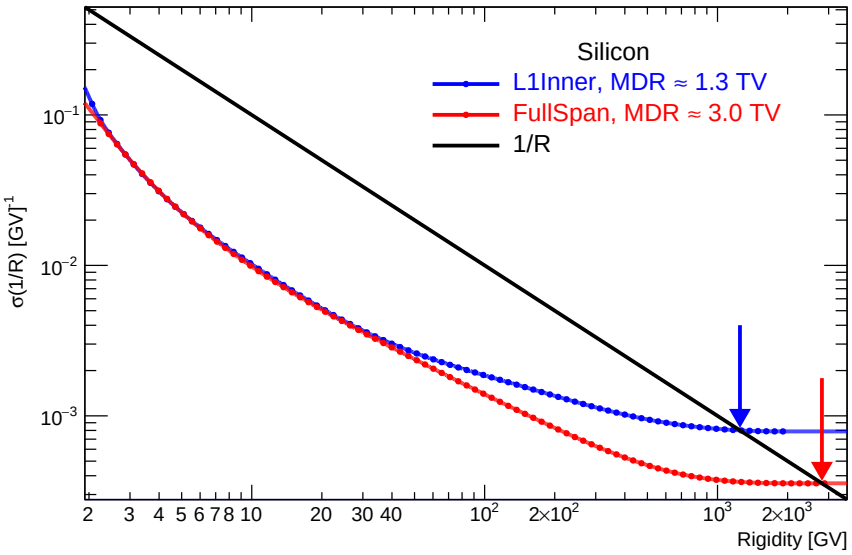

Figure 3-29: The σ of the Gaussian core of the Silicon nuclei rigidity resolution as function of generated rigidity, shown in full circle, and its parameterization, shown as solid curve, for L1Inner (blue) and FullSpan (red) geometries respectively. The black line is the 1/R function. The MDR is determined by the value of the crossing between the parameterization and the 1/R function, indicating by the arrows.

3.4.2 Forward Unfolding Method (FUM)

The principle of Forward Unfolding [114] is find the true flux (as function of the true rigidity, R_{gen} by iteratively comparing the folded event rate (in reconstructed rigidity R_{rec}) measured from data, $f_i^{data}(R_{rec})$ (Eq. (3.2)), to the one calculated from a flux model, acceptance and rigidity resolution function, $f_i^{cal}(R_{rec})$. At each iteration the flux model is readjusted until convergence.

The folded event rate can be calculated by the formula below:

$$f_{i,rec}^{cal} = \frac{1}{\Delta R_{rec}} \int_{\frac{1}{R_i}}^{\frac{1}{R_i}+\Delta\frac{1}{R_i}} d\frac{1}{R_{rec}} \int_0^{\infty} d\frac{1}{R_{gen}} \Phi(\frac{1}{R_{gen}}) A_{eff}(\frac{1}{R_{gen}}) Res(R_{gen}, \frac{1}{R_{rec}} - \frac{1}{R_{gen}}) \tag{3.19}$$

where $\Phi(\frac{i}{R_{gen}})$ is the flux model as function of $1/R_{gen}$ (spline function, contains free parameters), $A_{eff}(\frac{1}{R_{gen}})$ is the effective acceptance as function of $1/R_{gen}$ and $Res(R_{gen}, \frac{1}{R_{rec}} - \frac{1}{R_{gen}})$ is the parametrized Rigidity resolution function obtain in Section 3.4.1.

By minimizing the χ^2 between $f_i^{data}(R_{rec})$ and $f_i^{cal}(R_{rec})$ with different flux model parameterizations, the flux model which best describes the true incoming flux can be obtained. The χ^2 is defined as:

$$\chi^2 = \sum_i \left(\frac{f_i^{data}(R_{rec}) - f_i^{cal}(R_{rec})}{\sigma_i} \right)^2, \tag{3.20}$$

where σ_i is the statistical error of the folded event rate $f_i^{data}(R_{rec})$. Considering that the two geometries, L1Inner and FullSpan, are measuring the same incoming Silicon nuclei flux, one common flux model should be able to minimize the rates measured in the two geometries at the same time. So, in practice, the combined χ^2 for L1Inner and FullSpan geometries, defined as:

$$\chi^2_{comb} = \sum_i \left(\frac{f_{i,L1I}^{data}(R_{rec}) - f_{i,L1I}^{cal}(R_{rec})}{\sigma_i^{L1I}} \right)^2 + \sum_i \left(\frac{f_{i,FS}^{data}(R_{rec}) - f_{i,FS}^{cal}(R_{rec})}{\sigma_i^{FS}} \right)^2, \tag{3.21}$$

is minimized. Because of the different MDRs, the fluxes obtained from two geometries are used in different rigidity ranges: the L1Inner flux is used up to 1.3 TV and above only the FullSpan result is used. So, the sum of the χ^2 runs on different rigidity ranges for the two geometries.

Once the true flux is obtained, as the flux model which minimizes the combined χ^2 (Eq. (3.21)), the unfolding factor C_{uf}, defined as the ratio between folded and unfolded event rates, is calculated from the true flux model, the effective acceptance and the rigidity

resolution function as:

$$C_{uf} = \frac{f^{cal}_{i,rec}}{f^{cal}_{i,gen}} = \frac{\int_{\frac{1}{R_i}}^{\frac{1}{R_i}+\Delta\frac{1}{R_i}} d\frac{1}{R_{rec}} \int_0^\infty d\frac{1}{R_{gen}} \Phi(\frac{1}{R_{gen}}) A_{eff}(\frac{1}{R_{gen}}) Res(R_{gen}, \frac{1}{R_{rec}} - \frac{1}{R_{gen}})}{\int_{\frac{1}{R_i}}^{\frac{1}{R_i}+\Delta\frac{1}{R_i}} d\frac{1}{R_{gen}} \Phi(\frac{1}{R_{gen}}) A_{eff}(\frac{1}{R_{gen}})} \quad (3.22)$$

The unfolding factors for Silicon nuclei in the two geometries from the obtained common true flux model are shown in Fig. 3-30. Below 3 GV, the raw event count (Fig. 3-2) and the effective acceptance (Fig. 3-15) for FullSpan geometry is very low, which cannot provide valid estimation of the bin-to-bin migration and gives a very high unfolding factor. At low rigidity up to 20 GV, the particle's multi-scattering inside the AMS-02 introduces large energy loss, corresponding to 10-20% correction for the bin-to-bin migration. Due to the better rigidity resolution at high rigidity, as seen from Fig. 3-29, the unfolding factor for FullSpan geometry is smaller than the one for L1Inner geometry.

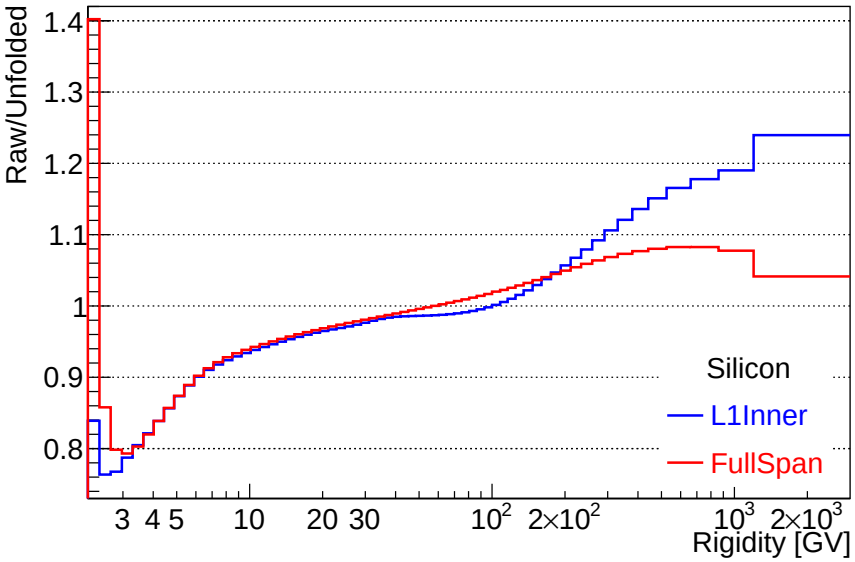

Figure 3-30: The Silicon nuclei unfolding factors for L1Inner (Blue) and FullSpan (Red) geometries as function of the reconstructed rigidity.

3.4.3 Unfolded Flux

The bin-to-bin migration is corrected applying the unfolding factor calculated by Eq. (3.22) to the raw event count. The unfolded Silicon nuclei flux multiplied by $R^{2.7}$ in both the

L1Inner and FullSpan geometries obtained from the corrected event counts is shown in Fig. 3-31.

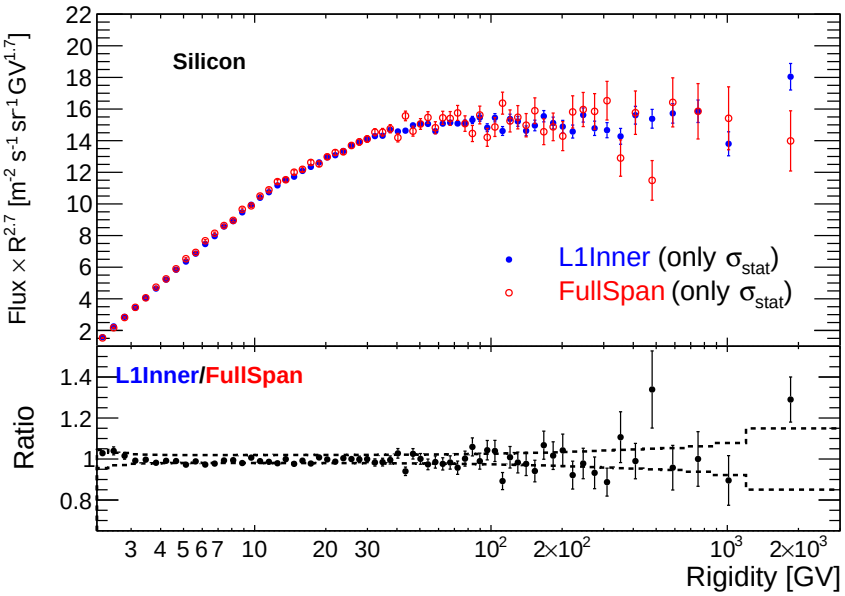

Figure 3-31: The Silicon nuclei flux after correction for the bin-to-bin migration and multiplied by $R^{2.7}$ as function of the true rigidity for the L1Inner (blue points) and FullSpan (red open circles) geometries. The bottom panel shows the ratio between the Silicon nuclei flux measured in the L1Inner and the FullSpan geometries. The error bars show the statistical error and the dashed black lines show the total flux error, which is the quadratic sum of the statistical error and the systematic uncertainties (see Section 3.6).

3.5 Survival Probability

The AMS collaboration has carried out an extensive study on the nuclei interaction cross section to optimize the simulation of the nuclei interaction with the AMS material.

The differences of the nuclei interaction between Data and MC, due to the material or/and inelastic cross section description, can be estimated by the MC-to-data ratio of survival probabilities ε_{Sur}, the portion of survived events passing through the AMS material, which can be expressed as [108]:

$$\varepsilon_{Sur} = e^{-n\sigma} \tag{3.23}$$

where n the total number of all species of target nuclei per area and σ the nuclear inelastic

cross section of Silicon nuclei projectiles averaged over all species of target nuclei presents in the AMS material.

The description of the nuclei interaction in the Monte Carol simulation has been tuned based on the comparison of Tracker L1→L2 and L8→L9 survival probabilities between data and simulation. The remaining small difference will be accounted as a correction to the total flux normalization. Such a correction will not change the flux shape so as the bin-to-bin migration, hence the correction is applied after unfolding. Error of the MC-to-data survival probability ratios (statistic error and systematic uncertainty from the estimation procedure) are accounted as systematic uncertainties of the flux, as discussed in detail in Section 3.6.1.2.

For light nuclei (Z<8), survival probabilities are estimated using samples collected when the ISS attitude was such that the AMS-02 was flying horizontally. In such configuration, cosmic ray nuclei particles can enter the AMS-02 detector from the Tracker L9 as well as from the Tracker L1 (as in normal flight configuration). For these runs, the survival probability in the upper part of the AMS-02 detector (from Tracker L1 to Tracker L2) can be studied using particles entering from the Tracker L9 outside the ECAL acceptance, while the survival probability in the lower part of the AMS-02 (from Tracker L8 to Tracker L9) can be studied using particles entering from the opposite direction.

However, for heavy nuclei (such as Silicon), the statistics collected during horizontal runs is too low (only ∼0.13% of the total exposure time). Hence to perform a similar study, new estimation methods using only downward going events (from Tracker L1 to Tracker L9) in nominal flight configuration have been developed [108]. The estimation of the L1→L2 and L8→L9 survival probabilities for and the corresponding flux correction for Silicon nuclei will be discussed in this section.

3.5.1 L1→L2 survival probability

3.5.1.1 L1→L2 survival probability estimation in nominal flight configuration

The L1→L2 survival probability depends on the simulation of inelastic cross sections and the description of the material in the upper part of the AMS-02 (mainly the TRD and the upper TOF). Events fragmented between the Tracker L1 and L2 produce secondary

particles into the Inner Tracker, raising the number of ACC signals. Before February 2016, those events were rejected by the trigger which required the number of ACC hits to be less than 5. To accurately evaluate the survival probability, only events collected after February 2016 are used, when the trigger setting was modified requiring the number of ACC hits to be less than 8. With such settings, most of the fragmented events pass the trigger selection and are stored, hence an unbiased sample is available.

To study the L1→L2 survival probability, Silicon nuclei events are selected by Tracker L1 and their charge distribution measured by the Inner Tracker is used to extract the number of events survived without fragmenting. The ratio between the sample selected by the Tracker L1 charge within [13.5,14.5], $N_{tot} \equiv N_{Z=14}^{L1}$, and the survived events selected from the sample requiring Inner Tracker Charge to be within [13.5,14.5], $N_{Z'=Z}^{Inner}$, can be expressed as:

$$\frac{N_{Z'=Z}^{Inner}}{N_{Z=14}^{L1}} = \varepsilon_{Z=14}^{L12Sur}\varepsilon_{Z=14}^{Inner,sel} \approx \varepsilon_{Z}^{L12Sur} \tag{3.24}$$

where $\varepsilon_{Z=14}^{L12Sur}$ is the L1→L2 survival probability for Silicon nuclei, $\varepsilon_{Z=14}^{Inner,sel}$ is the efficiency that Silicon nuclei events have measured Inner Tracker charge within [13.5,14.5]. Due to the charge resolution of Inner Tracker, events fragmented when traversing the material between Tracker L1 and L2 with charge $Z' < Z = 14$ will not fall in the Inner Tracker charge selection range [13.5,14.5], so $\varepsilon_{Z'<Z}^{Inner,sel} \approx 0$ can be assumed safely. While almost all the survived Silicon nuclei events will fall in the Silicon channel, i.e. $\varepsilon_{Z=14}^{Inner,sel} \approx 1$, the survival probability can be computed from the fraction of the survived events.

The detailed sample selection includes:

- Inner Tracker track selection, including Inner Tracker hit pattern and track fit quality, to have a well measured rigidity;
- Selection for unbiased Tracker L1 hit, whose charge is corrected by the Inner Tracker rigidity (the same as those hits used for the L1 Big Z efficiency): XY-combined hit within the fiducial volume with good charge status and the L1 charge should be within [13.5,14.5]. The L1 hit is not required to be attached to the Inner Tracker track, otherwise events fragmented between the Tracker L1 and L2 with large direction change would be rejected, introducing a bias on the sample.
- Information from Tracker L9 are not selected in order to maximize the statistic.

The Inner Tracker charge distribution of the selected sample for Data and MC in a selected rigidity bin is shown in Fig. 3-32.

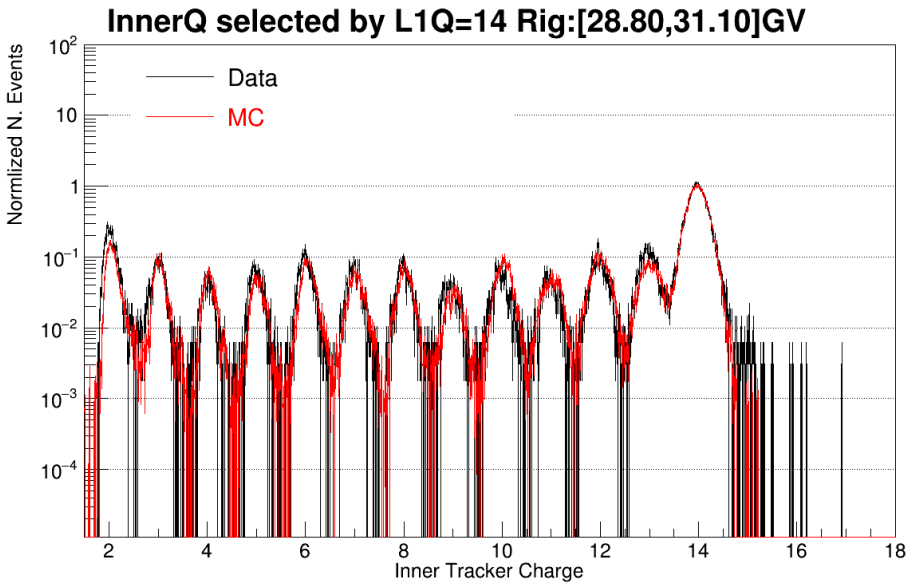

Figure 3-32: Inner Tracker Charge distribution after selecting Silicon events by selecting the Tracker L1 charge to be within the range [13.5,14.5].

Due to the limited charge resolution of a single Tracker layer, the sample selected by the Tracker L1 charge might also contain nearby elements, for example Aluminum (Z=13). This can be clearly seen from Fig. 3-32 where the Inner Tracker charge distributions for data and MC are in good agreement for all fragmented channels with $Z' < Z = 14$ except for Aluminum, because of the contamination from Aluminum nuclei events in the data sample. Indeed, the Monte Carlo sample contains only Silicon simulated events. To correctly account for the L1→L2 survival probability for data sample, the contamination in the data sample is estimated as discussed next.

Estimation of the contamination of the data sample for the L1→L2 survival probability

A charge template fit method, similar to the estimation of below L1 background, is used to estimate the contamination of the data sample selected by the Tracker L1 charge. The Tracker L1 charge distribution selected by all but L1 charge cut is fitted by the charge template obtained from the Tracker L2 charge distribution, exactly the same as the one

used for below L1 background estimation (Section 3.2.2.1). The contamination is obtained by integrating the charge templates in the L1 charge selection interval, namely [13.5,14.5] for Silicon nuclei.

Fig. 3-33 shows the template fit of the Tracker L1 charge distribution for the L1→L2 survival probability sample before applying L1 charge cut for a selected rigidity bin. Fig. 3-34 presents the contamination within the L1 charge selection range of Silicon as function of rigidity from Oxygen up to Sulfur. The contamination of the Silicon nuclei sample is dominated by Al, the neighbor nuclei, while the contamination from another neighbor, P (Z=15), is much less due to the lower relative abundance. The contamination from other nuclei is negligible due to larger difference in the charge or/and the lower relative abundance.

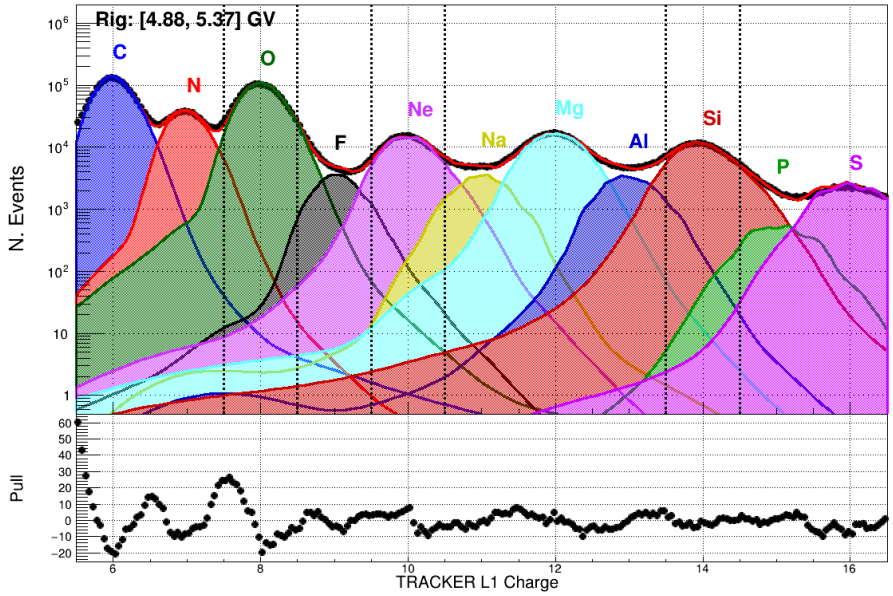

Figure 3-33: The charge template fit of the Tracker L1 charge distribution for the L1→L2 survival probability sample without any L1 charge cut for nuclei from Oxygen (Z=8) to Sulfur (Z=16).

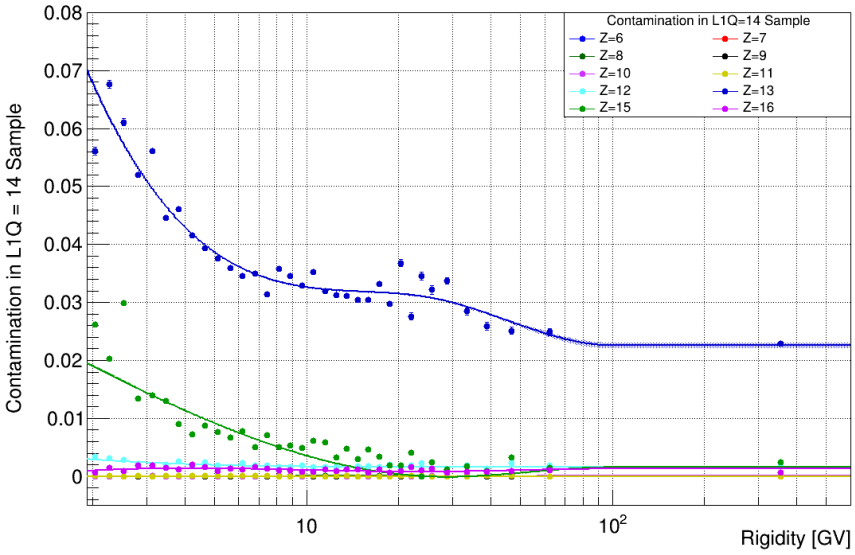

Figure 3-34: The portion of contamination in the L1→L2 survival probability sample selected by Tracker L1 charge within [13.5,14.5] as function of reconstructed rigidity from Oxygen (Z=8) up to Aluminum (Z=13), Phosphorus (Z=15) and Sulfur (Z=16).

Contamination subtraction for L1→L2 survival probability

With the presence of nearby charges in the data sample, the number of events within the Inner Tracker selection range [13.5,14.5] is expressed as:

$$\begin{aligned} N^{inner}_{Z'=Z} &= \varepsilon^{L12Sur}_{Z=14} N^{L1}_{Z=14} + \sum_{Z''>Z} P^{Z''}_{Z} N^{L1}_{Z''} \\ &= \varepsilon^{L12Sur}_{Z} f^{Z}_{Z} N_{tot} + \sum_{Z'>Z} P^{Z'}_{Z} f^{Z}_{Z'} N_{tot} \approx \varepsilon^{L12Sur}_{Z} f^{Z}_{Z} N_{tot}, \end{aligned} \tag{3.25}$$

where $P^{Z''}_{Z}$ is the probability that heavier nuclei with $Z'' > Z = 14$ measured by Tracker L1 charge fragment into Silicon after traversing Tracker L1 to L2; $N^{L1}_{Z''}$ is the number of events with charge Z'' within the sample; $f^{Z}_{Z(Z'')}$ is the fraction of events with charge $Z(Z'')$ in the sample selected by Tracker L1 charge; N_{tot} is the total number of events in the sample including contamination. In practice, the presence of the contamination will not change the number of events measured by the Inner tracker as survived $Z = 14$ since:

- for Z'<Z: events will not fall into Z channel (due to good resolution of Inner Tracker);
- for Z'>Z: the number of events with charge changing from Z'→Z is negligible since *the breaking-up probability* $P^{Z'>Z}_{Z}$ *is small* (<10%, as discussed Section 3.5.1.2) and

most importantly it's scaled by a *small contamination fraction* $f^{Z}_{Z'>Z}$ (few percent as show in Fig. 3-34).

Hence the contamination-corrected L1→L2 survival probability is expressed as:

$$\varepsilon_Z^{L12Sur} = \frac{N_Z^{inner}}{f_Z^Z N_{tot}}.$$

Fig. 3-35 shows the estimated L1→L2 survival probability for data (without and with the sample background correction) and MC. Fig. 3-36 is MC-to-data ratio of the L1→L2 survival probability together with a constant fit. The large difference of the estimated L1→L2 survival probability between data and MC at rigidity below 10 GV (more than 10%) is due to:

- The model used at low rigidity for inelastic cross section simulation have limited performance especially for heavy nuclei, hence a bias on the data and MC for survival probability at low rigidity is expected;
- The rigidity measured by Inner Tracker is the one after fragmentation, hence a rigidity change of both the direction and value is expected. The bias on the inelastic cross section between Data and MC will introduce a different behavior on the change of the rigidity, i.e. different rigidity migration, which enhances the difference of the estimated L1→L2 survival probability.

3.5.1.2 Study of the partial cross section

Events with charge measured by Inner Tracker less than the lower edge of the selection range, $Z' < Z$, estimate the number of fragmented Silicon nuclei (Z=14) due to interaction between Tracker L1 and L2, mainly in the TRD and upper ToF. The breaking-up probability of Silicon nuclei on the AMS material and hence its partial cross section, can be estimated from the portion of fragmented events.

As the contamination of the selected L1 charge sample from nearby charges is not negligible, the number of events in Z'(<Z) channel selected by Inner Track charge in the

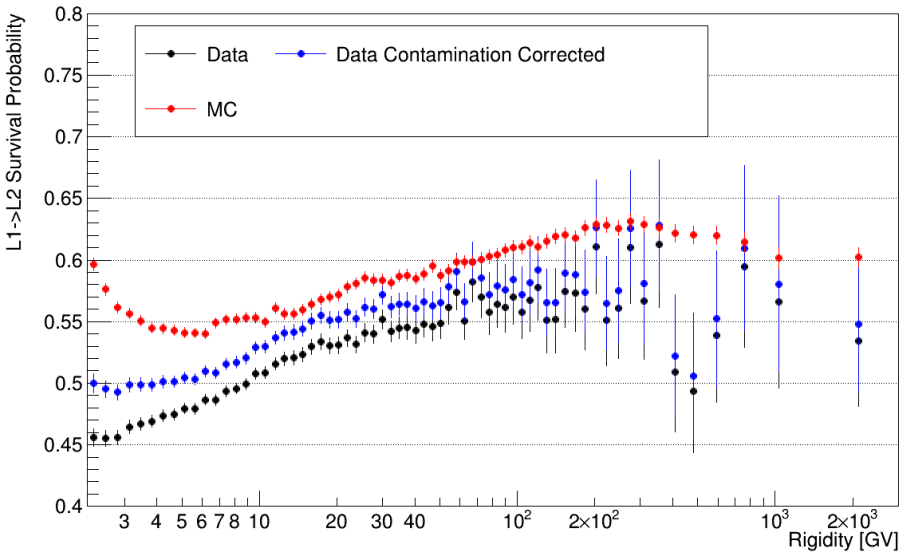

Figure 3-35: The L1→L2 survival probability from data sample without background contamination correction (black), from data sample after background contamination correction (blue) and from MC simulation sample (red).

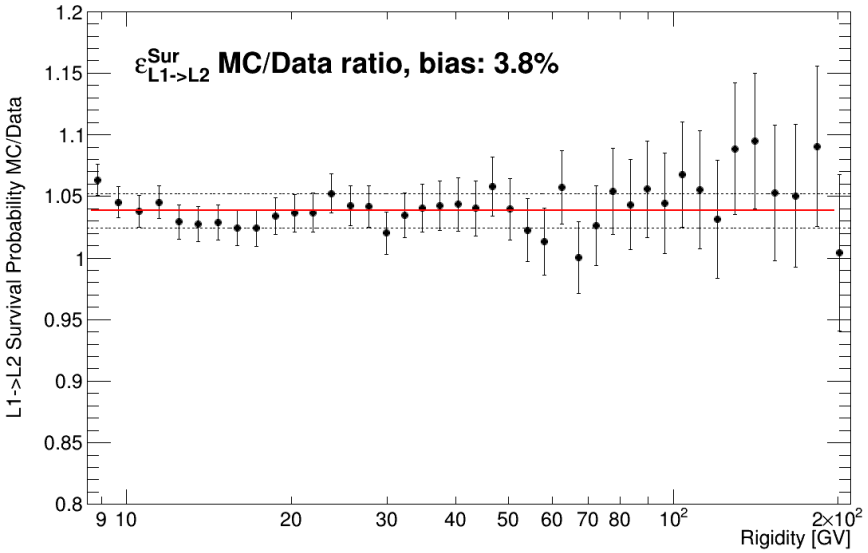

Figure 3-36: MC-to-data ratio of the L1→L2 survival probability (black full circle) with a constant fit (red solid line). The black dashed band shows the systematic uncertainty, as discussed in Section 3.6.1.2.

presence of contamination can be expressed as:

$$N_{Z'}^{inner} = \varepsilon_{Z'}^{L12Sur} N_{Z'}^{L1Z} + \sum_{Z''>Z'} P_{Z'}^{Z''} N_{Z''}^{L1Z}. \tag{3.26}$$

To simplify the problem, the breaking-up probability from Z"($\neq$Z) to Z' ($P_{Z'}^{Z''\neq Z}$) can be replaced by the one from Z to Z' ($P_{Z'}^{Z}$) since:

- Difference between them ($P_{Z'}^{Z''\neq Z} - P_{Z'}^{Z}$) should be small;
- most importantly, this difference is again scaled by a *small contamination fraction* $f_{Z''>Z',Z''\neq Z}^{Z}$.

Hence the expression can be simplified into:

$$\begin{aligned} N_{Z'}^{inner} &\approx (\varepsilon_{Z'}^{L12Sur} f_{Z'}^{Z} + P_{Z'}^{Z} \sum_{Z''>Z'} f_{Z''}^{Z}) N_{tot} \\ \rightarrow P_{Z'}^{Z} &\approx \frac{N_{Z'}^{inner}}{N_{tot} \sum_{Z''>Z'} f_{Z''}^{Z}} - \frac{\varepsilon_{Z'}^{L12Sur} f_{Z'}^{Z}}{\sum_{Z''>Z'} f_{Z''}^{Z}} \end{aligned} \tag{3.27}$$

For Z' close to Z, for example Z'=Z-1 or Z'=Z-2, the survival probability for Z' can be replaced by the one for Z with the same argument as above, i.e. a small difference $\varepsilon_{Z'<Z}^{L12Sur} - \varepsilon_{Z}^{L12Sur}$ scaled by a small contamination fraction $f_{Z'<Z}^{Z}$. The breaking-up probability is then expressed as:

$$P_{Z'}^{Z} \approx \frac{N_{Z'}^{inner}}{N_{tot} \sum_{Z''>Z'} f_{Z''}^{Z}} - \frac{\varepsilon_{Z}^{L12Sur} f_{Z'}^{Z}}{\sum_{Z''>Z'} f_{Z''}^{Z}}. \tag{3.28}$$

For Z' much lower than Z, due to the negligible contamination ($f_{Z'}^{Z} \approx 0$ hence $\sum_{Z''>Z'} f_{Z''}^{Z} \approx 1$), the breaking-up probability is simplified to:

$$P_{Z'}^{Z} \approx \frac{N_{Z'}^{inner}}{N_{tot}}. \tag{3.29}$$

The breaking-up probabilities from Silicon nuclei to even charge channel (Oxygen, Neon and Magnesium) and to odd charge channel (Fluorine, Sodium and Aluminum) for MC simulation and data after background correction are shown in Fig. 3-37. Fragmentation into odd charge channel have better Data/MC agreements while the breaking-up probability into even charge channel have larger bias. Such bias on the breaking-up probabilities brings systematic uncertainty into the Top-of-Instrument correction for lower

charge produced from Silicon, since the TOI corrections are purely obtained from MC and depend on the simulation of partial inelastic cross section into different charge channel. The estimation of the systematic uncertainty of the TOI corrections is discussed in Section 3.6.2.2.

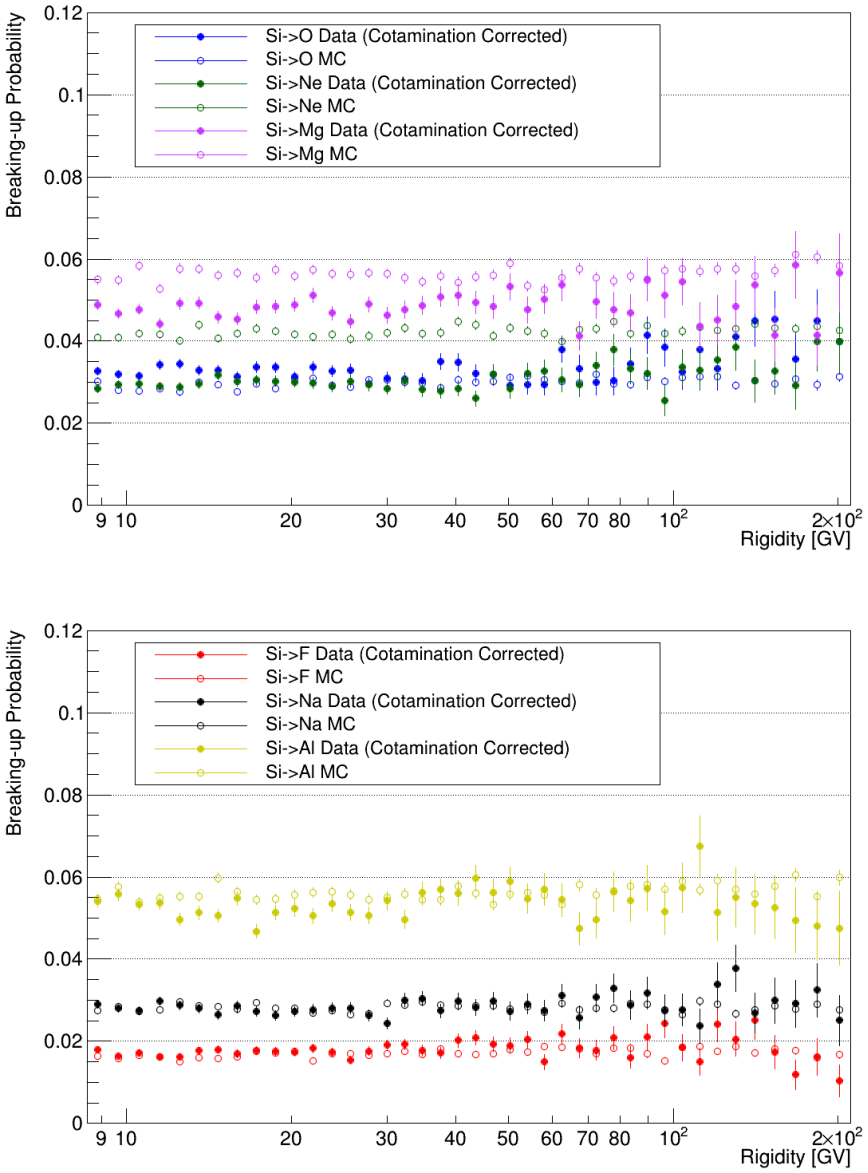

Figure 3-37: The breaking-up probabilities from Silicon to even charge channel (top): Oxygen (blue), Neon (green) and Magnesium (magenta), and odd charge channel (bottom): Fluorine (red), Sodium (black) and Aluminum (yellow) from data sample after contamination correction (full circle) and MC sample (open circle) respectively.

3.5.2 L8→L9 survival probability

The L8→L9 Survival probability can be obtained by counting how many events will pass the unbiased L9 hit selections for nuclei Z from a sample of nuclei Z survived to fragmentation up to the Tracker L8. Due to the finite charge resolution of a single Tracker layer, it's difficult to select the survived events with $Z' = Z$ ($N^{L9}_{Z'=Z}$) using only the unbiased Tracker L9 charge (see Fig. 3-38). Instead, "survived" events with $Z' \geq Z-1$ ($N^{L9}_{Z'\geq Z-1}$), i.e. the sum of events survived to fragmentation ($N^{L9}_{Z'=Z}$) and fragmented events with $Z' = Z-1$ ($N^{L9}_{Z'=Z-1}$), are selected. With these events, the probability that particle "survived" with $Z' \geq Z-1$ when traverses the Tracker L8 to L9 $\varepsilon^{L8\to L9}_{Z'\geq Z-1}$:

$$\varepsilon^{L8\to L9}_{Z'\geq Z-1} = \varepsilon^{L8\to L9}_{Z'=Z} + P^{L8\to L9}_{Z\to Z'=Z-1}, \tag{3.30}$$

is estimated, where $\varepsilon^{L8\to L9}_{Z'=Z}$ the Tracker L8→L9 survival probability and $P^{L8\to L9}_{Z\to Z'=Z-1}$ the breaking-up probability from Z to Z-1 when particle traverses the material between Tracker L8 and L9. As the breaking-up probability is small, the MC-to-data ratio of the Tracker L8→L9 survival probability $\varepsilon^{L8\to L9}_{Z'=Z}$ can be approximated by the ratio of $\varepsilon^{L8\to L9}_{Z'\geq Z-1}$. For simplification, $\varepsilon^{L8\to L9}_{Z'\geq Z-1}$ will be referred as the Tracker L8→L9 survival probability hereafter.

To obtain the Tracker L8→L9 survival probability $\varepsilon^{L8\to L9}_{Z'\geq Z-1}$, the sample and the survived events are selected by:

- Sample (N^{L8}_{Z}): L1Inner event selection + L9 fiducial volume + ECAL fiducial volume;
- Selected events from the sample ($N^{L9}_{Z'\geq Z-1}$): sample selection + unbiased L9 hit selection, requiring unbiased L9 XY-combined hits and unbiased L9 charge $Q^{L9}_{unbiased} > Z-1.5$.

The ratio $N^{L9}_{Z'\geq Z-1}/N^{L8}_{Z}$ can then be expressed as:

$$N^{L9}_{Z'\geq Z-1}/N^{L8}_{Z} = \varepsilon^{L8\to L9}_{Z'\geq Z-1}\varepsilon^{L9Sel}_{Z'\geq Z-1} + (1-\varepsilon^{L8\to L9}_{Z'\geq Z-1})\varepsilon^{L9Sel}_{Z'<Z-1} \approx \varepsilon^{L8\to L9}_{Z'\geq Z-1}\varepsilon^{L9Sel}_{Z'\geq Z-1},$$

since fragmented events with Tracker L9 charge $Z' < Z-1$ will have much smaller efficiency to pass the unbiased L9 selection, i.e. $\varepsilon^{L9Sel}_{Z'<Z-1} \ll \varepsilon^{L9Sel}_{Z'\geq Z-1}$, which is further

scaled by a small fraction $(1 - \varepsilon^{L8\to L9}_{Z'\geq Z-1})$. To obtain the survival probability $\varepsilon^{L8\to L9}_{Z}$ from this sample, the unbiased Tracker L9 selection efficiency $\varepsilon^{L9Sel}_{Z'\geq Z-1}$ is needed.

The unbiased Tracker L9 selection efficiency $\varepsilon^{L9Sel}_{Z'\geq Z-1}$ can be estimated using a sample of nuclei Z survived from fragmentation after passing the Tracker L9. Such a sample is obtained by requiring particles to behave as Minimum Ionizing Particles (MIPs) in ECAL:

- Denominator (N^{L8MIP}_{Z}): L1Inner selection + L9 fiducial volume + ECAL fiducial volume + ECAL MIPs selection. The ECAL MIPs selection requires the center of gravity of ECAL energy deposition on the first layer to be near the cell with maximum deposited energy and the ratio S3/S5$\geq$ 0.98, where S3 (S5) is the sum of the deposited energy in the maximum cell together with its two (four) neighbor cells.
- Numerator ($N^{L9MIP}_{Z'\geq Z-1}$): Denominator + unbiased L9 selection (same as for $N^{L9}_{Z'\geq Z-1}$).

Fig. 3-38 shows the unbiased L9 charge distribution without or with the ECAL MIPs selection. Even with the ECAL MIPs cut, the sample are still not purely non-fragmented events, i.e. the fraction of non-fragmented events in the ECAL MIPs sample (the purity P^{MIPs}_{Z}) is less than 1, as seen from the charge distribution. The reasons that fragmented events can pass the ECAL MIPs cut includes:

- the size of an ECAL cell is roughly 1 cm and most of the fragments might hit only a few ECAL cells;
- most of the fragments might not enter the ECAL;
- fragments do not deposit a significant amount of energy in the ECAL.

However, the ratio between $N^{L9MIP}_{Z'\geq Z-1}/N^{L8MIP}_{Z}$ can be expressed as:

$$N^{L9MIP}_{Z'\geq Z-1}/N^{L8MIP}_{Z} = P^{MIP}_{Z'\geq Z-1}\varepsilon^{L9Sel}_{Z'\geq Z-1} + (1 - P^{MIPs}_{Z'\geq Z-1})\varepsilon^{L9Sel}_{Z'<Z-1} \approx P^{MIPs}_{Z'\geq Z-1}\varepsilon^{L9Sel}_{Z'\geq Z-1}$$

for a similar reasoning that $\varepsilon^{L9Sel}_{Z'<Z-1} \ll \varepsilon^{L9Sel}_{Z'\geq Z-1}$ and it's scaled by a small amount of impurity $(1 - P^{MIP}_{Z'\geq Z-1})$. Hence the ECAL MIPs sample can still be used to calculate the unbiased Tracker L9 efficiency $\varepsilon^{L9Sel}_{Z'\geq Z-1}$ after the estimation of the non-fragmented portion of the sample $P^{MIP}_{Z'\geq Z-1}$.

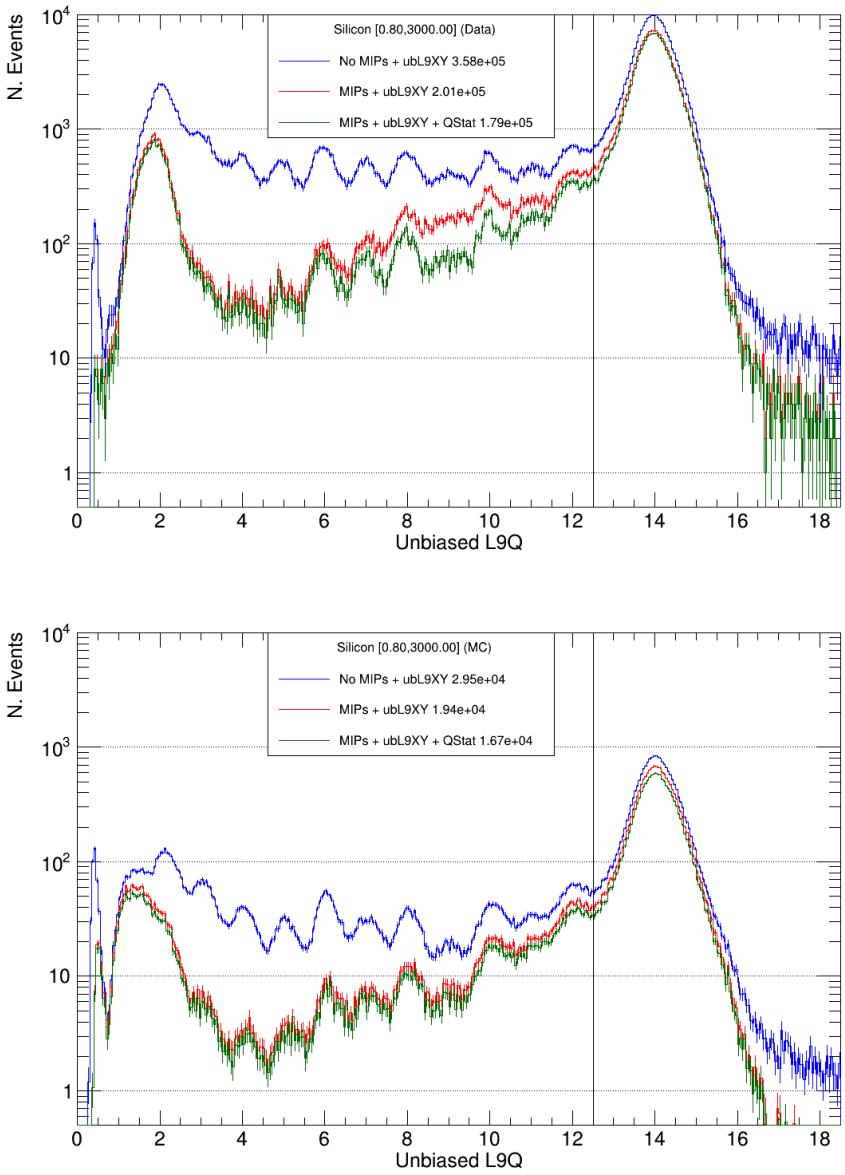

Figure 3-38: Unbiased Tracker L9 charge distribution from the sample without ECAL MIPs selection (blue), with ECAL MIPs selection (red) and with ECAL MIPs selection and L9 charge status (green) for data (top) and MC (bottom).

The purity of the ECAL MIPs sample $P^{MIP}_{Z'\geq Z-1}$ can be obtained by applying only the unbiased Tracker L9 charge cut on the ECAL MIPs sample, i.e.

$$\frac{N_Z^{L9Q\geq Z-1}}{N_Z^{L8MIP}} = P^{MIP}_{Z'\geq Z-1}\cdot\varepsilon^{L9Q\geq Z-1}_{Z'\geq Z-1} + (1-P^{MIP}_{Z'\geq Z-1})\cdot\varepsilon^{L9Q\geq Z-1}_{Z'<Z-1} \approx P^{MIP}_{Z'\geq Z-1}\cdot\varepsilon^{L9Q\geq Z-1}_{Z'\geq Z-1}$$

To obtain $P^{MIP}_{Z'\geq Z-1}$, the efficiency for the selection of Tracker L9 charge $Z'\geq Z-1$, $\varepsilon^{L9Q\geq Z-1}_{Z'\geq Z-1}$, must be estimated first: it can be obtained from the Tracker L1 and L2 charge distribution since the charge distribution between each single Silicon Tracker is similar, i.e. $\varepsilon^{L9Q\geq Z-1}_{Z'\geq Z-1}\approx\varepsilon^{L1Q(L2Q)\geq Z-1}_{Z'\geq Z-1}$.

In summary, the estimation of L8→L9 survival probability $\varepsilon^{L8\to L9}_{Z'\geq Z-1}$ proceeds through the following steps:

- Estimate the charge cut efficiency, $\varepsilon^{L9Q\geq Z-1}_{Z'\geq Z-1}$, from Tracker L1 and L2 charge distribution;
- Calculate the purity of the ECAL MIPs sample, $P^{MIP}_{Z'\geq Z-1}$ using the obtained $\varepsilon^{L9Q\geq Z-1}_{Z'\geq Z-1}$;
- Calculate the unbiased L9 selection efficiency, $\varepsilon^{L9Sel}_{Z'\geq Z-1}$, from the ECAL MIPs sample and its purity $P^{MIP}_{Z'\geq Z-1}$;
- Calculate the L8→L9 survival probability, $\varepsilon^{L8\to L9}_{Z'\geq Z-1}$ from L1Inner sample and $\varepsilon^{L9Sel}_{Z'\geq Z-1}$.

3.5.2.1 L9 charge cut efficiency estimated from L1 and L2 charge distribution

The Tracker L1 charge sample is selected by the two upper ToF layer charges and the Inner Tracker charge to be within [13.5,14.5] for Silicon nuclei. The Tracker L2 charge sample is selected by the Tracker L1 charge, the two Upper ToF layers charge and the Tracker L3-L8 charge to be within the same selection ranges. To have better agreement between the data and MC, another set of samples applying the charge status cut, same as the one applied in event selection for external layer charges (Section 3.2.1), are also used to study the Tracker charge cut efficiency.

Fig. 3-39 shows the data and MC charge distributions of Silicon nuclei for the Tracker L1 without and with charge status cut, the Tracker L2 without and with charge status cut at a selected rigidity bin. Fig. 3-40 shows the resulting Silicon nuclei Tracker charge cut efficiency $\varepsilon^{L9Q\geq Z-1}_{Z'\geq Z-1}$ using these samples for data and MC.

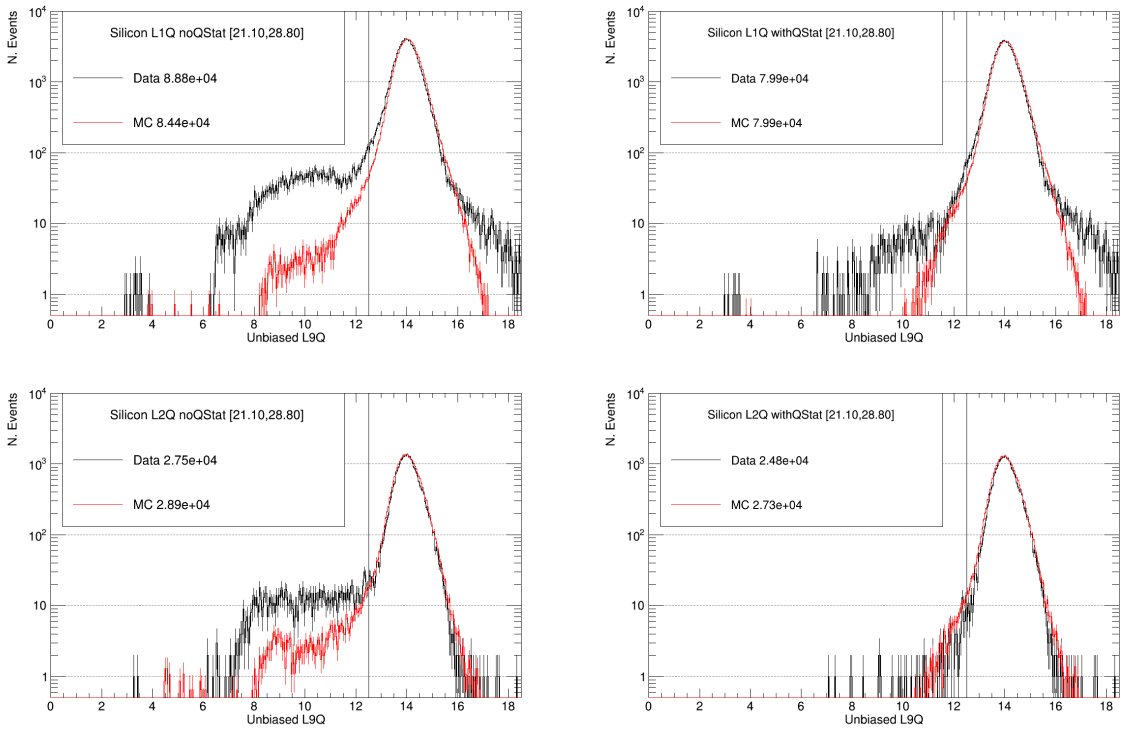

Figure 3-39: The Tracker charge distribution, selected as Silicon nuclei, of the Tracker L1 without charge status cut (top left), the Tracker L1 with charge status cut (top right), the Tracker L2 without charge status cut (bottom left), the Tracker L2 with charge status cut (bottom right) for Data (black) and MC (red) respectively. The black lines indicate the charge cut range $Q > Z - 1.5$, i.e. $Q > 12.5$ for Silicon nuclei.

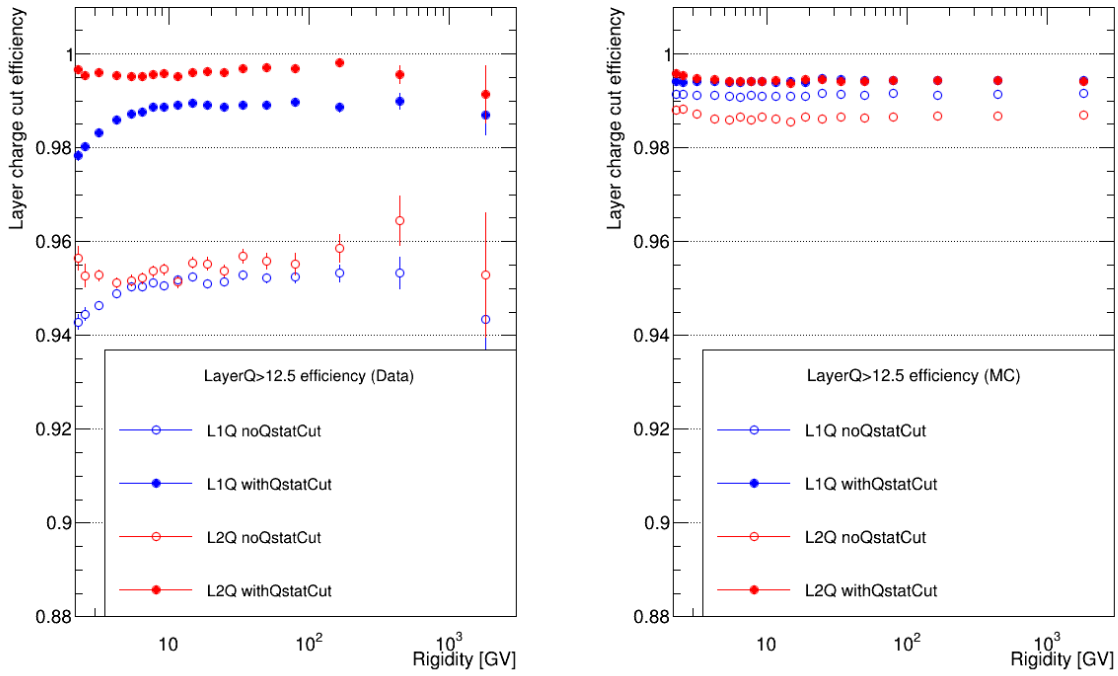

Figure 3-40: Tracker layer charge cut efficiency $\varepsilon^{L9Q\geq Z-1}_{Z'\geq Z-1}$ for data (left) and MC (right) obtained from different charge sample: the Tracker L1 without charge status cut (blue open circle), the Tracker L1 with charge status cut (blue full circle), the Tracker L2 without charge status cut (red open circle), the Tracker L2 with charge status cut (red full circle).

3.5.2.2 Purity of ECAL MIPs sample

With the estimated Tracker charge cut efficiency $\varepsilon^{L9Q\geq Z-1}_{Z'\geq Z-1}$, the purity of the ECAL MIPs sample can be calculated by the fraction of events in the sample with unbiased L9 charge $\geq Z-1$. Existence of an unbiased Tracker L9 hit on top of the ECAL MIPs sample (red histogram in Fig. 3-38) is required to have a well measured unbiased L9 charge, which will not change the purity of sample. When using the Tracker charge cut efficiency estimated from the Tracker L1 or L2 charge distribution with charge status cut, the charge status cut on unbiased L9 is also applied to the ECAL MIPs sample (green histogram in Fig. 3-38) to be compatible.

Fig. 3-41 shows the purity of ECAL MIPs sample $P^{MIP}_{Z'\geq Z-1}$ for Silicon nuclei using Tracker layer charge cut efficiency estimated from different charge sample for data and MC respectively. Fig. 3-42 shows the MC-to-data ratio for all these purities. A similar rigidity dependence for all of them is shown with a small difference on the absolute value.

3.5.2.3 Unbiased L9 selection efficiency calculated from ECAL MIPs sample

After the estimation of the purity of ECAL MIPs sample $P^{MIP}_{Z'\geq Z-1}$, the efficiency of unbiased Tracker L9 selection $\varepsilon^{L9Sel}_{Z'\geq Z-1}$, including existence of an unbiased Tracker L9 XY-combined hits with good charge status and the charge to be $> Z-1.5$ (> 12.5 for Silicon), can be calculated from the ECAL MIPs sample. Fig. 3-43 shows the unbiased Tracker L9 selection efficiencies calculated using ECAL MIPs sample with the purity estimated from different charge sample for Silicon nuclei. Fig. 3-44 shows the MC-to-data ratios for all these efficiencies.

3.5.2.4 Estimation of the Tracker L8→L9 Survival probability

The L8→L9 Survival probability $\varepsilon^{L8\to L9}_{Z'\geq Z-1}$ can then be estimated by using the L1Inner sample (N^{L8}_{Z}) together with the efficiency obtained from ECAL MIPs sample for the unbiased L9 selection and L9Q$> Z-1.5$.

Fig. 3-45 shows the L8→L9 survival probabilities $\varepsilon^{L8\to L9}_{Z'\geq Z-1}$ calculated from the L1Inner sample with the unbiased L9 selection efficiencies estimated using different charge sample.

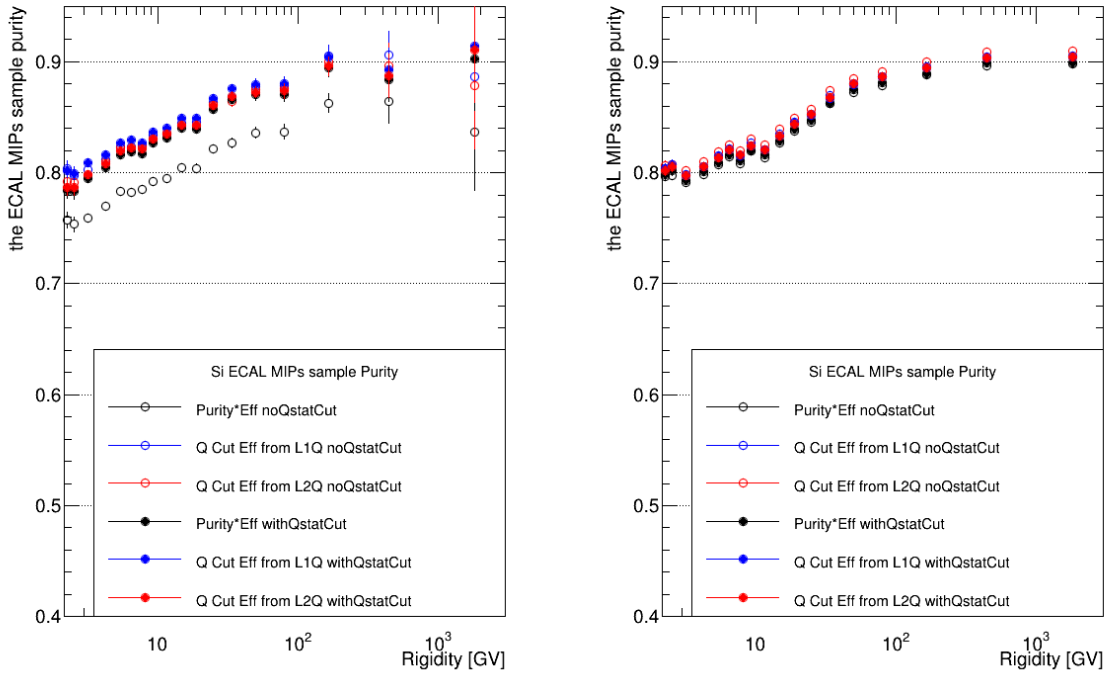

Figure 3-41: Purity of ECAL MIPs sample for Data (left) and MC (right) obtained using charge cut efficiency from different charge sample: the Tracker L1 without charge status cut (blue open circle), the Tracker L1 with charge status cut (blue full circle), the Tracker L2 without charge status cut (red open circle), the Tracker L2 with charge status cut (red full circle).

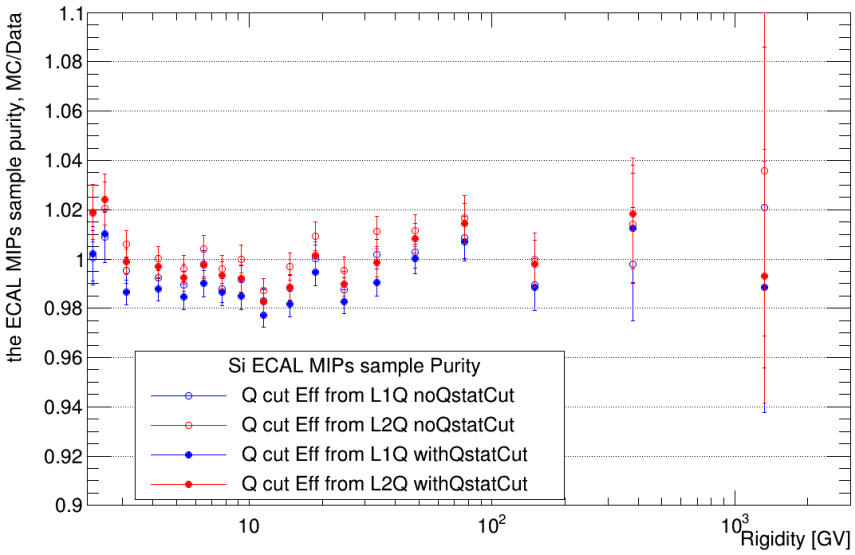

Figure 3-42: The MC-to-data ratio of the ECAL MIPs sample purity obtained using Tracker layer charge cut efficiency from different charge sample: the Tracker L1 without charge status cut (blue open circle), the Tracker L1 with charge status cut (blue full circle), the Tracker L2 without charge status cut (red open circle), the Tracker L2 with charge status cut (red full circle).

Fig. 3-46 shows the MC-to-data ratios for all these survival probabilities.

From the estimated Purity of ECAL sample as well as the unbiased L9 selection efficiency, it seen that results using charge efficiency obtained from L1 charge sample with charge status cut are different from results using other samples for data for $\sim 1\%$. Similarly, the L2 charge sample without charge status cut are different from results using other samples for MC for $\sim 1\%$. Using these results introduces additional MC and data difference to the Tracker L8→L9 survival probability, which comes from the difference of the Tracker Layer charge. So the final results is then the average of results, obtained from the L1 charge sample without charge status cut (blue open circle) and the L2 charge sample with charge status cut (red full circle), and the bias between the average and these two results is taken into account as a systematic uncertainty. Fig. 3-47 shows the MC-to-data ratio of $\varepsilon^{L8\to L9}_{Z'\geq Z-1}$ using the average unbiased L9 selection efficiency together with the systematic uncertainty band, which will be discussed in detail in Section 3.6.1.2.

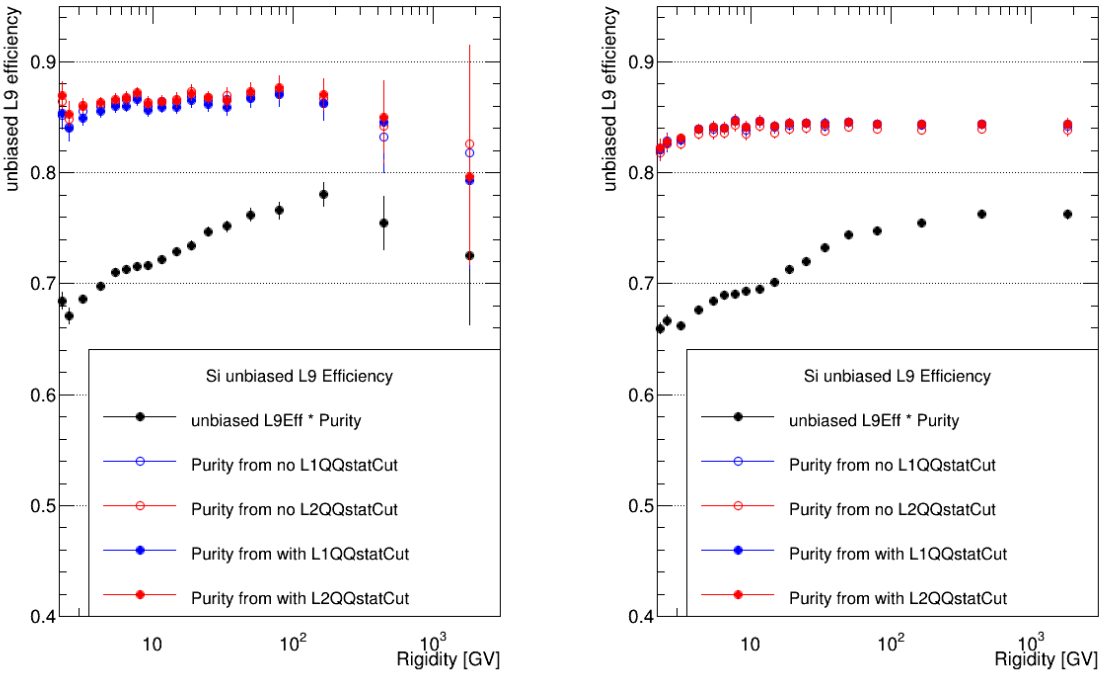

Figure 3-43: Unbiased L9 selection efficiencies from ECAL MIPs sample for Data (left) and MC (right) using Purity estimated with different charge cut efficiency from the Tracker L1 without charge status cut (blue open circle), the Tracker L1 with charge status cut (blue full circle), the Tracker L2 without charge status cut (red open circle), the Tracker L2 with charge status cut (red full circle) sample.

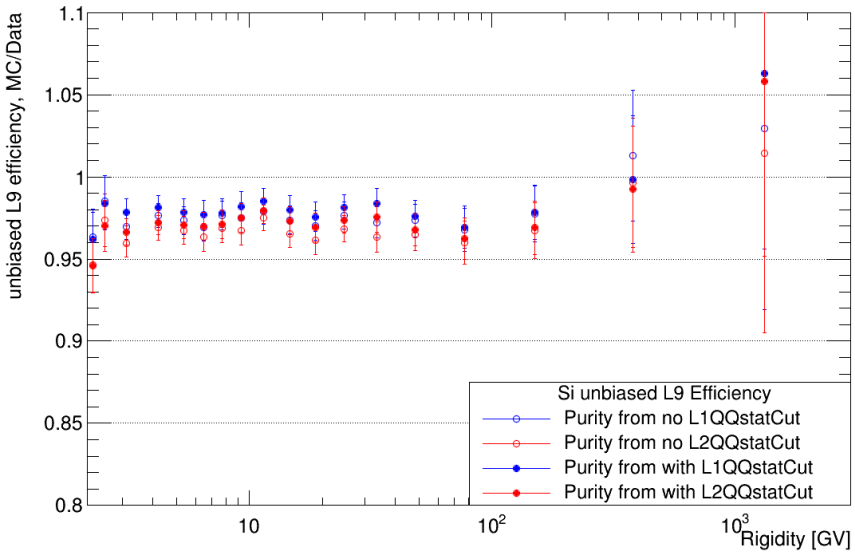

Figure 3-44: The MC-to-data ratio of Unbiased L9 selection efficiency obtained using charge cut efficiency from different charge sample: the L1Q without charge status cut (blue open circle), the L1Q with charge status cut (blue full circle), the L2Q without charge status cut (red open circle), the L2Q with charge status cut (red full circle).

3.5.3 Total flux normalization correction to the difference on Inelastic interaction between Data and MC

As explained before, the difference on the description of inelastic interactions of incoming nuclei on the AMS material between data and MC introduces a different total flux normalization, i.e. different normalization of effective acceptance between data and MC. The data MC difference on inelastic interaction between the Tracker L8 to L9 has already taken into account by the data-over-MC Tracker L9 efficiency ratio as discussed in Section 3.3.3.6, which contains the L8→L9 survival probability as well as the Tracker L9 detection and charge selection efficiency. The remaining difference comes from the survival probability of incoming particle traversing the AMS material from above the Tracker L1 up to the Tracker L8, $\varepsilon^{Sur}_{\rightarrow L8}$, including 1) supporting material above the Tracker L1 $\varepsilon^{Sur}_{\rightarrow L1}$, 2) material between the Tracker L1 and L2 $\varepsilon^{Sur}_{L1\rightarrow L2}$, mainly TRD as well as Upper Tof, and 3) material between the Tracker L2 and L8 $\varepsilon^{Sur}_{L2\rightarrow L8}$, i.e. the Inner Tracker. The main contribution is the material between the Tracker L1 and L2 (i.e. TRD and Upper TOF). The contribution of supporting material and Inner Tracker, mostly made of C and Al, is much less but still not negligible, as discussed in Section 3.5.3.

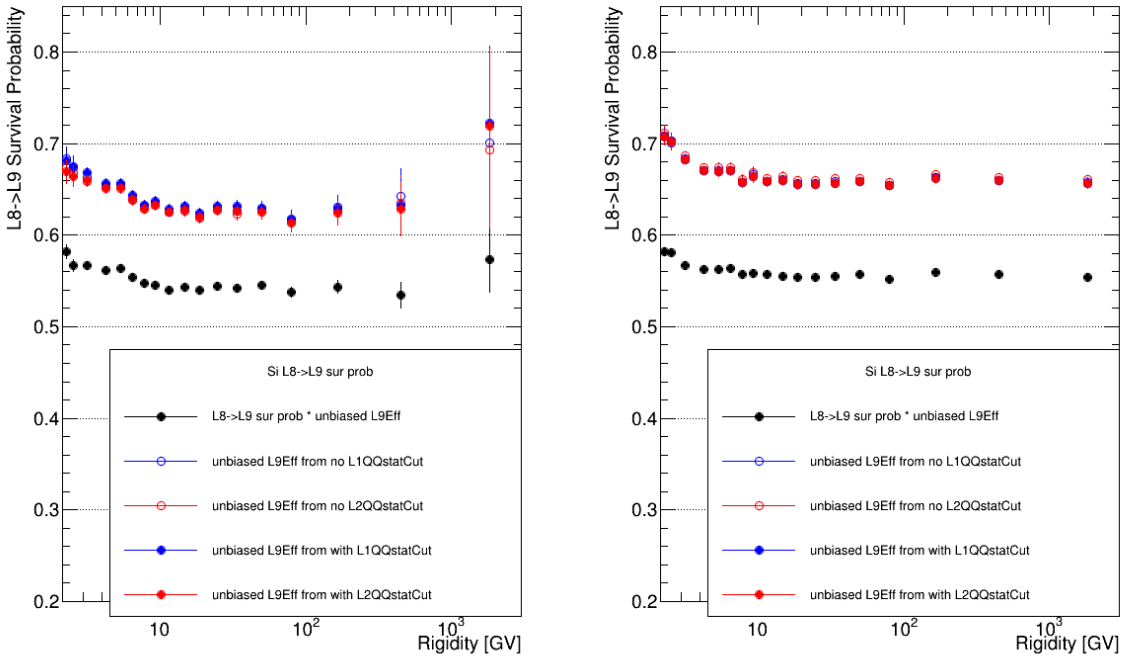

Figure 3-45: The L8→L9 survival probabilities from L1Inner sample for Data (left) and MC (right) using Purity estimated using different charge cut efficiency from the L1Q without charge status cut (blue open circle), the L1Q with charge status cut (blue full circle), the L2Q without charge status cut (red open circle), the L2Q with charge status cut (red full circle) sample.

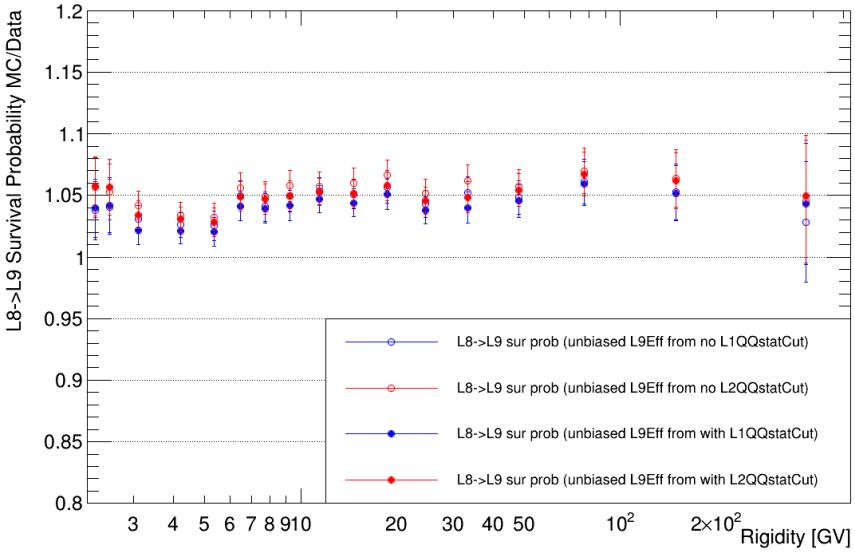

Figure 3-46: MC-to-Data ratio of L8→L9 survival probabilities obtained using charge cut efficiency from different charge sample: 1) L1Q without charge status cut (blue open circle), 2) L1Q with charge status cut (blue full circle), 3) L2Q without charge status cut (red open circle), 4) L2Q with charge status cut (red full circle).

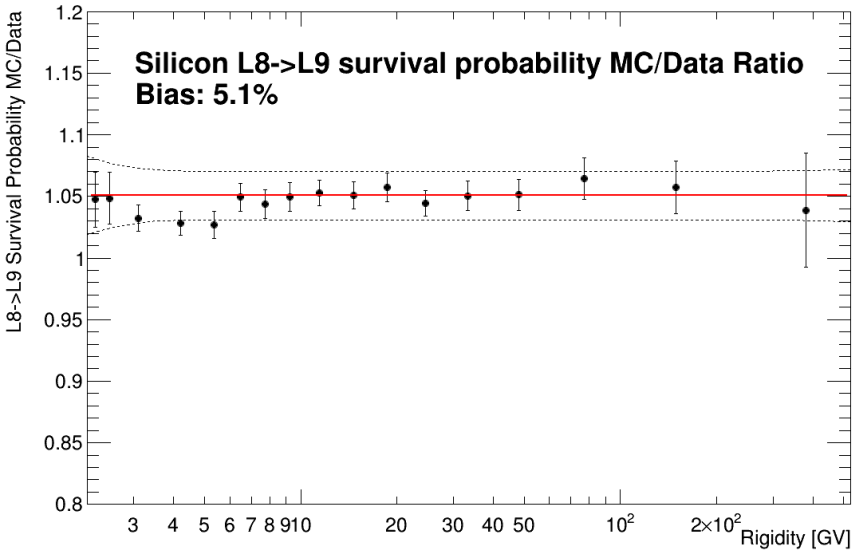

Figure 3-47: MC-to-Data ratio of L8→L9 survival probabilities obtained using average charge cut efficiency from charge sample: the L1Q with charge status cut and the L2Q with charge status cut. The solid red line shows the constant fit and dash black line indicates the systematic uncertainty band, which is estimated in Section 3.6.1.2.

However, $\varepsilon^{Sur}_{\rightarrow L1}$ and $\varepsilon^{Sur}_{L2\rightarrow L8}$ cannot be estimated from data, since:

- $\varepsilon^{Sur}_{\rightarrow L1}$: there is no measurement above the Tracker L1, hence there is no way to select an incoming sample of know composition;
- $\varepsilon^{Sur}_{L2\rightarrow L8}$: without using the Inner Tracker, there is no way to perform a precise rigidity measurement as well as selection of a clean sample and identification of the outgoing nuclei.

Instead, $\varepsilon^{Sur}_{\rightarrow L8}$ and its MC-to-Data ratio can be re-scaled from the Tracker L1→L2 and L8→L9 survival probabilities using the material amount ratios for different parts of the AMS-02 detector.

Ratio of Material amounts from MC

Neglecting the change of average inelastic cross section σ in Eq. (3.23) for different parts of the AMS-02 detector, the survival probability for particle traversing different AMS material only depends on the materials amounts n. Hence from the ratio of the logarithms of the survival probability, the ratio of material amounts can be obtained:

$$\frac{log(\varepsilon^{Sur}_{1})}{log(\varepsilon^{Sur}_{2})} = \frac{-n_1\sigma_1}{-n_2\sigma_2} \approx \frac{n_1}{n_2}, \tag{3.31}$$

where n_i the total amounts of material; σ_i the average inelastic cross section for different parts of detector respectively, where the difference on the average inelastic cross section due to slightly different material composition has been neglected, i.e. $\sigma_i \approx \sigma$.

To obtain the survival probability on different AMS material, the MC truth information can be used to select non-fragmented events up to any parts of the detector. For example, the survival probability from above Tracker L1 up to the i-th Silicon Tracker Layer can be obtained by:

- Sample: Linear extrapolation of MC particle from the generation plane to be within the fiducial volume for the i-th Tracker Layer;
- Selection for survived events: MC particle does not fragment at least up to the i-th Tracker Layer,

while the survival probability between two Tracker layers, Layer i and j, can be obtained by:

- Sample: Linear extrapolation of MC particle from generation plane to be within the certain Silicon Tracker fiducial volume and MC particle does not fragment at least up to the i-th Tracker Layer;
- Selection for survived events: MC particle does not fragment at least up to the j-th Tracker Layer.

The survival probabilities from above Tracker L1 up to 1) Tracker L1, 2) Tracker L2, 3) Tracker L8 and 4) Tracker L9 from Silicon MC using MC truth information are shown in Fig. 3-48; the breakdown of the survival probability in different parts of the AMS-02 detector, 1) above Tracker L1 up to Tracker L1 $\varepsilon^{Sur}_{\rightarrow L1}$, 2) L1→L2 $\varepsilon^{Sur}_{L1\rightarrow L2}$, 3) L2→L8 $\varepsilon^{Sur}_{L2\rightarrow L8}$ and 4) L8→L9 $\varepsilon^{Sur}_{L8\rightarrow L9}$, are shown as Fig. 3-49.

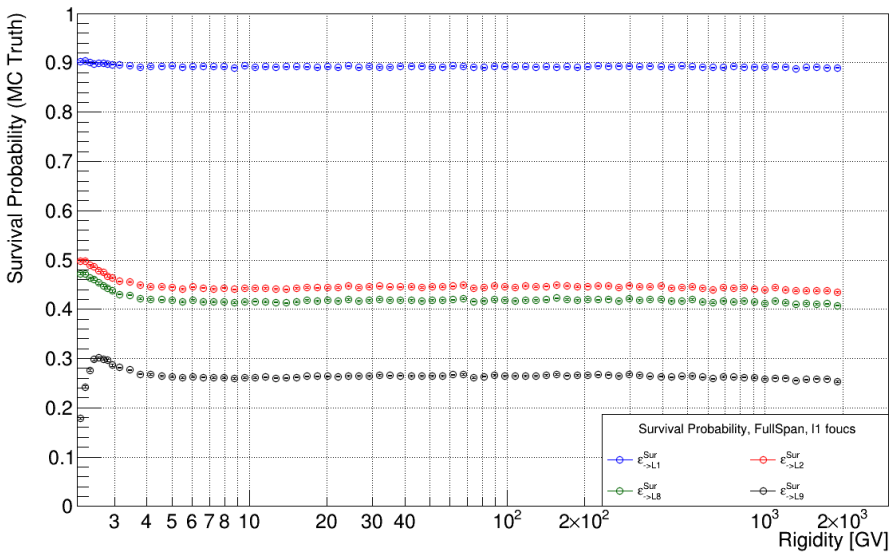

Figure 3-48: Survival probability from above Tracker L1 up to 1) Tracker L1 (blue circle), 2) Tracker L2 (red circle), 3) Tracker L8 (green circle) and 4) Tracker L9 (black circle) for Silicon using MC truth.

By doing the ratio of the logarithm of the survival probabilities, the ratios of the material amounts for different parts of the AMS-02 over that from above Tracker L1 up to L8 from MC can be obtained, as shown by Fig. 3-50 together with constant fits (solid lines). The material between the Tracker L1 and L2, mainly the TRD and the upper

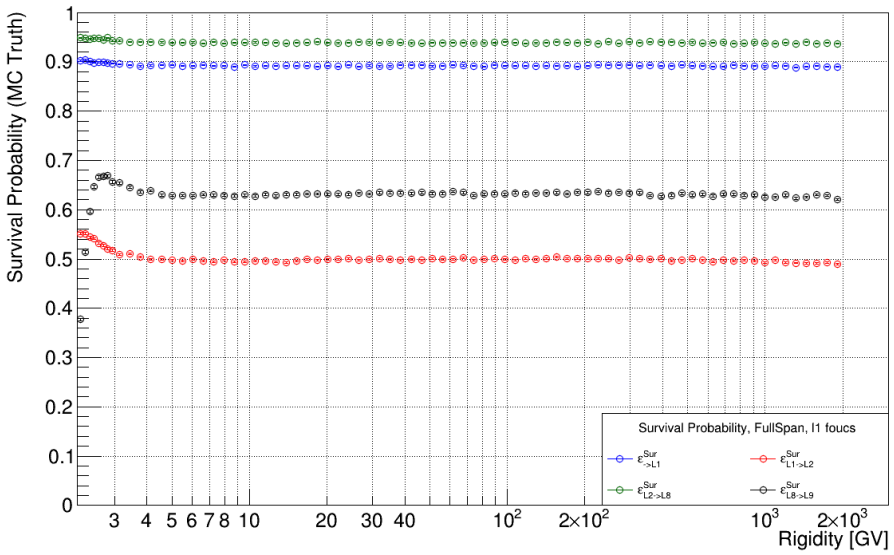

Figure 3-49: the survival probability in different parts of AMS, 1) above Tracker L1 up to Tracker L1 $\varepsilon^{Sur}_{\rightarrow L1}$ (blue circle), 2) L1→L2 $\varepsilon^{Sur}_{L1\rightarrow L2}$ (red circle), 3) L2→L8 $\varepsilon^{Sur}_{L2\rightarrow L8}$ (green circle) and 4) L8→L9 $\varepsilon^{Sur}_{L8\rightarrow L9}$ (black circle) for Silicon using MC truth.

TOF, makes up of $\sim$ 80% of the total material from above Tracker L1 up to L8. The supporting material above Tracker L1 contributes $\sim$ 7% and the material between the Tracker L2 up to L8 (i.e. Inner Tracker) contributes $\sim$ 13% to the total material from above Tracker L1 up to L8, which are not negligible.

By assuming the same portion of bias of material amounts between data and MC simulation for any parts of the detector, i.e. $n_i^{Data}/n_i^{MC} \approx n_j^{Data}/n_j^{MC} = 1+\delta$, the true ratios of material amount can be estimated by the ratio obtained from MC, i.e.

$$\frac{n_i^{Data}}{n_j^{Data}} \approx \frac{n_i^{MC}}{n_j^{MC}}. \tag{3.32}$$

Hence the MC-to-data ratio of the survival probability between different parts of the AMS material can be re-scaled into each other using the obtained ratios of material amount:

$$\begin{aligned}\frac{\varepsilon_i^{Sur,MC}}{\varepsilon_i^{Sur,Data}} &= \frac{e^{-n_i^{MC}\sigma^{MC}}}{e^{-n_i^{Data}\sigma^{Data}}} \approx \frac{e^{-n_j^{MC}\sigma^{MC}\frac{n_i^{MC}}{n_j^{MC}}}}{e^{-n_j^{Data}\sigma^{Data}\frac{n_i^{MC}}{n_j^{MC}}}} = \left(\frac{e^{-n_j^{MC}\sigma^{MC}}}{e^{-n_j^{Data}\sigma^{Data}}}\right)^{\frac{n_i^{MC}}{n_j^{MC}}} \\ &= \left(\frac{\varepsilon_j^{Sur,MC}}{\varepsilon_j^{Sur,Data}}\right)^{n_i^{MC}/n_j^{MC}}.\end{aligned} \tag{3.33}$$

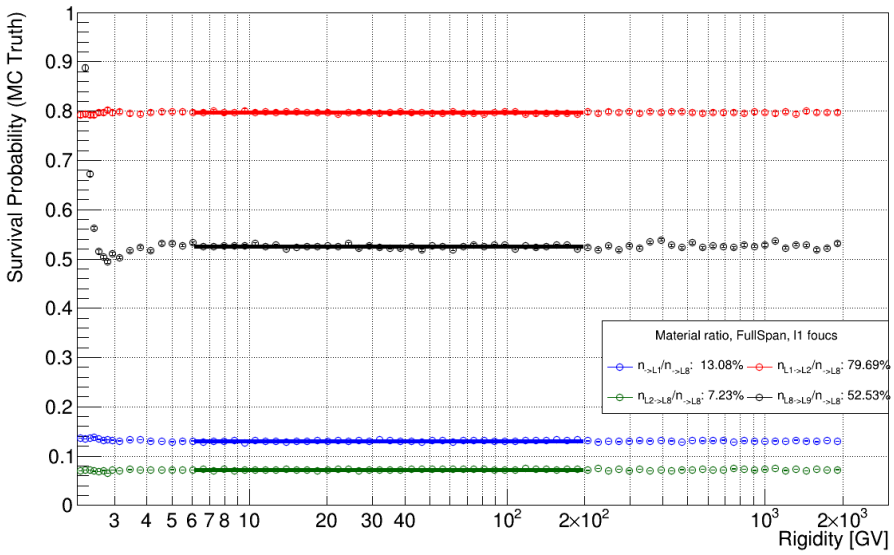

Figure 3-50: Ratio of material amounts of 1) above Tracker L1 up to L1 (blue circle), 2) Tracker L1 up to L2 (red circle), 3) Tracker L2 up to L8 (green circle) and 4) Tracker L8 up to L9 (black circle) over the total materials above Tracker L1 up to L8. Constant fits are applied to each of them to retrieve the ratio.

With the obtained MC-to-data ratio of $\varepsilon^{Sur}_{L1\to L2}$ (Section 3.5.1), as well as the ratio of material amounts obtained using the MC Truth information, the MC-to-data ratio of $\varepsilon^{Sur}_{\to L1}$ can be re-scaled from the ratio of $\varepsilon^{Sur}_{L1\to L2}$. The obtained ratio of $\varepsilon^{Sur}_{\to L1}$ can also be verified by the independent estimation using the result of $\varepsilon^{Sur}_{L8\to L9}$ (Section 3.5.2).

The average of MC-to-data ratio of $\varepsilon^{Sur}_{\to L1}$ re-scaled from $\varepsilon^{Sur}_{L1\to L2}$ and $\varepsilon^{Sur}_{L8\to L9}$ will be accounted as the total flux normalization correction and applied to the unfolded flux obtained in Section 3.4.3. The bias between estimated results from $\varepsilon^{Sur}_{L1\to L2}$ and $\varepsilon^{Sur}_{L8\to L9}$ is accounted as the systematic uncertainty of the flux normalization correction, which will be discussed in detail in Section 3.6.1.2.

The MC-to-data ratio of $\varepsilon^{Sur}_{\to L8}$ re-scaled from the ratio of $\varepsilon^{Sur}_{L1\to L2}$ is shown in Fig. 3-51.

$\varepsilon^{Sur}_{\to L8}$ re-scaled from $\varepsilon^{Sur}_{L8\to L9}$

The description of the AMS material between Tracker L8 and L9 has 3−4% known missing, i.e. the simulated material amounts, $n'_{L8\to L9}$, and the material amounts estimated during the construction of the AMS-02, $n_{L8\to L9}$, satisfied that $n'_{L8\to L9} = n_{L8\to L9}(1-\delta)$ with

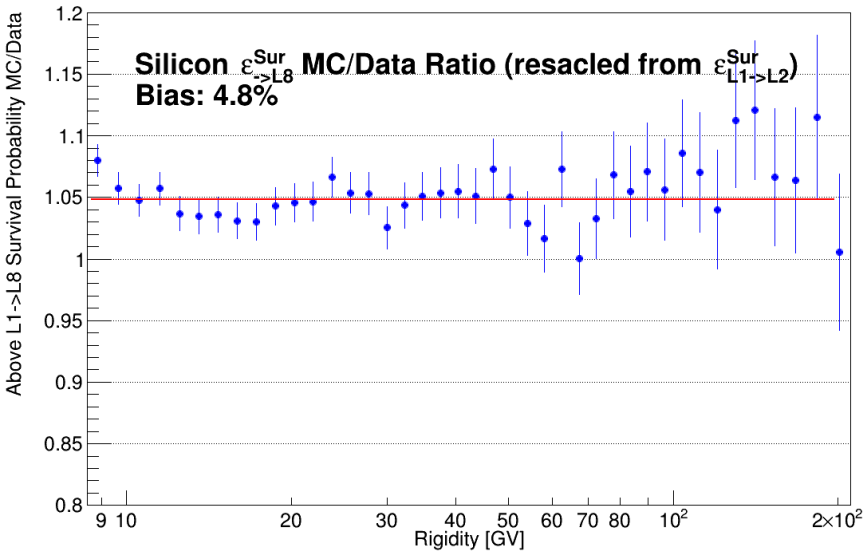

Figure 3-51: MC-to-Data ratio of Above Tracker L1 up to L8 survival probabilities re-scaled from L1→L2 survival probability. The solid red line shows the constant fit and dashed black lines represent the systematic uncertainty band re-scaled from the one for L1→L2 survival probability.

$\delta = 3.5\%$ in average. Adding back those missing material for the MC survival probability by:

$$\varepsilon^{Sur,MC}_{L8\to L9} = e^{-n_{L8\to L9}\sigma} = e^{-n'_{L8\to L9}\sigma\frac{n_{L8\to L9}}{n'_{L8\to L9}}} = e^{-n'_{L8\to L9}\sigma\frac{n_{L8\to L9}}{n'_{L8\to L9}}} = (\varepsilon'^{Sur,MC}_{L8\to L9})^{1/(1-\delta)} \quad (3.34)$$

The updated MC-to-Data ratio of $\varepsilon^{Sur,MC}_{L8\to L9}$ after adding back the missing material in MC (taking $\delta = 3.5\%$) is shown in Fig. 3-52.

The MC-to-Data ratio of $\varepsilon^{Sur}_{\to L8}$ re-scaled from the ratio of $\varepsilon^{Sur}_{L8\to L9}$ is shown in Fig. 3-53. Due to the missing material, the obtained ratio of material amounts from Fig. 3-50 will also need to be corrected, i.e. $n_{L8\to L9}/n_{\to L8} = n'_{L8\to L9}/n_{\to L8}/(1-\delta)$.

Compared to the result re-scaled from $\varepsilon^{Sur,MC/Data}_{L1\to L2}$, ∼1% bias can be found which might due to different material bias between Data and MC on the upper part (Tracker L1 to L2) and lower part (Tracker L8 to L9) of the AMS-02. Difference between the estimation using upper part and lower part of AMS-02 can be more clearly seen by comparing the estimated $\varepsilon^{Sur,MC/Data}_{L1\to L2}$ with the one re-scaled from $\varepsilon^{Sur,MC/Data}_{L8\to L9}$. Using the ratio of $\varepsilon^{Sur}_{L1\to L2}$ and $\varepsilon^{Sur}_{L8\to L9}$ obtained using MC truth, the ratio of material amounts between Tracker L1 to L2 and Tracker L8 to L9 can be estimated. The comparison of re-scaled $\varepsilon^{Sur}_{L1\to L2}$ from

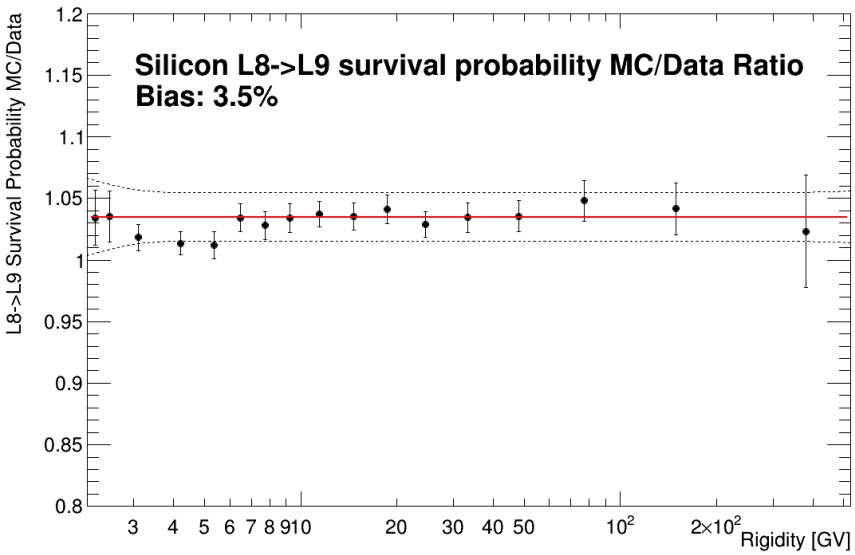

Figure 3-52: MC-to-Data ratio of L8→L9 survival probability obtained using average charge cut efficiency from charge sample: 1) L1Q with charge status cut and 2) L2Q with charge status cut. The MC survival probability $\varepsilon_{L8\to L9}^{Sur,MC}$ has already been corrected for the missing material. The solid red line shows the constant fit and the dashed black line represents the systematic uncertainty band.

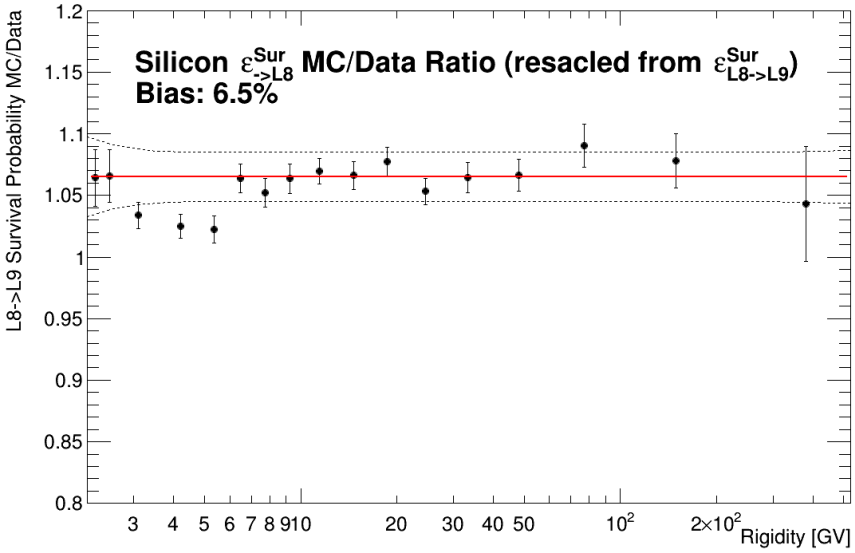

Figure 3-53: The MC-to-data ratio of Above Tracker L1 up to L8 survival probabilities re-scaled from L8→L9 survival probability after adding a correction for the missing material $\delta = 3.5\%$. The solid red line shows the constant fit and the dashed black line indicates the systematic uncertainty band re-scaled from the one for L8→L9 survival probability.

$\varepsilon^{Sur}_{L8\to L9}$ together with $\varepsilon^{Sur}_{L1\to L2}$ estimated in Section 3.5.1 is shown in Fig. 3-54, showing $\sim$1% bias between these results. Similar bias can also be seen between results for $\varepsilon^{Sur}_{L8\to L9}$, as shown in Fig. 3-55.

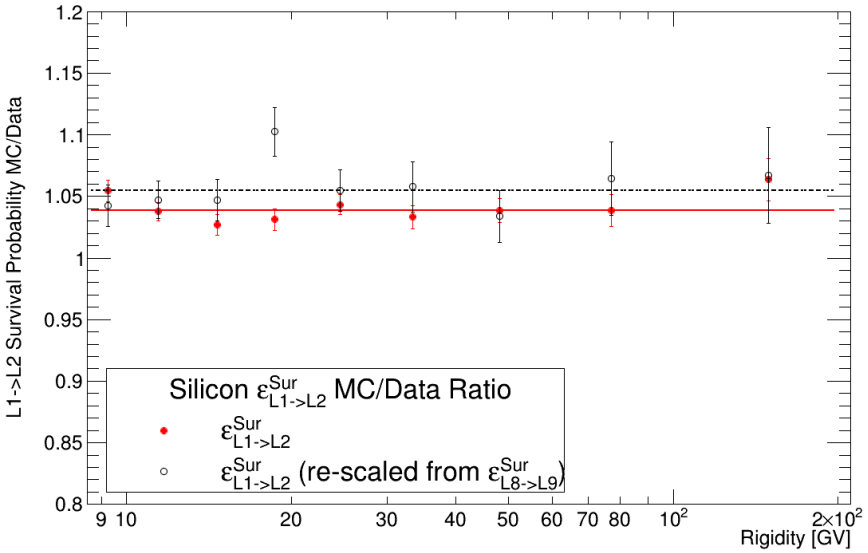

Figure 3-54: The MC-to-data ratio of the Tracker L1 to L2 survival probability (red full circle) and the one re-scaled from the Tracker L8→L9 survival probability (black open circle). The lines show the fits to a constant value.

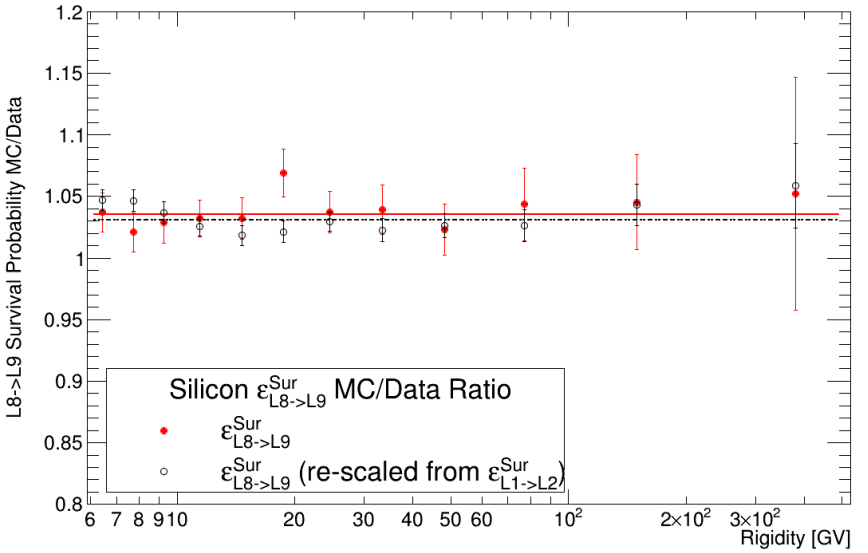

Figure 3-55: The MC-to-data ratio of the Tracker L8 to L9 survival probability (red full circle) and the one re-scaled from the Tracker L1→L2 survival probability (black open circle). The lines show the fits to a constant value.

The total flux normalization correction

The final MC-to-data ratio of Above Tracker L1 to L8 survival probability, $\varepsilon_{\rightarrow L8}^{Sur,MC/Data}$ is taken as the average between the results re-scaled from $\varepsilon_{L1\rightarrow L2}^{Sur,MC/Data}$ and $\varepsilon_{L8\rightarrow L9}^{Sur,MC/Data}$, as shown in Fig. 3-56. The final flux normalization correction is then taken as the constant fitted value of $\varepsilon_{\rightarrow L8}^{Sur,MC/Data}$ at rigidity range of 6-200 GV, which is ∼1.06. This correction is applied to the unfolded flux (see Fig. 3-31) obtained in Section 3.4.

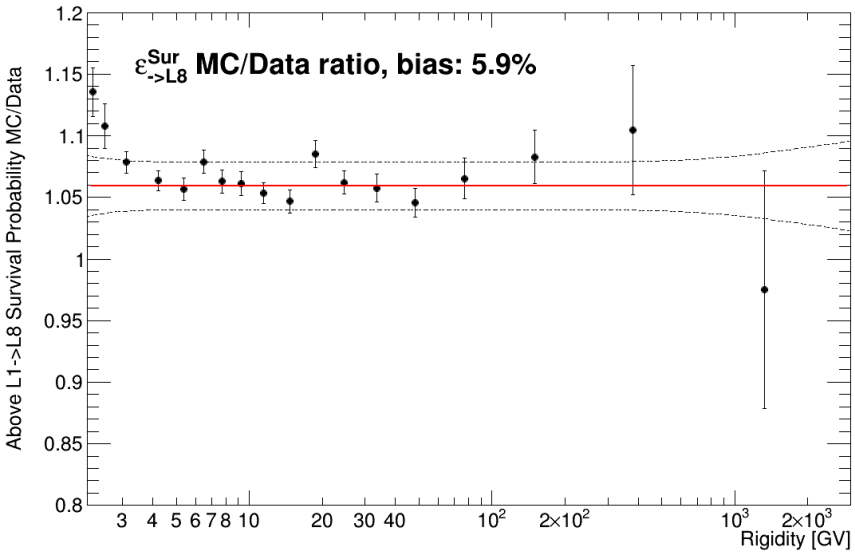

Figure 3-56: The MC-to-data ratio of the Silicon nuclei survival probability from Above Tracker L1 up to L8 averaged between the results re-scaled from $\varepsilon_{L1\rightarrow L2}^{Sur,MC/Data}$ and $\varepsilon_{L8\rightarrow L9}^{Sur,MC/Data}$. The solid red line shows the fit to a constant value between 6 GV to 200 GV, which is used for the total flux normalization correction, and the dashed black lines indicate the systematic uncertainty band as discussed later in Section 3.6.1.2 and shown in Fig. 3-82.

3.6 Systematic uncertainties

In the flux measurements, assumptions are made to simplify the estimation for some of the inputs and certain methods are adopted for fits and parametrizations as explained in the previous section. However, the choice of assumptions and methods might introduce systematic uncertainties to the final flux. In this chapter, all the flux calculation procedures are examined again by verifying the assumptions or/and applying alternative methods.

By these systematic uncertainty studies, the obtained flux is verified and the potential bias is accounted as systematic uncertainties to the final flux, as will be presented in Section 3.6.6.

Systematic uncertainties may arise from:

- Trigger efficiency and Acceptance, mainly due to the Data MC difference itself or the correction for such difference (efficiency ratios, total flux normalization correction etc.);
- Background estimation, coming from the estimation method themselves;
- Unfolding procedure, coming from the unfolding method (forward unfolding in this work) and the description of the Tracker rigidity resolution function;
- Absolute rigidity scale;
- Geomagnetic cutoff safety factor.

3.6.1 Trigger efficiency and acceptance

One of the main sources of systematic uncertainty for the Silicon nuclei flux study comes from the potential difference between the AMS-02 MC simulation and data, which can be separated into two parts:

- differences in the description of the detector response and event reconstruction of incoming nuclei;
- differences in the description of the nuclei interaction inside the AMS-02 detector, which can arise from differences in the inelastic nuclei cross section and in the AMS material in the simulation software.

3.6.1.1 Detector response and event reconstruction

Differences in the detector response and event reconstruction have already been taken into account by the correction on the effective acceptance using the data-to-MC efficiency ratios for different sub-detectors (see Section 3.3.3). Hence the systematic uncertainty comes from the description and parameterization of these corrections, which depends on:

1. the definition of the sample for efficiency estimation;

2. uncertainties in the parameterizations of efficiency, efficiency ratios and effective acceptances;
3. validity of the assumption of the high-rigidity behavior of the efficiency ratios.

Efficiency sample definition

Efficiency, so as the efficiency ratios, estimated from selected sample might be different from the true efficiency, introducing bias on the correction to the effective acceptance. To examine the dependence of the efficiency ratios on the sample selection, all efficiency ratios have been recalculated from samples selected by tightening the charge selections range by 75%, 60% and 50%. All the efficiency ratios are found to be stable within statistic uncertainties, as shown in Figs. 3-57–3-61.

Uncertainty of parameterizations

Parameterizations of the efficiency ratios are used in the flux calculation in order to smooth out fluctuations due to limited statistic of the samples for efficiency estimation. The uncertainties in the parameterizations are estimated by 68% confidence interval of the fit. The relative error of parameterization, confidence interval band over the center value of the fit, is used as contribution to the total systematic uncertainty of the final flux as the flux is proportional to the efficiency ratio.

The uncertainty in the parameterization of the effective acceptance due to statistical fluctuation is calculated and contributes to the total systematic uncertainty in the same way and shown in Fig. 3-62. Fits of these relative uncertainties are used to estimate the systematic uncertainties in order to smooth out statistical fluctuations.

Uncertainty on the high-rigidity behavior of efficiency ratios

When parameterizing the data/MC ratios for the L1 Big Z Efficiency, the L1 Pick up Efficiency, the Inner Tracking Efficiency and the L9 Efficiency, they're assumed to be constant above a certain rigidity, since the detector responses are not expected to have rigidity dependence at high rigidity. This assumption is based on the following considerations:

- at high rigidity, incoming nuclei with different rigidity behave in a similar way

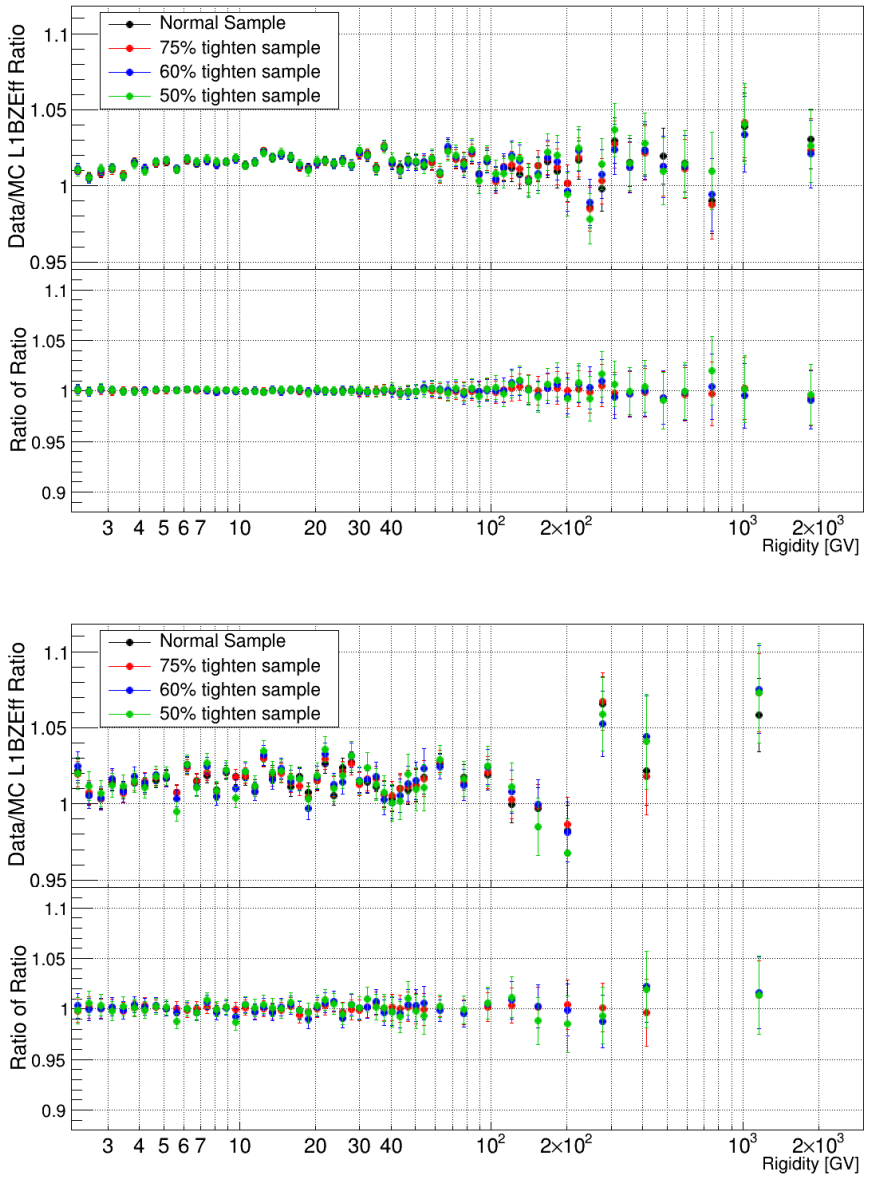

Figure 3-57: The Silicon nuclei $L1$ Big Z efficiency data/MC ratios obtained from different sample selections.

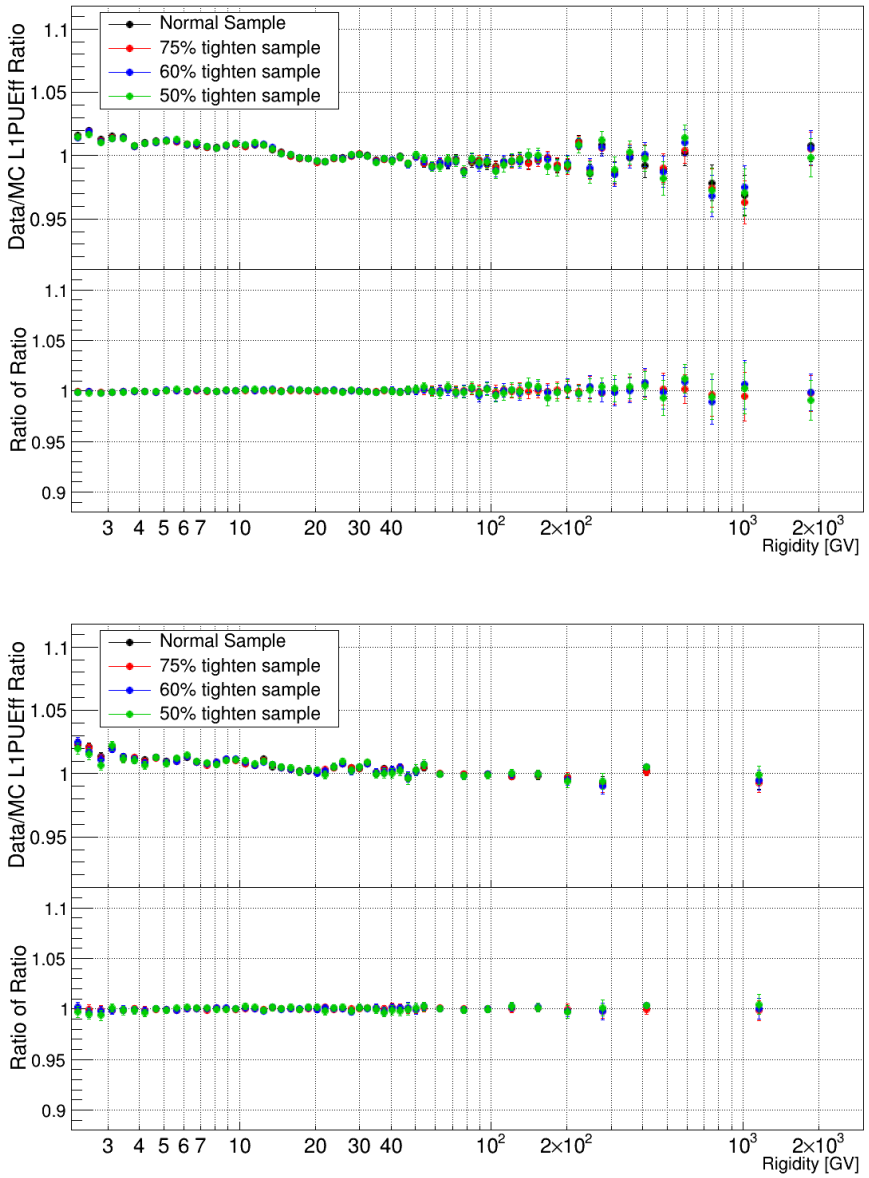

Figure 3-58: The Silicon nuclei $L1$ Pick up efficiency data/MC ratios obtained from different sample selections.

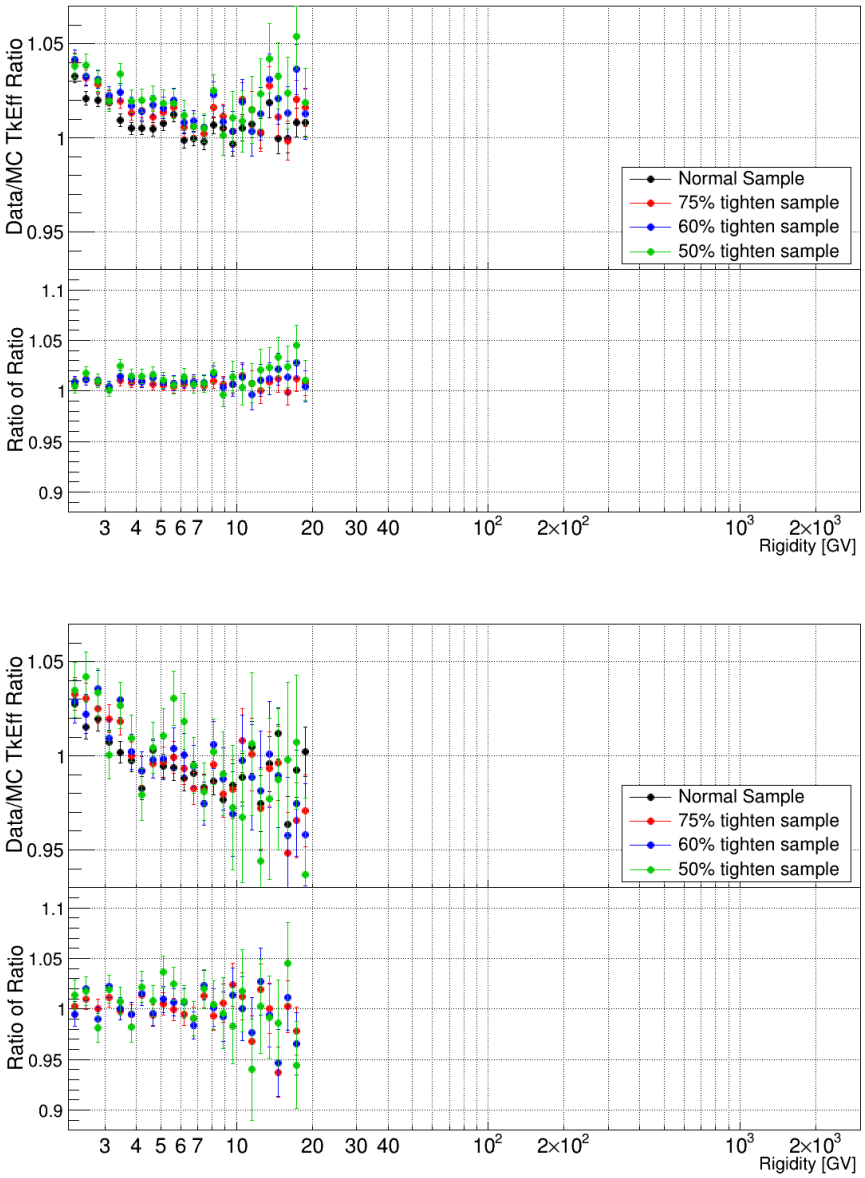

Figure 3-59: The Silicon nuclei Inner Tracking efficiency data/MC ratios obtained from different sample selections.

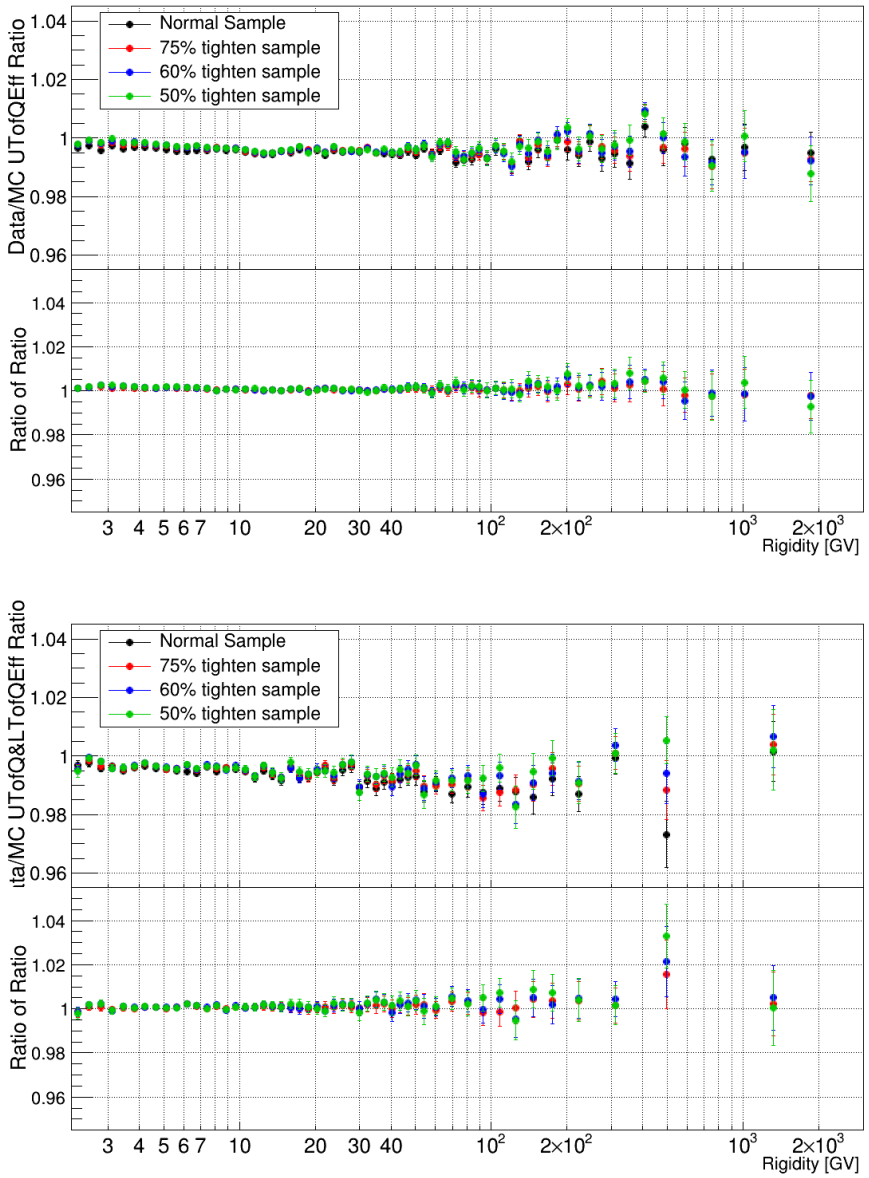

Figure 3-60: The Silicon nuclei Tof charge efficiency data/MC ratio obtained from different sample selections.

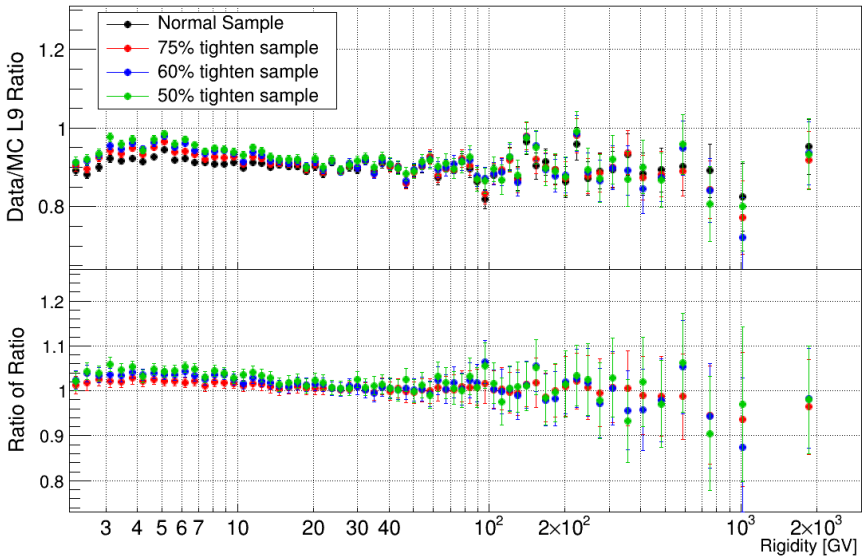

Figure 3-61: The Silicon nuclei L9 efficiency data/MC ratio obtained from different sample selections.

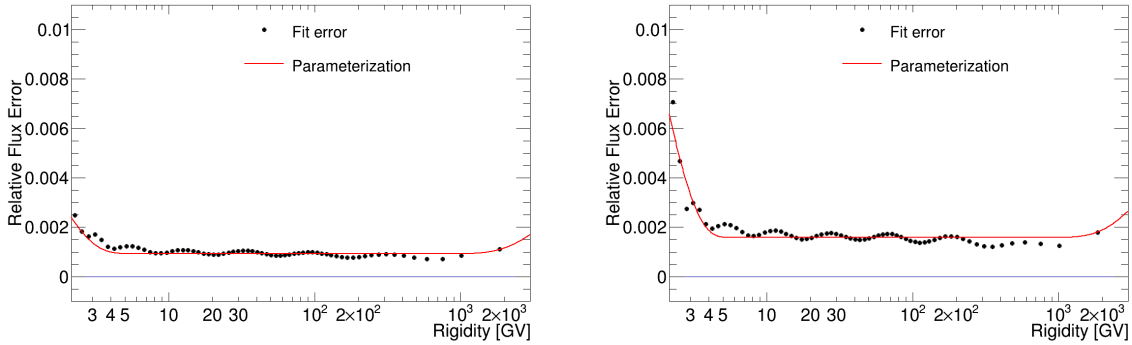

Figure 3-62: Systematic uncertainty arising from the parameterization of the Silicon nuclei effective acceptance for L1Inner (left) and the FullSpan (right) geometries. The black points show the relative errors calculated as the confidence interval band over the center value of the fit, and the red solid lines are the parameterization of these points.

because they traverse the AMS-02 detector almost in a straight line;

- incoming nuclei will behave like MIPs at high rigidity, depositing similar amounts of energy in the Silicon Tracker and the TOF;
- the Silicon Tracker charge has been calibrated to have no rigidity dependence.

On the contrary, at low rigidity nuclei will undergo multi-scatterings inside the AMS material, in addition their deposited energy exhibit larger dependence the nuclei energy, hence rigidity dependencies are expected.

The systematic uncertainties arising from the assumption of the high-rigidity behavior of the efficiencies are estimated by the relative deviation of efficiencies from a constant at high rigidity as function of generated rigidity from MC simulated events. Each of these efficiencies are fitted linearly above a certain rigidity and the deviation of the fit result from a constant is used as the estimation of this systematic uncertainty. Again, fits are used to estimate the relative deviation instead of the data points to smooth out statistical fluctuations. Figs. 3-63–3-66 show the fits of the efficiencies, the L1 Big Z Efficiency, the L1 Pick up Efficiency, the Inner Tracking Efficiency and the L9 Efficiency, in generated rigidity at high rigidity and their relative deviation from a constant.

The corresponding systematic uncertainties of the efficiency ratios are shown in Figs. 3-67–3-73. Relative systematic uncertainties are smoothed by spline fits. The total systematic uncertainty from efficiencies and efficiency ratios together with the breakdown are shown in Fig. 3-74 for the L1Inner and FullSpan geometries.

3.6.1.2 Uncertainty from the description of nuclei interactions in the AMS material in the Monte Carlo simulation

Inaccuracies in the description of the nuclei interactions inside the AMS-02 detector in the Monte Carlo simulation due to uncertainties in the inelastic cross sections and to the imperfect description of the AMS material, introduce an additional correction to the total flux normalization. This correction, $\varepsilon_{\rightarrow \mathrm{L8}}^{\mathrm{Sur,MC/Data}}$, is estimated through rescaling the Tracker L1→L2 and L8→L9 survival probabilities, $\varepsilon_{\mathrm{L1}\rightarrow\mathrm{L2}}^{\mathrm{Sur}}$ and $\varepsilon_{\mathrm{L8}\rightarrow\mathrm{L9}}^{\mathrm{Sur}}$ (Section 3.5.3). The systematic uncertainty of the survival probability ratios is factorized into systematic uncertainties coming from 1) the normalization of the correction, which is rigidity-independent, and 2) the rigidity dependence of the correction at low and high rigidity.

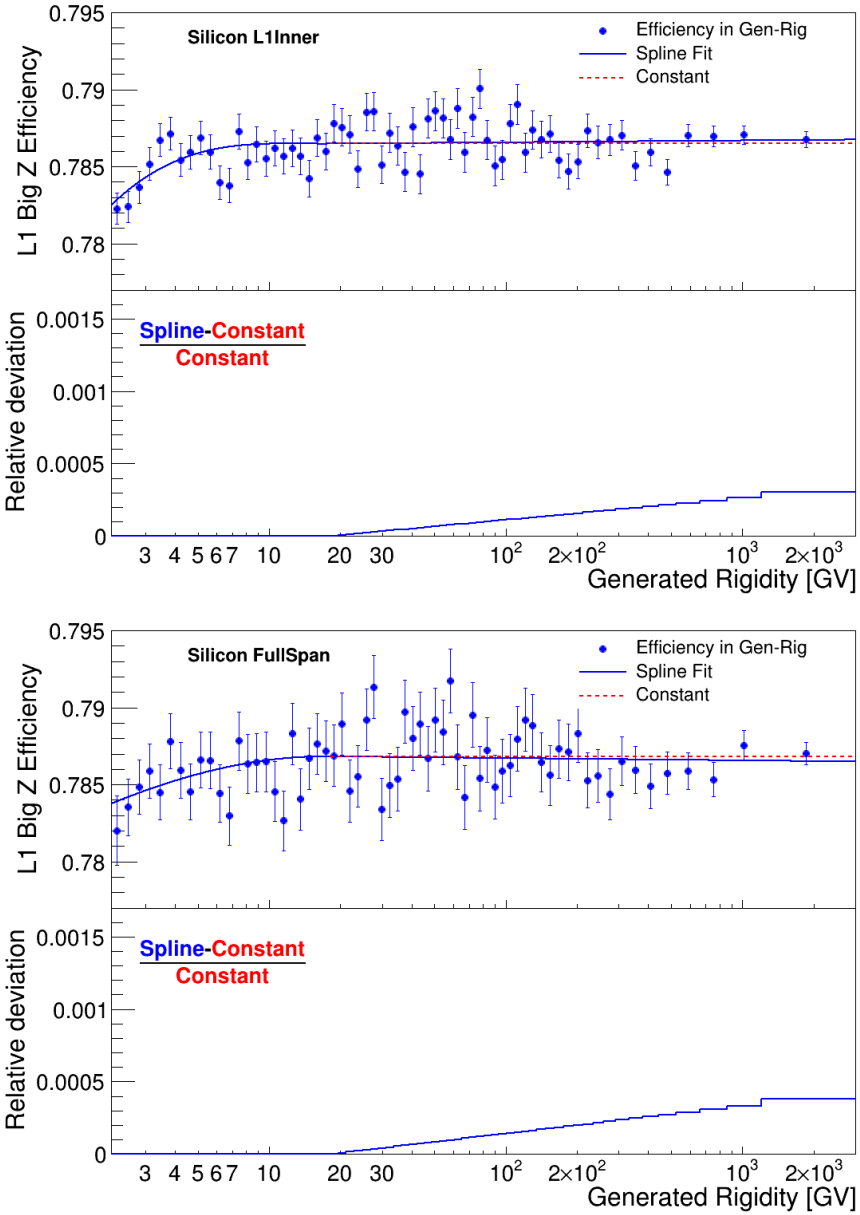

Figure 3-63: The Silicon nuclei Tracker L1 Big Z efficiency as function of the generated rigidity for L1Inner (left) and the FullSpan (right) geometries. The bottom panels show the relative deviation of the fit (blue solid line) to the constant value (red dashed line).

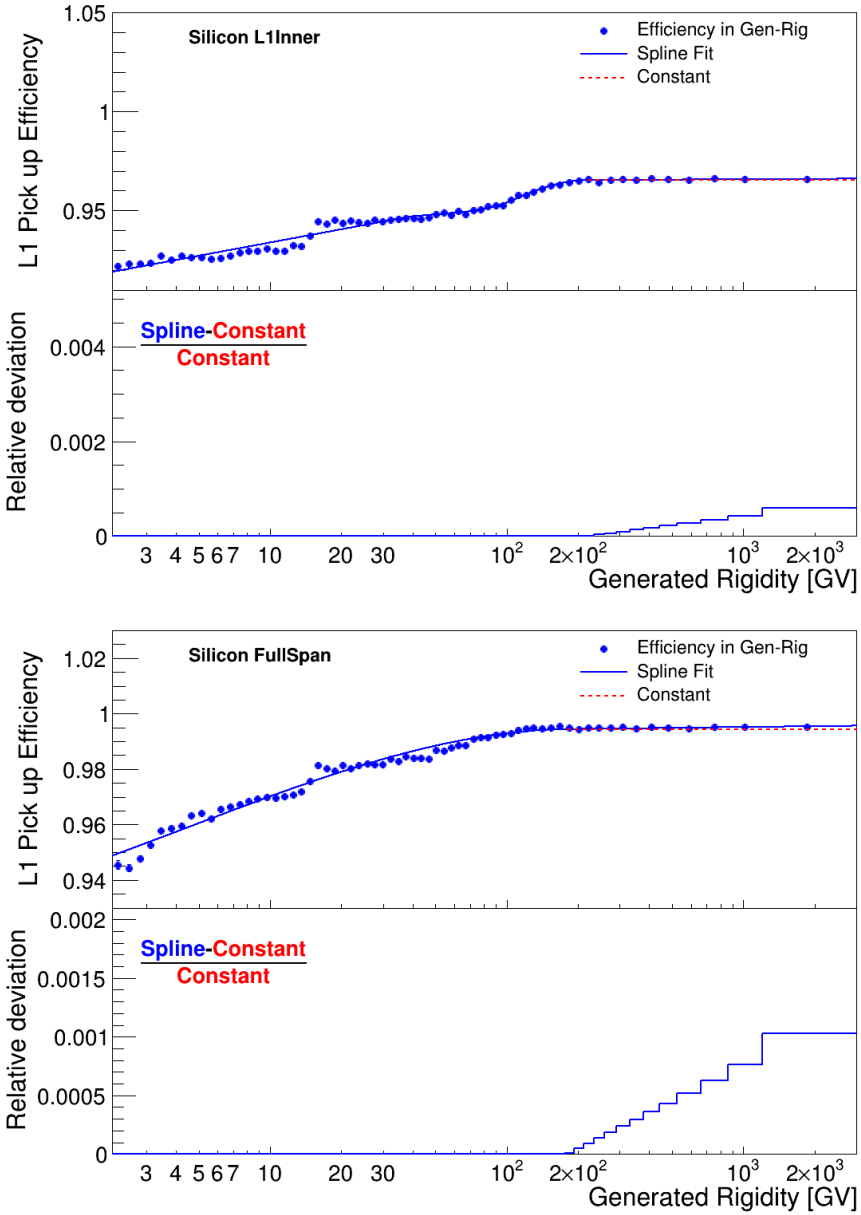

Figure 3-64: The Silicon nuclei Tracker L1 pick up efficiency as function of the generated rigidity for L1Inner (left) and the FullSpan (right) geometries. The bottom panels show the relative deviation of the fit (blue solid line) to the constant value (red dashed line).

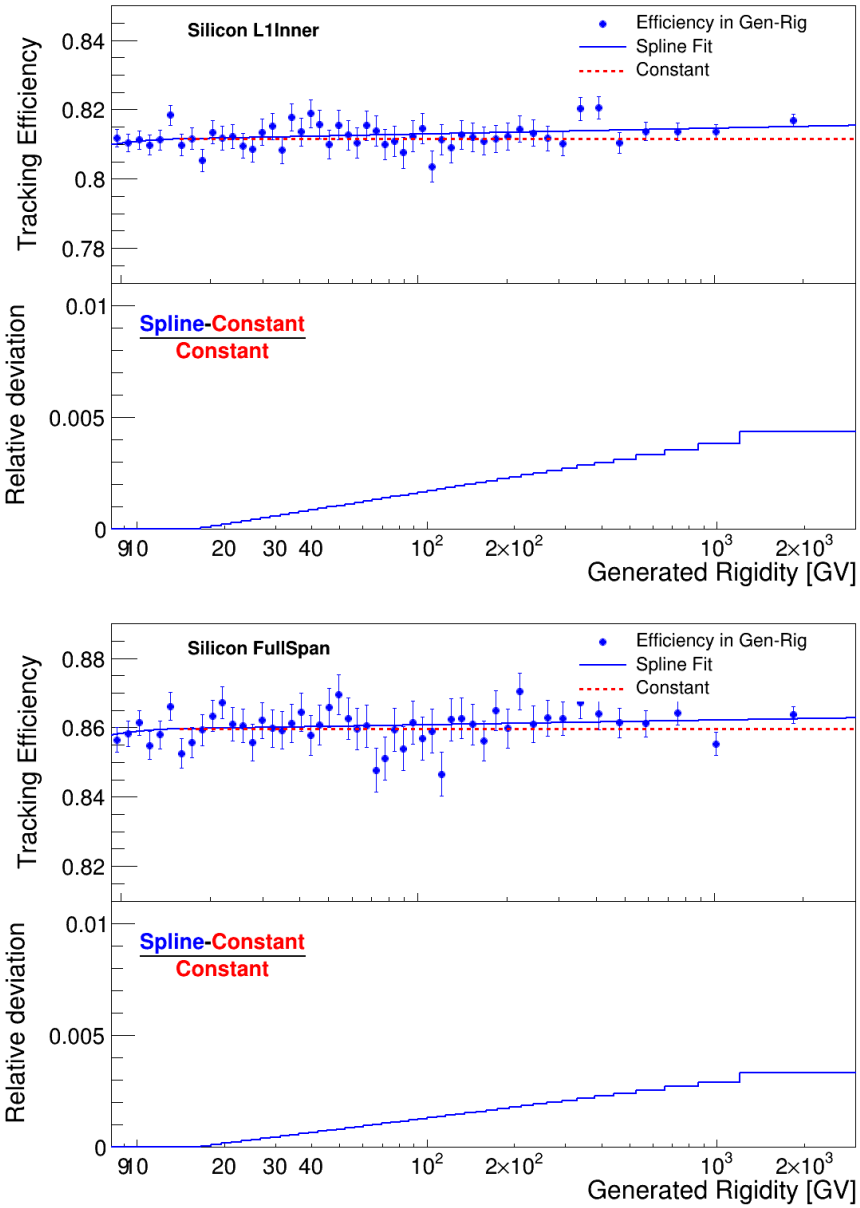

Figure 3-65: The Silicon nuclei Inner Tracking efficiency as function of the generated rigidity for L1Inner (left) and the FullSpan (right) geometries. The bottom panels show the relative deviation of the fit (blue solid line) to the constant value (red dashed line).

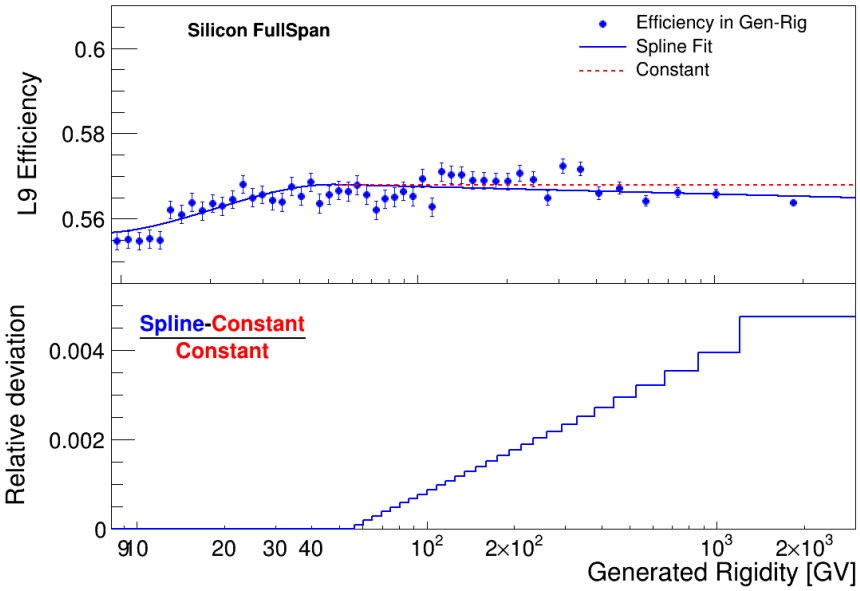

Figure 3-66: The Silicon nuclei Tracker L9 efficiency as function of generated rigidity for L1Inner (left) and the FullSpan (right) geometries. The bottom panel shows the relative deviation of the fit (blue solid line) to the constant value (red dashed line).

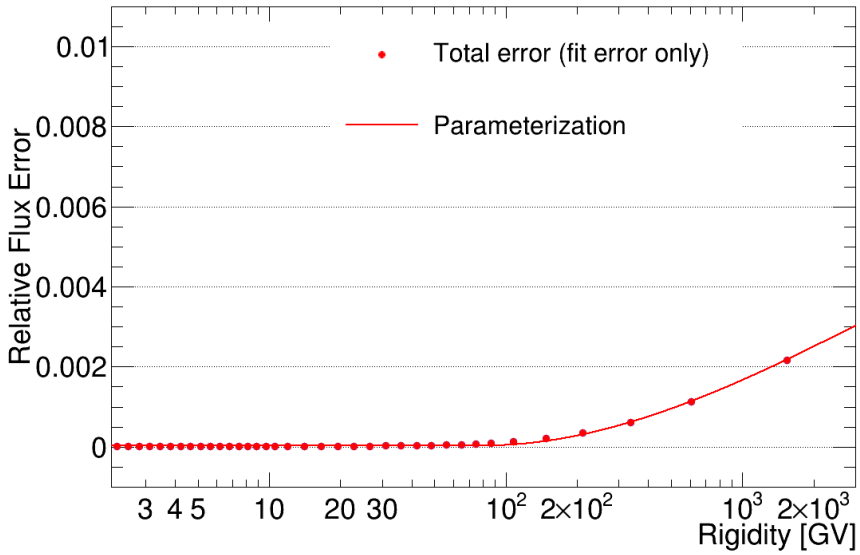

Figure 3-67: Systematic uncertainty from the fit error of the Silicon nuclei DAQ efficiency for L1Inner geometry.

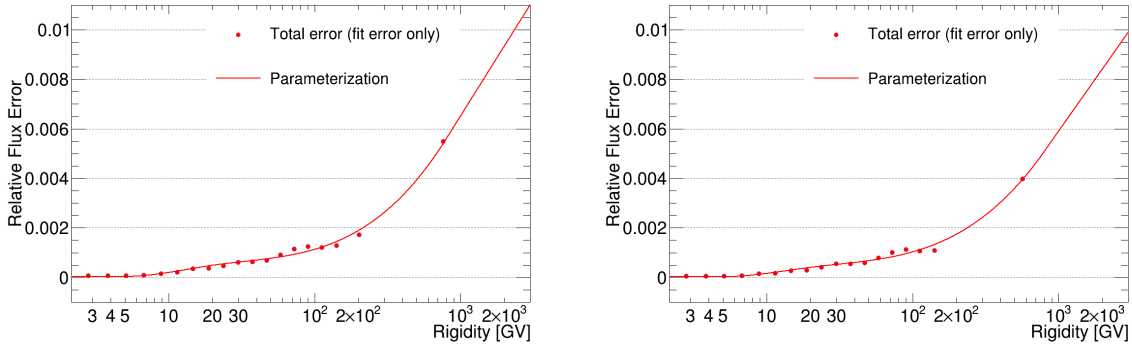

Figure 3-68: Systematic uncertainty from the fit error of the Silicon nuclei trigger efficiency ratio for L1Inner (left) and the FullSpan (right) geometries.

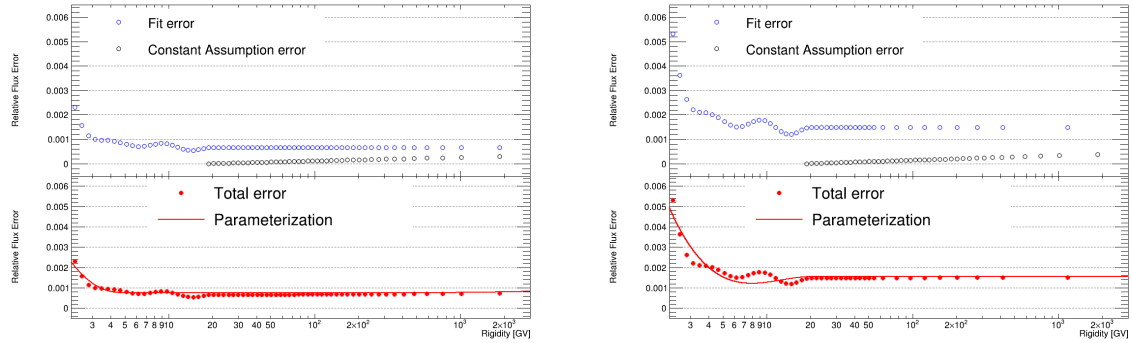

Figure 3-69: Systematic uncertainty of the Silicon nuclei L1 Big Z efficiency ratio for L1Inner (left) and FullSpan (right) respectively, which is the quadratic sum of fit error and constant assumption error.

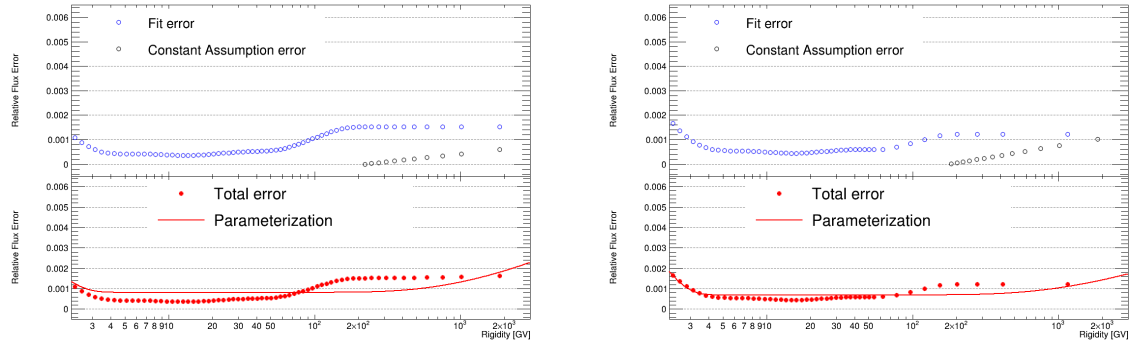

Figure 3-70: Systematic uncertainty of the Silicon nuclei L1 Pick up efficiency ratio for L1Inner (left) and FullSpan (right) respectively, which is the quadratic sum of fit error and constant assumption error.

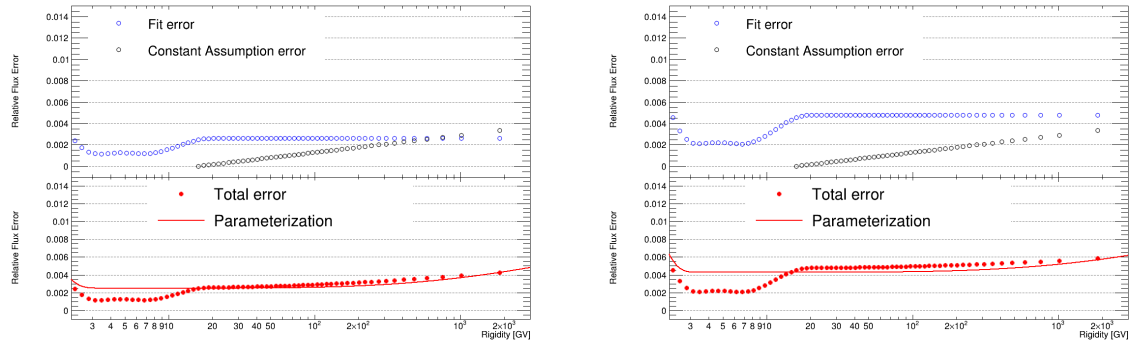

Figure 3-71: Systematic uncertainty of the Silicon nuclei Inner Tracking efficiency ratio for L1Inner (left) and FullSpan (right) respectively, which is the quadratic sum of fit error and constant assumption error.

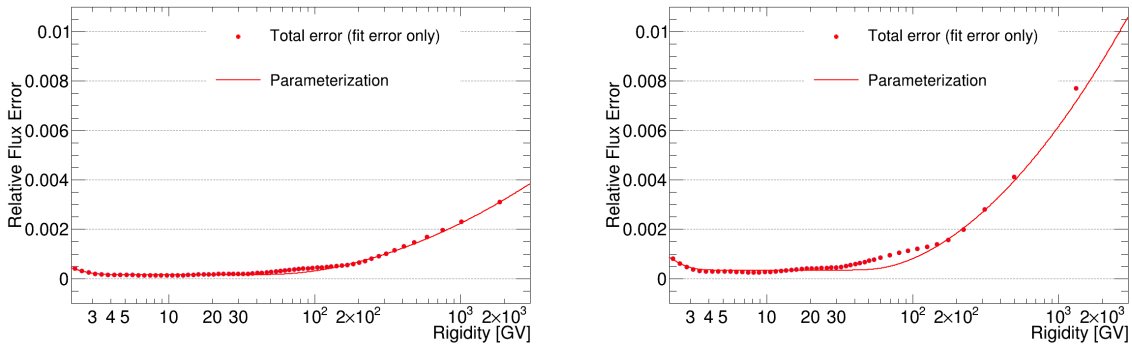

Figure 3-72: Systematic uncertainty of the Silicon nuclei Tof charge efficiency ratio for L1Inner (left) and FullSpan (right) respectively, which contains only fit error.

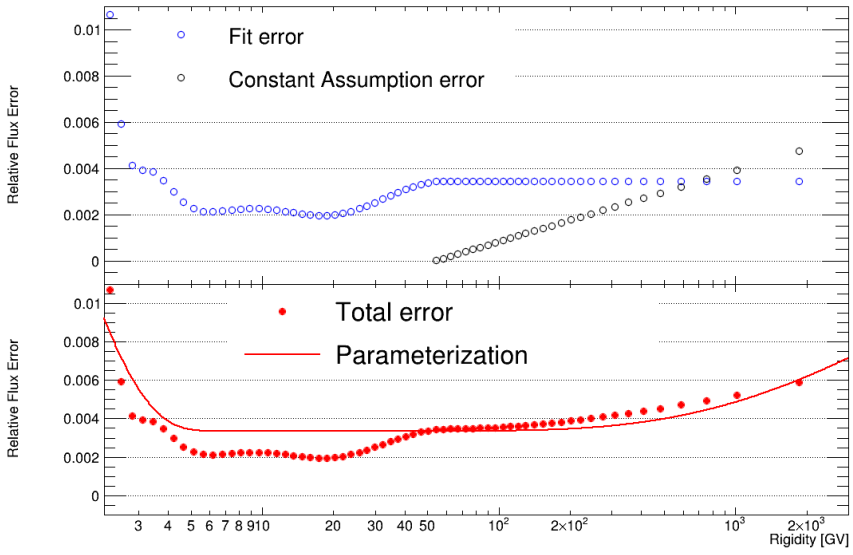

Figure 3-73: Systematic uncertainty of the Silicon nuclei L9 efficiency ratio for FullSpan geometry, which is the quadratic sum of fit error and constant assumption error.

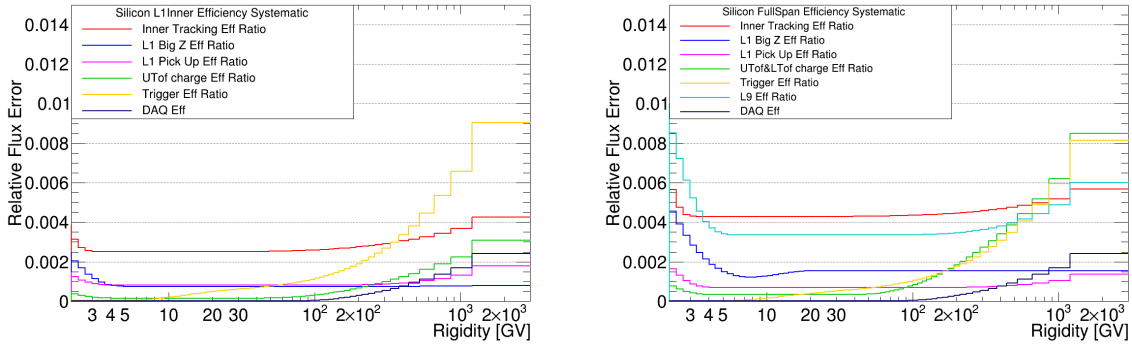

Figure 3-74: Total systematic uncertainty of the Silicon nuclei DAQ efficiency and other efficiency ratios for L1Inner (left) and FullSpan (right) geometry together with the breakdown.

The Glauber-Gribov Q model is used to parameterize the inelastic cross sections in the MC simulation. The rigidity dependence of inelastic cross sections is reflected in the rigidity dependence of the survival probabilities. Therefore, the deviation from a constant of the survival probability at high rigidity is considered as a systematic uncertainty on the knowledge of the rigidity dependence of inelastic cross sections.

Systematic uncertainty on the normalization

The limited statistic introduces an uncertainty, i.e. the statistical error $\sigma_{\text{stat}}^{\varepsilon_{\text{L1}\to\text{L2}}^{\text{Sur,MC/data}}}$, on the normalization of the estimated MC-to-data ratio of $\varepsilon_{\text{L1}\to\text{L2}}^{\text{Sur}}$. The corresponding uncertainty is obtained by a constant fit on the relative statistical errors, $\sigma_{\text{stat}}^{\varepsilon_{\text{L1}\to\text{L2}}^{\text{Sur,MC/data}}}/\varepsilon_{\text{L1}\to\text{L2}}^{\text{Sur}}$, at rigidities between 10 - 100 GV, where the estimation method for $\varepsilon_{L1\to L2}^{Sur}$ is valid, as shown in Fig. 3-75.

Similarly, the systematic uncertainty of $\varepsilon_{\text{L8}\to\text{L9}}^{\text{Sur}}$ due to limited statistics is estimated by a constant fit on the relative statistical errors, $\sigma_{\text{stat}}^{\varepsilon_{\text{L8}\to\text{L9}}^{\text{Sur,MC/data}}}/\varepsilon_{\text{L8}\to\text{L9}}^{\text{Sur}}$, as shown in Fig. 3-76. Additionally, the bias of $\varepsilon_{\text{L8}\to\text{L9}}^{\text{Sur}}$ estimated using the Tracker L9 charge efficiency $\varepsilon_{\text{L9QEff}}$ calculated from different Tracker layers charge distributions with different selections (Section 3.5.2), introduces another source of uncertainty on the normalization of $\varepsilon_{\text{L8}\to\text{L9}}^{\text{Sur}}$. The final value of $\varepsilon_{\text{L8}\to\text{L9}}^{\text{Sur,MC/data}}$ is computed from the average of the results obtained using charge efficiency estimated from the L1 charge distribution requiring a good charge status and the L2 charge distribution without requiring a good charge status. The relative bias from the final value of those estimated using charge efficiency estimated from the L1 charge dis-

tribution without requiring a good charge status and the L2 charge distribution requiring a good charge status (shown as the black full circles in Fig. 3-76), is accounted as a systematic uncertainty of $\varepsilon^{\mathrm{Sur,MC/data}}_{\mathrm{L8\to L9}}$. The final rigidity-independent systematic uncertainty of $\varepsilon^{\mathrm{Sur,MC/data}}_{\mathrm{L8\to L9}}$ is obtained as the quadratic sum of the two uncertainties discussed, shown as the red solid line in Fig. 3-76. For each of these two uncertainties the fit to a constant value (blue and black lines in Fig. 3-76) is used to compute the total contribution to the systematic uncertainty of the flux.

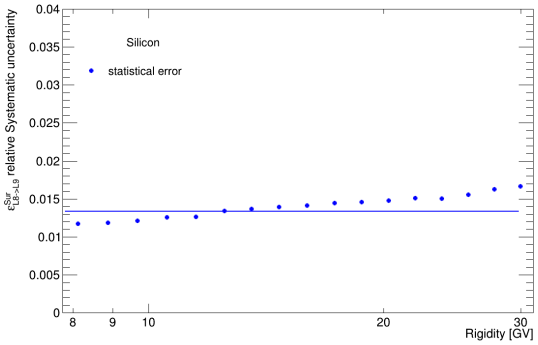

Figure 3-75: Systematic uncertainties of the normalization of $\varepsilon^{\mathrm{Sur,MC/data}}_{\mathrm{L1\to L2}}$ for Silicon nuclei from statistical error (blue circle and blue solid line for constant fit).

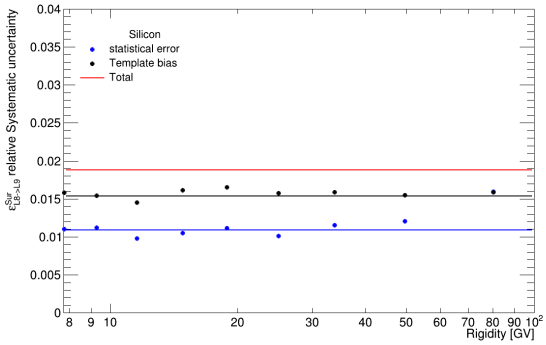

Figure 3-76: Systematic uncertainties of the normalization of $\varepsilon^{\mathrm{Sur,MC/data}}_{\mathrm{L8\to L9}}$ for Silicon nuclei from 1) statistical error (blue circle and blue solid line for constant fit), 2) bias from charge samples for L9 charge efficiency (black circle and black solid line for constant fit), 3) total systematic uncertainty (the quadratic sum of constant fits of 1) and 2), red solid line).

As the final flux normalization correction (MC-to-data ratio of above Tracker L1 up to L8 survival probability $\varepsilon^{\mathrm{Sur,MC/data}}_{\mathrm{\to L8}}$) is the average of ratios re-scaled from $\varepsilon^{\mathrm{Sur,MC/data}}_{\mathrm{L1\to L2}}$ and $\varepsilon^{\mathrm{Sur,MC/data}}_{\mathrm{L8\to L9}}$, the average of the systematic uncertainty of the normalization from $\varepsilon^{\mathrm{Sur,MC/data}}_{\mathrm{L1\to L2}}$ and $\varepsilon^{\mathrm{Sur,MC/data}}_{\mathrm{L8\to L9}}$ after re-scaling will be the rigidity-independent systematic uncertainty of $\varepsilon^{\mathrm{Sur,MC/data}}_{\mathrm{\to L8}}$. Furthermore, the bias between re-scaled ratios from $\varepsilon^{\mathrm{Sur,MC/data}}_{\mathrm{L1\to L2}}$ and $\varepsilon^{\mathrm{Sur,MC/data}}_{\mathrm{L8\to L9}}$ is accounted as another systematic uncertainty arising from the estimation methods. The total systematic uncertainty of the normalization of $\varepsilon^{\mathrm{Sur,MC/data}}_{\mathrm{\to L8}}$ is shown in Fig. 3-77, contributing 1.5% to the total flux systematic uncertainty.

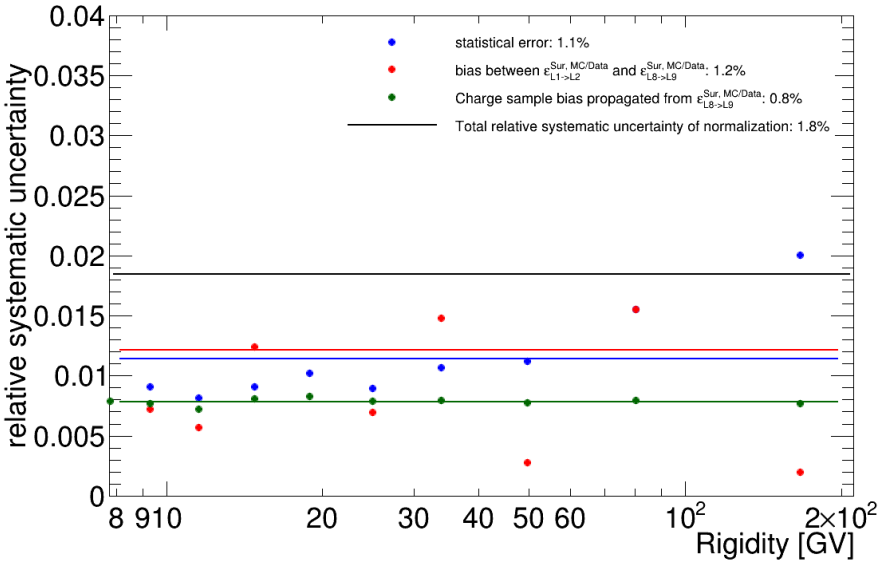

Figure 3-77: Total systematic uncertainties of the normalization of $\varepsilon^{\mathrm{Sur,MC/data}}_{\rightarrow \mathrm{L8}}$ (black solid line), which is the quadratic sum of the constant fitted value of its breakdowns: 1) statistical error (blue), 2) bias between the results re-scaled from $\varepsilon^{\mathrm{Sur,MC/data}}_{\mathrm{L1}\rightarrow\mathrm{L2}}$ and $\varepsilon^{\mathrm{Sur,MC/data}}_{\mathrm{L8}\rightarrow\mathrm{L9}}$ (red), 3) charge efficiency sample bias propagated from $\varepsilon^{\mathrm{Sur,MC/data}}_{\mathrm{L8}\rightarrow\mathrm{L9}}$ (green). Solid lines are the constant fits for breakdowns respectively.

Systematic uncertainty on the rigidity dependence at low rigidity

As the data and MC sample used to estimate the $\varepsilon^{\mathrm{Sur}}_{\mathrm{L1}\rightarrow\mathrm{L2}}$ are not representative at low rigidity (see discussion in Section 3.5.1), the large difference between the data and MC at low rigidity doesn't reflect the real bias. On the other hand, the MC-to-data ratio of $\varepsilon^{\mathrm{Sur}}_{\mathrm{L8}\rightarrow\mathrm{L9}}$ shows a small rigidity dependence at rigidity below 10 GV. This dependence is taken as the uncertainty of the survival probability on the rigidity dependence due to the rigidity dependence of the simulated inelastic cross sections. It's estimated from fitting the $\varepsilon^{\mathrm{Sur,MC/data}}_{\mathrm{L8}\rightarrow\mathrm{L9}}$ to a spline function at low rigidity (Fig. 3-78).

The same as the re-scaling of the MC-to-data ratio of the survival probability, the relative rigidity dependence, $\varepsilon^{\mathrm{Sur,MC/data}}_{\mathrm{L8}\rightarrow\mathrm{L9}}(R)/\varepsilon^{\mathrm{Sur,MC/data}}_{\mathrm{L8}\rightarrow\mathrm{L9}}(10GV)$, can be re-scaled to the relative rigidity dependence of $\varepsilon^{\mathrm{Sur,MC/data}}_{\rightarrow\mathrm{L8}}$ and $\varepsilon^{\mathrm{Sur,MC/data}}_{\mathrm{L1}\rightarrow\mathrm{L2}}$ at low rigidity. The relative deviations from the MC-to-data ratio at ∼10 GV for all three survival probabilities are shown in Fig. 3-79. Those deviation at low rigidity of the survival probability MC-to-data ratios from the value at ∼10 GV are considered as a rigidity-dependent systematic uncertainty and are added in quadrature to the total systematic uncertainty.

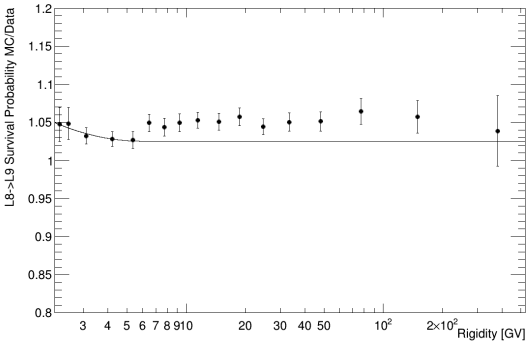

Figure 3-78: The MC-to-Data ratio of $\varepsilon^{Sur}_{L8\to L9}$ (black full circle) together with the spline fit at low rigidity (black solid line).

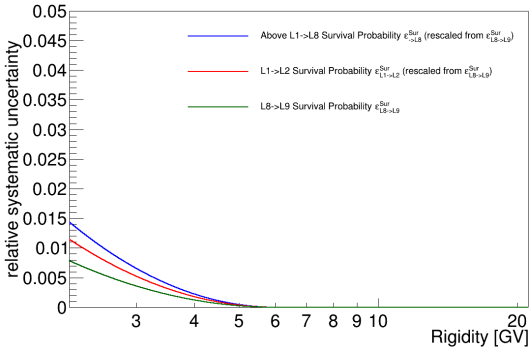

Figure 3-79: The relative deviation from constant at low rigidity for the MC-to-Data ratio of 1) $\varepsilon^{Sur}_{\to L8}$ (re-scaled from $\varepsilon^{Sur,MC/Data}_{L8\to L9}$, blue solid line), 2) $\varepsilon^{Sur}_{L1\to L2}$ (re-scaled from $\varepsilon^{Sur,MC/Data}_{L8\to L9}$, red solid line) and 3) $\varepsilon^{Sur}_{L8\to L9}$ (green solid line).

Systematic uncertainty on the rigidity dependence at high rigidity

Due to the limited statistics, survival probabilities between Tracker L1→L2 and L8→L9, especially for data, can only be estimated up to ∼100 GV, hence the rigidity dependence of the MC-to-data ratio of the survival probabilities cannot be estimated. Instead, the rigidity dependence of the survival probability from MC simulation, reflecting the rigidity dependence of the inelastic cross sections used in MC, is accounted as the systematic uncertainty at high rigidity.

Using the MC truth information, the survival probabilities as function of generated rigidity can be obtained and fitted with a spline fit above 100 GV, as shown in Fig. 3-80 . The relative deviation from a constant of the survival probabilities above 200 GV (Fig. 3-81) is accounted as a systematic uncertainty and is added in quadrature to the total systematic uncertainty.

Total systematic uncertainty of flux normalization correction

The total systematic uncertainty of the flux normalization correction (the Above Tracker L1 to L8 MC-to-Data ratio, $\varepsilon^{Sur,MC/Data}_{\to L8}$), is obtained from the quadratic sum of the systematic uncertainties from the rigidity-independent normalization and from the rigidity dependence at low and high rigidity (Fig. 3-82). The systematic uncertainty is dominated

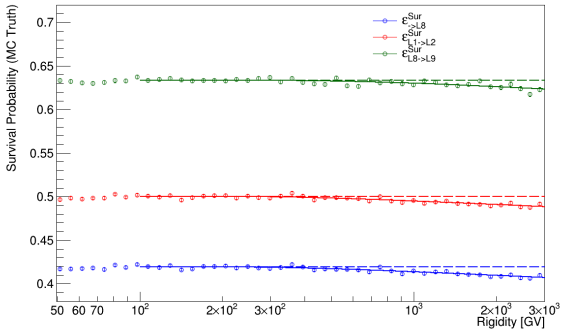

Figure 3-80: Silicon survival probability from MC using MC truth for 1) $\varepsilon^{Sur}_{\rightarrow L8}$ (blue solid line), 2) $\varepsilon^{Sur}_{L1\rightarrow L2}$ (red solid line) and 3) $\varepsilon^{Sur}_{L8\rightarrow L9}$ (green solid line). The solid lines are the spline fits above 100 GV and the dash lines indicate the constant values from the fit result at 200 GV respectively.

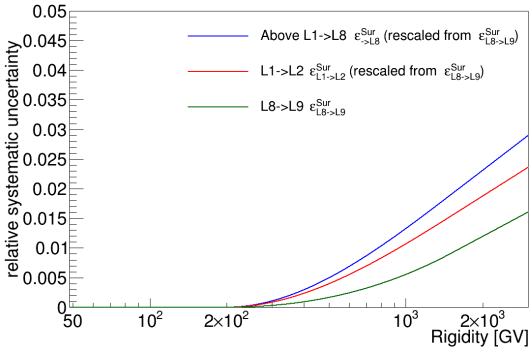

Figure 3-81: The high rigidity relative deviation of 1) $\varepsilon^{Sur}_{\rightarrow L8}$ (blue solid line), 2) $\varepsilon^{Sur}_{L1\rightarrow L2}$ (red solid line) and 3) $\varepsilon^{Sur}_{L8\rightarrow L9}$ (green solid line).

by the 2% systematic uncertainty from the normalization in the entire rigidity range. Below 5 GV and above 200 GV, the systematic uncertainty goes up by 1-2% due to the contribution from the uncertainty of the rigidity dependence of the inelastic cross section at low and high rigidity.

3.6.2 Background estimation

3.6.2.1 Below Tracker L1

The background from heavier nuclei fragmenting below the Tracker L1, i.e. mostly interacting with the TRD and upper TOF, is studied by the Tracker L1 charge template fit with charge template obtained from the Tracker L2 charge distribution (see Section 3.2.2.1). The systematic uncertainty for this background is then resulting from the potential difference between the Tracker L1 and L2 charge distributions. Besides charge templates from the Tracker L2 charge distribution, templates built from the Tracker L1 charge distribution of a sample of unfragmented nuclei are built and used for the Tracker L1 charge template fit. The difference between the estimated background using these two different sets of charge templates is then taken as the systematic uncertainty of the below Tracker L1 background due to the uncertainty of the charge template.

To select unfragmented nuclei samples, incoming particles are required to have charge

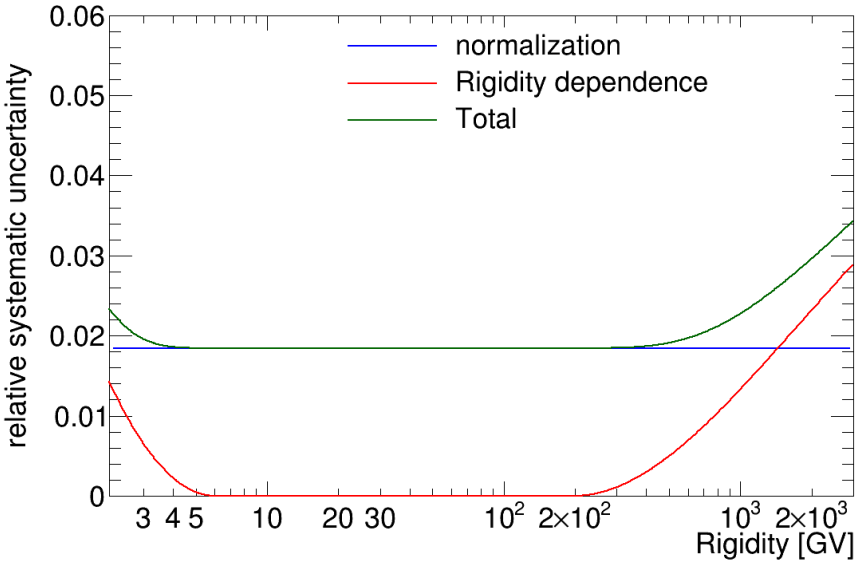

Figure 3-82: Total systematic uncertainties of $\varepsilon^{Sur,MC/Data}_{\rightarrow L8}$ (green solid line), which is the quadratic sum of its breakdowns: 1) systematic uncertainty of its normalization (blue solid line), 2) systematic uncertainty of its rigidity dependence at low and high rigidity (red solid line).

measured by two layers of the upper TOF and Inner Tracker compatible with Silicon nuclei, i.e. charge measured by these sub-detectors to be both within [13.5,14.5]. Furthermore, selections on the secondary Tracker track (2nd track), i.e. reconstructed Tracker track besides the one with maximum energy, can further clean up the sample from events containing fragmented particles. For events with fragmented particles, more than one nucleus or protons, i.e. the fragmentation products, traverse the Inner Tracker resulting more than one reconstructed Tracker track with the same rigidity sign. On the contrary, events for which no fragmentation occurs, contain only one reconstructed track or another track from delta ray with low energy and/or opposite sign of the rigidity. Therefore, events without fragmentation can be selected by the following cuts:

1. only one Tracker track;
2. in case a 2nd track is reconstructed in the Tracker, it should not pass the reconstruction quality cut requiring at least three X-side and five Y-side hits in the Inner Tracker, since it's likely to be a delta ray emitted from the incoming particle;
3. in case a 2nd track is reconstructed in the Tracker, the 2nd track and the main track are required to have opposite bending direction, since in this case the 2nd track is

again mostly likely produced by a delta ray instead of being a fragmentation product;

4. in case a 2nd track is reconstructed in the Tracker, its rigidity is required to be low, since this is compatible with a delta ray rather than a fragmentation product.

Comparisons between the Tracker L1 charge distribution from samples selected requiring that the charge measured by the upper TOF layers and by the Inner Tracker is within [13.5,14.5] and applying different 2nd Tracker track selection are shown in Fig. 3-83.

It shows that the selection cuts 1) and 2) are most effective in removing the fragmented events from nuclei heavier than Silicon.

Charge templates are then built from the Tracker L1 charge distribution of samples passing either selection cut 1) or 2). The difference between the estimations of the below Tracker L1 background obtained using the Tracker L1 and L2 charge templates (Fig. 3-84) is small, so that its contribution to the total systematic uncertainty of the flux is negligible.

3.6.2.2 Above Tracker L1

The Top-Of-the-Instrument correction is the product of the acceptance ratios and flux ratios, which introduces two systematic uncertainties independently.

The potential inaccuracy in the Monte Carlo description of the partial cross sections will change the normalization of the acceptance ratios. Such inaccuracy has already been estimated as the MC-to-data ratio of the breaking-up probability (Section 3.5.1.2) and biases of 10-20% have been observed for the even charge to even charge channel. Such biases contribute to the systematic uncertainty of the Top-Of-the-Instrument correction for the same amount, i.e. 10-20%. Since the correction for Silicon nuclei produced by fragmentation of heavier nuclei is negligible ($< 0.5\%$ over the entire rigidity range), such systematic uncertainty is also negligible.

The uncertainty of the flux ratio (arising from statistical error, which is 100% uncorrelated between the heavier nuclei and the Silicon nuclei, as well as systematic uncertainties) also contributes to the uncertainty into the Top-Of-the-Instrument correction and hence to the final flux. However, this contribution is even smaller than that coming from the bias on the breaking-up probability, so that its contribution can be neglected.

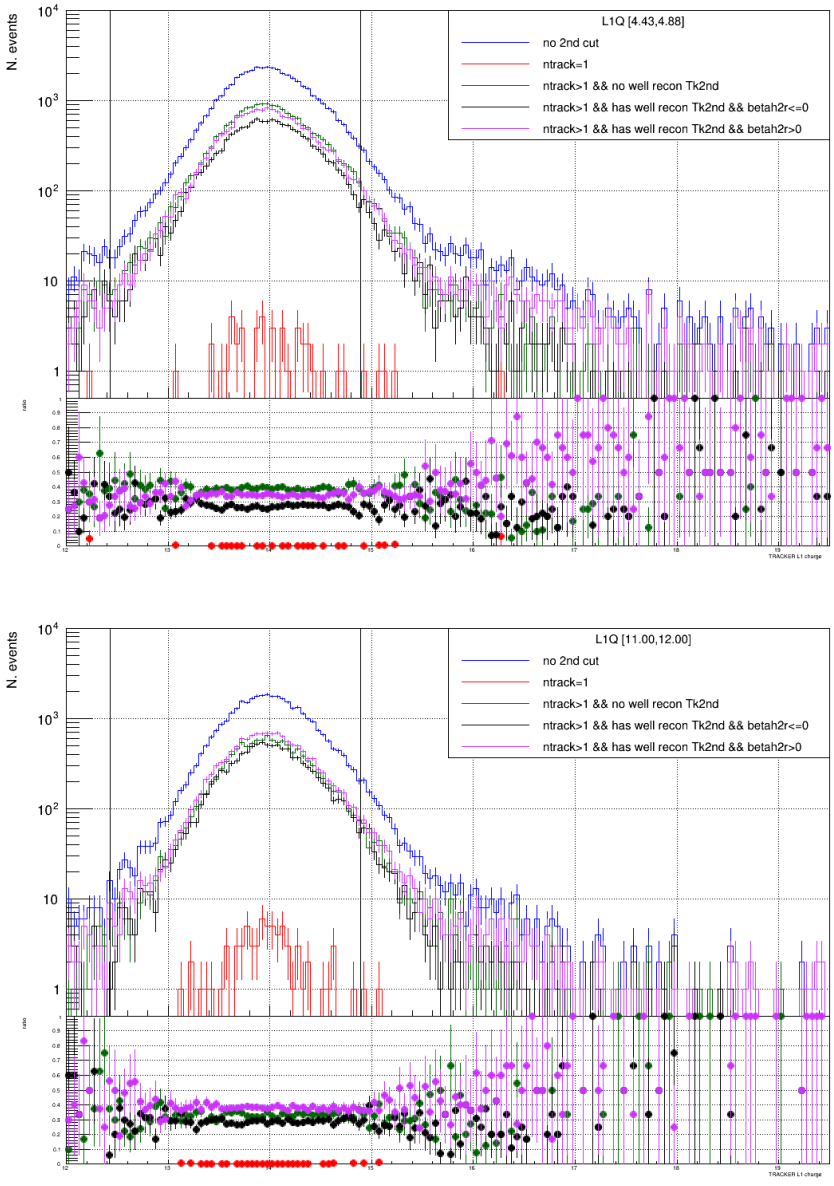

Figure 3-83: Tracker L1 charge sample requiring two layers of Upper TOF and Inner Tracker charge to be within [13.5,14.5] and 1) not applying any 2nd track cut (blue), 2) only one Tracker track (red), 3) a 2nd track is reconstructed in the Tracker, the 2nd track not pass the reconstruction quality cut (green), 4) a 2nd track is reconstructed in the Tracker and it passed the reconstruction quality cut, the 2nd track and the main track have opposite bending direction (black), and 5) a 2nd track is reconstructed in the Tracker and it passed the reconstruction quality cut, the 2nd track and the main track have same bending direction (magenta). The bottom panel shows the ratio between charge distributions with 2nd track cut over the one without any 2nd track cut (blue). The top and bottom plots show the charge distribution in rigidity bins [4.43,4.88] GV and [11.0,12.0] GV respectively.

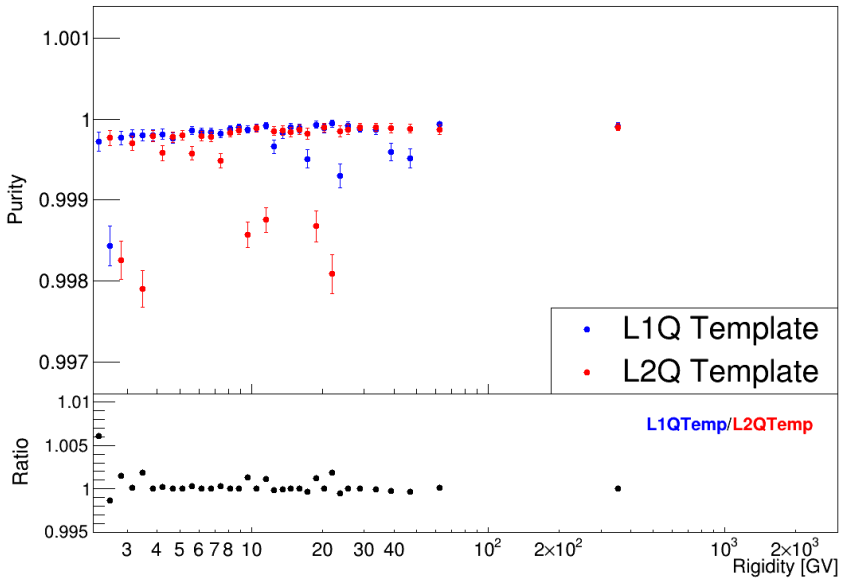

Figure 3-84: Purity of Silicon within the L1 charge selection region in different rigidity bin obtained using 1) L1 charge template (blue) and 2) L2 charge template (red). Bottom panel shows the ratio of two purity.

3.6.3 Unfolding

The systematic uncertainties from the forward unfolding method come from:

- dependence of the minimization result on the node positions of the spline fit to the flux model;
- uncertainty on the description of the rigidity resolution function;
- uncertainty of the final minimization results due to limited statistics.

3.6.3.1 Node position of the spline fit to the flux model

The node positions of the spline fit to the flux model influence the final flux model obtained from the minimization. This contribution to the systematic uncertainty has been estimated performing the minimization using different sets of node positions. The node positions have been varied as follows:

- shifting all the node positions at the same time by 5 to 20%;
- shifting each node position individually by 5 to 20%;
- fix one node position and shifting all the other node positions by 5 to 20%;
- removing one of the nodes and keep all the others.

The flux model which gives minimum χ^2 among all these sets of node positions is chosen, while the rest of the results having a valid minimum after the minimization, are used to define the systematic uncertainty. Flux models and the corresponding spectral indices from all sets of node positions are shown in Fig. 3-85. The relative difference of the unfolding factors from these flux models to the one with minimum χ^2 in the L1Inner and FullSpan geometries are shown in Fig. 3-86. The resulting systematic uncertainty band is computed such that the relative differences of 68% of the unfolding factors in each rigidity bin is lower than or equal to the band value.

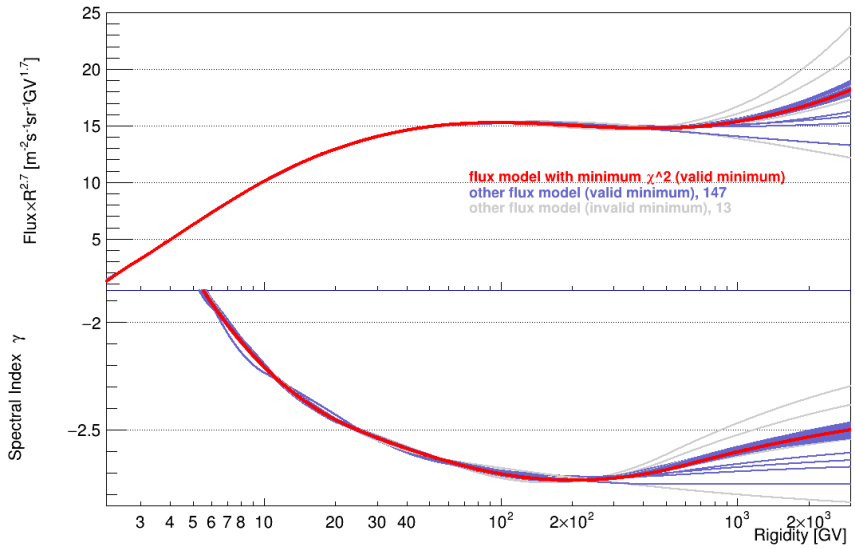

Figure 3-85: Final flux models (top panel) and spectral indices (bottom panel) after the minimization procedure obtained from different sets of the spline fit node positions for the Silicon nuclei. The red line is the result which has the global minimum χ^2, the blue lines are the results with valid minimum and the gray lines are the results with invalid minimum.

3.6.3.2 Rigidity Resolution Function

The systematic uncertainty due to the uncertainty on describing the rigidity resolution function is studied by repeating the unfolding procedure varying the width of the core Gaussian (σ) by 5% and independently the non-Gaussian tail by 10%. Fig. 3-87 shows the ratio of the unfolding factors obtained with these different sets of rigidity resolution functions to the one obtained from the original resolution function for the Silicon nuclei

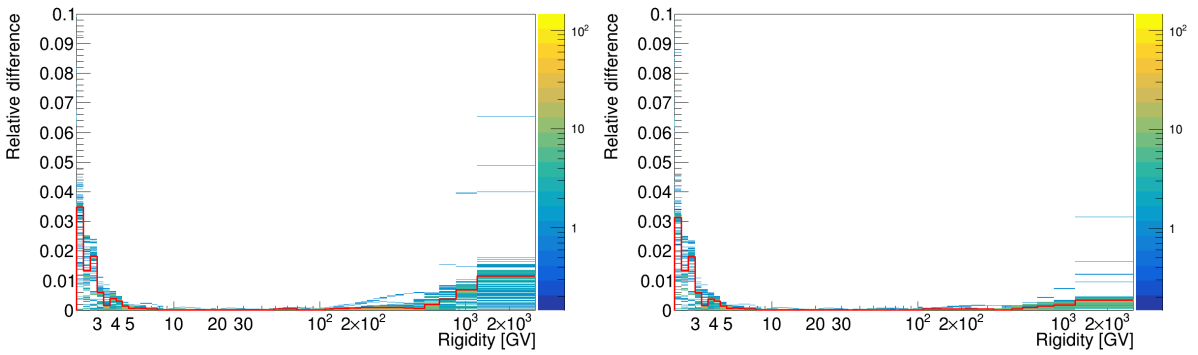

Figure 3-86: Relative differences between the unfolding factors obtained from different node positions of the spline fit to the flux model, and the global minimum results for the Silicon nuclei in the L1Inner (left) and the FullSpan (right) geometries. The systematic uncertainty band (solid red line) is set such that 68% of the results have relative difference smaller than or equal to the band value in each rigidity bin.

in the L1Inner and FullSpan geometries. The systematic uncertainty is obtained as the quadrature of the relative differences of the unfolding factors obtained varying the width of the core Gaussian by 5% and the non-Gaussian tail by 10%.

3.6.3.3 Uncertainty due to limited statistic

The final flux model resulting from the minimization procedure has fitting errors on the parameters (the y node positions) due to limited statistics of event counts, which introduce uncertainty into the unfolding factors and hence the final flux. The final flux model together with its uncertainty is shown in Fig. 3-88. The corresponding uncertainty on the unfolding factor is estimated computing the unfolding factor from the flux model inclusive of its uncertainty. The difference between the two unfolding factors is accounted as the systematic uncertainty. The unfolding factor from the final flux model and its uncertainty deriving from limited statistics are shown in Fig. 3-89.

3.6.3.4 Total systematic uncertainty from the unfolding procedure

The total systematic uncertainty from the unfolding procedure for Silicon nuclei, obtained as the quadratic sum of systematic uncertainties from all the three sources, is shown in Fig. 3-90 in the L1Inner and FullSpan geometries. Its contribution to the total systematic uncertainty of the Silicon nuclei flux is $\sim 4\%$ at 2 GV, negligible up 100 GV, and raises

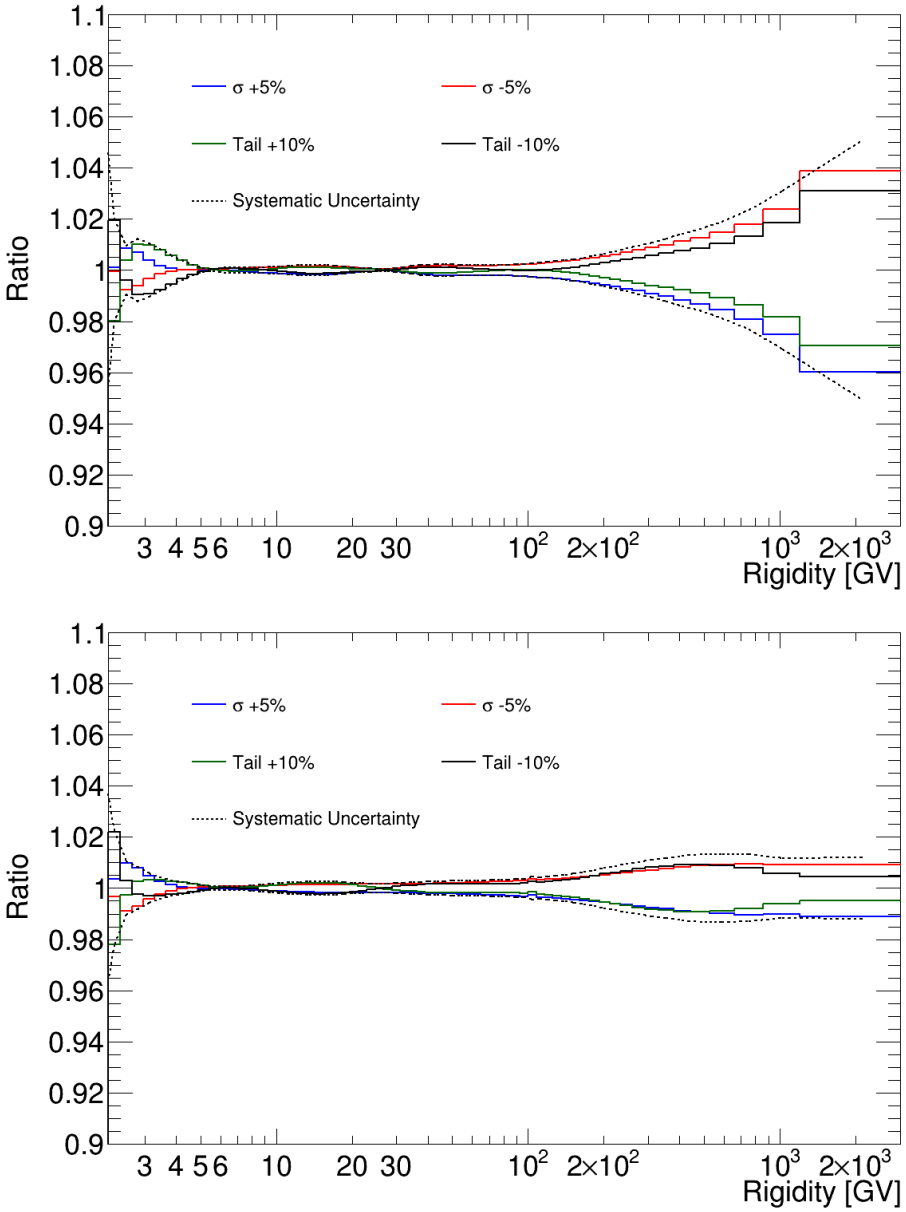

Figure 3-87: Ratios of the unfolding factors obtained from different sets of rigidity resolution functions to those resulting from the original resolution function for the Silicon nuclei, in the L1Inner (top) and FullSpan (bottom) geometries.

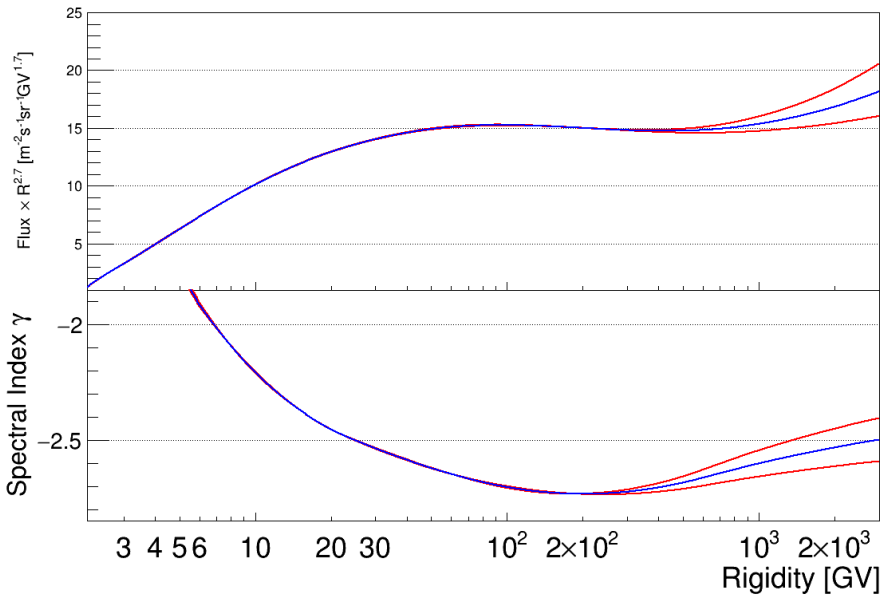

Figure 3-88: Final flux model (blue, top panel) and spectrum index (blue, bottom panel) for Silicon nuclei together with the uncertainty band on the flux model due to limited statistics of event counts (red).

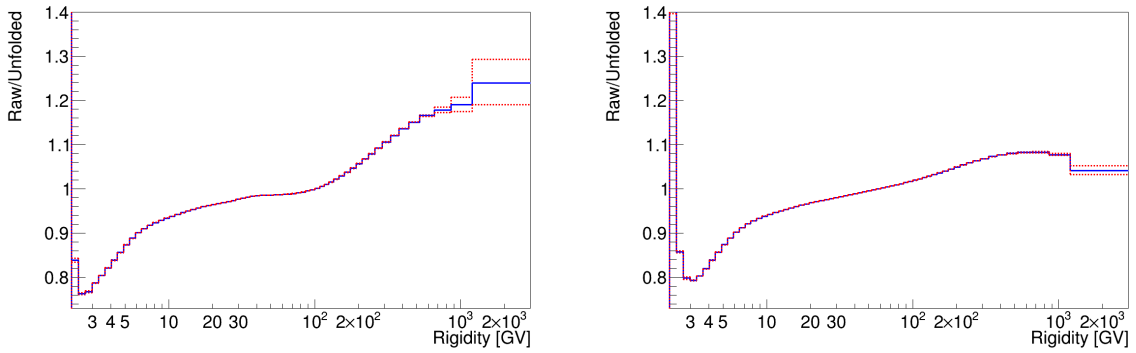

Figure 3-89: Unfolding factors calculated from the final flux model (blue) and those from the flux model inclusive of the error from the minimization procedure (red) for the Silicon nuclei in the L1Inner (left) and the FullSpan (right) geometries.

up to 3% in the L1Inner geometry at 1.2 TV and $< 2.5\%$ in the FullSpan geometry at 3 TV.

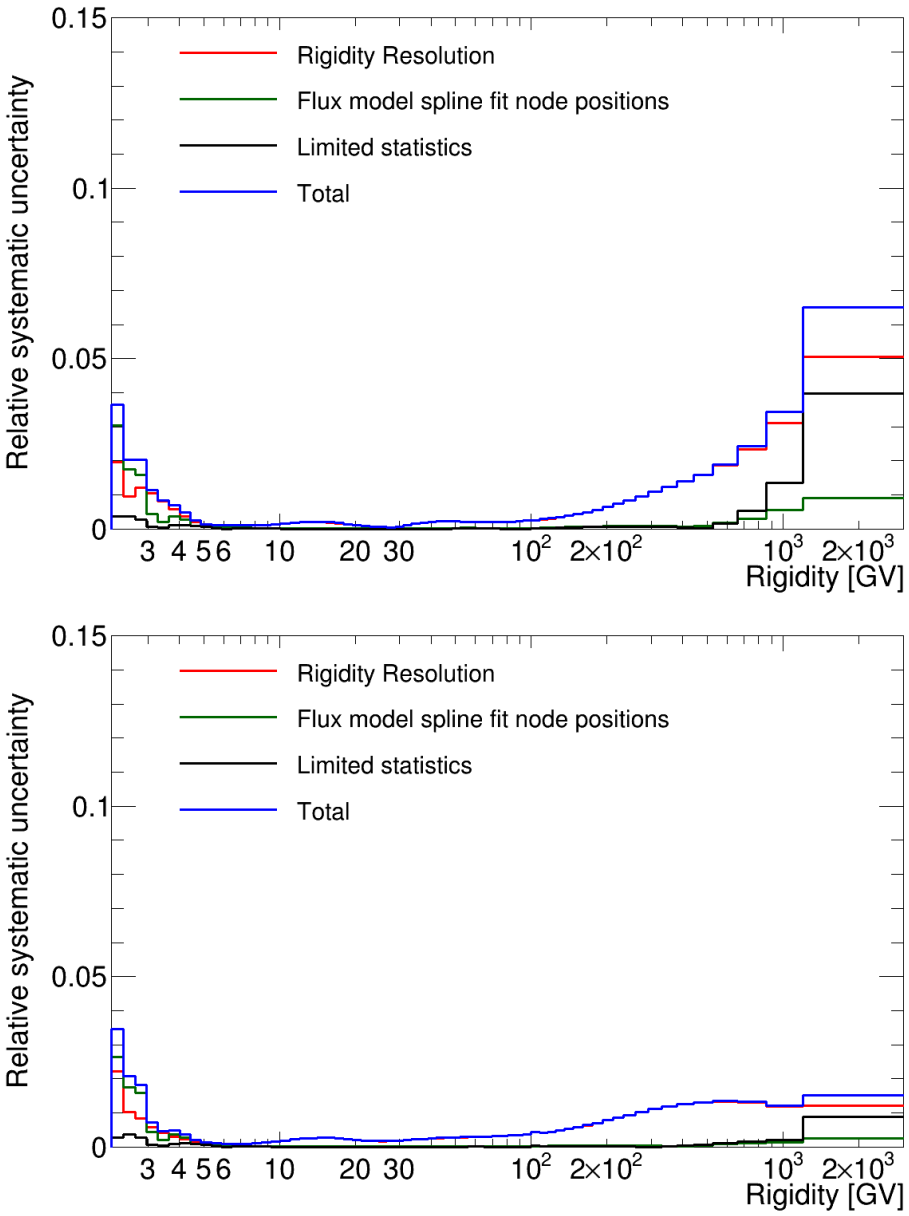

Figure 3-90: Total systematic uncertainties from the unfolding procedure (blue) together with its breakdown for the Silicon nuclei in L1Inner (left) and the FullSpan (right) geometries.

3.6.4 Absolute rigidity scale

There are two sources which potentially shift the absolute rigidity scale, the Tracker misalignment and the uncertainty in the magnetic field mapping.

Tracker misalignment arise from small mechanical shifts of the supporting structure which may have occurred during the launch, or can currently occur because of temperature variations given the ISS orbit configuration with respect to the sun (Section 2.1). The absolute rigidity scale shift due to the tracker misalignment is studied using the ISS positron and electron data. Combining the energy measured by ECAL for $e^{\pm}$, the absolute rigidity scale for Tracker can be calibrated using the fact that $e^{\pm}$ tracks have different bending directions inside the magnetic field, hence the shift of the absolute rigidity scale has an opposite effect on the measured rigidity for $e^{\pm}$ respectively [115]. After correction of the main shift, the remaining uncertainty, $1/30$ TV^{-1} is accounted as a source of flux systematic uncertainty.

The uncertainty on the magnetic field mapping of the AMS-02 permanent magnet performed before launch is 0.25%. An additional 0.1% comes from on-orbit temperature corrections. They add up to a total of 0.27% uncertainty on the absolute rigidity scale, i.e. $R \cdot (1 \pm 0.27\%)$.

The shift of the absolute rigidity scale introduces bias on the mean of the rigidity resolution while keeping its shape unchanged. To study its influence on the final flux, a set of unfolding have been performed using rigidity resolution functions with shifted mean. Namely, to study the impact of:

- tracker misalignment: the mean is shifted by $\pm 30^{-1}$ TV^{-1} $= 0.33 \times 10^{-4}$ GV^{-1};
- magnetic field mapping uncertainty: the mean is shifted by $\frac{1}{R_t(1\pm 0.27\%)} - \frac{1}{R_t} \approx \mp 0.27\%/R_t$.

The ratios between the resulting unfolding factors to the one without variation for the Silicon nuclei are shown in Fig. 3-91 in the L1Inner and FullSpan geometries. The relative difference of the unfolding factors from the Tracker misalignment and the Magnetic field mapping uncertainty are added in quadrature as the total systematic uncertainty due to the absolute rigidity scale uncertainty.

3.6.5 Geomagnetic cutoff safety factor

A safety factor of 1.2 is applied on the maximum geomagnetic cutoff in order to make sure that only nuclei coming from outside the geomagnetic field are selected for the flux

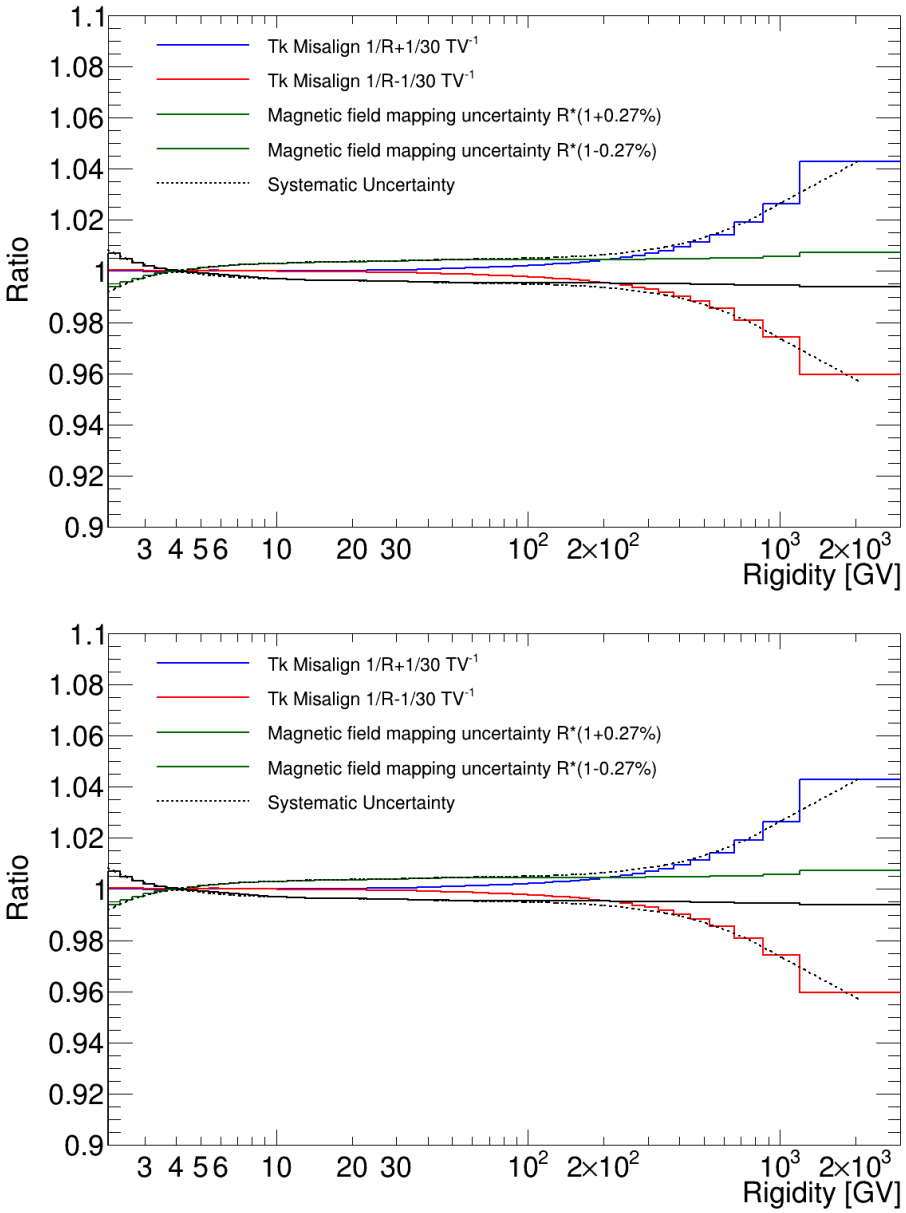

Figure 3-91: Ratios of the unfolding factors obtained shifting the absolute rigidity scale, the Tracker misalignment (blue: $+1/30$ TV^{-1}, red: $-1/30$ TV^{-1}) and the magnetic field mapping uncertainty (green: $+0.27\%$, black: -0.27%), to that with no shift, for the Silicon nuclei in the L1Inner (top) and FullSpan (bottom) geometries. The dotted lines represent the total contribution of the absolute rigidity scale uncertainty to the systematic uncertainty band of the flux.

study. To examine the influence of the choice of the safety factor (potentially changes of the trapped particle portion in the selected data samples) on the final flux, new fluxes are obtained varying the safety factors from 1.0 to 1.4. Exposure time and event counts, and hence the event rats, are recalculated accordingly Figs. 3-92–3-94. Efficiencies and efficiency ratios are also recalculated, since the data efficiency samples are selected applying the geomagnetic cutoff. Each of these new fluxes is then unfolded independently.

The resulting ratios of the exposure times (Fig. 3-92) and event counts (Fig. 3-93) are similar and cancel out each other when calculating the event rates, which are then compatible to 1 within the statistical error (Fig. 3-94). Also, the ratios of raw fluxes (Fig. 3-95) are similar to the ratios of event rates, indicating that the safety factor has no big effect on the efficiency ratios as well. In conclusion, the possible mixture of trapped particle into the selected event samples due to the choice of the geomagnetic safety factor has negligible effect on the final flux.

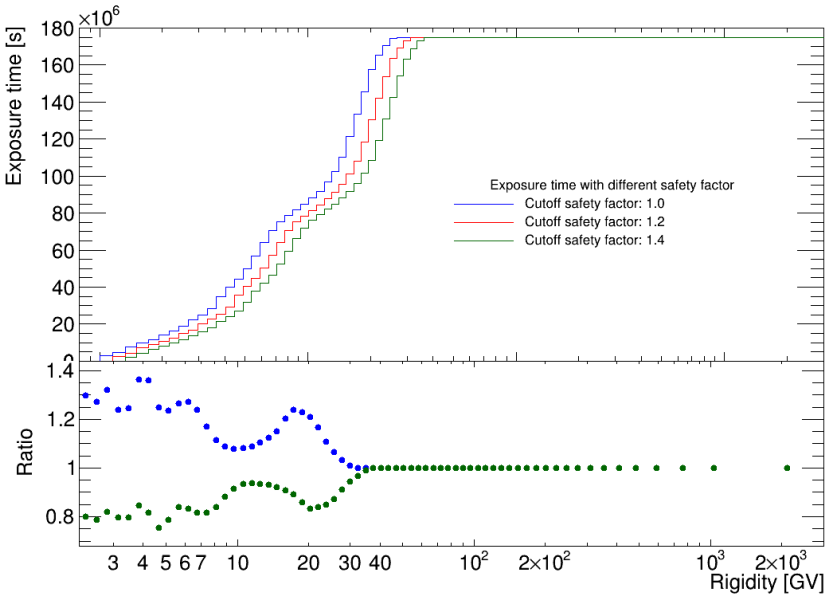

Figure 3-92: The exposure time for different value of the maximum geomagnetic cutoff safety factor: 1.0 (blue), 1.2 (the nominal value, red) and 1.4 (green). The bottom panel shows the ratio of the results with safety factor values 1.0 (blue) and 1.4 (green) to that from the nominal safety factor value of 1.2.

3.6.6 Total systematic uncertainty

The total systematic uncertainties for the Silicon nuclei in the L1Inner and FullSpan ge-

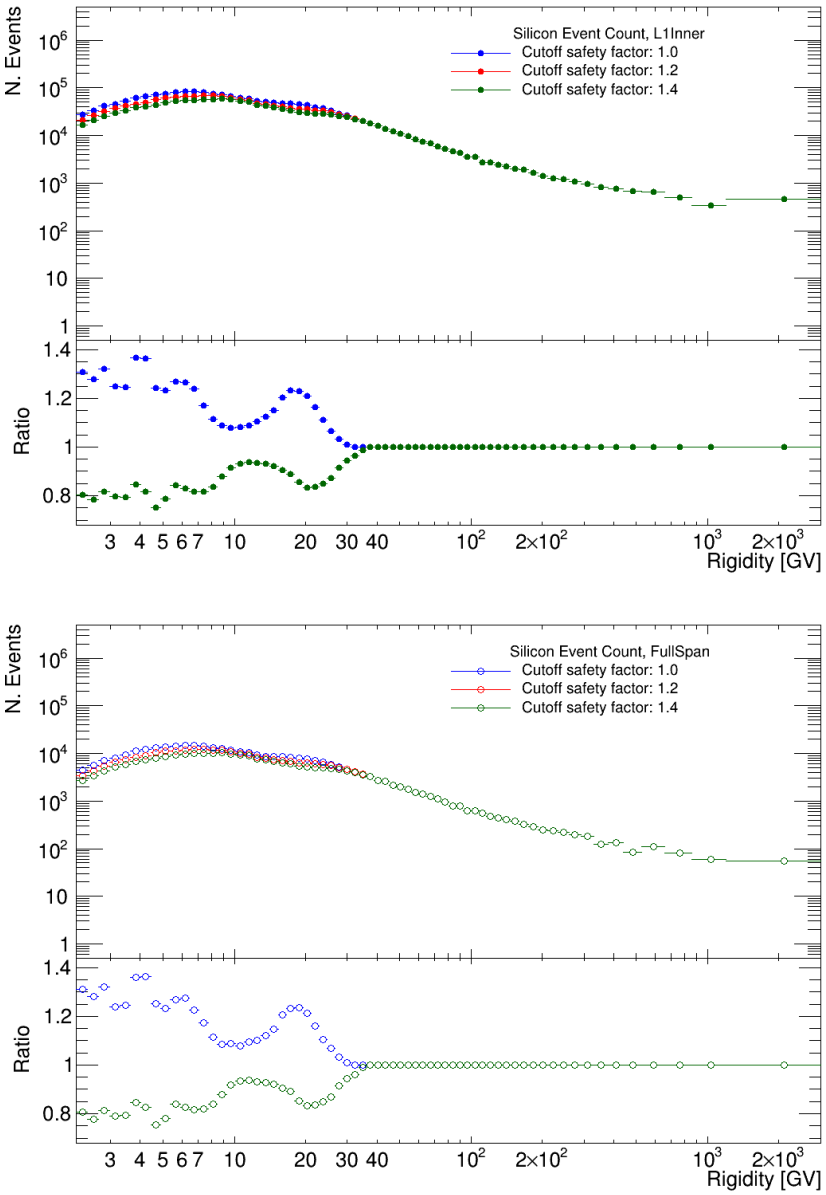

Figure 3-93: The Silicon nuclei event counts for different values of the maximum geomagnetic cutoff safety factor: 1.0 (blue), 1.2 (the nominal value, red) and 1.4 (green) for L1Inner (left) and the FullSpan (right) geometries. The bottom panel shows the ratio of the results obtained from safety factor values 1.0 (blue) and 1.4 (green) over the nominal safety factor value of 1.2.

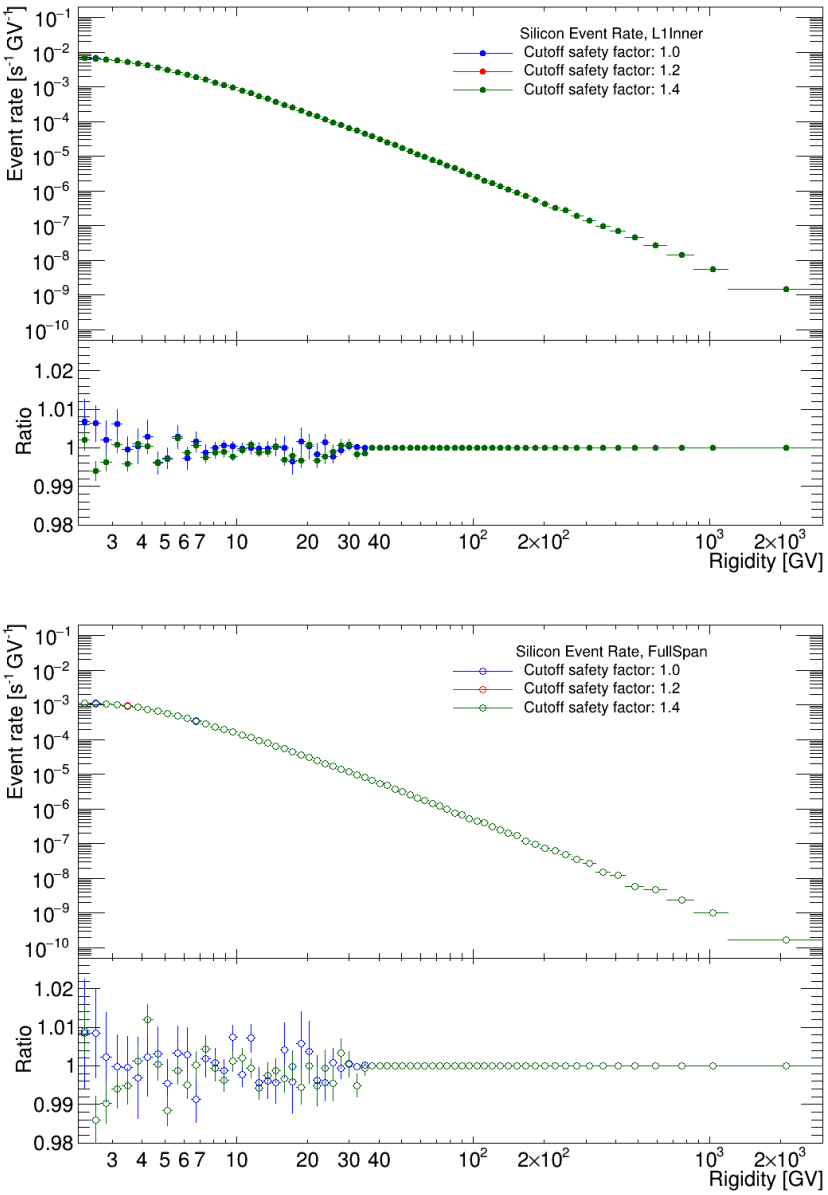

Figure 3-94: The Silicon nuclei event rates for different value of the maximum geomagnetic cutoff safety factor: 1.0 (blue), 1.2 (the nominal value, red) and 1.4 (green) in the L1Inner (left) and the FullSpan (right) geometries. The bottom panel shows the ratio of the results obtained from safety factor values 1.0 (blue) and 1.4 (green) over the nominal safety factor value of 1.2.

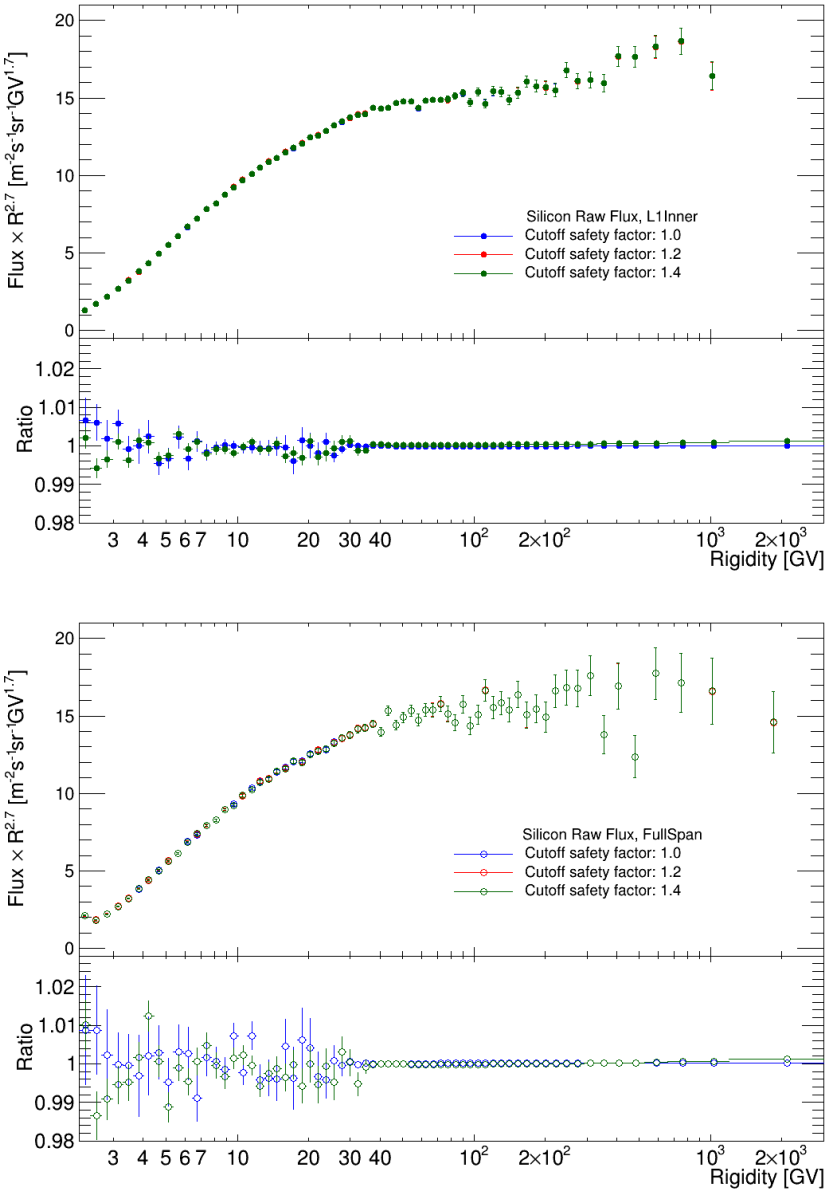

Figure 3-95: The Silicon nuclei raw fluxes obtained using different values of the maximum geomagnetic cutoff safety factor: 1.0 (blue), 1.2 (the nominal value, red) and 1.4 (green) in the L1Inner (left) and the FullSpan (right) geometries. The bottom panel shows the ratio of the results obtained from safety factor values 1.0 (blue) and 1.4 (green) over the nominal safety factor value of 1.2.

ometries are obtained adding in quadrature of all the contributions from sources discussed above, and they are shown in Fig. 3-96. The total systematic uncertainty is below 3% from 5 to 100 GV, and raise up to $\sim$ 5% at 3 TV in the FullSpan geometry. At rigidity below 100 GV, the systematic uncertainty is dominated by the one from the acceptance, namely the systematic uncertainty of the normalization of the effective acceptance due to uncertainty on the normalization of the nuclei interaction inside the AMS-02 detector. While at higher rigidity the systematic uncertainty is dominated by those from the unfolding procedure and due to the uncertainty on the absolute rigidity scale.

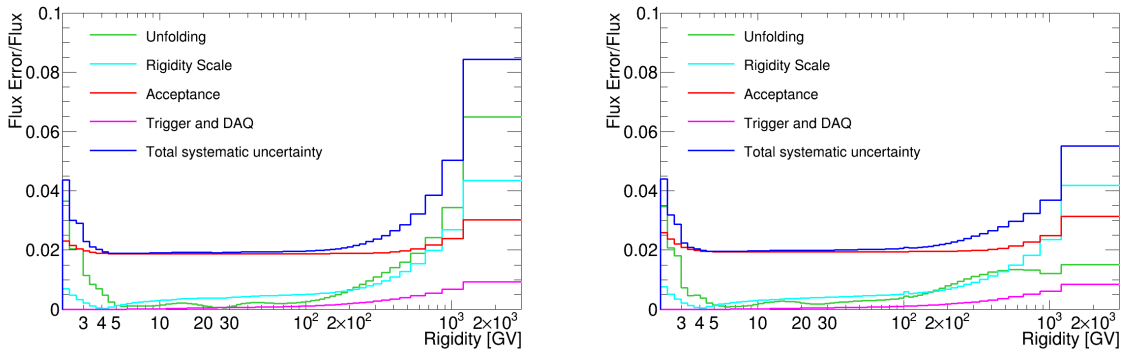

Figure 3-96: The total systematic uncertainties of the Silicon nuclei fluxes (blue) in the L1Inner (left) and the FullSpan (right) geometries. The contributions from unfolding, rigidity scale, acceptance estimation, and Trigger and DAQ efficiencies are shown as the green, cyan, red and magenta lines respectively.

3.7 Final Silicon Flux

As discussed before, the L1Inner result is only valid up to $\sim$1.3 TV (the MDR of the L1Inner geometry), so above that rigidity the FullSpan result is used. Due to $\sim$5 times larger acceptance (Fig. 3-15), the L1Inner data sample has more statistics than the FullSpan, hence below 1.3 TV the L1Inner result is used since the statistical error is smaller.

The breakdown of the statistical and systematic uncertainties for the final combined flux is shown as Fig. 3-97.

The Silicon nuclei flux obtained combining the results from the L1Inner and FullSpan geometries, as explained above, after the total flux normalization correction accounting

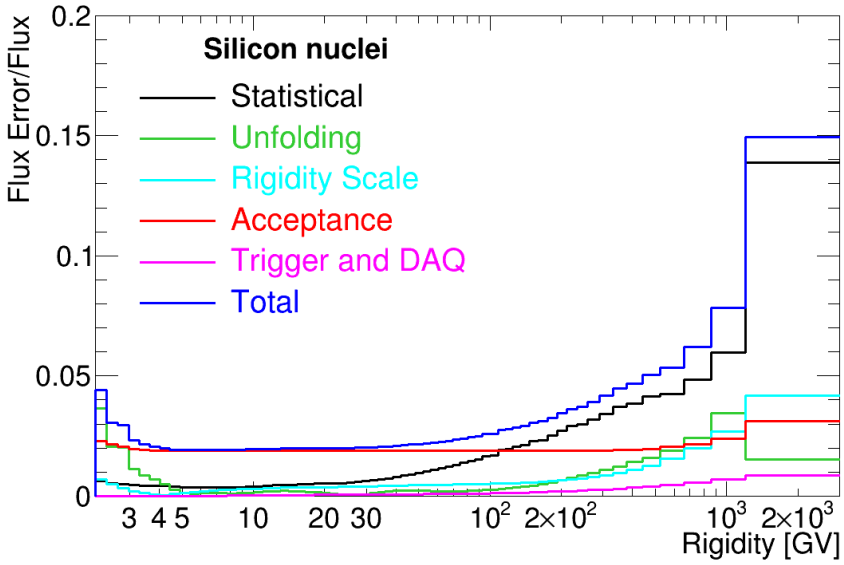

Figure 3-97: Total flux error (statistical error and systematic uncertainties) and its break down for the Silicon nuclei flux as function of the true rigidity.

for the difference of the nuclei interaction inside the AMS-02 detector between data and MC simulation (Section 3.5) multiplied by $R^{2.7}$ is shown in Fig. 3-98. The spectral index, defined as:

$$\gamma = \frac{d(log(\Phi)}{d(logR)} \tag{3.35}$$

is obtained by performing single power law fits on non-overlapping rigidity intervals bounded by 7.09, 12.0, 16.6, 28.8, 45.1, 86.5, 192.0, 441.0 and 3000.0 GV. The data points of the flux and the spectral index are placed along the abscissa calculated for a flux $\propto R^{-2.7}$ [116].

As seen from Fig. 3-98, the Silicon nuclei flux deviates from a single power law. At rigidity above 200 GV, a spectrum break, similar as those observed in the lighter primary and secondary cosmic ray nuclei fluxes from proton up to Oxygen, also exists in the Silicon nuclei flux.

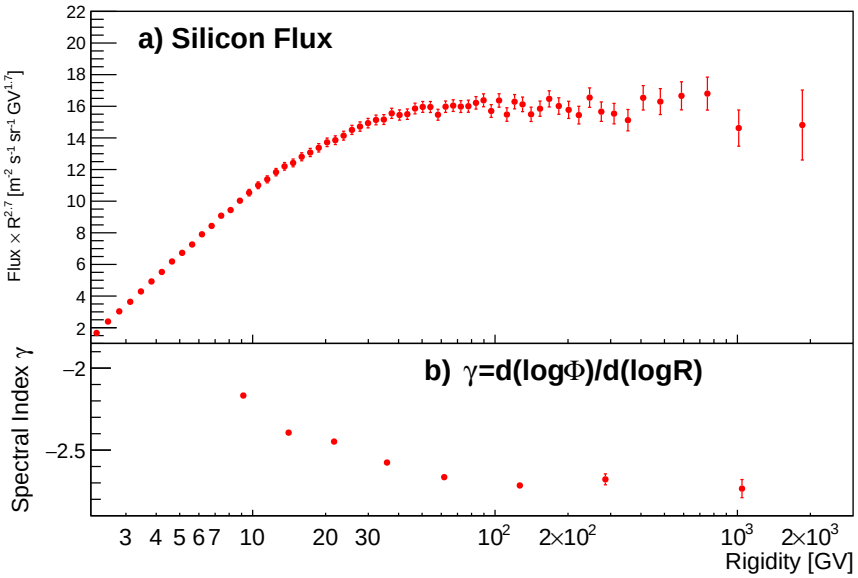

Figure 3-98: a) The final Silicon nuclei flux at the top of the AMS-02 detector multiplied by $R^{2.7}$ as a function of the true rigidity. The points below 1.2 TV are those measured from the L1Inner data sample, while the point above 1 TV corresponding to the rigidity bin $[1200, 3000]$ GV, is measured from the FullSpan data sample. The error bars correspond to the quadratic sum of the statistical error and the total systematic uncertainty; b) The spectral index of the Silicon nuclei flux as function of the true rigidity obtained from fitting the flux to a single power law in non-overlapping rigidity intervals.

3.8 Comparison to previous experiments

The cosmic-ray Silicon nuclei fluxes have been measured in different ranges of kinetic energy per nucleon: below a few GeV by CRIS [117] and ALICE[74]; in the GeV-TeV ranges by Ichimura93 [75], HEAO-3-C2 [76], ATIC2 [77], CREAM-II [78] and TRACKER [79, 80].

To compare with previous measurements, the Silicon nuclei flux presented in this work has been expressed as function of kinetic energy per nucleon E_k, using the formula:

$$E_k = \frac{\sqrt{Z^2R^2 + M^2} - M}{A}, \tag{3.36}$$

with Z the charge, M the mass and A the atomic mass number. Measurements of the isotopic composition of Silicon nuclei in cosmic rays, currently available only at low energies with E_k/n below a few GeV/n, have shown that the most abundant isotope is ^{28}Si (∼86%), while ^{29}Si and ^{30}Si (about 6% each) [118–123]. Therefore, the rigidity is converted to E_k assuming that the sample is entirely ^{28}Si.

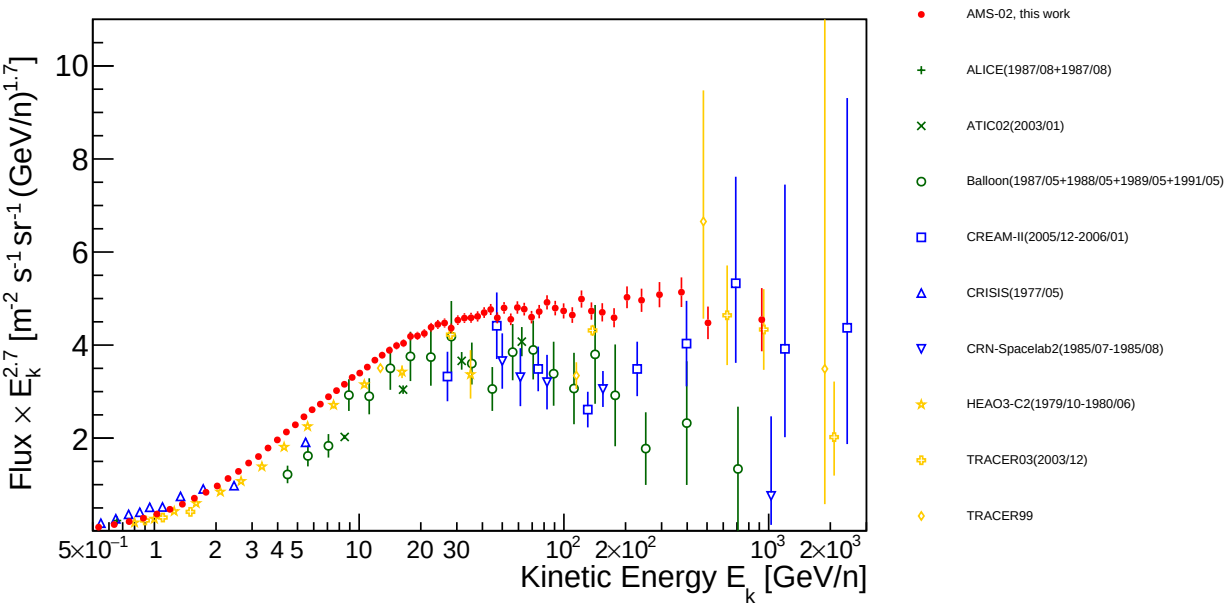

Figure 3-99: The Silicon nuclei flux at the top of the AMS-02 detector (red points) as function of kinetic energy per nucleon E_k multiplied by $E_k^{2.7}$, together with results from previous experiments [124]. For the AMS result, the kinetic energy per nucleon is computed from the rigidity assuming the sample contains only the most abundant isotope observed in Silicon cosmic ray, that is ^{28}Si [118–123].

Chapter 4

Comparison of the Silicon nuclei flux with lighter primary cosmic ray nuclei fluxes

To better understand its rigidity dependence, the Silicon nuclei flux is compared to two lighter primary cosmic ray nuclei fluxes: 1) Oxygen, which is around five times more abundant than Silicon, and 2) Neon, which has a similar abundance as Silicon. In this chapter, the flux analysis for Neon and Oxygen nuclei will be presented first, followed by comparisons between the flux of Silicon nuclei to those of Neon and Oxygen.

4.1 The Oxygen and Neon nuclei fluxes

The Oxygen nuclei flux presented in this work is an update to the AMS-02 published result based on the first 5 years data set [2]. The study presented here is based on the same data set used for the Silicon nuclei flux measurement, that is the 7 years data including up-to-date calibrations, as the new Silicon Tracker charge calibration. For both the Oxygen and Neon fluxes, the same binning as that used for the Silicon is used to ease the comparison among the three rigidity spectra.

4.1.1 Event count

The selection cuts for Oxygen and Neon nuclei events are similar as those for Silicon nuclei with optimized charge selection ranges according to different charge resolutions:

- Tracker L1: [6.74,8.74] for Oxygen, and [8.82367,10.6718] for Neon;
- Upper TOF: [7.4,9.5] Oxygen, and [9.3525,11.5] for Neon;
- Inner Tracker: [7.55,8.45] Oxygen, and [9.60744,10.3926] for Neon;
- (FullSpan only) Lower TOF: >7.4 Oxygen, and >9.3525 for Neon;
- (FullSpan only) Tracker L9: [7.5,9.8] Oxygen, and [9.42884,11.1763] for Neon.

During the first 7 years operation, the AMS-02 detector has collected 12.5 million Oxygen nuclei and 1.8 million Neon nuclei events. Figs. 4-1 and 4-2 show the Oxygen and Neon nuclei event count distributions as a function of the reconstructed rigidity. The exposure time for Oxygen and Neon nuclei is the same as that presented for the Silicon nuclei since it does not depend on the particle charge (Section 3.1). The corresponding 7 years event rates for the Oxygen and Neon nuclei are shown in Figs. 4-3 and 4-4.

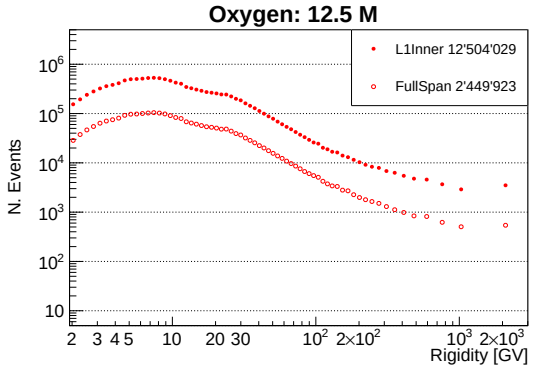

Figure 4-1: The AMS-02 7 years Oxygen nuclei event counts as a function of the reconstructed rigidity for L1Inner (red full circle) and FullSpan (red open circle) geometries respectively.

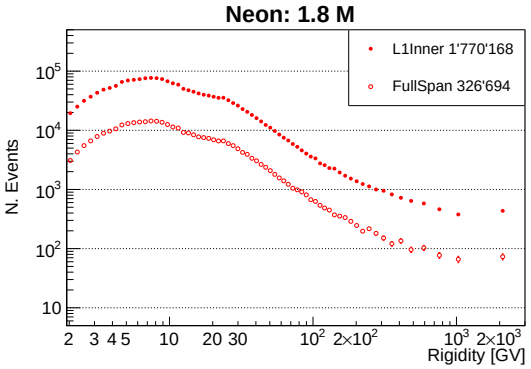

Figure 4-2: The AMS-02 7 years Neon nuclei event counts as a function of the reconstructed rigidity for L1Inner (red full circle) and FullSpan (red open circle) geometries respectively.

The below Tracker L1 contamination (Section 3.2.2.1) in the Oxygen and Neon nuclei event samples as a function of the reconstructed rigidity is calculated in the same way as discussed for the Silicon nuclei in Section 3.2.2.1. For both the Oxygen and Neon nuclei, the contamination is found to be negligible over the entire rigidity range as shown in Fig. 4-5.

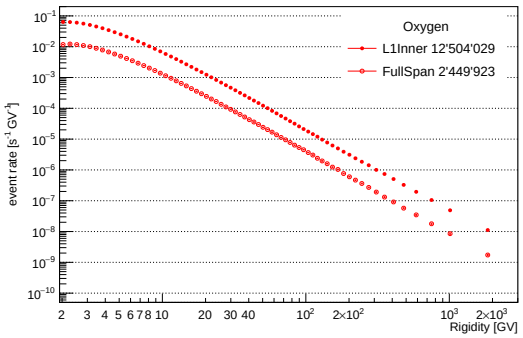

Figure 4-3: The AMS-02 7 years Oxygen nuclei event rates as a function of the reconstructed rigidity for L1Inner (red full circle) and FullSpan (red open circle) geometries respectively.

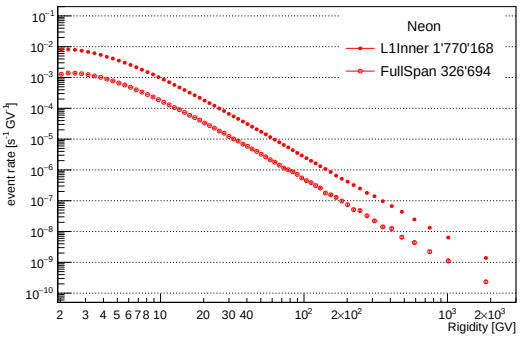

Figure 4-4: The AMS-02 7 years Neon nuclei event rates as a function of the reconstructed rigidity for L1Inner (red full circle) and FullSpan (red open circle) geometries respectively.

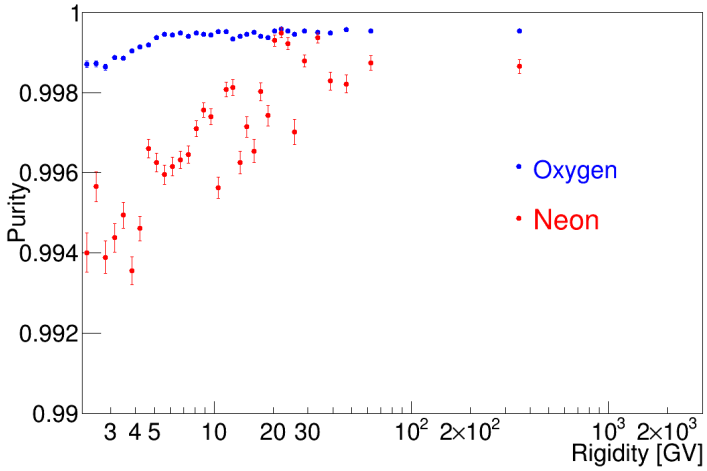

Figure 4-5: Purity of the Oxygen and Neon nuclei event samples within the Tracker L1 charge selection region as a function of the reconstructed rigidity.

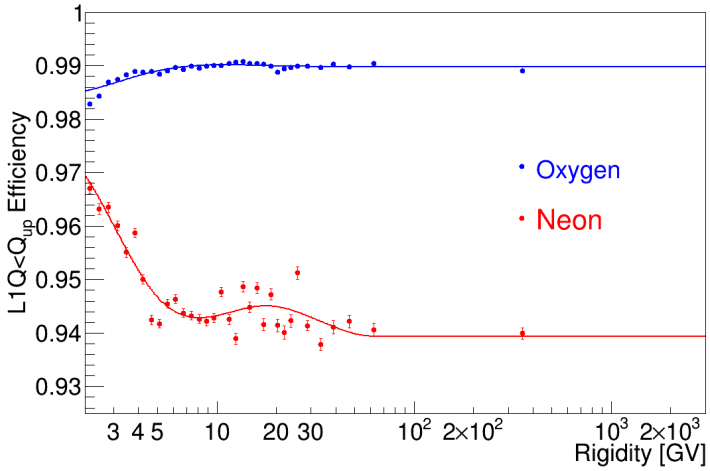

Figure 4-6: The Tracker L1 charge cut efficiency and its parameterization as a function of the reconstructed rigidity for Oxygen (blue) and Neon (red) nuclei.

Similar as the Silicon nuclei, the Oxygen nuclei sample has negligible above Tracker L1 contamination from nearby heavier nuclei (Section 3.2.2.2), namely Neon, Magnesium and Silicon, since their natural abundance is about 5 times less than that of Oxygen (Fig. 1-3). On the other hand, the abundances of Neon, Magnesium and Silicon nuclei are similar, so the above Tracker L1 contamination in the selected Neon nuclei event sample, mainly produced by interaction of incoming Magnesium and Silicon nuclei, is found to be $< 3\%$ at 10 GV and to decrease with increasing rigidity (Fig. 4-7).

The Neon nuclei average DAQ efficiency for the first 7 years of operation as function of the reconstructed rigidity is shown in Fig. 4-8, compared to that for the Silicon nuclei. Lighter nuclei have smaller data size because they deposit smaller amounts of energy and produce fewer secondary particles when traversing the AMS material. Hence the DAQ efficiency for lighter nuclei is higher than those for heavier nuclei. The Neon nuclei has $\sim 100\%$ DAQ efficiency as seen from Fig. 4-8. The DAQ efficiency for the Oxygen nuclei is even higher, hence no DAQ efficiency correction is needed for the Oxygen nuclei event counts.

4.1.2 Effective acceptance

The effective acceptances for the Oxygen and Neon nuclei in the L1Inner and FullSpan geometries without efficiency corrections are shown in Fig. 4-9, together with those for

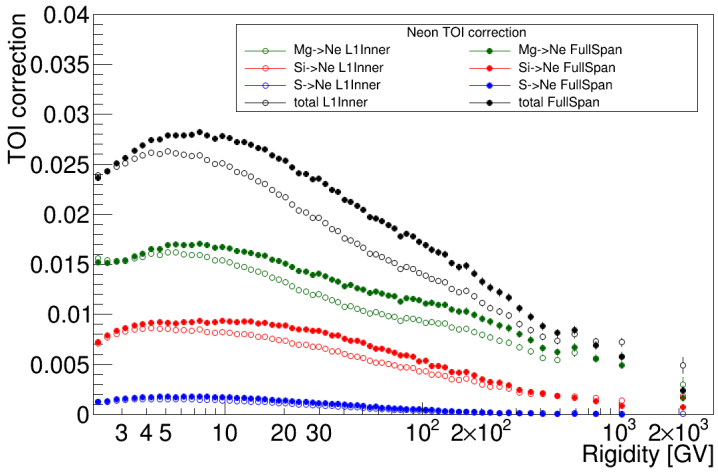

Figure 4-7: The contamination of the Neon nuclei data sample arising from Neon nuclei produced by interactions of Magnesium (green), Silicon (red), and Sulfur (blue) nuclei above the Tracker L1 for the L1Inner (open circle) and the FullSpan (full circle) geometries. As seen, the contribution from Sulfur is negligible. The total contamination (black), sum of the contribution from all nuclei, is used as the Top-Of-The-Instrument correction.

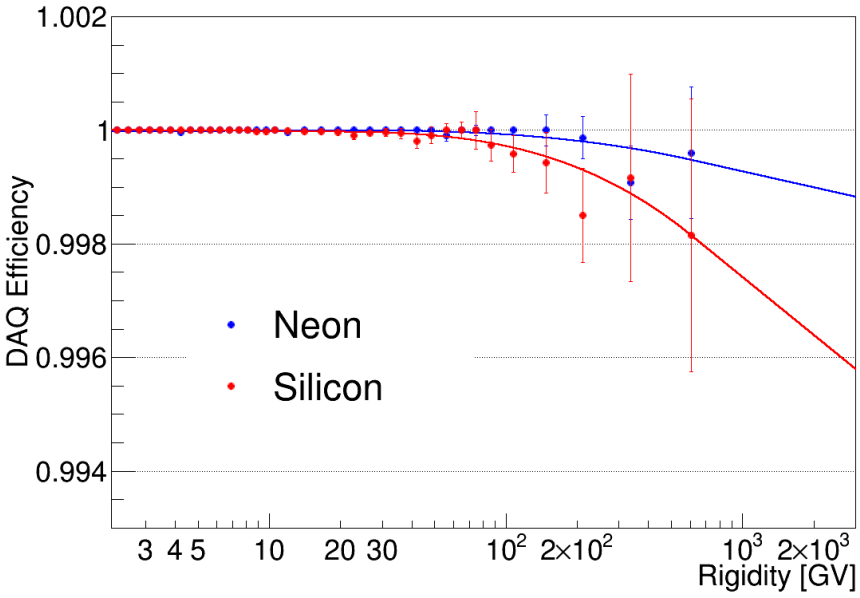

Figure 4-8: The average DAQ efficiency for the first 7 years of data taking (full circle) and the spline fit to the DAQ efficiency (solid curve) for Neon nuclei (red) and Silicon nuclei (blue) as function of the reconstructed rigidity.

the Silicon nuclei. Due to the increasing inelastic nuclei cross sections as function of the charge, heavier nuclei have lower survival probability when traversing the AMS material, hence the effective acceptances decrease from lighter nuclei to heavier nuclei.

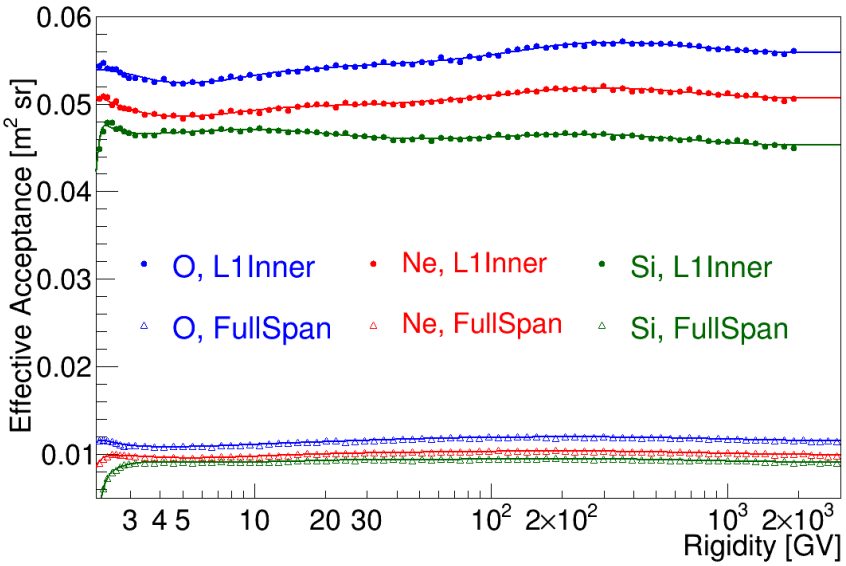

Figure 4-9: Effective acceptances in L1Inner (full circle) and FullSpan (open triangle) geometries for Oxygen (blue), Neon (red) and Silicon (green) nuclei as function of the generated rigidity. The solid curves represent the spline fit to acceptances.

The data-to-MC efficiency ratios for the Oxygen and Neon nuclei are shown in Figs. 4-10 and 4-11. Similar to the Silicon nuclei, the total correction for the sample in the L1Inner geometry is close to 1 for both nuclei. The correction for the FullSpan geometry is dominated by the Tracker L9 efficiency ratio, mainly due to the bias in the Monte Carlo description of the survival probability from Tracker L8 to L9.

The raw Oxygen and Neon nuclei fluxes multiplied by $R^{2.7}$ before the bin-to-bin migration correction are shown in Fig. 4-12.

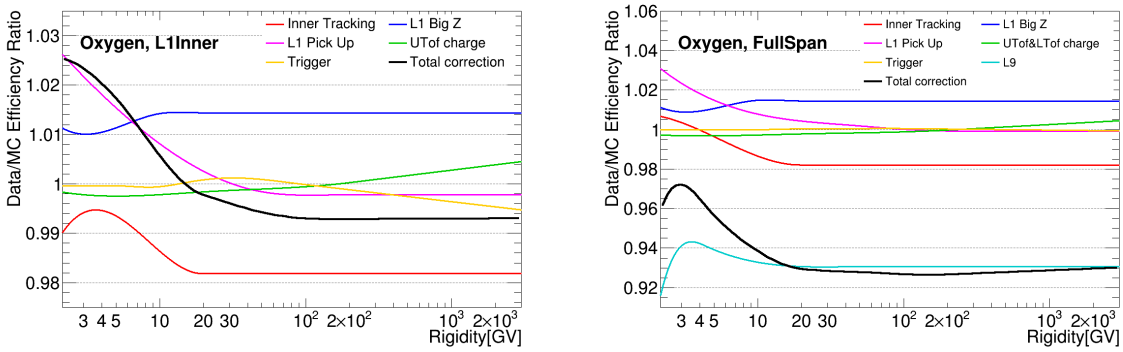

Figure 4-10: The Oxygen nuclei data/MC efficiency ratio parameterizations together with the total correction (black curve) obtained from the product of the spline fits for all efficiency ratios as function of the reconstructed rigidity for the L1Inner (left) and the FullSpan (right) geometries.

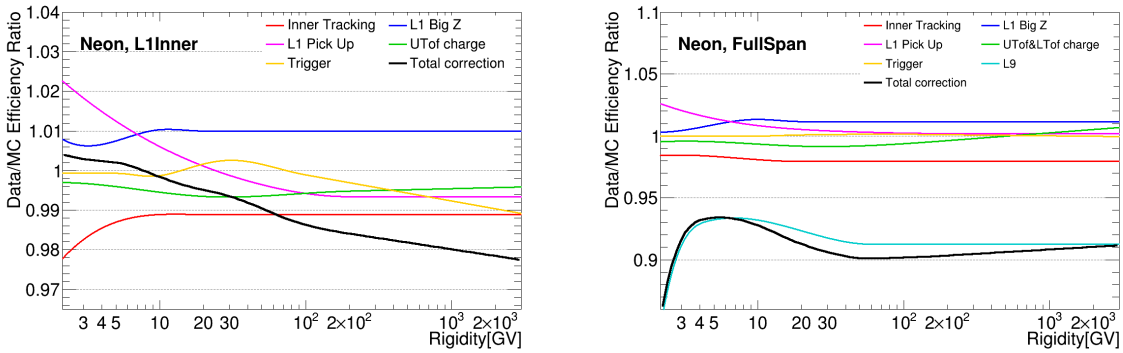

Figure 4-11: The Neon nuclei data/MC efficiency ratio parameterizations together with the total correction (black curve) obtained from the product of the spline fits for all efficiency ratios as function of the reconstructed rigidity for the L1Inner (left) and the FullSpan (right) geometries.

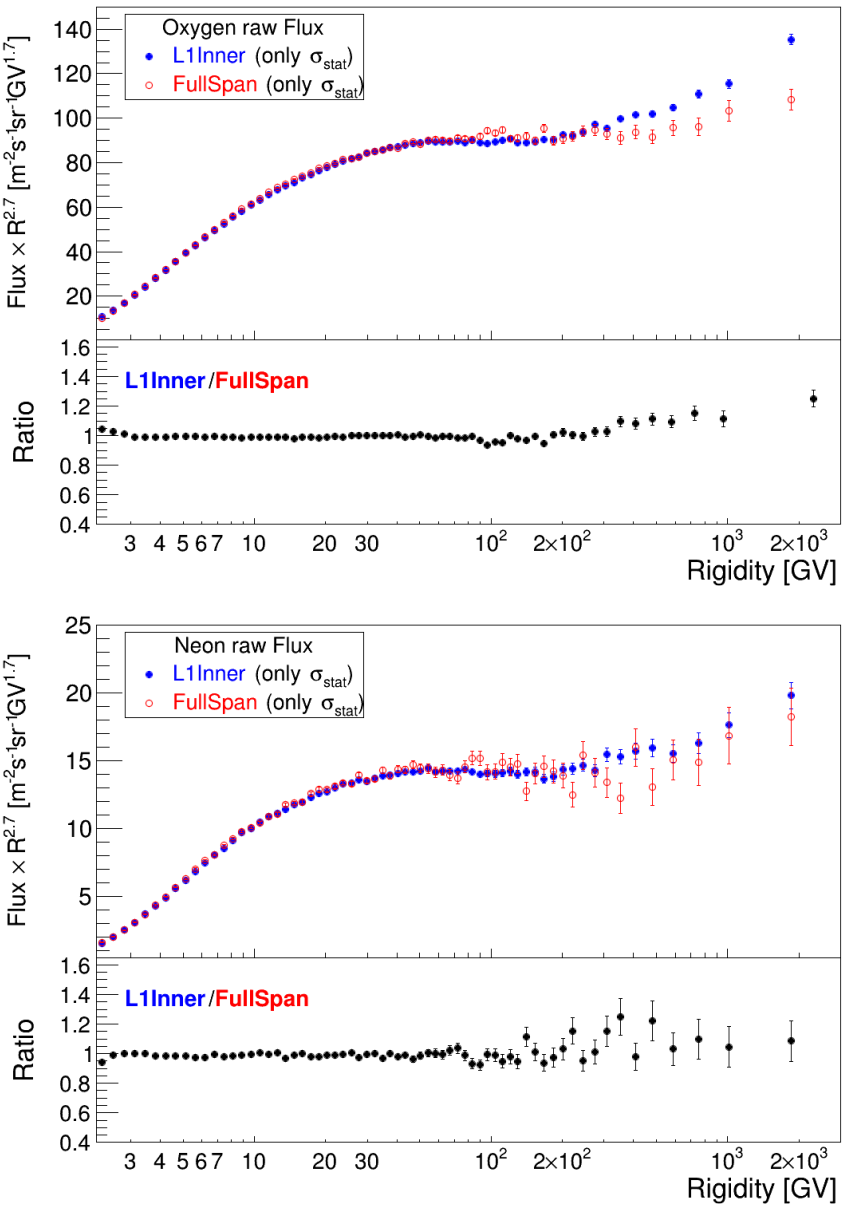

Figure 4-12: The 7 years Oxygen (top) and Neon (bottom) nuclei raw flux (that is before the correction of the event counts for the bin-to-bin migration) multiplied by $R^{2.7}$ as function of the reconstructed rigidity for the L1Inner (blue full circle) and the FullSpan (red empty circle) geometries.

4.1.3 Unfolding

Similarly, the Forward unfolding method (Section 3.4.2) is then applied to obtain the unfolding factor for the Oxygen and Neon nuclei. The width of the core Gaussian, σ, of the Oxygen and Neon rigidity resolution as function of the MC generated rigidity are shown in Fig. 4-13. All of them have similar MDR: ∼1.3 TV in L1Inner geometry and ∼3.0 TV in FullSpan geometry.

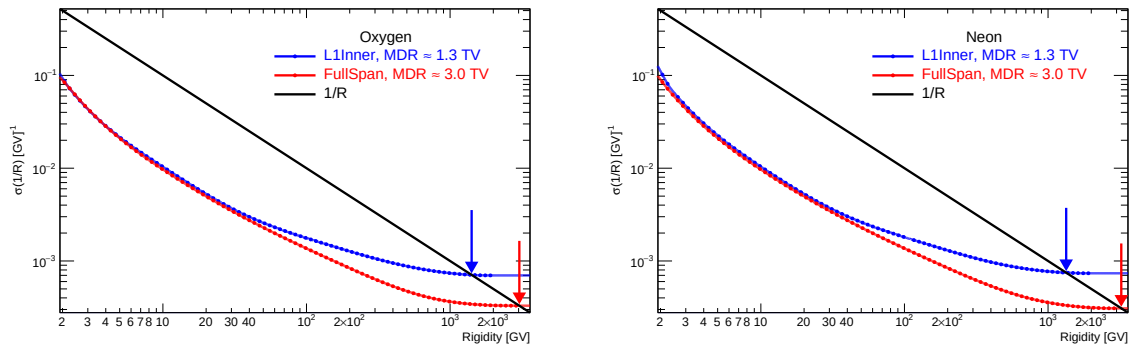

Figure 4-13: The σ of the core Gaussian for the Oxygen (left) and the Neon (right) rigidity resolution as function of the MC generated rigidity(full circle), and their parameterization (solid curve), for the L1Inner (blue) and the FullSpan (red) geometries. The black line is the 1/R function. The MDR value is determined as the value of the crossing between the parameterizations and the 1/R function, indicating by the arrows.

The unfolding factor for the Oxygen and Neon nuclei in the two geometries are shown in Fig. 4-14. The unfolded Oxygen and Neon nuclei fluxes multiplied by $R^{2.7}$, obtained from the event counts corrected by the unfolding factor, are shown in Fig. 4-15 for the L1Inner and FullSpan geometries.

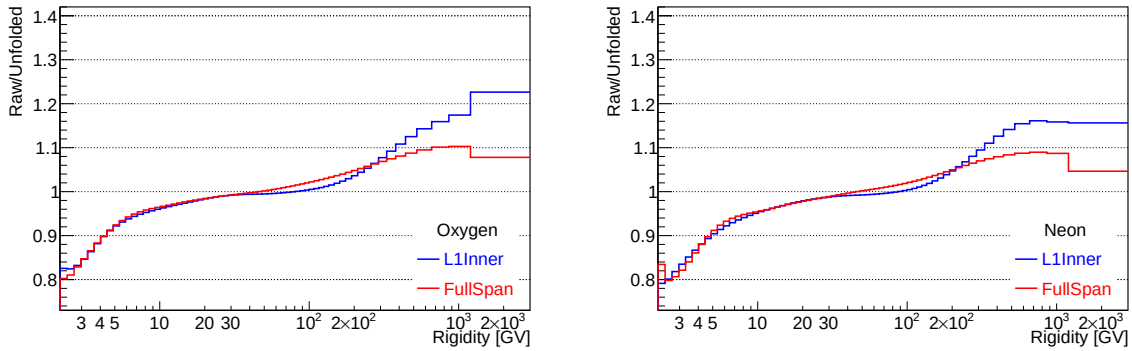

Figure 4-14: The Oxygen and Neon unfolding factors for the L1Inner (blue) and the FullSpan (red) geometries as function of the reconstructed rigidity.

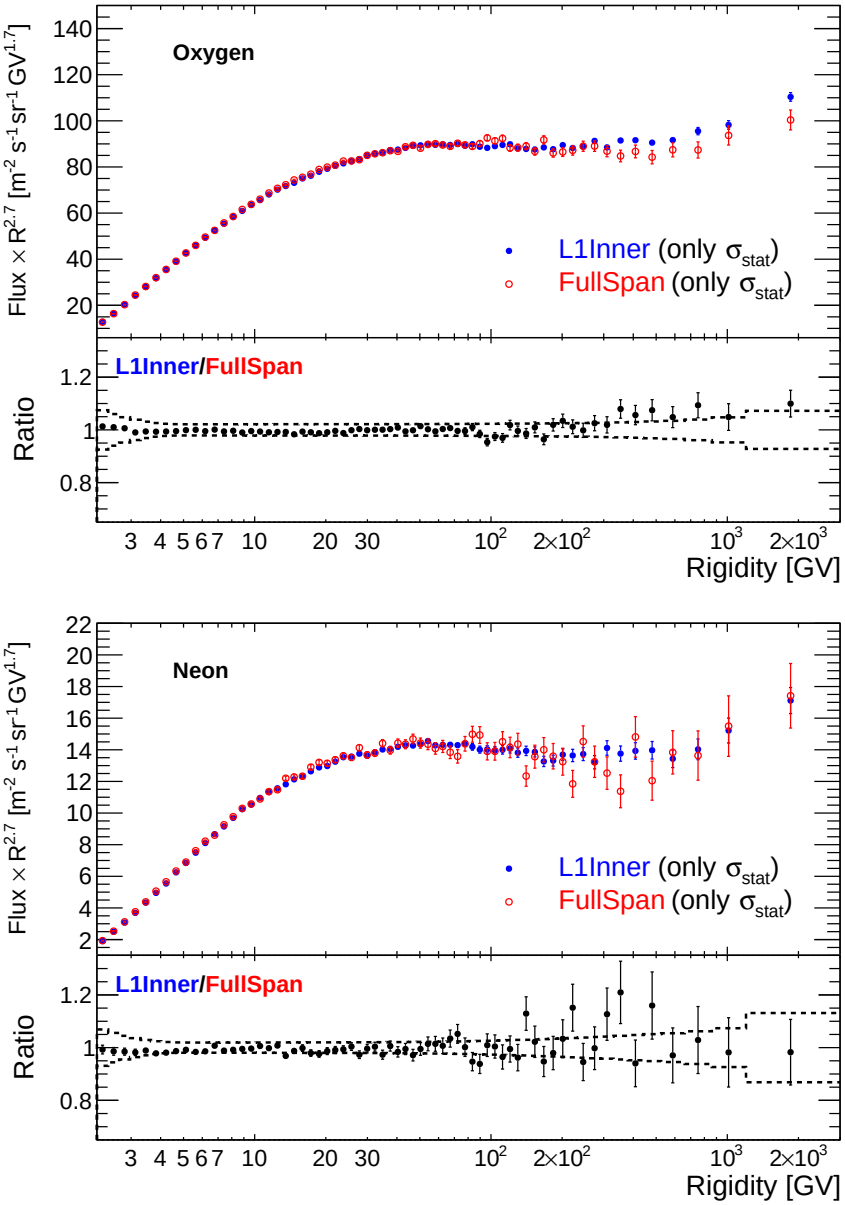

Figure 4-15: The Oxygen (top) and Neon (bottom) nuclei fluxes multiplied by $R^{2.7}$ after correction for the bin-to-bin migration as function of the true rigidity for the L1Inner (blue points) and the FullSpan (red open circles) geometries. The bottom panels show the ratio between the flux measured in the L1Inner geometry and that in the FullSpan geometry. The error bars show the statistical error and the dashed black lines show the total flux error, which is the quadratic sum of the statistical error and the systematic uncertainties shown in Fig. 4-17.

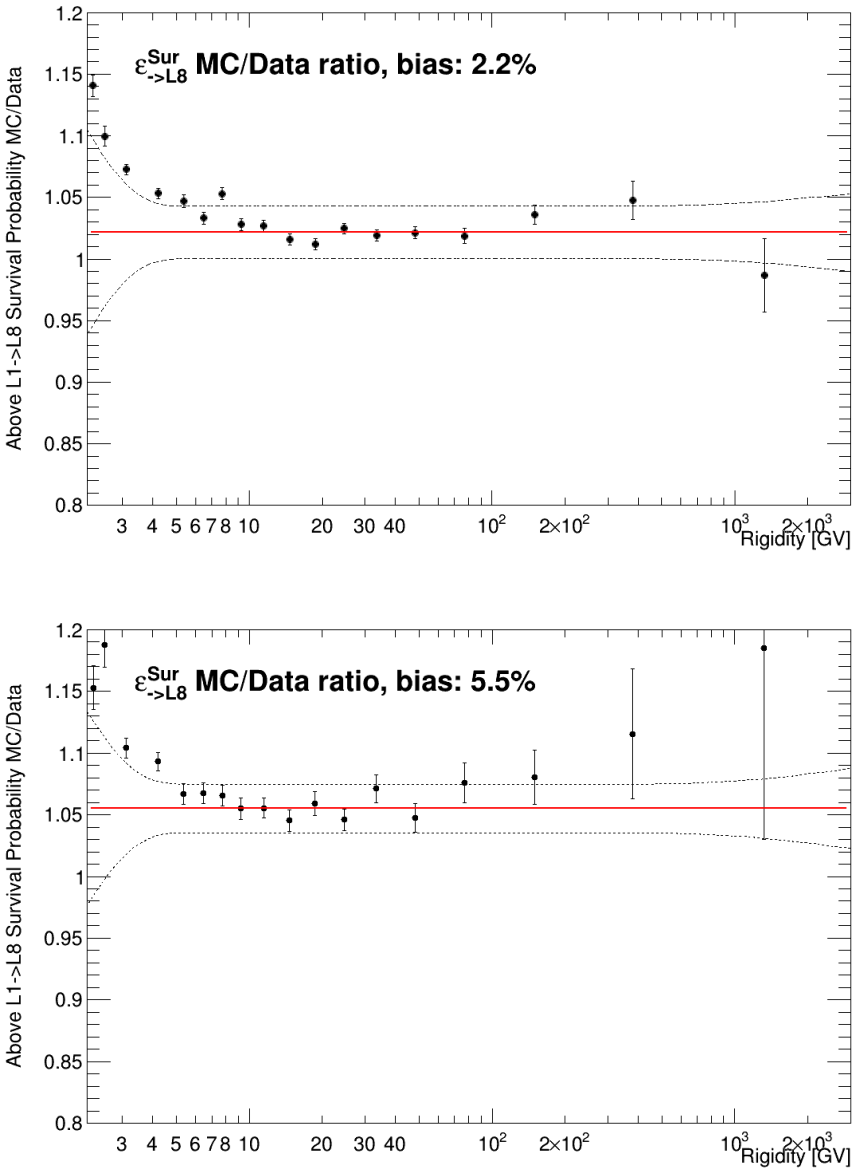

Figure 4-16: The MC-to-data ratio of the Oxygen (top) and Neon (bottom) nuclei survival probability from Above Tracker L1 up to L8 ($\varepsilon^{Sur,MC/Data}_{\rightarrow L1}$). The solid red lines show fits to a constant value between 6 GV to 200 GV, which are used for the total flux normalization corrections, and the dashed black lines indicate the systematic uncertainty band.

4.1.4 Final flux

The difference on the survival probability between data and Monte Carol simulation is also studied for Oxygen and Neon nuclei following the same procedure as for Silicon nuclei (see Section 3.5). The resulting total correction accounts to 2.2% for Oxygen nuclei and 5.5% for the Neon nuclei (Fig. 4-16).

The systematic uncertainties for the Oxygen and Neon nuclei fluxes have been evaluated with the same procedures as for Silicon nuclei (Section 3.6), and the breakdowns of the total flux errors for these two nuclei are shown in Fig. 4-17.

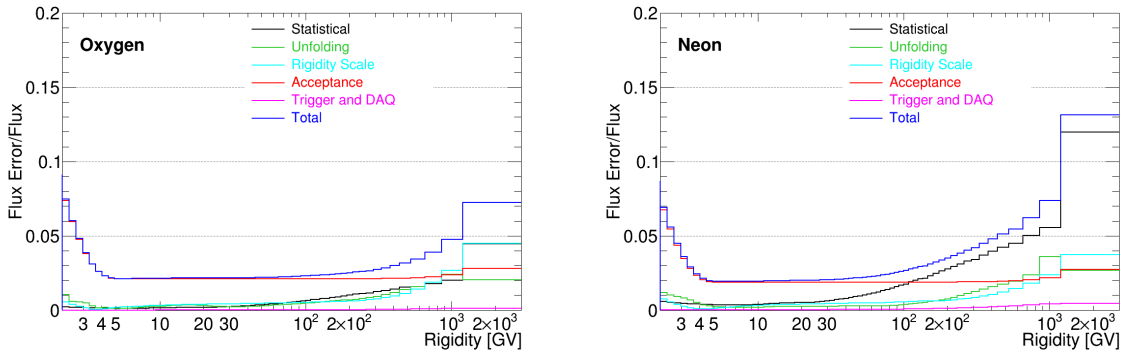

Figure 4-17: Total flux error (statistical error and systematic uncertainties) and its breakdown for the Oxygen (left) and Neon (right) nuclei fluxes as function of the true rigidity.

The combined flux (FullSpan for rigidities above 1.2 TV and L1Inner below) after applying the total flux normalization correction and multiplied by $R^{2.7}$, and the spectral indices as function of the true rigidity are shown in Fig. 4-18 for Oxygen nuclei and in Fig. 4-19 for Neon nuclei. The Oxygen nuclei flux presented in this work and its spectral index are compatible with the AMS-02 published result based on the first 5 years data set [2], as shown in Fig. 4-20. As seen, similar as the Silicon nuclei flux, both the Oxygen and Neon nuclei fluxes deviate from a single power law and harden above $\sim$ 200 GV.

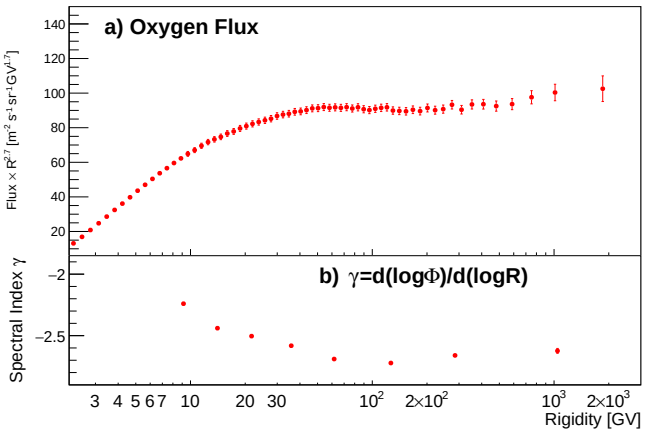

Figure 4-18: a) The final Oxygen nuclei flux after unfolding, flux normalization correction and multiplied by $R^{2.7}$ as function of the true rigidity. The points below 1200 GV results from the measurement on the L1Inner geometry, while the FullSpan geometry sample has been used for the last bin $[1200, 3000]$ GV. The indicated errors are the quadratic sum of the statistical error and the systematic uncertainties; b) The spectral index of the Oxygen nuclei flux as function of the true rigidity.

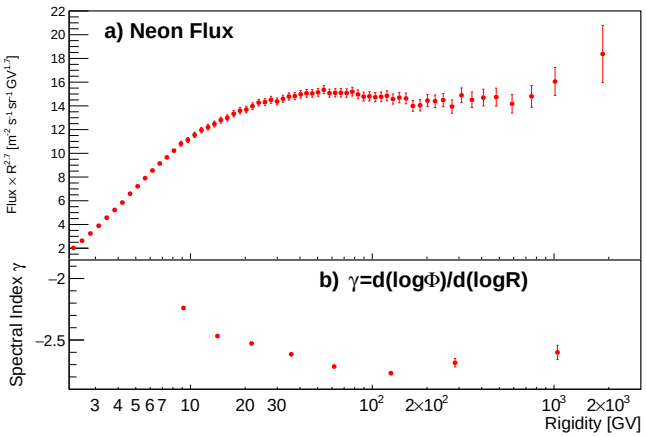

Figure 4-19: a) The final Neon nuclei flux after unfolding, flux normalization correction and multiplied by $R^{2.7}$ as function of the true rigidity. The points below 1200 GV results from the measurement on the L1Inner geometry, while the FullSpan geometry sample has been used for the last bin $[1200, 3000]$ GV. The indicated errors are the quadratic sum of the statistical error and the systematic uncertainties; b) The spectral index of the Neon nuclei flux as function of the true rigidity.

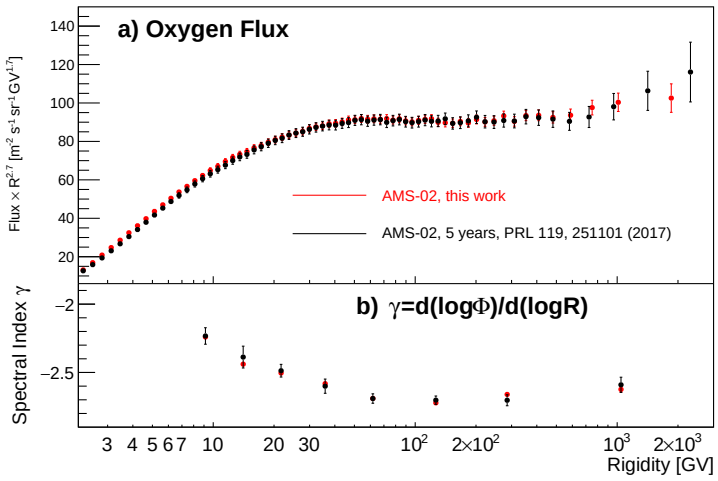

Figure 4-20: a) The final Oxygen nuclei flux after unfolding, flux normalization correction and multiplied by $R^{2.7}$ as function of the true rigidity(red), compared with the AMS-02 published result based on the first 5 years data set [2] (black); b) The spectral index of the Oxygen nuclei flux as function of the true rigidity, compared with the one for the AMS-02 published result [2] (black) recalculated in the same rigidity intervals.

4.1.5 Comparison to previous measurements

Measurements of the cosmic-ray Oxygen and Neon nuclei fluxes have been performed in different ranges of kinetic energy per nucleon: below a few GeV by CRIS [117] and ALICE[74]; in the GeV-TeV ranges by Ichimura93 [75], HEAO-3-C2 [76], ATIC2 [77], CREAM-II [78] and TRACKER [79, 80, 125].

To compare with previous measurements, the Oxygen and Neon nuclei fluxes presented in this work have been expressed as a function of kinetic energy per nucleon E_k using Eq. (3.36). Measurements of the isotopic composition of Oxygen nuclei in cosmic rays, currently available only at low energies with $E_k < 1$ GeV/n, have shown that the most abundant isotope is ^{16}O (∼85%), while ^{17}O to be ∼ 10% and ^{18}O to be ∼ 4% [118, 123, 126]. Similarly, the most abundant isotope of Neon is found to be ^{20}Ne (∼60%), while ^{21}Ne to be ∼ 12% and ^{22}Ne to be ∼ 31%[118–123, 127]. Therefore, the rigidity of the Oxygen and Neon is converted to E_k assuming that the sample is entirely ^{16}O and ^{20}Ne respectively.

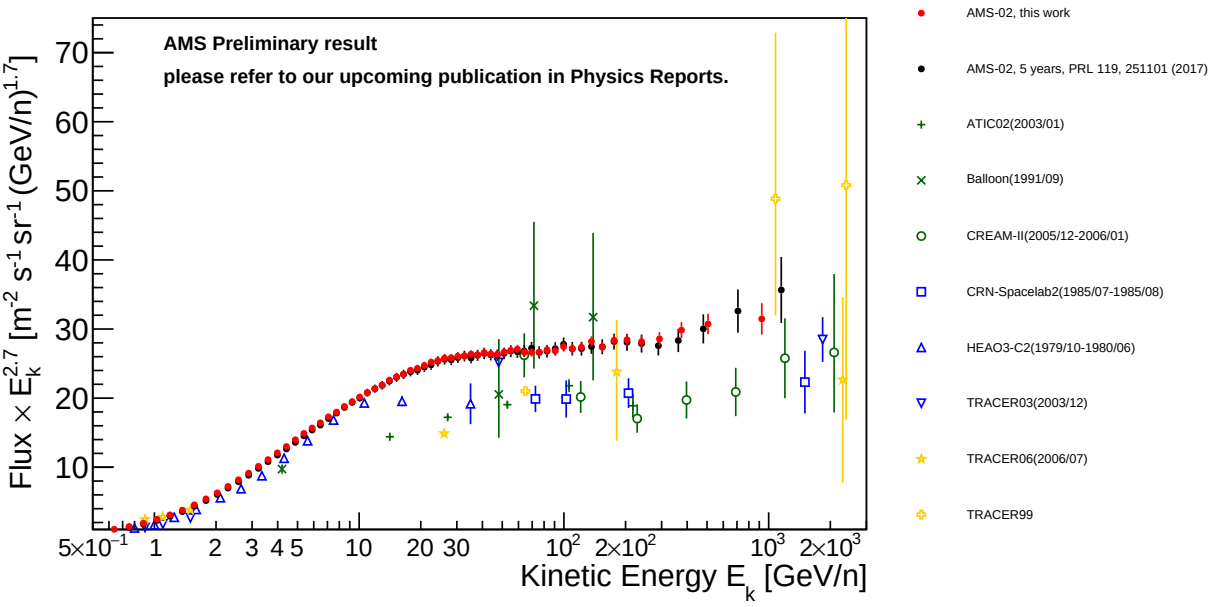

Figure 4-21: The Oxygen nuclei flux at the top of the AMS-02 detector (red points) as function of kinetic energy per nucleon E_k multiplied by $E_k^{2.7}$, together with results from previous experiments [124]. For the AMS result, the kinetic energy per nucleon is computed from the rigidity assuming that the sample contains only the most abundant isotope observed in Oxygen cosmic ray, that is ^{16}O [118, 123, 126].

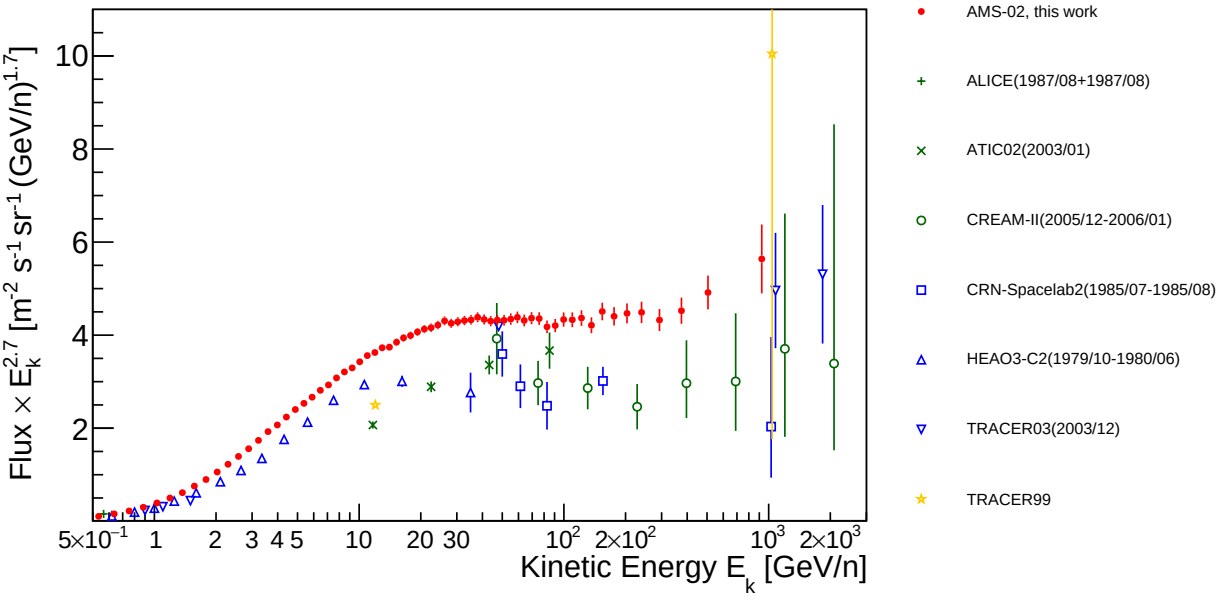

Figure 4-22: The Neon nuclei flux at the top of the AMS-02 detector (red points) as function of kinetic energy per nucleon E_k multiplied by $E_k^{2.7}$, together with results from previous experiments [124]. For the AMS result, the kinetic energy per nucleon is computed from the rigidity assuming that the sample contains only the most abundant isotope observed in Neon cosmic ray, that is ^{20}Ne [118–122].

4.2 Rigidity dependence of primary cosmic ray nuclei Oxygen, Neon and Silicon fluxes

To compare the rigidity dependences of the Silicon and Neon nuclei fluxes, the Si-to-Ne nuclei flux ratio has been analyzed (Fig. 4-23). This ratio is observed to increase with increasing rigidity and the to reach a plateau becoming rigidity independent. To determine the rigidity value R_0 where the two fluxes have identical rigidity dependence, the Si-to-Ne ratio has been fitted to the following function:

$$\frac{\Phi_{\mathrm{Si}}}{\Phi_{\mathrm{Ne}}} = \begin{cases} k(R/R_0)^{\delta}, & R \leq R_0 \\ k, & R > R_0 \end{cases}, \tag{4.1}$$

where k is a constant. to examine the rigidity interval where Ne and Si have identical rigidity dependence. The fit yields $k^{\mathrm{Si/Ne}} = 1.086 \pm 0.008$, $R_0^{\mathrm{Si/Ne}} = 87.8 \pm 12$ GV and $\delta^{\mathrm{Si/Ne}} = 0.065 \pm 0.002$. Considering the lower edge of the bin where $R_0^{\mathrm{Si/Ne}}$ falls in, it can be concluded that the Neon and Silicon nuclei fluxes have identical rigidity dependences above 86.5 GV.

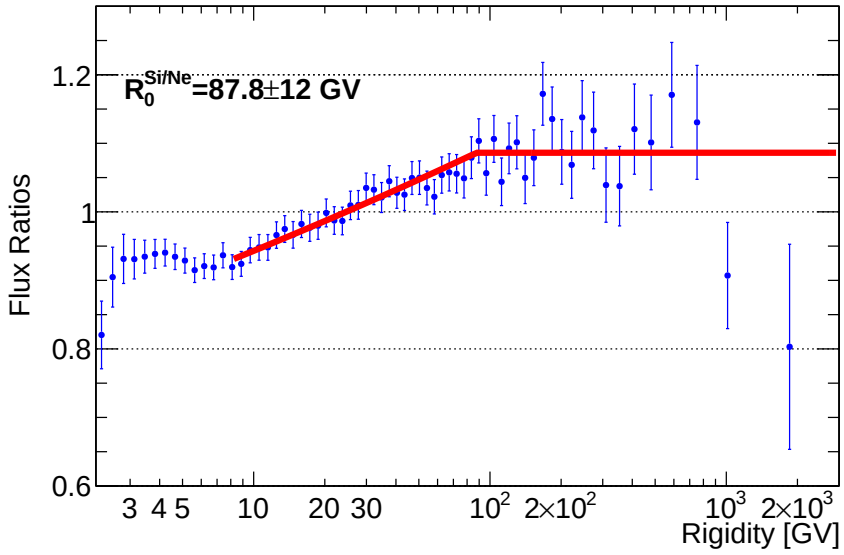

Figure 4-23: The Silicon-to-Neon flux ratio as function of the true rigidity. The solid red line shows the fit of the flux ratio to Eq. (4.1).

Previously, the AMS-02 has observed that Helium, Carbon and Oxygen fluxes have

identical rigidity dependences above 60 GV [2]. So to compare Neon and Silicon to this group of primary cosmic ray nuclei, the Ne-to-O and Si-to-O flux ratios are studied (Fig. 4-24). The Ne-to-O ratio increase with increasing rigidity up to about 10 GV where it starts to decrease; while the Si-to-O ratio increases with rigidity up to 86.5 GV where it starts to decrease similarly to the Ne-to-O one. To examine in detail their rigidity dependence at high rigidities, the two ratios are fitted above 20 GV to the following double power law:

$$\frac{\Phi_{\mathrm{Ne,Si}}}{\Phi_{\mathrm{O}}} = \begin{cases} C(R/86.5\ \mathrm{GV})^{\Delta}, & R \leq 86.5\ \mathrm{GV} \\ C(R/86.5\ \mathrm{GV})^{\delta}, & R > 86.5\ \mathrm{GV} \end{cases}, \tag{4.2}$$

where C is a constant. The fitted values are $k^{\mathrm{Ne/O}} = 0.1898 \pm 0.0008$, $\Delta^{\mathrm{Ne/O}} = -0.028 \pm 0.004$, $\delta^{\mathrm{Ne/O}} = -0.033 \pm 0.009$ and $k^{\mathrm{Si/O}} = 0.1878 \pm 0.0007$, $\Delta^{\mathrm{Si/O}} = 0.029 \pm 0.004$, $\delta^{\mathrm{Si/O}} = -0.030 \pm 0.011$. As seen, above 86.5 GV, both the Ne-to-O and Si-to-O flux ratios have spectral indices significantly different from zero, indicating that both Neon and Silicon nuclei spectra are softer by a single power law compared to the He, C and O spectra.

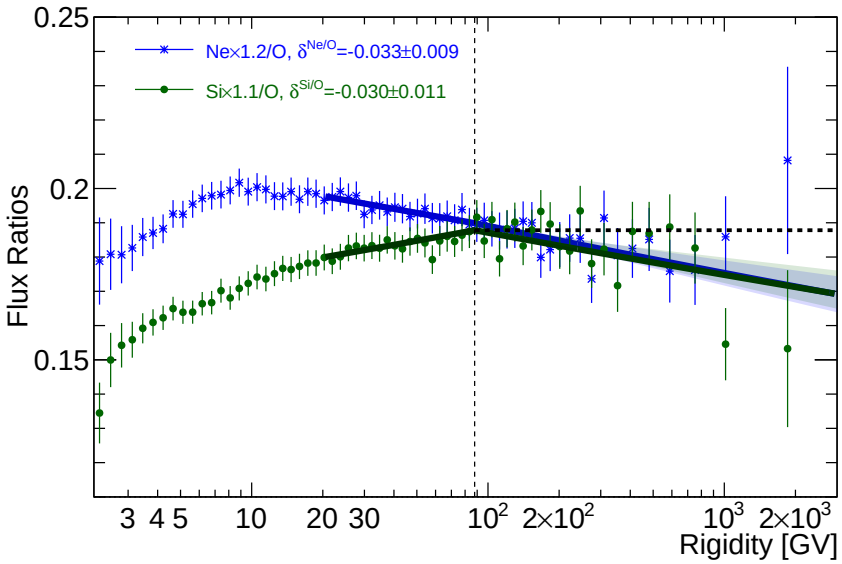

Figure 4-24: The Neon-to-Oxygen (blue triangle) and Silicon-to-Oxygen (red square) nuclei flux ratios as function of the true rigidity together with their fit to Eq. (4.2) shown by the blue and green line respectively. Shaded areas show the confidence interval of the fits.

It can be concluded that, two different groups of primary cosmic ray nuclei have been

observed, namely the He, C, O group, and the Ne, Si group. Nuclei in each of the two groups have identical rigidity dependence, but two groups have distinctly different rigidity spectra, with the Ne, Si group being softer than the He, C, O group.

The work on the Neon and Silicon nuclei flux measurements are compatible with results from other two independent AMS groups (Figs. 4-25 and 4-26), and has contributed to the AMS Ne-Mg-Si paper [128]. The Magnesium nuclei flux measurement was done by another colleague in the university of Geneva group and is not presented in this thesis. The work on the Oxygen nuclei flux measurements is compatible with the result from another independent AMS groups (Fig. 4-27), and has contributed to the upcoming AMS publication in Physics Reports [129].

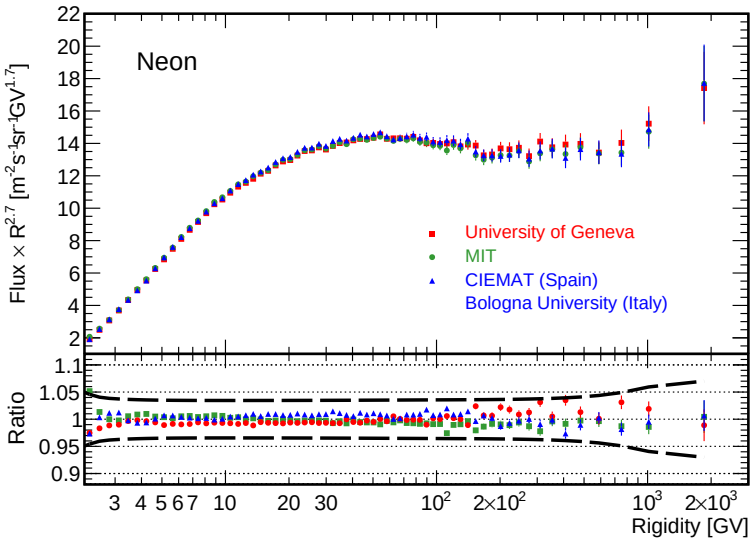

Figure 4-25: The final Neon nuclei flux multiplied by $R^{2.7}$ as function of the true rigidity obtained from the analysis performed by the University of Geneva group (this work, red squares), the MIT group (green points) and the CIEMAT and Bologna university group (blue triangles). The bottom panel shows the ratio between each of these results with their average (red squares, green points and blue triangles) together with the systematic uncertainty band (black dashed lines). As seen the three results are compatible with each other within the systematic uncertainty.

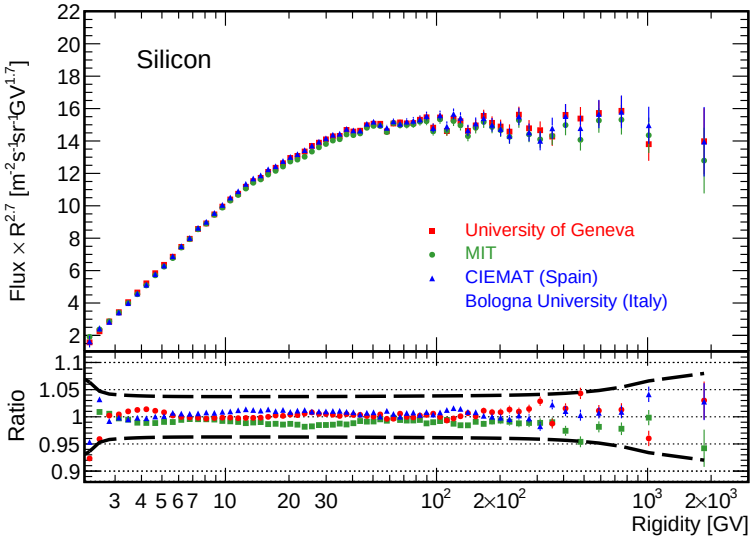

Figure 4-26: The final Silicon nuclei flux multiplied by $R^{2.7}$ as function of the true rigidity obtained from the analysis performed by the University of Geneva group (this work, red squares), the MIT group (green points) and the CIEMAT and Bologna university group (blue triangles). The bottom panel shows the ratio between each of these results with their average (red squares, green points and blue triangles) together with the systematic uncertainty band (black dashed lines). As seen the three results are compatible with each other within the systematic uncertainty.

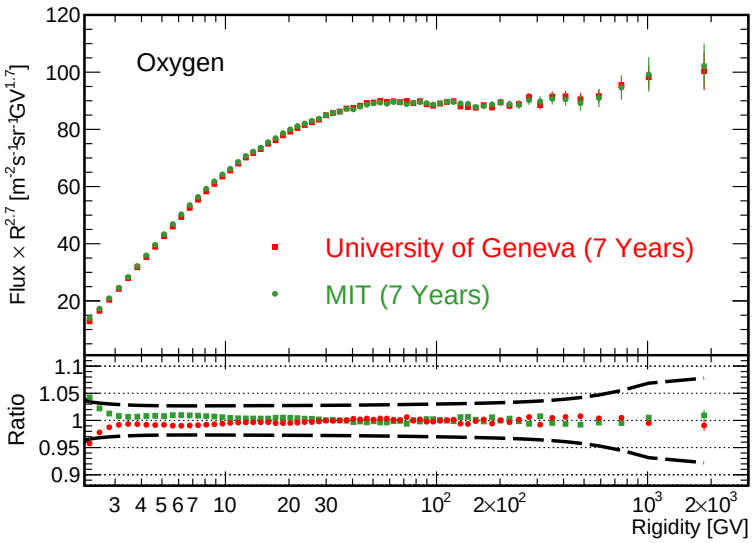

Figure 4-27: The final Oxygen nuclei flux multiplied by $R^{2.7}$ as function of the true rigidity obtained from the analysis of the 7-year AMS-02 data set performed by the University of Geneva group (this work, red squares) and the MIT group (green points). The bottom panel shows the ratio between each of these results with their average (red squares and green points) together with the systematic uncertainty band (black dashed lines). As seen the two results are compatible within the systematic uncertainty.

Conclusions and outlook

Over the last few decades, cosmic-ray Neon and Silicon nuclei fluxes have been measured in different kinetic energy per nucleon ranges: below a few GeV by CRIS [117] and ALICE[74]; in the GeV-TeV ranges by Ichimura93 [75], HEAO-3-C2 [76], ATIC2 [77], CREAM-II [78] and TRACKER [79, 80]. These measurements are affected by large errors, typically more than 20% at 50 GeV/n, and none of them have been performed in rigidity.

In this thesis, the precision measurements of the Neon and Silicon nuclei fluxes for rigidities ranging from 2.15 GV to 3 TV based on 1.8 million Neon and 1.6 million Silicon nuclei events collected by the AMS-02 detector during its first 7 years (May 19, 2011 to May 26, 2018) of operations are presented. In addition, the Oxygen nuclei flux measurement, previously published by the AMS-02 [2], has been updated with the 7-years data set with 12.5 million Oxygen nuclei events, and most importantly based on the same data taking period, detector calibration and event reconstruction software as the Neon and Silicon nuclei flux measurements. Systematic uncertainties of these three fluxes have been evaluated in detail. These are the first measurements of the cosmic-ray Neon and Silicon nuclei fluxes as function of rigidity, with accuracy of about 5% at 100 GV, allowing a detailed study of the rigidity dependence of the Neon and Silicon nuclei spectra. Above 86.5 GV, the two spectra are found to have identical rigidity dependence. From the analysis of their spectral indices, it's found that both fluxes harden at about 200 GV, similar as what has been previously observed for lighter cosmic-ray nuclei [2, 3], deviating from a single power law. Then the Neon and Silicon nuclei spectral shapes have been compared to that of light cosmic-ray Helium, Carbon and Oxygen nuclei, which have been previously found to exhibit identical rigidity dependence above 60 GV [2]. By the comparison to the Oxygen nuclei spectrum, it's found that the Neon and Silicon nuclei spectra have a

significantly softer rigidity dependence. Therefore, it can be concluded that there are at least two groups of primary cosmic rays: The Helium, Carbon and Oxygen group, and the Neon and Silicon group.

Heavier nuclei, due to larger inelastic cross sections, can only propagate smaller distances in the ISM before fragmentation compared to lighter nuclei, effectively sampling different propagation volumes of the Galaxy. Hence the different rigidity dependence between the two primary cosmic ray groups might be a hint of the non-homogeneous cosmic ray propagation [81].

Precision flux measurements of primary cosmic ray nuclei heavier than Silicon, such as Sulfur and Iron, will answer the question on how many classes of primary cosmic ray exist and will give new additional information to understand the origin of these different classes. Future measurements of the heavy secondary cosmic ray nuclei fluxes, such as Fluorine, will further deepen the understanding of the origin, acceleration and propagation of cosmic rays. The AMS-02 detector, which has recently undergone the installation of an Upgraded Tracker Thermal Pump System (UTTPS) [130–133], will continue collecting cosmic ray data for the entire ISS lifetime, providing cosmic ray flux measurements with unprecedented precision up to at least Nickel (Z=28).

Bibliography

[1] M. Aguilar and et al. "Precision Measurement of the Helium Flux in Primary Cosmic Rays of Rigidities 1.9 GV to 3 TV with the Alpha Magnetic Spectrometer on the International Space Station". In: *Phys. Rev. Lett.* 115 (21 Nov. 2015), p. 211101. DOI: 10.1103/PhysRevLett.115.211101.

[2] M. Aguilar and et al. "Observation of the Identical Rigidity Dependence of He, C, and O Cosmic Rays at High Rigidities by the Alpha Magnetic Spectrometer on the International Space Station". In: *Phys. Rev. Lett.* 119 (25 Dec. 2017), p. 251101. DOI: 10.1103/PhysRevLett.119.251101.

[3] M. Aguilar and et al. "Observation of New Properties of Secondary Cosmic Rays Lithium, Beryllium, and Boron by the Alpha Magnetic Spectrometer on the International Space Station". In: *Phys. Rev. Lett.* 120 (2 Jan. 2018), p. 021101. DOI: 10.1103/PhysRevLett.120.021101.

[4] M. Aguilar et al. "Precision Measurement of Cosmic-Ray Nitrogen and its Primary and Secondary Components with the Alpha Magnetic Spectrometer on the International Space Station". In: *Phys. Rev. Lett.* 121 (5 July 2018), p. 051103. DOI: 10.1103/PhysRevLett.121.051103.

[5] Carl D. Anderson. "The Positive Electron". In: *Phys. Rev.* 43 (6 Mar. 1933), pp. 491–494. DOI: 10.1103/PhysRev.43.491.

[6] Seth H. Neddermeyer and Carl D. Anderson. "Note on the Nature of Cosmic-Ray Particles". In: *Phys. Rev.* 51 (10 May 1937), pp. 884–886. DOI: 10.1103/PhysRev.51.884.

[7] C. M. G. LATTES, G. P. S. OCCHIALINIDR., and C. F. POWELLDR. "Observations on the Tracks of Slow Mesons in Photographic Emulsions*". In: *Nature* 160.4066 (Oct. 1947), pp. 453–456. ISSN: 1476-4687. DOI: 10.1038/160453a0.

[8] William Hanlon. URL: http://www.physics.utah.edu/~whanlon/spectrum.html (visited on 11/10/2019).

[9] M. Tanabashi et al. (Particle Data Group). "Review of Particle Physics". In: *Phys. Rev. D* 98 (3), p. 030001. DOI: 10.1103/PhysRevD.98.030001.

[10] Andreas Haungs, Heinigerd Rebel, and Markus Roth. "Energy spectrum and mass composition of high-energy cosmic rays". In: *Reports on Progress in Physics* 66.7 (June 2003), pp. 1145–1206. DOI: 10.1088/0034-4885/66/7/202.

[11] R.U. Abbasi et al. "Observation of the ankle and evidence for a high-energy break in the cosmic ray spectrum". In: *Physics Letters B* 619.3 (2005), pp. 271–280. ISSN: 0370-2693. DOI: https://doi.org/10.1016/j.physletb.2005.05.064.

[12] R.U. Abbasi et al. "Measurement of the flux of ultra high energy cosmic rays by the stereo technique". In: *Astroparticle Physics* 32.1 (2009), pp. 53–60. ISSN: 0927-6505. DOI: https://doi.org/10.1016/j.astropartphys.2009.06.001.

[13] J. Abrahamet al. (Pierre Auger Collaboration). "Measurement of the energy spectrum of cosmic rays above 10^{18} eV using the Pierre Auger Observatory". In: *Physics Letters B* 685.4 (2010), pp. 239–246. ISSN: 0370-2693. DOI: https://doi.org/10.1016/j.physletb.2010.02.013.

[14] Thomas K. Gaisser, Ralph Engel, and Elisa Resconi. *Cosmic Rays and Particle Physics*. 2nd ed. Cambridge University Press, 2016. DOI: 10.1017/CBO9781139192194.

[15] Thomas K. Gaisser and Todor Stanev. "High-energy cosmic rays". In: *Nuclear Physics A* 777 (2006), pp. 98–110. DOI: https://doi.org/10.1016/j.nuclphysa.2005.01.024.

[16] O. Deligny. "Cosmic-Ray Anisotropies: A Review". In: *25th European Cosmic Ray Symposium*. Dec. 2016. arXiv: 1612.08002 [astro-ph.HE].

[17] M. Amenomori et al. "Large-Scale Sidereal Anisotropy of Galactic Cosmic-Ray Intensity Observed by the Tibet Air Shower Array". In: *The Astrophysical Journal* 626.1 (May 2005), pp. L29–L32. DOI: 10.1086/431582.

[18] M. Amenomori et al. "Anisotropy and Corotation of Galactic Cosmic Rays". In: *Science* 314.5798 (2006), pp. 439–443. ISSN: 0036-8075. DOI: 10.1126/science.1131702. eprint: https://science.sciencemag.org/content/314/5798/439.full.pdf.

[19] G. Guillian et al. "Observation of the anisotropy of 10 TeV primary cosmic ray nuclei flux with the Super-Kamiokande-I detector". In: *Phys. Rev. D* 75 (6 Mar. 2007), p. 062003. DOI: 10.1103/PhysRevD.75.062003.

[20] A. A. Abdo et al. "THE LARGE-SCALE COSMIC-RAY ANISOTROPY AS OBSERVED WITH MILAGRO". In: *The Astrophysical Journal* 698.2 (June 2009), pp. 2121–2130. DOI: 10.1088/0004-637x/698/2/2121.

[21] M. Aglietta et al. "EVOLUTION OF THE COSMIC-RAY ANISOTROPY ABOVE 10^{14} eV". In: *The Astrophysical Journal* 692.2 (Feb. 2009), pp. L130–L133. DOI: 10.1088/0004-637x/692/2/l130.

[22] J. K. de Jong. *Observations of Large Scale Sidereal Anisotropy in 1 and 11 TeV cosmic rays from the MINOS experiment*. 2011. arXiv: 1201.2621 [hep-ex].

[23] Di Sciascio, G. "Measurement of Cosmic Ray Spectrum and Anisotropy with ARGO-YBJ". In: *EPJ Web of Conferences* 52 (2013), p. 04004. DOI: 10.1051/epjconf/20125204004.

[24] B. Bartoli et al. "Medium scale anisotropy in the TeV cosmic ray flux observed by ARGO-YBJ". In: *Phys. Rev. D* 88 (8 Oct. 2013), p. 082001. DOI: 10.1103/PhysRevD.88.082001.

[25] A. U. Abeysekara et al. "OBSERVATION OF SMALL-SCALE ANISOTROPY IN THE ARRIVAL DIRECTION DISTRIBUTION OF TeV COSMIC RAYS WITH HAWC". In: *The Astrophysical Journal* 796.2 (Nov. 2014), p. 108. DOI: 10.1088/0004-637x/796/2/108.

[26] M. G. Aartsen et al. “ANISOTROPY IN COSMIC-RAY ARRIVAL DIRECTIONS IN THE SOUTHERN HEMISPHERE BASED ON SIX YEARS OF DATA FROM THE ICECUBE DETECTOR”. In: *The Astrophysical Journal* 826.2 (Aug. 2016), p. 220. DOI: 10.3847/0004-637x/826/2/220.

[27] M. G. Aartsen et al. “OBSERVATION OF COSMIC-RAY ANISOTROPY WITH THE ICETOP AIR SHOWER ARRAY”. In: *The Astrophysical Journal* 765.1 (Feb. 2013), p. 55. DOI: 10.1088/0004-637x/765/1/55.

[28] Arthur H. Compton and Ivan A. Getting. “An Apparent Effect of Galactic Rotation on the Intensity of Cosmic Rays”. In: *Phys. Rev.* 47 (11 June 1935), pp. 817–821. DOI: 10.1103/PhysRev.47.817.

[29] L. J. Gleeson and W. I. Axford. “The compton-getting effect”. In: *Astrophysics and Space Science* 2.4 (Dec. 1968), pp. 431–437. ISSN: 1572-946X. DOI: 10.1007/BF02175919.

[30] R. Cowsik et al. “Steady State of Cosmic-Ray Nuclei—Their Spectral Shape and Path Length at Low Energies”. In: *Phys. Rev.* 158 (5 June 1967), pp. 1238–1242. DOI: 10.1103/PhysRev.158.1238.

[31] Stefano Gabici et al. “The origin of Galactic cosmic rays: Challenges to the standard paradigm”. In: *International Journal of Modern Physics D* 28.15 (2019), p. 1930022. DOI: 10.1142/S0218271819300222. eprint: https://doi.org/10.1142/S0218271819300222.

[32] M. Aguilar and et al. “Precision Measurement of the Boron to Carbon Flux Ratio in Cosmic Rays from 1.9 GV to 2.6 TV with the Alpha Magnetic Spectrometer on the International Space Station”. In: *Phys. Rev. Lett.* 117 (23 Nov. 2016), p. 231102. DOI: 10.1103/PhysRevLett.117.231102.

[33] M. Kachelrieß and D.V. Semikoz. “Cosmic ray models”. In: *Progress in Particle and Nuclear Physics* 109 (2019), p. 103710. ISSN: 0146-6410. DOI: https://doi.org/10.1016/j.ppnp.2019.07.002.

[34] Drury, Luke O´C. and Strong, Andrew W. "Power requirements for cosmic ray propagation models involving diffusive reacceleration; estimates and implications for the damping of interstellar turbulence". In: *A&A* 597 (2017), A117. DOI: 10.1051/0004-6361/201629526.

[35] N. E. Yanasak et al. "Measurement of the Secondary Radionuclides10Be,26Al,36Cl,54Mn, and14C and Implications for the Galactic Cosmic-Ray Age". In: *The Astrophysical Journal* 563.2 (Dec. 2001), pp. 768–792. DOI: https://doi.org/10.1086/323842.

[36] ENRICO Fermi. "On the Origin of the Cosmic Radiation". In: *Phys. Rev.* 75 (8 Apr. 1949), pp. 1169–1174. DOI: 10.1103/PhysRev.75.1169.

[37] W. Baade and F. Zwicky. "Cosmic Rays from Super-Novae". In: *Proceedings of the National Academy of Sciences* 20.5 (1934), pp. 259–263. ISSN: 0027-8424. DOI: 10.1073/pnas.20.5.259.

[38] Malcolm S. Longair. *High Energy Astrophysics*. 3rd ed. Cambridge University Press, 2011. DOI: 10.1017/CBO9780511778346.

[39] Ptuskin, V. S. and Zirakashvili, V. N. "On the spectrum of high-energy cosmic rays produced by supernova remnants in the presence of strong cosmic-ray streaming instability and wave dissipation". In: *A&A* 429.3 (2005), pp. 755–765. DOI: 10.1051/0004-6361:20041517.

[40] A M Hillas. "The cosmic-ray knee and ensuing spectrum seen as a consequence of Bell's self-magnetized SNR shock acceleration process". In: *Journal of Physics: Conference Series* 47 (Oct. 2006), pp. 168–177. DOI: 10.1088/1742-6596/47/1/021.

[41] G. Giacinti, M. Kachelrieß, and D. V. Semikoz. "Escape model for Galactic cosmic rays and an early extragalactic transition". In: *Phys. Rev. D* 91 (8 Apr. 2015), p. 083009. DOI: 10.1103/PhysRevD.91.083009.

[42] M. Amenomori et al. "Cosmic-ray energy spectrum around the knee obtained by the Tibet experiment and future prospects". In: *Advances in Space Research* 47.4 (2011), pp. 629–639. ISSN: 0273-1177. DOI: https://doi.org/10.1016/j.asr.2010.08.029.

[43] W.D. Apel et al. "KASCADE-Grande measurements of energy spectra for elemental groups of cosmic rays". In: *Astroparticle Physics* 47 (2013), pp. 54–66. ISSN: 0927-6505. DOI: https://doi.org/10.1016/j.astropartphys.2013.06.004.

[44] M Nagano et al. "Energy spectrum of primary cosmic rays above 1017.0eV determined from extensive air shower experiments at Akeno". In: 18.2 (Feb. 1992), pp. 423–442. DOI: 10.1088/0954-3899/18/2/022.

[45] Etienne Parizot. "Cosmic Ray Origin: Lessons from Ultra-High-Energy Cosmic Rays and the Galactic/Extragalactic Transition". In: *Nuclear Physics B - Proceedings Supplements* 256-257 (2014). Cosmic Ray Origin – Beyond the Standard Models, pp. 197–212. ISSN: 0920-5632. DOI: https://doi.org/10.1016/j.nuclphysbps.2014.10.023.

[46] M. Unger and Pierre Auger Collaboration. "Highlights from the Pierre Auger Observatory". In: *35th International Cosmic Ray Conference (ICRC2017)*. Vol. 301. International Cosmic Ray Conference. Jan. 2017, p. 1102. arXiv: 1710.09478 [astro-ph.HE].

[47] G Giacinti et al. "Cosmic ray anisotropy as signature for the transition from galactic to extragalactic cosmic rays". In: *Journal of Cosmology and Astroparticle Physics* 2012.07 (July 2012), pp. 031–031. DOI: 10.1088/1475-7516/2012/07/031.

[48] V. Berezinsky, A.Z. Gazizov, and S.I. Grigorieva. "Dip in UHECR spectrum as signature of proton interaction with CMB". In: *Physics Letters B* 612.3 (2005), pp. 147–153. ISSN: 0370-2693. DOI: https://doi.org/10.1016/j.physletb.2005.02.058.

[49] A. Aab et al. "Evidence for a mixed mass composition at the 'ankle' in the cosmic-ray spectrum". In: *Physics Letters B* 762 (2016), pp. 288–295. ISSN: 0370-2693. DOI: https://doi.org/10.1016/j.physletb.2016.09.039.

[50] Kenneth Greisen. "End to the Cosmic-Ray Spectrum?" In: *Phys. Rev. Lett.* 16 (17 Apr. 1966), pp. 748–750. DOI: 10.1103/PhysRevLett.16.748.

[51] G. T. Zatsepin and V. A. Kuzmin. "Upper limit of the spectrum of cosmic rays". In: *JETP Lett.* 4 (1966). [Pisma Zh. Eksp. Teor. Fiz.4,114(1966)], pp. 78–80.

[52] S. W. Barwick et al. "The Energy Spectra and Relative Abundances of Electrons and Positrons in the Galactic Cosmic Radiation". In: *The Astrophysical Journal* 498.2 (May 1998), pp. 779–789. DOI: 10.1086/305573.

[53] M. A. DuVernois et al. "Cosmic-Ray Electrons and Positrons from 1 to 100 GeV: Measurements with HEAT and Their Interpretation". In: *The Astrophysical Journal* 559.1 (Sept. 2001), pp. 296–303. DOI: 10.1086/322324.

[54] O. Adriani et al. "Cosmic-Ray Positron Energy Spectrum Measured by PAMELA". In: *Phys. Rev. Lett.* 111 (8 Aug. 2013), p. 081102. DOI: 10.1103/PhysRevLett.111.081102.

[55] M. Aguilar et al. "Electron and Positron Fluxes in Primary Cosmic Rays Measured with the Alpha Magnetic Spectrometer on the International Space Station". In: *Phys. Rev. Lett.* 113 (12 Sept. 2014), p. 121102. DOI: 10.1103/PhysRevLett.113.121102.

[56] M. Aguilar et al. "Towards Understanding the Origin of Cosmic-Ray Positrons". In: *Phys. Rev. Lett.* 122 (4 Jan. 2019), p. 041102. DOI: 10.1103/PhysRevLett.122.041102.

[57] G. Ambrosi et al. "Direct detection of a break in the teraelectronvolt cosmic-ray spectrum of electrons and positrons". In: *Nature* 552.7683 (Dec. 2017), pp. 63–66. ISSN: 1476-4687. DOI: 10.1038/nature24475.

[58] Dan Hooper and Tim Linden. "Measuring the local diffusion coefficient with H.E.S.S. observations of very high-energy electrons". In: *Phys. Rev. D* 98 (8 Oct. 2018), p. 083009. DOI: 10.1103/PhysRevD.98.083009.

[59] M. Aguilar et al. "Antiproton Flux, Antiproton-to-Proton Flux Ratio, and Properties of Elementary Particle Fluxes in Primary Cosmic Rays Measured with the Alpha Magnetic Spectrometer on the International Space Station". In: *Phys. Rev. Lett.* 117 (9 Aug. 2016), p. 091103. DOI: 10.1103/PhysRevLett.117.091103.

[60] R. Cowsik, B. Burch, and T. Madziwa-Nussinov. "THE ORIGIN OF THE SPECTRAL INTENSITIES OF COSMIC-RAY POSITRONS". In: *The Astrophysical Journal* 786.2 (Apr. 2014), p. 124. DOI: 10.1088/0004-637x/786/2/124.

[61] O. Adriani and et al. "PAMELA Measurements of Cosmic-Ray Proton and Helium Spectra". In: *Science* 332.6025 (2011), pp. 69–72. ISSN: 0036-8075. DOI: 10.1126/science.1199172.

[62] M. Aguilar and et al. "Precision Measurement of the Proton Flux in Primary Cosmic Rays from Rigidity 1 GV to 1.8 TV with the Alpha Magnetic Spectrometer on the International Space Station". In: *Phys. Rev. Lett.* 114 (17 Apr. 2015), p. 171103. DOI: 10.1103/PhysRevLett.114.171103.

[63] Yoann Génolini et al. "Indications for a High-Rigidity Break in the Cosmic-Ray Diffusion Coefficient". In: *Phys. Rev. Lett.* 119 (24 Dec. 2017), p. 241101. DOI: 10.1103/PhysRevLett.119.241101.

[64] Nicola Tomassetti. "ORIGIN OF THE COSMIC-RAY SPECTRAL HARDENING". In: *The Astrophysical Journal* 752.1 (May 2012), p. L13. DOI: 10.1088/2041-8205/752/1/l13.

[65] Nicola Tomassetti. "Cosmic-ray protons, nuclei, electrons, and antiparticles under a two-halo scenario of diffusive propagation". In: *Phys. Rev. D* 92 (8 Oct. 2015), p. 081301. DOI: 10.1103/PhysRevD.92.081301.

[66] Roberto Aloisio and Pasquale Blasi. "Propagation of galactic cosmic rays in the presence of self-generated turbulence". In: 2013.07 (July 2013), pp. 001–001. DOI: 10.1088/1475-7516/2013/07/001.

[67] Pasquale Blasi, Elena Amato, and Pasquale D. Serpico. "Spectral Breaks as a Signature of Cosmic Ray Induced Turbulence in the Galaxy". In: *Phys. Rev. Lett.* 109 (6 Aug. 2012), p. 061101. DOI: 10.1103/PhysRevLett.109.061101.

[68] Carmelo Evoli et al. "Origin of the Cosmic Ray Galactic Halo Driven by Advected Turbulence and Self-Generated Waves". In: *Phys. Rev. Lett.* 121 (2 July 2018), p. 021102. DOI: 10.1103/PhysRevLett.121.021102.

[69] A D Erlykin and A W Wolfendale. "The spectral shapes of hydrogen and helium nuclei in cosmic rays". In: *Journal of Physics G: Nuclear and Particle Physics* 42.7 (May 2015), p. 075201. DOI: 10.1088/0954-3899/42/7/075201.

[70] Yutaka Ohira and Kunihito Ioka. "COSMIC-RAY HELIUM HARDENING". In: *The Astrophysical Journal* 729.1 (Feb. 2011), p. L13. DOI: 10.1088/2041-8205/729/1/l13.

[71] Adrian Hanusch, Tatyana V. Liseykina, and Mikhail Malkov. "Acceleration of Cosmic Rays in Supernova Shocks: Elemental Selectivity of the Injection Mechanism". In: *The Astrophysical Journal* 872.1 (Feb. 2019), p. 108. DOI: 10.3847/1538-4357/aafdae.

[72] A. Abramowski et al. "Acceleration of petaelectronvolt protons in the Galactic Centre". In: *Nature* 531.7595 (Mar. 2016), pp. 476–479. ISSN: 1476-4687. DOI: 10.1038/nature17147.

[73] Isabelle A. Grenier, John H. Black, and Andrew W. Strong. "The Nine Lives of Cosmic Rays in Galaxies". In: *Annual Review of Astronomy and Astrophysics* 53.1 (2015), pp. 199–246. DOI: 10.1146/annurev-astro-082214-122457. eprint: https://doi.org/10.1146/annurev-astro-082214-122457.

[74] J.A. Esposito et al. "The ALICE instrument and the measured cosmic ray elemental abundances". In: *Astroparticle Physics* 1.1 (1992), pp. 33–45. ISSN: 0927-6505. DOI: https://doi.org/10.1016/0927-6505(92)90007-M.

[75] Masakatsu Ichimura et al. "Observation of heavy cosmic-ray primaries over the wide energy range from ∼100 GeV/particle to ∼100 TeV/particle: Is the celebrated "knee" actually so prominent?" In: *Phys. Rev. D* 48 (5 Sept. 1993), pp. 1949–1975. DOI: 10.1103/PhysRevD.48.1949.

[76] J. J. Engelmann et al. "Charge composition and energy spectra of cosmic-ray nuclei for elements from Be to Ni - Results from HEAO-3-C2." In: *Astronomy and Astrophysics* 233 (July 1990), pp. 96–111.

[77] A. D. Panov et al. “Energy spectra of abundant nuclei of primary cosmic rays from the data of ATIC-2 experiment: Final results”. In: *Bulletin of the Russian Academy of Sciences: Physics* 73.5 (May 2009), pp. 564–567. ISSN: 1934-9432. DOI: 10.3103/S1062873809050098.

[78] H. S. Ahn et al. “MEASUREMENTS OF THE RELATIVE ABUNDANCES OF HIGH-ENERGY COSMIC-RAY NUCLEI IN THE TeV/NUCLEON REGION”. In: *The Astrophysical Journal* 715.2 (May 2010), pp. 1400–1407. DOI: 10.1088/0004-637x/715/2/1400.

[79] F. Gahbauer et al. “A New Measurement of the Intensities of the Heavy Primary Cosmic-Ray Nuclei around 1 TeV amu-1”. In: *The Astrophysical Journal* 607.1 (May 2004), pp. 333–341. DOI: 10.1086/383304.

[80] M. Ave et al. “Composition of Primary Cosmic-Ray Nuclei at High Energies”. In: *The Astrophysical Journal* 678.1 (May 2008), pp. 262–273. DOI: 10.1086/529424.

[81] G. Jóhannesson et al. “BAYESIAN ANALYSIS OF COSMIC RAY PROPAGATION: EVIDENCE AGAINST HOMOGENEOUS DIFFUSION”. In: *The Astrophysical Journal* 824.1 (June 2016), p. 16. DOI: 10.3847/0004-637x/824/1/16.

[82] Carmelo Evoli, Roberto Aloisio, and Pasquale Blasi. “Galactic cosmic rays after the AMS-02 observations”. In: *Phys. Rev. D* 99 (10 May 2019), p. 103023. DOI: 10.1103/PhysRevD.99.103023.

[83] P. Picozza et al. “PAMELA – A payload for antimatter matter exploration and light-nuclei astrophysics”. In: *Astroparticle Physics* 27.4 (2007), pp. 296–315. ISSN: 0927-6505. DOI: https://doi.org/10.1016/j.astropartphys.2006.12.002.

[84] K. Lübelsmeyer et al. “Upgrade of the Alpha Magnetic Spectrometer (AMS-02) for long term operation on the International Space Station (ISS)”. In: *Nuclear Instruments and Methods in Physics Research Section A: Accelerators, Spectrometers, Detectors and Associated Equipment* 654.1 (2011), pp. 639–648. ISSN: 0168-9002. DOI: https://doi.org/10.1016/j.nima.2011.06.051.

[85] M. Aguilar et al. "The Alpha Magnetic Spectrometer (AMS) on the International Space Station: Part I – results from the test flight on the space shuttle". In: *Physics Reports* 366.6 (2002), pp. 331–405. ISSN: 0370-1573. DOI: https://doi.org/10.1016/S0370-1573(02)00013-3.

[86] B. Alpat et al. "The internal alignment and position resolution of the AMS-02 silicon tracker determined with cosmic-ray muons". In: *Nuclear Instruments and Methods in Physics Research Section A: Accelerators, Spectrometers, Detectors and Associated Equipment* 613.2 (2010), pp. 207–217. ISSN: 0168-9002. DOI: https://doi.org/10.1016/j.nima.2009.11.065.

[87] Pierre Saouter. "Nuclei identification with the AMS-02 silicon tracker and measurement of cosmic ray nuclei fluxes". PhD thesis. Université de Genève, 2014.

[88] Sonia Natale and Stefan Schael. "The AMS-2 Tracker Alignment System: design and performance". In: *Proceedings, 31st International Cosmic Ray Conference (ICRC2009): Lodz, Poland. 7-15 July 2009*. 2009, p. 1344.

[89] G. Ambrosi et al. "Alignment of the AMS-02 silicon Tracker". In: *Proceedings, 33rd International Cosmic Ray Conference (ICRC2013): Rio de Janeiro, Brazil, July 2-9, 2013*. 2013, p. 1260.

[90] G. Ambrosi et al. "The spatial resolution of the silicon tracker of the Alpha Magnetic Spectrometer". In: *Nuclear Instruments and Methods in Physics Research Section A: Accelerators, Spectrometers, Detectors and Associated Equipment* 869 (2017), pp. 29–37. ISSN: 0168-9002. DOI: https://doi.org/10.1016/j.nima.2017.07.014.

[91] G. Ambrosi et al. "AMS-02 Track reconstruction and rigidity measurement". In: *Proceedings, 33rd International Cosmic Ray Conference (ICRC2013): Rio de Janeiro, Brazil, July 2-9, 2013*. 2013, p. 1064.

[92] J. Alcaraz. "Track fitting in slightly inhomogeneous magnetic fields". In: *Nuclear Instruments and Methods in Physics Research Section A: Accelerators, Spectrometers, Detectors and Associated Equipment* 553.3 (2005), pp. 613–619. ISSN: 0168-9002. DOI: https://doi.org/10.1016/j.nima.2005.07.021.

[93] Y. Jia et al. "Nuclei charge measurement by the Alpha Magnetic Spectrometer silicon tracker". In: *Nuclear Instruments and Methods in Physics Research Section A: Accelerators, Spectrometers, Detectors and Associated Equipment* 972 (2020), p. 164169. ISSN: 0168-9002. DOI: https://doi.org/10.1016/j.nima.2020.164169.

[94] G. Alberti et al. *Development of a Thermal Control System with Mechanically Pumped CO2 Two-Phase Loops for the AMS-02 Tracker on the ISS*. 2013. arXiv: 1302.4294 [physics.ins-det].

[95] V. Bindi et al. "Calibration and performance of the AMS-02 time of flight detector in space". In: *Nuclear Instruments and Methods in Physics Research Section A: Accelerators, Spectrometers, Detectors and Associated Equipment* 743 (2014), pp. 22–29. ISSN: 0168-9002. DOI: https://doi.org/10.1016/j.nima.2014.01.002.

[96] Ph. von Doetinchem et al. *The Anticoincidence Counter System of AMS-02*. 2009. arXiv: 0906.1068 [astro-ph.IM].

[97] Matthew Krafczyk. "A precision measurement of the cosmic ray positron fraction on the International Space Station". PhD thesis. Massachusetts Institute of Technology, Jan. 2016.

[98] Thomas Kirn. "The AMS-02 TRD on the international space station". In: *Nuclear Instruments and Methods in Physics Research Section A: Accelerators, Spectrometers, Detectors and Associated Equipment* 706 (2013). TRDs for the Third Millenium, pp. 43–47. ISSN: 0168-9002. DOI: https://doi.org/10.1016/j.nima.2012.05.010.

[99] Hu Liu et al. "The RICH detector of AMS-02: 5 years of operation in space". In: *Nuclear Instruments and Methods in Physics Research Section A: Accelerators, Spectrometers, Detectors and Associated Equipment* 876 (2017). The 9th international workshop on Ring Imaging Cherenkov Detectors (RICH2016), pp. 5–8. ISSN: 0168-9002. DOI: https://doi.org/10.1016/j.nima.2016.12.011.

[100] C. Adloff et al. "The AMS-02 lead-scintillating fibres Electromagnetic Calorimeter". In: *Nuclear Instruments and Methods in Physics Research Section A: Accel-*

erators, Spectrometers, Detectors and Associated Equipment 714 (2013), pp. 147–154. ISSN: 0168-9002. DOI: https://doi.org/10.1016/j.nima.2013.02.020.

[101] M. Aguilar et al. "First Result from the Alpha Magnetic Spectrometer on the International Space Station: Precision Measurement of the Positron Fraction in Primary Cosmic Rays of 0.5–350 GeV". In: *Phys. Rev. Lett.* 110 (14 Apr. 2013), p. 141102. DOI: 10.1103/PhysRevLett.110.141102.

[102] A. Basili et al. "The TOF-ACC flight electronics for the fast trigger and time of flight of the AMS-02 cosmic ray spectrometer". In: *Nuclear Instruments and Methods in Physics Research Section A: Accelerators, Spectrometers, Detectors and Associated Equipment* 707 (2013), pp. 99–113. ISSN: 0168-9002. DOI: https://doi.org/10.1016/j.nima.2012.12.089.

[103] F. Cadoux et al. "The Electromagnetic Calorimeter Trigger System for the AMS-02 Experiment". In: *IEEE Transactions on Nuclear Science* 55.2 (Apr. 2008), pp. 817–821. ISSN: 1558-1578. DOI: 10.1109/TNS.2008.918517.

[104] ANDREI KOUNINE. "THE ALPHA MAGNETIC SPECTROMETER ON THE INTERNATIONAL SPACE STATION". In: *International Journal of Modern Physics E* 21.08 (2012), p. 1230005. DOI: 10.1142/S0218301312300056. eprint: https://doi.org/10.1142/S0218301312300056.

[105] J. Allison et al. "Recent developments in Geant4". In: *Nuclear Instruments and Methods in Physics Research Section A: Accelerators, Spectrometers, Detectors and Associated Equipment* 835 (2016), pp. 186–225. ISSN: 0168-9002. DOI: https://doi.org/10.1016/j.nima.2016.06.125.

[106] J. Allison et al. "Geant4 developments and applications". In: *IEEE Transactions on Nuclear Science* 53.1 (2006), pp. 270–278.

[107] S. Agostinelli et al. "Geant4—a simulation toolkit". In: *Nuclear Instruments and Methods in Physics Research Section A: Accelerators, Spectrometers, Detectors and Associated Equipment* 506.3 (2003), pp. 250–303. ISSN: 0168-9002. DOI: https://doi.org/10.1016/S0168-9002(03)01368-8.

[108] Q. Yan et al. "Measurements of nuclear interaction cross sections with the Alpha Magnetic Spectrometer on the International Space Station". In: *Nuclear Physics A* 996 (2020), p. 121712. ISSN: 0375-9474. DOI: https://doi.org/10.1016/j.nuclphysa.2020.121712.

[109] M.A. Abdu et al. "South Atlantic magnetic anomaly ionization: A review and a new focus on electrodynamic effects in the equatorial ionosphere". In: *Journal of Atmospheric and Solar-Terrestrial Physics* 67.17 (2005). Space Geophysics, pp. 1643–1657. ISSN: 1364-6826. DOI: https://doi.org/10.1016/j.jastp.2005.01.014.

[110] J. Alcaraz et al. "Leptons in near earth orbit". In: *Physics Letters B* 484.1 (2000), pp. 10–22. ISSN: 0370-2693. DOI: https://doi.org/10.1016/S0370-2693(00)00588-8.

[111] C. C. Finlay et al. "International Geomagnetic Reference Field: the eleventh generation". In: *Geophysical Journal International* 183.3 (Dec. 2010), pp. 1216–1230. ISSN: 0956-540X. DOI: 10.1111/j.1365-246X.2010.04804.x. eprint: https://academic.oup.com/gji/article-pdf/183/3/1216/1785065/183-3-1216.pdf.

[112] Erwan Thébault et al. "International Geomagnetic Reference Field: the 12th generation". In: *Earth, Planets and Space* 67.1 (May 2015), p. 79. ISSN: 1880-5981. DOI: 10.1186/s40623-015-0228-9.

[113] J.D. Sullivan. "Geometric factor and directional response of single and multi-element particle telescopes". In: *Nuclear Instruments and Methods* 95.1 (1971), pp. 5–11. ISSN: 0029-554X. DOI: https://doi.org/10.1016/0029-554X(71)90033-4.

[114] J. Albert et al. "Unfolding of differential energy spectra in the MAGIC experiment". In: *Nuclear Instruments and Methods in Physics Research Section A: Accelerators, Spectrometers, Detectors and Associated Equipment* 583.2 (2007), pp. 494–506. ISSN: 0168-9002. DOI: https://doi.org/10.1016/j.nima.2007.09.048.

[115] J. Berdugo et al. "Determination of the rigidity scale of the Alpha Magnetic Spectrometer". In: *Nuclear Instruments and Methods in Physics Research Section A: Accelerators, Spectrometers, Detectors and Associated Equipment* 869 (2017),

pp. 10–14. ISSN: 0168-9002. DOI: https://doi.org/10.1016/j.nima.2017.07.012.

[116] G.D. Lafferty and T.R. Wyatt. "Where to stick your data points: The treatment of measurements within wide bins". In: *Nuclear Instruments and Methods in Physics Research Section A: Accelerators, Spectrometers, Detectors and Associated Equipment* 355.2 (1995), pp. 541–547. ISSN: 0168-9002. DOI: https://doi.org/10.1016/0168-9002(94)01112-5.

[117] K. A. Lave et al. "GALACTIC COSMIC-RAY ENERGY SPECTRA AND COMPOSITION DURING THE 2009-2010 SOLAR MINIMUM PERIOD". In: *The Astrophysical Journal* 770.2 (June 2013), p. 117. DOI: 10.1088/0004-637x/770/2/117.

[118] W. R. Webber, J. C. Kish, and D. A. Schrier. "Cosmic Ray Isotope Measurements with a New Cerenkov X Total Energy Telescope". In: *19th International Cosmic Ray Conference (ICRC19), Volume 2*. Vol. 2. International Cosmic Ray Conference. Aug. 1985, p. 88.

[119] J. S. Young et al. "The elemental and isotopic composition of cosmic rays - Silicon to nickel". In: *Astrophysical Journal* 246 (June 1981), pp. 1014–1030. DOI: 10.1086/158997.

[120] P. Ferrando et al. "Measurement of the isotopic composition of cosmic-rays at 3 GeV/n using a new geomagnetic method". In: *Astronomy and Astrophysics* 193.1-2 (Mar. 1988), pp. 69–80.

[121] R. A. Mewaldt et al. "High resolution measurements of galactic cosmic-ray neon, magnesium, and silicon isotopes". In: *Astrophysical Journal* 235 (Jan. 1980), pp. L95–L99. DOI: 10.1086/183166.

[122] W. R. Webber, A. Lukasiak, and F. B. McDonald. "Voyager Measurements of the Mass Composition of Cosmic-Ray Ne, Mg, Si and S Nuclei". In: *The Astrophysical Journal* 476.2 (Feb. 1997), pp. 766–770. DOI: 10.1086/303662.

[123] W. R. Webber. "The charge and isotopic composition of Z = 6-14 cosmic ray nuclei at their source". In: *The Astrophysical Journal* 252 (Jan. 1982), pp. 386–392. DOI: 10.1086/159565.

[124] D. Maurin et al. *Cosmic-ray database update: ultra-high energy, ultra-heavy, and anti-nuclei cosmic-ray data (CRDB v4.0)*. 2020. arXiv: 2005.14663 [astro-ph.HE].

[125] A. Obermeier et al. "ENERGY SPECTRA OF PRIMARY AND SECONDARY COSMIC-RAY NUCLEI MEASURED WITH TRACER". In: *The Astrophysical Journal* 742.1 (Nov. 2011), p. 14. DOI: 10.1088/0004-637x/742/1/14.

[126] A. Buffington, C. D. Orth, and T. S. Mast. "A measurement of cosmic-ray beryllium isotopes from 200 to 1500 MeV per nucleon." In: *The Astrophysical Journal* 226 (Nov. 1978), pp. 355–371. DOI: 10.1086/156616.

[127] P. S. Freier, J. S. Young, and C. J. Waddington. "The neutron-rich isotopes of cosmic-ray neon and magnesium". In: *The Astrophysical Journal, Letters* 240 (Aug. 1980), pp. L53–L58. DOI: 10.1086/183322.

[128] M. Aguilar et al. "Properties of Neon, Magnesium, and Silicon Primary Cosmic Rays Results from the Alpha Magnetic Spectrometer". In: *Phys. Rev. Lett.* 124 (21 May 2020), p. 211102. DOI: 10.1103/PhysRevLett.124.211102.

[129] AMS Collaboration. "The Alpha Magnetic Spectrometer (AMS) on the International Space Station: Part II - Results from the First Seven Years". In: *Physics Reports (to be published)* (2020).

[130] *AMS UTTPS EVA 1*. URL: https://blogs.nasa.gov/spacestation/2019/11/15/spacewalkers-complete-first-excursion-to-repair-cosmic-particle-detector/.

[131] *AMS UTTPS EVA 2*. URL: https://blogs.nasa.gov/spacestation/2019/11/22/astronauts-complete-intricate-tasks-during-second-cosmic-repair-spacewalk/.

[132] *AMS UTTPS EVA 3*. URL: https://blogs.nasa.gov/spacestation/2019/12/02/astronauts-wrap-up-third-spacewalk-for-cosmic-particle-detector-repairs/.

[133] *AMS UTTPS EVA 4*. URL: https://blogs.nasa.gov/spacestation/2020/01/25/astronauts-wrap-up-spacewalk-repair-job-on-cosmic-ray-detector/.